

Erosion-Oxidation of Mild Steel in a Fluidized Bed Environment

Thomas Edward Howes

St Catharine's College,
Cambridge

A dissertation submitted for the degree of Doctor of Philosophy in the
University of Cambridge

To Mum, Dad, Catherine and Alex

Preface

The work described herein is the authors own, except where others have been acknowledged or referenced in the text. It was carried out between October 1992 and October 1996 in the Department of Materials Science and Metallurgy under the supervision of Dr. J. A. Little. No part of this dissertation has been or is being submitted for the degree of Doctor of Philosophy in the University of Cambridge and does not exceed 60,000 words.

Some of the results in this thesis have been previously published in the following papers:

Howes, T. E., Rogers, P. M., Little, J. A. and Hutchings, I. M. (1995), "Erosion-corrosion of mild steel in a temperature gradient," Wear, **186-187**, 316-324.

Rogers, P. M., Howes, T. E., Little, J. A. and Hutchings, I. M. (1995), "Wastage of low alloy steels in a fluidized bed environment," Wear, **186-187**, 306-315.

November 1996

T. E. Howes

St Catharine's College

Cambridge

Acknowledgements

Thanks must go to my supervisors Drs. J. A. Little and I. M. Hutchings for their help and advice during my Ph.D. and special thanks to Dr. P. M. Rogers for his invaluable help and discussions about the finer points of erosion-corrosion. Thanks to all the Little Boys (Paul, Simon, Duncan, Ferhat, Cash, and Jen-hung) for making work in the lab such an enjoyable experience over these many years and also Servet and Atul for the lunch time excursions.

Funding was provided by the EPSRC and British Coal, and thanks the Drs. John Oakey and Nigel Simms for their help and industrial perspective on this work. Also thank you to Professors C. Humphreys and A. Windle for providing the laboratory facilities and to all the department's technical staff who have helped me.

Finally thanks to all my friends and family for their encouragement and support while I was writing up.

Erosion-Oxidation of Mild Steel in a Fluidized Bed Environment

Thomas Edward Howes

St Catharine's College, Cambridge

This thesis is a contribution to research into erosion-corrosion investigating the rapid wastage of in-bed heat exchanger tubing in fluidized bed combustors. Two main new areas of research were investigated; erosion-corrosion of mild steel in a temperature gradient and erosion-corrosion modelling.

It has been suggested that differences between the wastage behaviour measured in fluidized bed combustors and laboratory studies is due to laboratory tests being carried out isothermally (specimen and fluidized bed at the same temperature) whereas, in a FBC boiler, the fluidized bed is considerably hotter than the metal heat exchanger tubing. The fluidized bed test rig was modified to increase the temperature gradient between the specimen and the fluidized bed from initial tests conducted by Rogers (1992b). Tests were carried out over a range of bed temperatures (300 - 500° C) and cooled specimen surface temperatures (175 - 500° C) with a maximum temperature difference between the two of 250° C. It was discovered that the temperature of the wear scar during a test was up to 200° C hotter than the temperature at the back of the specimen where the specimen temperature was initially measured in tests by Rogers (1992b). After temperature calibration tests the wastage of the specimens in a temperature gradient were very similar to the wastage of specimens exposed isothermally at the same metal temperature.

Short term oxidation experiments were conducted on mild steel to obtain oxidation kinetics for erosion-corrosion modelling. It was found that the initial apparent parabolic rate constant was an order of magnitude larger than at longer time. Erosion studies were conducted with the aim to obtain quantitative data on the particle flux and the erosive behaviour of the bed with temperature. Results were not accurate enough to yield quantitative data but provided an estimate of the particle flux in the fluidized bed test rig.

Results obtained from the short term oxidation and erosion studies were used in simple erosion-oxidation models to construct erosion-corrosion regime maps which tended to predict metal erosion to higher temperatures than observed experimentally. Predictions of material wear from the combination of an oxide removal and spalling mechanism predicted sensible wastage rates which agreed with experimental results.

Contents

Introduction	1
Chapter 1 - Wear	
1.1. Introduction	3
1.2. Erosion	3
1.2.1. Ductile Erosion.....	3
1.2.2. Brittle erosion.....	7
1.2.3. Impact variables	10
(i) Time	10
(ii) Impact Velocity.....	10
(iii) Impact Angle.....	11
(iv) Particle Size	11
(v) Material Properties.....	12
(vi) Particle Shape.....	12
(vii) Particle Hardness	13
(viii) Particle flux.....	13
(ix) Temperature	13
1.3. Abrasion	13
1.3.1. Mechanisms.....	14
1.3.2. Test Variables.....	15
(i) Material Hardness	16
(ii) Time	16
(iii) Particle size	16
(iv) Particle Hardness	16
(v) Load	16
1.3.3. Models.....	16
1.3.3.1. Ductile Models.....	16
1.3.3.2. Brittle models.....	17

Chapter 2 - Oxidation

2.1. Introduction	19
2.2. Thermodynamics of Oxidation	19
2.3. Nucleation and Growth of Oxide	21
2.3.1. Initial stages of oxidation	21
2.3.2. Growth of oxide	21
(i) Parabolic rate law.....	22
(ii) Linear rate law.	22
(iii) Logarithmic rate laws.....	23
2.3.3. Non-planar reactions	23
2.4. Oxidation of Iron	24
2.4.1. Effect of experimental variables.....	25
2.5. Effect of adding alloying elements	29
2.5.1. Effect of cold work on low alloy steels.....	30
2.6. Stresses in oxide films	30
2.6.1. Growth stresses	30
(i) Volume differences between the oxide and metal. 30	
(ii) Epitaxial stresses.....	31
(iii) Compositional changes in the alloy or scale.....	31
(iv) Point defect stresses.....	31
(v) Oxide formation within the scale.....	31
(vi) Specimen geometry.....	31
2.6.2. Stress relief of growth stresses	32
2.6.3. Thermal stresses	32

Chapter 3 - Fluidized Bed Combustion

3.1. Introduction	33
3.2. Fluidized bed behaviour	33
3.2.1. Effect of particle size and density	34
3.2.2. Heat transfer in fluidized beds	35
3.3. Fluidized bed combustion (FBC)	36
3.4. Advantages of fluidized bed combustion	36
3.5. Types of combustor	37
3.5.1. Atmospheric fluidized bed combustors (AFBCs)	37

3.5.1.1.	Bubbling fluidized bed combustors	37
(i)	Industrial boilers	38
(ii)	Utility boilers	38
3.5.1.2.	Circulating fluidized bed combustors (CFBCs).....	38
3.5.2.	Pressurized fluidized bed combustors (PFBCs).....	39
3.6.	Wear problems experienced in FBCs.....	40
3.6.1.	Introduction	40
3.6.2.	Regions experiencing wear	41
(i)	AFBCs and PFBCs	41
(ii)	CFBCs.....	41
3.6.3.	Wear mechanisms	42
(i)	Intrinsic wear.....	42
(ii)	Bubble induced wear.....	42
(iii)	Long range flows.....	42
(iv)	In-bed jets.....	42
(v)	Local irregularities	43
3.6.4.	Factors effecting wastage	43
(i)	Metal temperature	43
(ii)	Coal and bed material	44
(iii)	Fluidization conditions	45
(iv)	Combustor design	46
(v)	Materials	47
3.6.5.	Methods of combating wastage.....	47
(i)	Changing combustor design.....	47
(ii)	External protection.....	48
(iii)	Wear resistant coatings and surface treatments	48
(iv)	CFBCs.....	48
(v)	Summary	49

Chapter 4 - Erosion - corrosion

4.1.	Introduction.....	50
4.2.	Low temperature and velocity laboratory studies	50
4.2.1.	Low flux	50
4.2.1.1.	Sethi & co-workers	50
4.2.1.2.	Levy & co-workers.....	52
4.2.2.	High flux	54

4.2.2.1.	The Cambridge rig	54
4.2.2.2.	The UMIST rig.....	62
4.2.2.3.	The Berkeley rig.....	65
4.2.2.4.	The NPL rig	69
4.3.	Mechanisms and modelling	70
4.3.1.	Comparison with other erosion-corrosion classifications	73
4.3.2.	Modelling wastage for different regimes	76
4.3.2.1.	Erosion enhanced corrosion	76
4.3.2.2.	Scale Flaking or Spalling	78
4.3.2.3.	Corrosion affected erosion regime	80
4.4.	Summary	80
 Chapter 5 - Experimental Methods		
5.1.	Introduction	83
5.2.	Erosion-corrosion apparatus	83
5.2.1.	Bed particles	85
5.2.2.	Test specimens	85
5.2.3.	Rig modifications	87
5.2.4.	Experimental procedure	90
(i)	Preliminaries	90
(ii)	Starting a test.....	91
(iii)	Shutting down	92
5.3.	Specimen measurement	92
5.3.1.	Analysis of data	94
5.3.2.	Analysis techniques	94
 Chapter 6 - Isothermal erosion-oxidation of mild and 316 stainless steel		
6.1.	Introduction	95
6.2.	Specimen Appearance	97
6.3.	Wastage behaviour	101
6.4.	Microscopic observations	106
(i)	Interference coloured oxide covered wear scar	107
(ii)	Alumina deposit	107
(iii)	Higher temperatures	108
6.5.	Conclusions	117

Chapter 7 - Erosion-oxidation of mild steel in a temperature gradient

7.1. Introduction	118
7.2. Test History	123
7.2.1. First Phase	123
7.2.2. Second Phase.....	123
7.2.3. Calibration of wear scar temperatures.....	124
7.3. Results	128
7.3.1. Specimen appearance	128
7.3.2. Specimen wastage behaviour	131
7.4. Discussion	136
7.4.1. Wastage - velocity behaviour	136
7.4.2. Wear scar appearance and temperature	138
7.4.2.1. Visual appearance	138
7.4.2.2. Microscopic appearance.....	140
7.4.3. Wastage - temperature behaviour.....	148
7.4.3.1. The effect of cooling on the fluidized bed	148
7.4.3.2. Alumina embedment.....	149
7.4.4. Origin of temperature increase over the wear scar	151
7.4.5. Summary	152
7.5. Conclusions	152

Chapter 8 - Short term oxidation

8.1. Introduction	154
8.2. Experimental methods	154
8.2.1. Experimental procedure	154
8.2.2. Analysis of data	156
8.2.2.1. Errors and calibration of temperature ramp	156
8.2.2.2. Calculation of rate constants	159
8.3. Results	160
8.3.1. Effect of temperature.....	160
8.3.2. Effect of surface preparation	168
8.4. Discussion	171
8.5. Conclusions	173

Chapter 9 - Erosion Studies

9.1. Introduction	175
9.2. Erosion drop tube experiments	175
9.2.1. Experimental methods.....	175
9.2.2. Results and discussion.....	177
(i) Drop tube specimens.....	177
(ii) Fluidized bed specimen.....	185
9.2.3. Summary	185
9.3. Short term exposure experiments	186
9.3.1. Introduction	186
9.3.2. Experimental methods.....	186
9.3.2. Results and discussion.....	188
9.3.2.1. Alumina particles	188
9.3.2.2. Glass beads.....	189
(i) Drop tube specimens.....	189
(ii) Fluidized bed specimens.....	190
9.3.3. Summary	190
9.4. Silica tube experiments	199
9.4.1. Introduction	199
9.4.2. Experimental methods.....	199
9.4.3. Results	200
9.4.4. Discussion	205
9.4.5. Conclusions	205

Chapter 10 - Erosion-corrosion modelling

10.1. Introduction	206
10.2. Erosion-corrosion maps	206
10.2.1. Definition of systems.....	206
10.2.2. Map construction.....	209
10.2.3. Results	211
10.2.3.1. Sundararajan's maps	211
10.2.3.2. Stack and Bray's maps	213
10.2.3.3. Fluidized bed rig values.....	214

(i) Sundararajan's maps	216
(ii) Stack and Bray's maps	222
10.2.4. Conclusions	224
10.3. Erosion-corrosion wear modelling	224
10.3.1. Introduction	224
10.3.2. Results and Discussion.....	226
10.3.2.1. Paralinear erosion-oxidation	226
10.3.2.2. Oxide removal and spalling erosion-oxidation models	230
10.3.3. Conclusions	232
Appendix A - FORTRAN program for constructing erosion- corrosion maps.....	236
Appendix B - Variables and constants used for erosion-corrosion map construction	238
Appendix C - FORTRAN program to calculate oxide profile over time	239
Chapter 11 - Conclusions and Future work	
11.1. Conclusions	241
11.2. Future work	242
Chapter 12 - References	244

Introduction

Fluidized bed combustion is a clean coal technology with many advantages over conventional boilers such as increased efficiency and better control of emissions. However, rapid wastage of heat-exchanger tubes by erosion-corrosion has been a problem in fluidized bed combustors (FBCs).

An experimental test rig was constructed (Little *et al.*, 1987) to investigate erosion-corrosion in a fluidized bed. Specimens, mainly high and low alloy steels, in the form of a bar were rotated in a horizontal plane within the fluidized bed experiencing an impact velocity of up to 3 m s^{-1} and at temperatures up to 800° C . Previous studies by Entwisle (1990), Ninham *et al.* (1989a, 1989b, 1991) and Rogers (1992b) investigated the behaviour of many high and low alloy steels, numerous coatings and the effect of a temperature gradient achieved by air and water cooling a tube specimen.

Continuing from the previous studies the effect of a temperature gradient on the erosion-corrosion of mild steel was investigated further by making modifications to the test rig to increase the temperature gradient between the specimen and the fluidized bed. This was investigated to simulate more closely the conditions found in fluidized bed combustor heat exchanger tubing as the wastage-temperature behaviour measured from isothermal tests (the specimen and fluidized bed at the same temperature) in laboratory studies differed from those observed in FBCs.

The other main area of work was modelling erosion-corrosion processes in the fluidized bed test rig as the few models that exist are at a lower stage of development when compared with corrosion and erosion models.. Experiments were conducted to obtain suitable data for simple erosion-corrosion models so that the experimental results and model predictions could be compared.

A review of literature in the relevant background areas of wear, oxidation, fluidized bed combustion and fluidized bed laboratory studies are described in Chapters One to Four respectively. The experimental methods for the fluidized bed test rig are described in Chapter Five. The results of exposing mild steel to a temperature gradient are described and discussed in Chapter Seven, with similar isothermal tests described in Chapter Six for comparison. Chapter Eight describes short term oxidation tests on

mild steel to obtain suitable kinetic data for erosion-corrosion models and Chapter Nine outlines several erosion studies using the test rig and an erosion drop tube to obtain quantitative values of particle flux and the erosive behaviour of the fluidized bed with temperature. Chapter Ten uses the data obtained in Chapters Eight and Nine in simple erosion-corrosion models to construct erosion-corrosion maps of dominant erosion-corrosion mechanisms and to model the material wastage in the fluidized bed test rig.

Chapter 1

Wear

1.1. Introduction

Wear is defined as the progressive loss of substance by contact between surfaces. Wear processes include; erosion, abrasion, fretting, corrosion wear, adhesive wear, cavitation, and surface fatigue wear. The material wastage of in-bed surfaces in a fluidized bed combustor may involve the action of erosion, abrasion, and corrosive wear. Erosion and abrasion are discussed below in sections 1.2 and 1.3 respectively and erosion-corrosion, which is a form of corrosive wear, is discussed in Chapter Four.

1.2. Erosion

Erosion and more specifically solid particle erosion occurs when discrete solid particles strike and rebound from a surface, with the dominant force on a particle usually being the contact force by the surface. Ductile and brittle erosive mechanisms are reviewed and then a brief summary of results for various impact variables are given.

1.2.1. Ductile Erosion

Ductile erosion is usually considered to occur when material is removed by a process of plastic deformation. Under the broad heading of plastic deformation four more specific mechanisms for material removal have been identified; (1) cutting, (2) ploughing and extrusion, (3) fatigue and (4) shear band formation.

One of the first erosion models, assuming a cutting or micromachining mechanism, was proposed by Finnie (1960) who considered the motion of particle tip cutting through the target material. An expression for the volume, Q , removed by a single impact of particle mass, m , and velocity, V was derived:

$$Q = \frac{mV^2}{p\Psi K} \left(\sin 2\alpha - \frac{6}{K} \sin^2 \alpha \right) \quad \tan \alpha \leq \frac{K}{6} \quad (1.1)$$

$$Q = \frac{mV^2}{p\Psi K} \left(\frac{K}{6} \cos^2 \alpha \right) \quad \tan \alpha \geq \frac{K}{6} \quad (1.2)$$

where α is the impact angle to the horizontal, K is the ratio of vertical to horizontal forces on the particle, Ψ is the ratio of depth of contact to depth of cut (both α and Ψ were approximated to 2) and p is the flow stress. The disadvantage of this theory was that it predicted no erosion for impact angles of 90° .

To account for erosion at normal incidence Bitter (1963) considered deformation wear as the dominant wear mechanism at this angle, and to be a completely different phenomenon to the cutting mechanism dominant at shallow angles. Thus the erosion process was the sum of these two mechanisms. The nature of this deformation wear was not suggested and at the time and experimental evidence for the existence of two distinct types of erosive wear was poor.

Neilson and Gilchrist (1968) simplified Bitter's approach by extending the formula to consider the horizontal component of the forces which are responsible for the cutting mechanism resulting in:

$$W = \frac{\frac{1}{2}MV^2 \cos^2 \alpha \sin \alpha}{\phi} + \frac{\frac{1}{2}M(V \sin \alpha - K)^2}{\varepsilon} \quad \alpha < \alpha_0 \quad (1.3)$$

and

$$W = \frac{\frac{1}{2}MV^2 \cos^2 \alpha}{\phi} + \frac{\frac{1}{2}M(V \sin \alpha - K)^2}{\varepsilon} \quad \alpha > \alpha_0 \quad (1.4)$$

where W is the erosion produced by M pounds of particles at an attack angle α and particle velocity V , K is the velocity component normal to the surface below which no erosion takes place in certain hard materials and α_0 is the angle of attack at which the residual parallel velocity component at small angles of attack. ϕ and ε are the units of kinetic energy that must be absorbed by the surface to release one unit mass of eroded material for cutting and deformation wear respectively.

Despite this all the above theories have parameters that are difficult to measure accurately, e.g. ϕ and ε .

Partly to account for the non-zero erosion at normal impact angles predicted by the cutting models, Tilly (1973) proposed a two stage mechanism involving fragmentation of particles. Particles of near-normal impact were seen to fragment sending a radial spray of fragments across the target at shallow angles, causing secondary damage by cutting. The velocities used by Tilly were very high (about 300 m s^{-1}) and at lower velocities particle fragmentation was believed to be of minor importance.

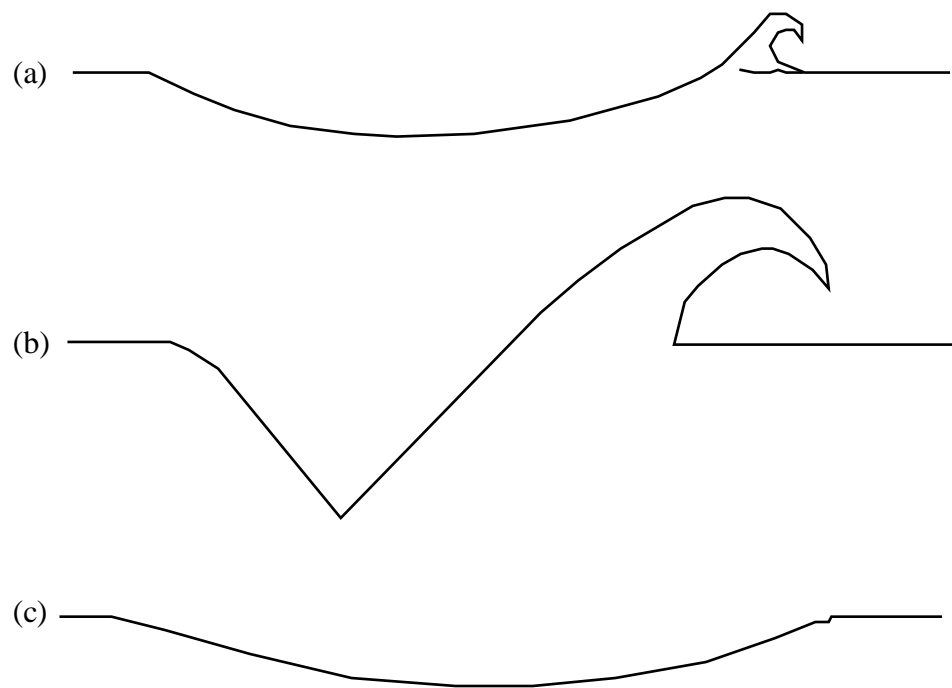


Fig. 1.1. Sections through craters formed by single impacts, after Hutchings (1979).

(a) Ploughing deformation by a spherical particle, (b) Type I cutting by an angular particle, (c) Type II cutting by an angular particle.

Winter and Hutchings (1974) and subsequently Hutchings (1979) in a study of large single spherical and angular (square plates) particle impacts, identified three basic types of impact damage (Fig. 1.1). Blunt particles deformed the surface by ploughing, displacing the material sideways with about 10% to 25% displaced forwards into a lip. Only at large velocities was the lip removed by a single impact, and it was concluded that at lower velocities subsequent impacts would remove the fragile lips, resulting in material loss. Angular particles caused damage by two types of cutting, type I and type II, depending on the orientation of the particle as it strikes the surface. Type I cutting

occurs when the particle is rolling forwards, indenting the surface and raising a prominent lip. Again multiple impacts are required for material loss. If the particle rolled backwards a true machining action was seen to occur, in which the edge of the particle cut a chip from the surface. This was termed Type II cutting and occurs over only a narrow range of particle geometries and impact orientations. It has since been shown (Bellmen and Levy, 1981) that the predominant mode of material removal is normally one of ploughing, with cutting becoming significant only at shallow impact angles and with angular particles.

Observations from several authors reported a different erosion mechanism at normal impact angles involving the formation and removal of platelets or small flakes over a large number of impacts. This led to fatigue based models proposed first by Mamoun (1975) and later extended by Hutchings (1981). These models assumed that any volume of material reaching a critical strain ε_c (considered as a material property and called erosion ductility) will be lost. Hutchings considered an average strain associated with each impact $\Delta\varepsilon_p$ and used random walk theory to predict the strain of a point on the surface after a number of impacts, thus:

$$\Delta\varepsilon_p N_f^{1/2} = \varepsilon_c \quad (1.5)$$

where N_f is the mean number of impacts to cause material detachment. From this and an assumption that all of the particle's kinetic energy is available to form an indentation, the erosion rate was derived as:

$$E = 0.033 \frac{\alpha \rho \sigma^{1/2} v^3}{\varepsilon_c^2 P^{3/2}} \quad (1.6)$$

where α is the fraction of indentation volume which represents the volume of plastically deformed material, ρ and σ are the target material and particle densities respectively, v is the impact velocity and P is the dynamic indentation hardness. The dynamic hardness is not necessarily equal to the static hardness measured by a hardness indenter because of the high strain rates involved during a particle impact. A velocity exponent of 3 is predicted which correlates well with experimentally obtained values. Also the insensitivity of erosion rate to heat treatment and cold work is qualitatively explained by the relationship between P and ε_c , as an increase in P (through heat treatment or cold work) is usually accompanied by a decrease in ε_c . However, the model did not explain

the excellent correlation between the erosion rate and the thermophysical properties of the target material, i.e. the specific heat multiplied by the change in temperature required to reach the target melting point. Sundararajan and Shewmon (1983) and Sundararajan (1983) proposed a model based on the formation and removal of an extruded lip. Lip formation was considered the result of the localisation of deformation in near surface regions and its separation determined once a critical strain had been exceeded. Thus this model was similar to Hutchings' model in the sense that a critical strain criterion was used, although the mechanism postulated was quite different.

Target melting as an erosion mechanism has been proposed by Smeltzer *et al.* (1970). Although experimental evidence of melting has been shown to occur for low melting point metals, its effect on material loss is probably very small.

Observations looking at platelet formation in more detail (Rickerby, 1980; Christman, 1979) documented the development of platelets at the intersections of craters. Bellman and Levy (1981) used these observations and their own to formulate a mechanism of platelet erosion on a ductile metal. They proposed that a surface temperature rise due to erosion leads to a softening of the near-surface region, so that a work-hardened layer beneath this acts as an anvil against which the softer layer is deformed. This has not been widely accepted and was later considered by Hutchings and Levy (1986), who postulated that a thermally softened layer was not an essential feature of the platelet erosion mechanism under all conditions.

1.2.2. Brittle erosion

Erosion of brittle materials take place by the formation and intersection of cracks. The morphology of the cracks formed has been studied extensively and has been shown to depend on several factors: particle shape, mass and velocity, and target material hardness and toughness. Two crack patterns have been identified and modelled, soft blunt particles tend cause purely elastic deformation and form conical Hertzian cracks (Fig. 1.2), whereas hard angular particles cause some plastic deformation and form radial cracks (Fig. 1.3). Hockey (1971) provided direct evidence for plastic flow in ceramics obtained from TEM studies of impact sites.

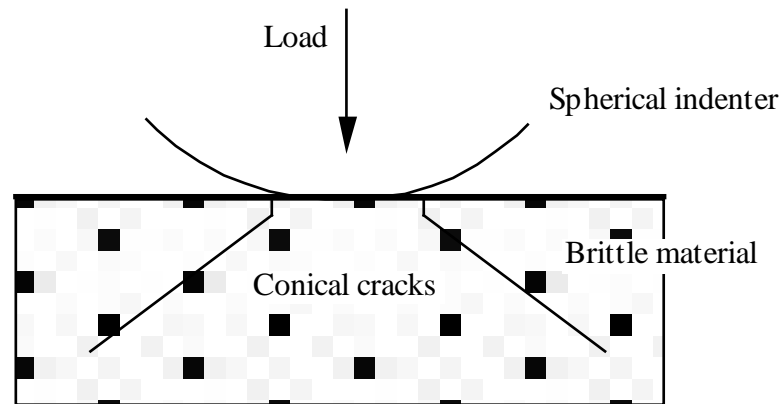


Fig. 1.2. Hertzian cracks formed in brittle materials after normal impact with rounded particles.

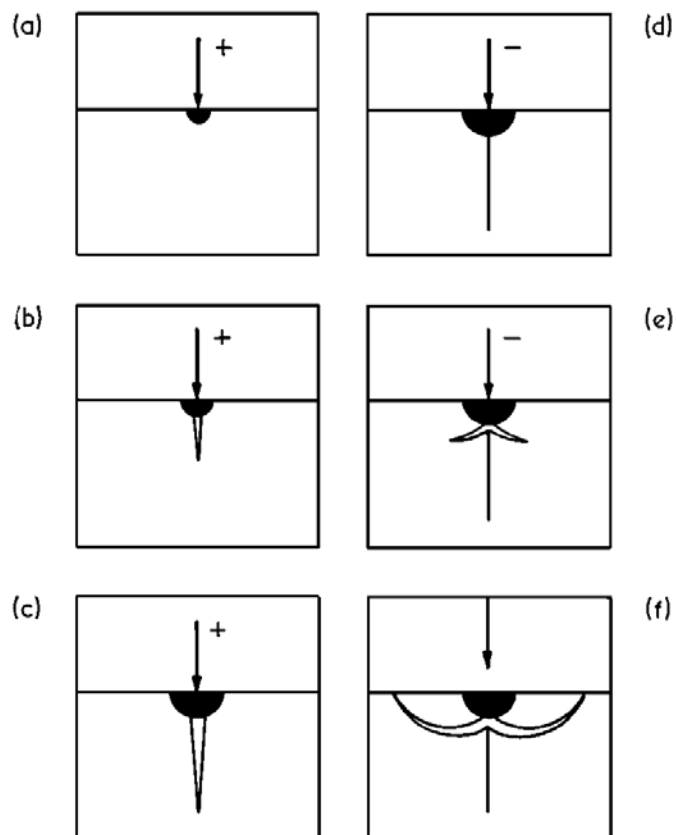


Fig. 1.3. The development of radial and lateral cracks in brittle solids. Radial crack forms during loading (+) half cycle, lateral crack during unloading (-) half-cycle. Fracture initiates from deformation zone (dark region) (Lawn and Swain, 1975; Evans and Wilshaw, 1976).

Hertz (1882) was the first to study the theoretical stresses caused by a sphere indenting a surface for purely elastic deformations. Several authors studied the formation of the conical Hertzian cracks and it was found that they initiate from pre-existing flaws and thus a minimum threshold stress (corresponding to a minimum impact velocity) is required for formation. Sheldon and Finnie (1966) proposed a model based upon the formation and intersection of Hertzian cracks and the equation derived for the normalised erosion (g/g) was:

$$E \propto r^a v^b \quad (1.7)$$

where r is the particle radius, v is the particle velocity and, a and b are related to the Weibull constants of the target material. Typical values for a and b are 4.0 - 4.2 and 2.6 - 3.0 respectively. Although a satisfactory agreement has been shown between theoretical and experimentally determined values of a and b this model is only valid for flat homogeneous surfaces with no plastic deformation. Therefore the model breaks down as erosion precedes when the surface is no longer flat, and at high velocities when plastic deformation occurs even with spherical particles (Lawn and Wilshaw, 1975).

As previously mentioned when plastic flow does occur, a second type of crack morphology is created. A study of these cracks by Lawn and Swain (1975), and Evans and Wilshaw (1976) using static indentation tests has shown radial cracks form during the loading part of the impact cycle and as the load is removed the residual stresses arising from the plastic deformation cause the formation of lateral cracks. Lateral cracks usually curve and propagate to the target surface, resulting in chip formation and loss of material from the surface.

Two major elastic-plastic theories have been developed and both assume lateral crack formation of size, c , determined by the relation (Lawn and Fuller, 1975).

$$\frac{P}{c^{3/2}} = \beta K_c \quad (1.8)$$

where P is the maximum normal load during impact, K_c is the critical stress intensity factor and β is a non dimensional constant. The volume, V , of material removed due to an impact was considered to be a cylinder of radius, c , and of depth, d , where d is the depth of the crack beneath the surface, thus;

$$V = \pi c^2 d \quad (1.9)$$

The two theories differed in their assumed dependence of impact load, P , on the kinetic and material parameters that are important to erosion. The theory by Evans *et al.* (1978) used a dynamic wave-propagation model to calculate P , and the erosion rate E (g/g) was derived as:

$$E \propto v_o^{3.2} r^{3.7} \frac{\rho^{1.6}}{K_c^{1.3} H^{0.25}} \quad (1.10)$$

where v_o was the initial particle velocity, r and ρ are the particle radius and density respectively, and K_c and H are the target material toughness and hardness. The second theory by Wiederhorn and Lawn (1979) assumes that the particle's kinetic energy is completely absorbed by plastic flow. The derivation of erosion rate leads to:

$$E \propto v_o^{2.4} r^{3.7} \frac{\rho^{1.2} H^{0.11}}{K_c^{1.3}} \quad (1.11)$$

These two models were compared with experimental results by Wiederhorn and Hockey (1983), and comparison was satisfactory with the dynamic theory in slightly better agreement. The lack of good agreement was explained by the variation in particle/target impact orientations, the incomplete formation of lateral cracks in materials of higher fracture toughness and the presence of microstructural features such as pores and weak grain boundaries. When materials contain inhomogeneous features, these models fail to predict erosion rates and, to date, no satisfactory predictive models have been developed.

1.2.3. Impact variables

(i) Time

Almost all authors have reported that mass loss varies linearly with mass of erodent used. For ductile materials an initial incubation period is often observed, particularly at high impact angles and high material ductility, where the erosion rate is low. This mass increase is also commonly associated with an incubation period due to erosive particle embedment. Brittle materials do not show any incubation period.

(ii) Impact Velocity

The erosion rate of both brittle and ductile materials can usually be expressed as a

power law function of velocity; $\varepsilon = kv^n$. The exponent, n , is typically in the range of 2 to 3 and often lies around 2.4 for ductile metals, and 2 to 4 for ceramics, although values as high as 6 have been reported (Finnie, 1960).

(iii) *Impact Angle*

The effect of impact angle on ductile and brittle materials is shown in Fig. 1.4. Ductile materials tend to have a maximum erosion rate at shallow impact angles (20° to 30°) and around a third of the maximum at normal incidence. Brittle materials erode increasingly with angle with a maximum at normal incidence.

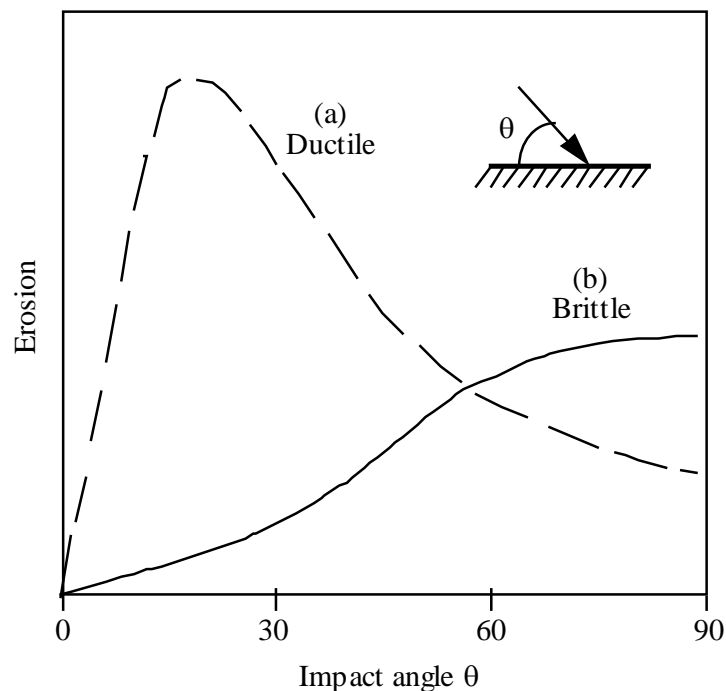


Fig. 1.4 . Typical dependence of erosion on impact angle θ , after Finnie *et al.* (1967). Ductile metals commonly show peak erosion at a shallow impact angle (curve a), while brittle materials often show maximum wear for normal incidence (curve b).

(iv) *Particle Size*

For ductile materials there is an increase in erosion with increasing particle size up to a critical diameter of around $100\ \mu\text{m}$ above which the erosion rate remains constant. Misra and Finnie (1981a) discussed the many theories that have been suggested to explain this effect and concluded that it is probably due to an actual increase in flow stress with indentation size. Brittle material erosion follows a power law with

exponents between 3 and 4, as predicted by the elastic-plastic fracture mechanisms.

(v) **Material Properties**

The correlation between measured material properties and the erosion rate is often not a simple one, particularly due to the high strains and strain rates experienced during erosion. The hardness of annealed metals has been found to follow an inverse relationship with the erosion rate, although thermal and work hardening have no effect (Fig. 1.5) (Finnie *et al.*, 1967) as it is thought that the surface becomes heavily cold worked during steady state erosion and may reach the limiting hardness of the material.

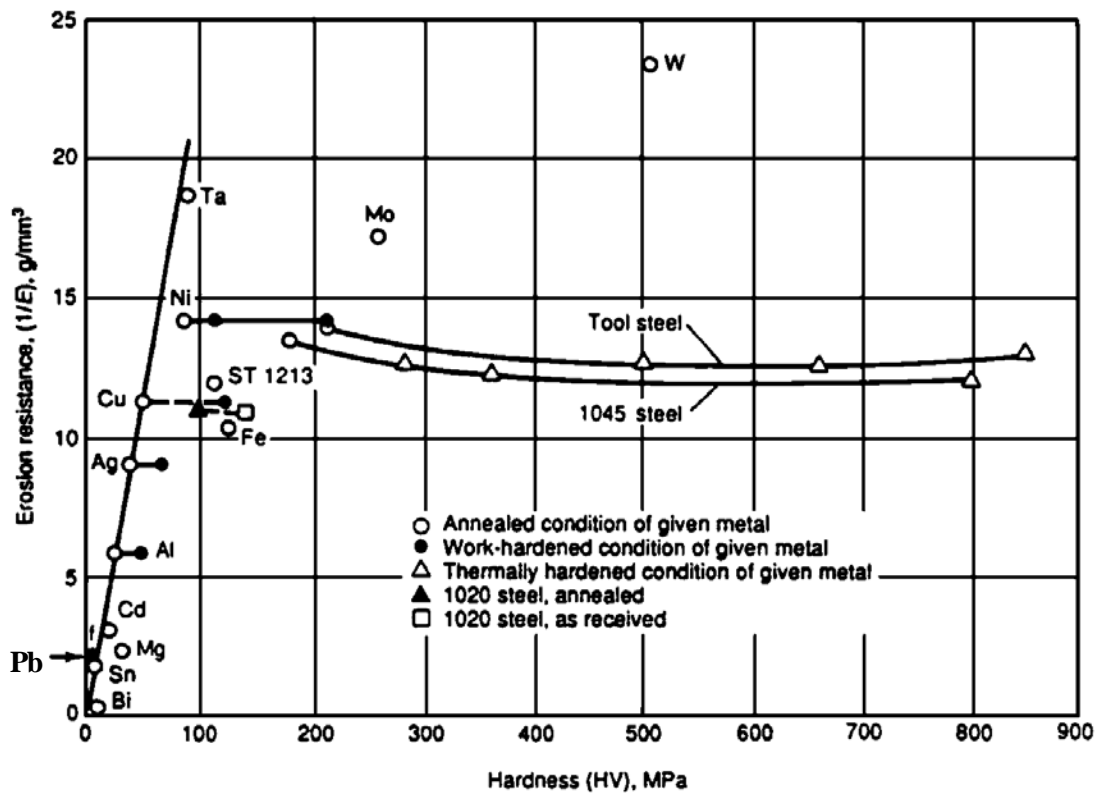


Fig. 1.5. Plot of erosion resistance versus static hardness for selected materials, after Finnie *et al.* (1967). Erosion was generated by 250 μm SiC impinging at the surface at an angle of 20° with a velocity of 76 m s^{-1} .

(vi) **Particle Shape**

Generally erosion rates of ductile materials increase with particle angularity, as sharper corners favour cutting mechanisms which remove more material per impact. For example Cousens and Hutchings (1983) found a ten fold increase in the erosion rate of

mild steel eroded with crushed glass when compared with glass spheres. The effect of angularity on brittle materials is discussed above, where plastic deformation is more likely to occur.

(vii) Particle Hardness

The ratio of particle hardness to target hardness (H_p/H_t) is an important factor for both brittle and ductile materials. The erosion rate of ductile materials decreases dramatically when $H_p/H_t < 1$, and Wada *et al.* (1992) have observed a relation $E \propto (H_p/H_t)^b$, where b is positive, for brittle materials irrespective of erosion mechanism.

(viii) Particle flux

As particle flux increases there is an observed decrease in erosion rate. Anand *et al.* (1987) have demonstrated that because of interference of the rebounding particles with incident particles, the surface is effectively shielded.

(ix) Temperature

Sundararajan (1990) has reviewed the effect of temperature in the absence of complications caused by corrosion and the effect is not simple. Some materials erode more rapidly with increasing temperature while the reverse is true for other materials.

1.3. Abrasion

Abrasive wear of a surface can be defined as material removal due to sliding contact with abrasive particles or a surface. Abrasion is typically categorised according to two types of contact: two body and three body abrasion (Fig. 1.6). Two body abrasion occurs when an abrasive slides along a surface, and three body abrasion occurs when abrasive particles are caught between two surfaces and are able to move relative to one another. Typically the abrasive wear rate for two-body abrasion is ten times that of three-body abrasion, probably because the average loose abrasive particle spends 90% of its time rolling and only 10% abrading (Rabinowicz *et al.*, 1961).

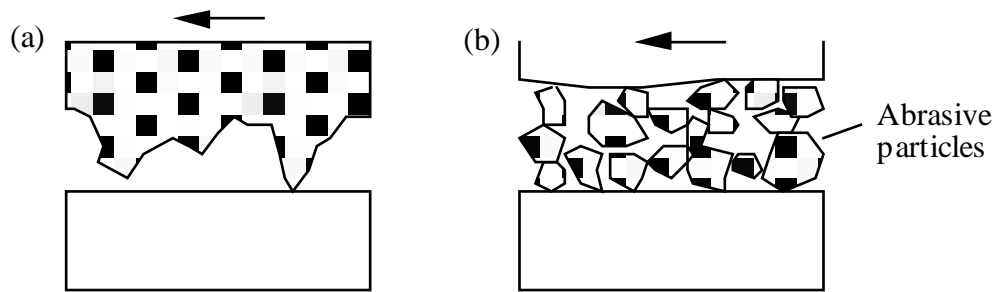
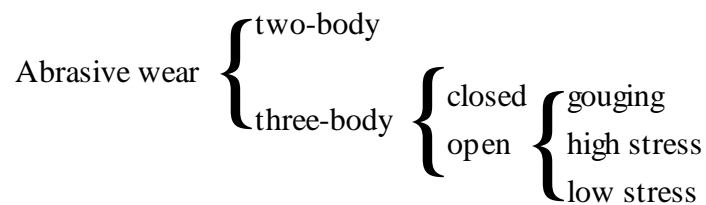


Fig. 1.6. A schematic diagram of abrasion types (a) Two body abrasion and (b) Three body abrasion.

Abrasion can be further classified as follows:



Closed and open three-body abrasive wear refer to the contact environments. Closed three-body abrasive wear occurs when the abrasive particles are trapped between two closely spaced surfaces so that the properties of one surface may effect the other. Open three-body abrasion occurs for widely spaces surfaces or when only one surface is involved in the wear process. Open three-body abrasion can be further classified into three groups: gouging when coarse abrasives cut in to the surface, high stress when the abrasive is crushed and low stress when the abrasive remains intact. The most dominant form of abrasion experienced in the fluidized bed test rig is probably low stress open three-body abrasion (Entwisle, 1990).

1.3.1. Mechanisms

Five abrasion mechanisms have been observed and four are shown in Fig. 1.7 in their idealised form. Microploughing occurs under light loads and material is displaced from a groove to the sides. This does not remove any material unless repeated displacement causes an accumulation of plastic deformation leading to material loss though microfatigue. When the ratio of shear strength of the contact interface relative to the

shear strength on the bulk rises high enough (from 0.5 to 1.0) it is found that a wedge can develop ahead of the abrasive tip (Kato, 1990) (not shown in Fig. 1.7). Pure microcutting results in material loss equal to the volume of the wear groove produced. Microcracking may occur when highly concentrated stresses are imposed by abrasive particles, particularly in the surface of brittle materials. Fragments are detached from the surface due to crack formation and propagation.

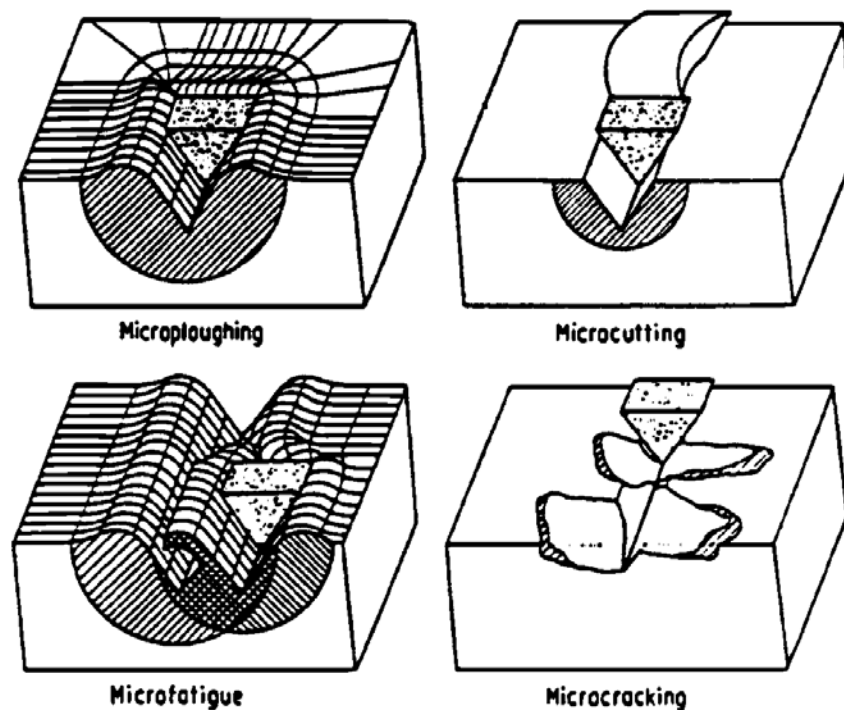


Fig. 1.7. Schematic diagram showing abrasion mechanisms, after Zum Gahr (1987).

Microploughing and microcutting are the dominant mechanisms in ductile materials, the proportion of each is dependant upon the angle at which an abrasive particle's tip is oriented relative to the abraded surface. There is usually a critical angle defined for a particular metal, at which a transition from microploughing to microcutting is observed with increasing angle. In practice this transition is more gradual (Zum Gahr, 1987).

1.3.2. Test Variables

Three body abrasion has been studied by Rabinowicz *et al.* (1961), Misra and Finnie (1980), and Misra (1981b) and their results are summarised below:

(i) Material Hardness

Its effect is similar to erosion in that the hardness of annealed metals is inversely proportional to the abrasion wear rate, and work hardening has no effect. Unlike erosion, thermal hardening has some, although reduced, effect.

(ii) Time

Linear wear rates with time are observed and as with high angle erosion an incubation period is observed. Two-body abrasion has no incubation period.

(iii) Particle size

Again as with erosion a critical particle size is observed, generally between 50 - 100 μm in diameter above which the wear rate is constant and below which the wear rate decreases with decreasing size.

(iv) Particle Hardness

There is a transition at around equal abrasive and material hardness, from a low wear rate to high wear rate as the particle hardness increases.

(v) Load

The wear loss first increases non-linearly with load then increases linearly, as compared with a purely linear relationship for two-body abrasion.

1.3.3. Models

Most models have only considered two-body abrasion, though they have some relevance to three-body abrasion in considering influential material properties. Ductile and brittle models are briefly discussed below.

1.3.3.1. Ductile Models

A simple model based on the removal of material by plastic deformation is given by the equation:

$$W_v = k \frac{L d}{H} \quad (1.12)$$

where W_v is the volume of material removed, L is the load, H is the material hardness, d is the sliding distance and k is a constant. Rabinowicz *et al.* (1961) derived this equation for a conical abrasive particle by assuming that the load applied is supported by plastic flow beneath the particle. It is known as Archard's equation who derived this equation for sliding wear. This equation correctly predicts the inverse relationship between annealed material hardness and wear rate but other material properties such as work hardening, ductility or fracture toughness are known to have an effect. More complex models have considered the various mechanical and thermophysical properties of the wearing material (Sundararajan, 1987) or used statistical approaches for treating multiple abrasive groovings (Jacobson *et al.*, 1987). Zum Gahr (1988) used the Archard's equation as the basis to derive an expression for the wear rate as:

$$W_v = f_{ab} A_v d \quad (1.13)$$

where

$$f_{ab} = \frac{A_v - (A_1 + A_2)}{A_v} \quad (1.14)$$

and A_v is the cross-sectional area of the wear groove and $(A_1 + A_2)$ represents the amount of material which is pushed to the groove sides by plastic deformation. The value of f_{ab} is therefore 1 for perfect cutting and 0 for pure ploughing. The factors which influence f_{ab} are the same factors that effect the abrasive wear rate. The poor wear resistance of a work hardened metal relative to an annealed metal of the same hardness can thus be explained, as the work hardened metal has a higher f_{ab} value.

1.3.3.2. Brittle models

Most brittle abrasion theories are based on the formation of lateral cracks as described for brittle erosion above. This means that the volume of material removed is much greater than the groove volume. The general assumption is that the lateral cracks form above a critical load, below which only plastic deformation occurs. This method was used by Evans and Marshall (1980), whose derivation is outlined below.

The critical load, P , depends on the hardness, H , and the toughness, K_c :

$$P \propto \frac{K_c^4}{H^3} \quad (1.15)$$

The lateral crack length c was given by:

$$c = k_1 \frac{(E/H)^{3/5} P^{5/8}}{K_c^{1/2} H^{1/8}} \quad (1.16)$$

where k_1 is a constant which depends only on the particle shape and E is the Young's Modulus of the material. The depth of the lateral cracks, b , is assumed to be proportional to the radius of the plastic zone, and given by:

$$b = k_2 \left(\frac{E}{H}\right)^{2/5} \left(\frac{P}{H}\right)^{1/2} \quad (1.17)$$

where k_2 is another material independent constant. The upper limit of material removed per particle, per unit sliding distance is $2bc$ so that for N particles in contact with the surface the volume wear rate will be:

$$W_v = k_3 N \frac{(E/H)^{3/5} P^{5/8}}{K_c^{1/2} H^{5/8}} \quad (1.18)$$

where k_3 is a material-independent constant.

Another similar analysis by Evans and Wilshaw (1976) used different equations for b and c to derive a similar equation:

$$W_v = k_4 N \frac{P^{5/4}}{K_c^{3/4} H^{1/2}} \quad (1.19)$$

where k_4 is a constant.

Both models predict wear rates considerably higher than those due to plastic mechanisms but only above a critical load. In this case a high material hardness and fracture toughness is important to increase wear resistance.

Chapter 2

Oxidation

2.1. Introduction

The theoretical background to oxidation is discussed in terms of thermodynamics and kinetics. As mild steel was the primary material used for this work the oxidation behaviour of iron is discussed along with the effect on oxidation of alloying additions used to form the common industrial steels. The sources of stress within an oxide film have also been discussed because of its importance in the removal of oxide, which may lead to rapid wastage under erosion-corrosion conditions.

2.2. Thermodynamics of Oxidation

Thermodynamically an oxide is likely to form on a metal surface when the Gibbs free energy change for the reaction is less than zero, assuming constant temperature and pressure. For the reaction between a metal, M, and oxygen, O:



the standard free energy, ΔG° , can be expressed as:

$$\Delta G^\circ = -RT \ln \left(\frac{a_{MO_2}}{a_M P_{O_2}} \right) \quad (2.2)$$

where ΔG° is the free energy change when all species are in their standard states, T is temperature, R is the gas constant, a_{MO_2} and a_M are the activities of the metal and oxide respectively and P_{O_2} is the partial pressure of oxygen. Assuming the activities of the metal and oxide to be unity, the equation becomes:

$$\Delta G^\circ = RT \ln P_{O_2} \quad (2.3)$$

This equation can be used to display the standard free energy of formation of metal oxides graphically in the form of an Ellingham diagram (Fig. 2.1). The reactivity of metals or stability of oxides increase moving down the graph, and the only metal thermodynamically stable at room temperature is gold (not shown). Despite this fact most reaction rates depend exponentially on temperature and thus are extremely sluggish at low temperatures.

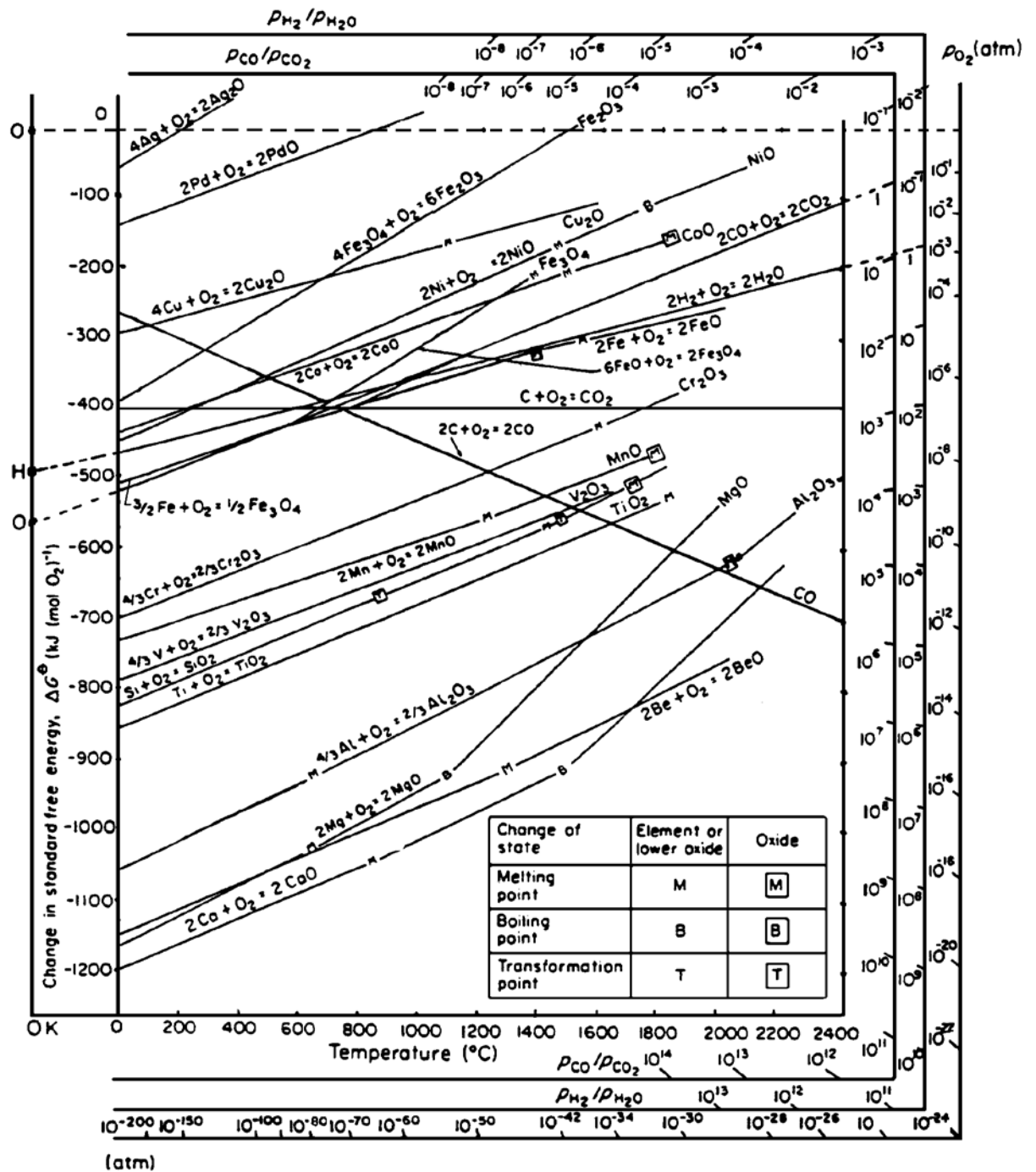


Fig. 2.1. Graph of ΔG° against temperature (Ellingham diagram) for the formation of common oxides, after Moore (1990).

2.3. Nucleation and Growth of Oxide

2.3.1. Initial stages of oxidation

For a truly clean surface exposed to oxygen, the initial oxidation can be divided into three main stages (Kofstad, 1988):

- (i) adsorption of oxygen gas on the surface,
- (ii) formation of individual oxide nuclei which grow laterally to form a continuous film
- (iii) further growth of the oxide film normal to the surface.

The adsorption is usually by a chemical or physical bond, with the latter bonded by relatively weak Van der Waals forces. The nucleation and growth of oxide nuclei are functions of the metal and its orientation, the temperature and the oxygen pressure. For example, the nucleation has been observed to start on surface defects or homogeneously, depending on the conditions.

2.3.2. Growth of oxide

At atmospheric pressures and relatively high temperatures a continuous oxide film is established very quickly. Once established the oxide film separates the metal from the oxygen gas so the reaction can only proceed through solid-state diffusion of one or both of the reactants through the film. The transport mechanisms for ionic oxides rely on cation and anion interstitials and vacancies, the combination of which depends on the material. To maintain a charge balance electrons must also be transported. Diffusion is enhanced by non-stoichiometry as this usually increases the number of lattice defects. The lattice type and jump frequency for diffusion is also an important factor influencing the rate of diffusion (Saunders, 1984). Al_2O_3 , for example, is based on an oxygen close packed structure with the cations located at the octahedral interstices. Although only two-thirds of these interstices are occupied, the self-diffusion rate is very low because the oxygen close packing is almost perfect and restricts the cation diffusion between interstices.

At low temperatures, when the driving force for diffusion is low, diffusion may take place preferentially along pores or low resistance paths such as grain boundaries (short-circuit diffusion). Perrow *et al.* (1968) and Hussey *et al.* (1977) showed that short

circuit diffusion was an important transport mechanism for the oxidation of nickel at 500° C and 600° C and iron (through magnetite) at 550° C, respectively.

The reaction rate of oxide formation usually follows one or more of three possible rate laws:

(i) **Parabolic rate law.**

This can be described as:

$$x^2 = 2k_p t + C \quad (2.4)$$

where x is the scale thickness, t is time, k_p is the parabolic rate constant and C is a constant. This law is followed by many metals once the oxide scale has reached a moderate thickness. Wager (simplified by Birks and Meier, 1983) derived this equation by assuming a compact and adherent scale, the rate determining step was ionic diffusion through the oxide and that thermodynamic equilibrium was established throughout the scale.

Perrow *et al.* (1968) showed that short-circuit diffusion could exhibit parabolic rate behaviour if the grain size remained the same, but with a higher rate constant than if calculated by Wager's theory or extrapolated from data obtained at higher temperatures.

(ii) **Linear rate law.**

Oxide growth sometimes proceeds at a constant rate and obeys the linear rate law, i.e.

$$x = k_l t + C' \quad (2.5)$$

where k_l is the linear rate constant, and C' is a constant. This is usually observed when the rate determining reaction step is a phase boundary process (Birks and Meier, 1983). For example, in the case for very thin films where diffusion through the scale is not rate limiting and the rate of oxide formation is usually dependant on the absorption of oxygen at the scale-gas interface. Linear rates of oxide formation may also occur when the oxide presents no barrier to diffusion, as in the case of volatile oxides or cracked films.

(iii) Logarithmic rate laws.

Metals oxidised under certain conditions, typically at low temperatures (below 400° C) and in the initial stages of oxide formation, are characterised by a rapid reaction rate which quickly reduces. Such behaviour conforms to rate laws described by logarithmic functions such as:

$$x = k_{\log} \log(t + t_0) + A \quad (\text{direct log law}) \quad (2.6)$$

and

$$\frac{1}{x} = B - k_{il} \log(t) \quad (\text{inverse log law}) \quad (2.7)$$

where A, B, t_0 , k_{\log} , k_{il} are constants at constant temperature. Measurement of initial oxide layers is often inaccurate and actual deviations from the stoichiometry of the bulk oxide may be unknown. These problems mean that the interpretation of logarithmic rate behaviour is the least understood area of metal oxidation. Theories proposed to explain logarithmic rate law behaviour have been summarised by Kofstad (1988). These have been based on; the adsorption of reactive species, the effects of electric fields developed across oxide layers, quantum-mechanical tunnelling through thin films, progressive blocking of low resistance diffusion paths, non-isothermal conditions in the oxide layer, and nucleation and growth processes.

2.3.3. Non-planar reactions

The above rate laws are based on the formation of a planar reaction front which is not always the case. One type of non-planar growth is the formation of oxide in the form of whiskers, blades and plates. Such growth never occurs during the initial stages of oxidation but is always associated with thicker scales and the whiskers always consist of the higher valence oxide. Whisker and blade formation for iron (Rapp, 1984), as for many other metals, have been shown to be enhanced by the presence of water vapour and cold work of the metal. A favoured mechanism for whisker and blade growth is short-circuit diffusion along the centre of the whisker or blade.

2.4. Oxidation of Iron

Iron oxidises to form a multilayered scale, the phase diagram is shown in Fig. 2.2. Below 570° C Fe_2O_3 and Fe_3O_4 form with Fe_3O_4 next to the metal, and above 570° C Fe_2O_3 , Fe_3O_4 and FeO form with FeO next to the metal.

FeO , the wüstite phase, is a p-type metal deficit semiconductor which can exist over a range of stoichiometry, $\text{Fe}_{0.95}\text{O}$ to $\text{Fe}_{0.88}\text{O}$ at 1000° C, for example. The very high concentrations of cation vacancies allows extremely high mobility of cations and electrons.

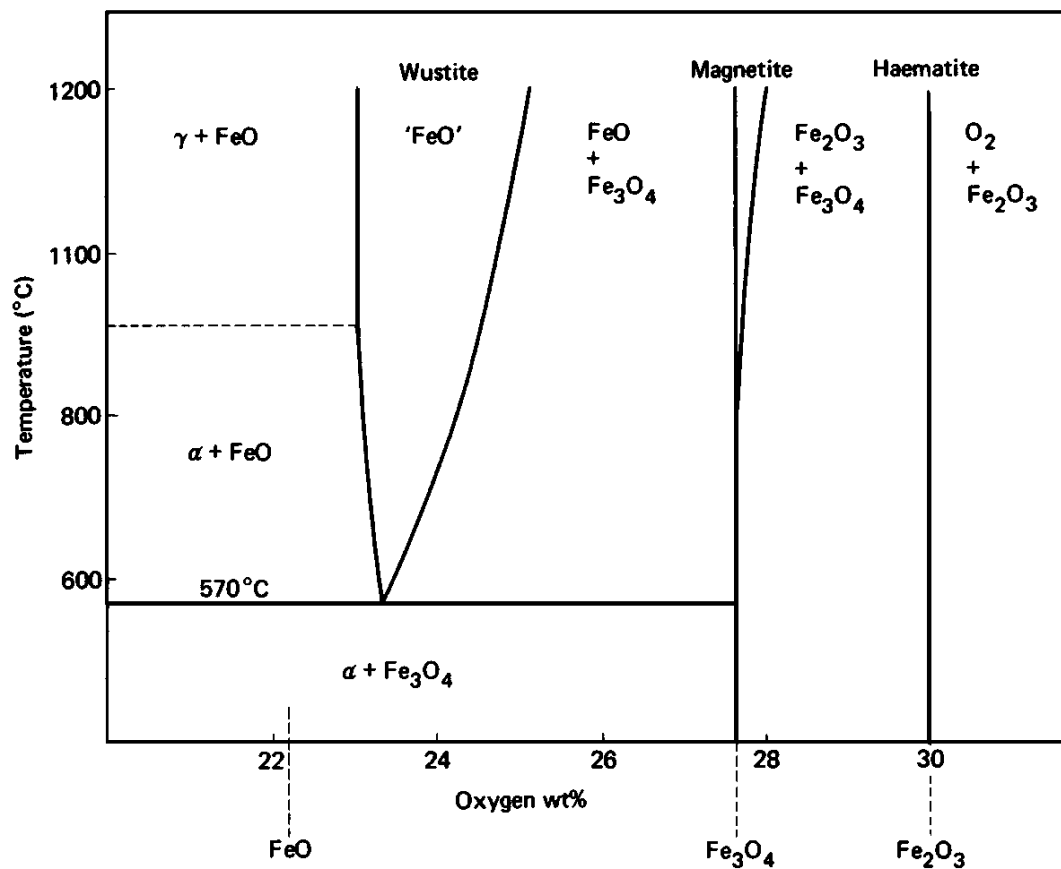


Fig. 2.2. The iron-oxygen phase diagram.

The magnetite phase, Fe_3O_4 , is an inverse spinel and therefore has Fe^{2+} ions on the octahedral sites with Fe^{3+} ions divided equally between the octahedral and tetrahedral sites. Defects occur on both sites allowing diffusion of ions over both tetrahedral and

octahedral sites. Only at high temperatures is a slight variation in stoichiometry found.

Haematite, Fe_2O_3 , exists in two forms, $\alpha\text{-Fe}_2\text{O}_3$ which is rhombohedral and $\gamma\text{-Fe}_2\text{O}_3$ which is cubic. Both cations and anions can diffuse through Fe_2O_3 with anions the dominant transport, and mobility is low.

The oxidation mechanism above 570°C is shown in Fig 2.3. The wüstite layer makes up the majority of the scale thickness due to the much greater mobility of its defects. At 1000°C the relative equilibrium thicknesses of $\text{FeO}:\text{Fe}_3\text{O}_4:\text{Fe}_2\text{O}_3$ are 95:4:1.

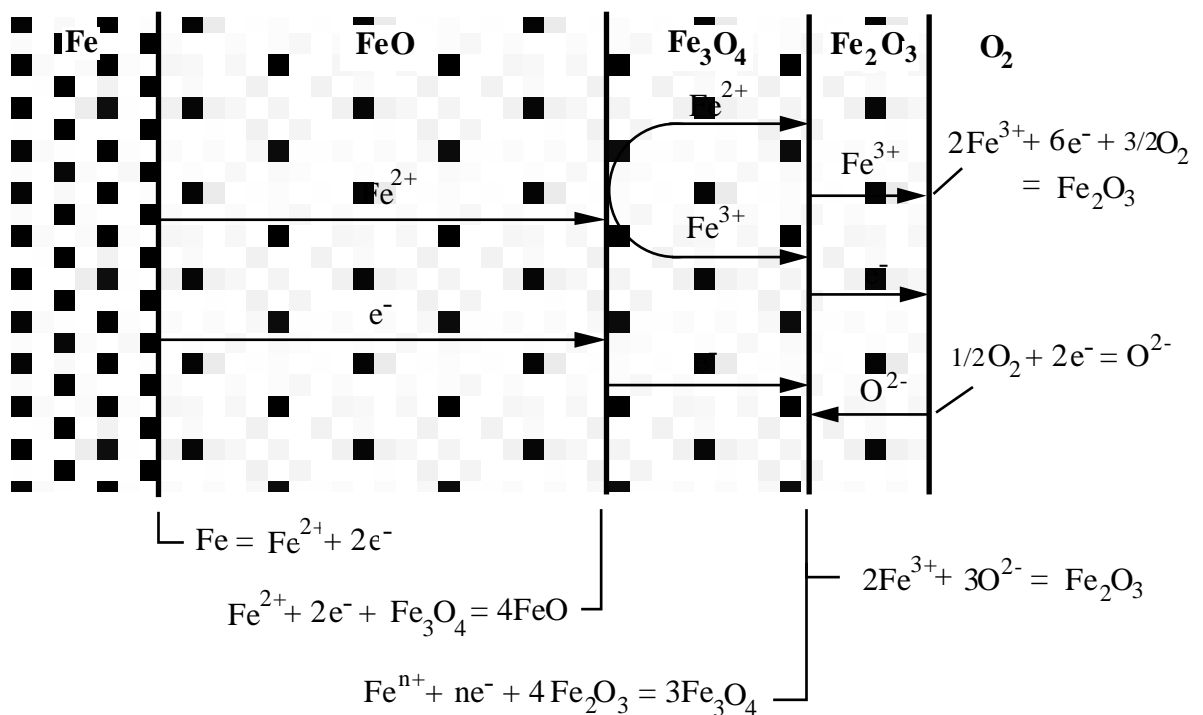


Fig. 2.3. Mechanisms of the oxidation of iron above 570°C .

2.4.1. Effect of experimental variables

At low temperature the formation of haematite and magnetite is highly dependant on oxygen pressure, impurities and the surface preparation. On atomically clean surfaces (reduced by hydrogen) only Fe_2O_3 forms below about 250°C and above this temperature Fe_3O_4 nucleates and grows below the Fe_2O_3 layer. The presence of a very thin oxide film causes Fe_3O_4 to form first and Fe_2O_3 nucleates and spreads over the Fe_3O_4 (Evans, 1968). Païdassi (1956) showed that the effect of H_2 reduction prior to

oxidation reduced the oxidation rate between 400° - 600° C due to formation of the more protective Fe₂O₃, the activation energy was also reduced from about 150 to 63 KJ mol⁻¹ between 450° and 600° C (Fig. 2.4).

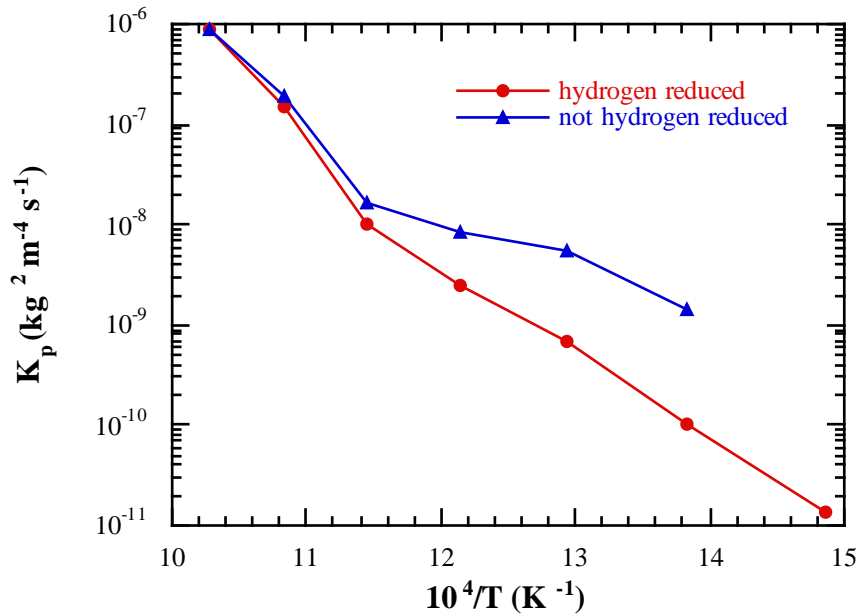


Fig. 2.4. Arrhenius plot of hydrogen reduced and not hydrogen reduced iron, after Païdassi (1956).

The effect of pressure has been studied by Boggs *et al.* (1965) between 200° - 450° C. It was found that Fe₃O₄ formed initially (surfaces were not atomically clean) then Fe₂O₃ formed on top reducing the oxidation rate. As the oxygen pressure was reduced the nucleation rate of Fe₂O₃ reduced allowing the more rapid oxidation of Fe₃O₄. Thus at lower pressures a higher oxidation rate was observed.

The oxidation rate and proportion of Fe₂O₃ to Fe₃O₄ is also influenced by crystallographic orientation (Sewell and Cohen, 1964). For example, the low index planes form a higher proportion of Fe₃O₄.

Caplan and Cohen (1966) showed that in the range 400 - 600° C cold work introduced by a range of surface preparations had the effect of increasing the oxidation rate (Fig. 2.5) and that increasing the cold work, by using coarser abrasives, increased the oxidation rate (Fig. 2.6). Annealed iron formed voids at the metal-oxide interface as cation vacancies moved inwards, which reduced the oxidation rate by impeding metal

transfer. Cold worked iron contained additional dislocations which acted as sinks for the vacancies. Above 650°C wüstite becomes plastic enough to prevent void formation.

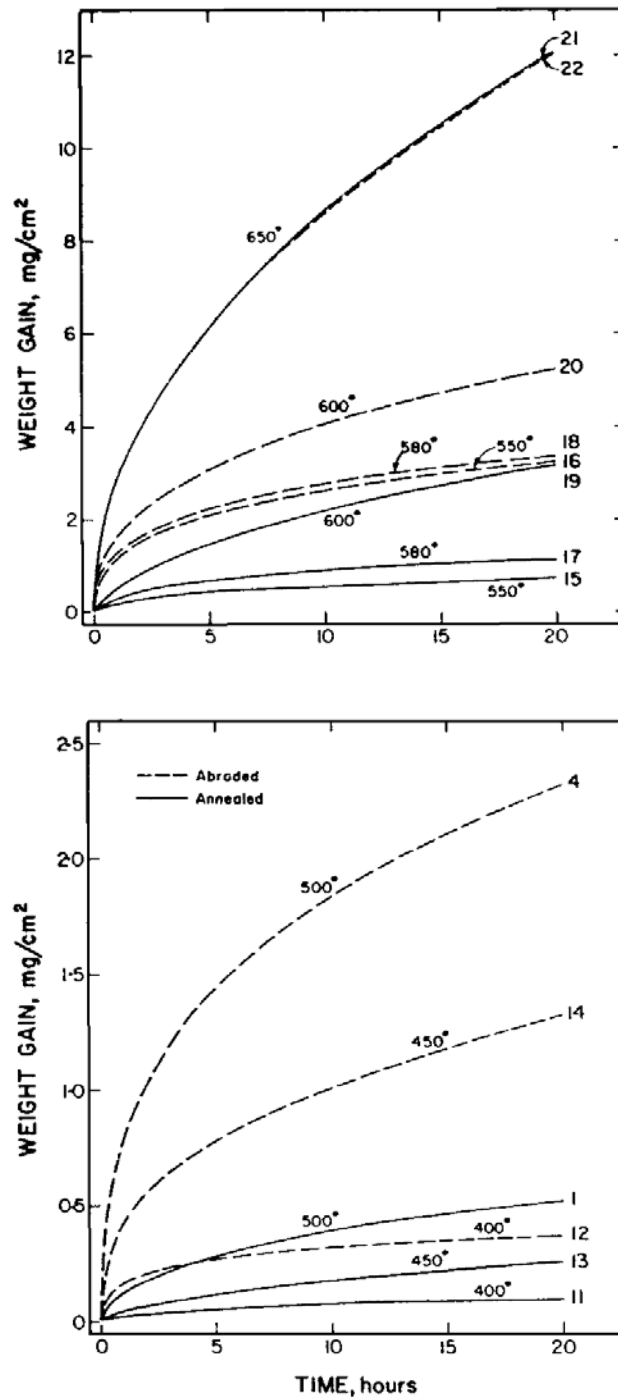


Fig. 2.5. Oxidation of Fe from 400° to 650°C showing the effect of abrasion (dashed curves) compared to annealed Fe (solid curves), after Caplan and Cohen (1966).

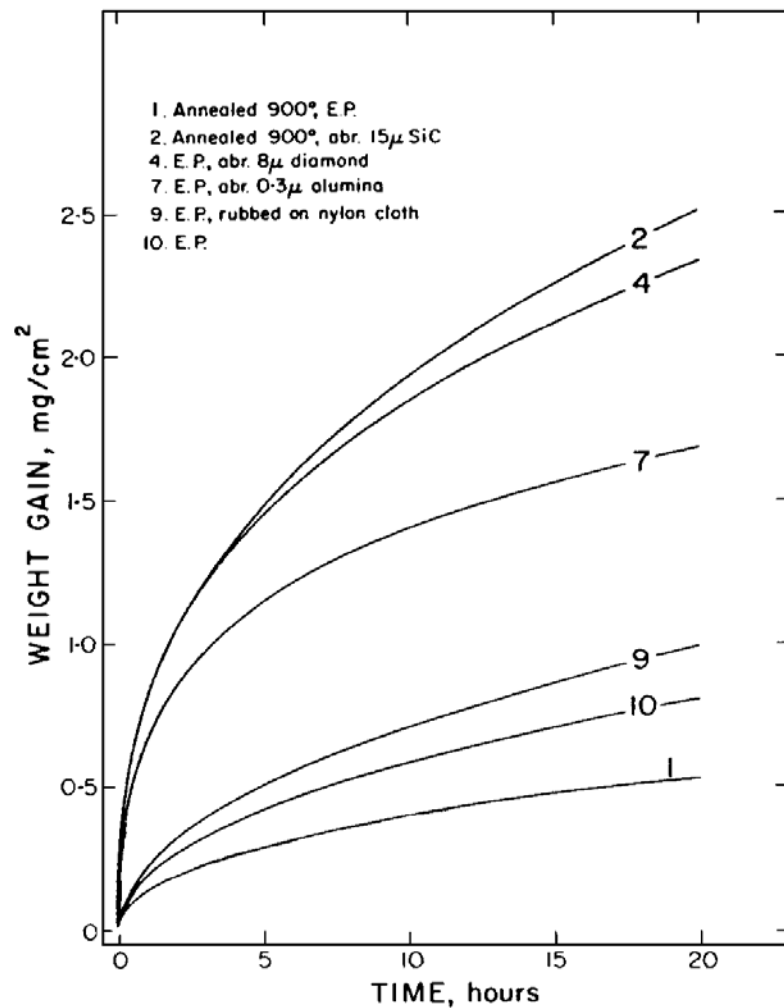


Fig. 2.6. Oxidation of Fe at 500° C in 1 atm oxygen after various specimen pretreatments. (E.P. = electropolished), after Caplan and Cohen (1966).

Price (1967) discussed the influence of recrystallization on the oxidation of a deformed specimen. It was suggested that for heavily deformed iron at 400° C recrystallization occurred slowly whereas at 600° C it was complete within a few minutes. This is also a contributing factor for the similar oxidation behaviour of annealed and unannealed iron above 600° C observed by Caplan and Cohan (1966). At high temperatures ($\approx 600^\circ\text{C}$) recrystallization occurred very fast so that the cold worked specimens behave in essentially the same way as annealed specimens and oxidised at similar rates. At lower temperatures ($\approx 400^\circ\text{C}$), however, cold work persists for the initial stages of oxidation preventing void formation; the rate of oxidation for cold worked iron was thus greater than for the annealed material. The effect of recrystallization combined with cold work results in the measurement of a low activation energy, as it raises the oxidation rate at

low temperatures but has little effect at high temperatures.

Other researchers have shown that other experimental variables such as surface roughness, gas flow rate, and specimen shape can also strongly influence the oxidation of iron (Fraunhofer and Pickup, 1970). Increased surface roughness in the absence of cold work was found to decrease the oxidation rate due to the formation of voids which act as diffusion barriers to iron ions (Eubanks *et al.*, 1962).

2.5. Effect of adding alloying elements

The addition of carbon to iron has the effect of making the oxidation rate more erratic. For example carbon diffuses to the base metal interface and reacts with iron oxide to evolve CO gas and develop a void. The oxidation rate may decrease if the void is stable, or increase oxidation if the pressure of CO induces cracking or if there is sufficient CO to facilitate oxygen transport. The effect of carbon and other alloying elements on high temperature oxidation is discussed in more detail by Chang and Wei (1989).

Chromium additions greater than 1.25 wt % improve the oxidation resistance of iron, and are thus used in many low alloy steels. An example is Fe - 2.25Cr - 1Mo where the chromium and molybdenum are added to improve oxidation resistance and mechanical strength respectively. Chromium in percentages of 12% and greater forms a continuous protective layer of Cr_2O_3 which greatly reduces the oxidation rate. At lower concentrations, although less effective, chromium improves oxidation in two ways; the wüstite phase is suppressed to higher temperatures and protective mixed Fe-Cr oxides are formed. Oxidation of an Fe-3% Cr alloy by Labun *et al.* (1982) at 700° - 800° C showed, at low oxygen pressures and short times, the formation of a 3 layered oxide structure; an inner layer of $(\text{Fe,Cr})_3\text{O}_4$ spinel then two outer layers of $\alpha\text{-Fe}_2\text{O}_3$. In air and at longer times a fourth layer was reported by Kahveci and Welsh (1983), a sesquioxide $(\text{Fe,Cr})_2\text{O}_3$ above the $(\text{Fe,Cr})_3\text{O}_4$ spinel.

Simms and Little (1987) investigated Fe - 2.25Cr - 1Mo at 550° C - 700° C in flowing oxygen and reported a three layered structure, an inner doped spinel M_3O_4 , a magnetite layer and outer haematite layer both devoid of chromium and molybdenum. Manganese was distributed evenly through the three oxides.

As early as 1929 Pfeil (1929) reported the segregation of elements, except manganese, in iron-transition metal alloys. Cox *et al.* (1972) later explained these observations

with a cation diffusion model, concluding that the cation mobility decreased in the order Fe, Mn, V, Ni, Cr.

2.5.1. Effect of cold work on low alloy steels

The effect of grain size and cold work on the oxidation resistance of Fe - 2.25Cr - 1Mo has been investigated by Singh Raman *et al.* (1989) and Khanna *et al.* (1985) respectively. The oxidation resistance between 600° - 800° C increases with grain size, weight gain and inverse grain diameter were linearly related. Cold work seemed to have negligible effect on the oxidation kinetics up to 700° C, beyond which there was a general reduction in oxidation. This decrease was attributed to an increase in Cr diffusion and hence formation of the doped spinel which slows the oxidation rate.

2.6. Stresses in oxide films

In order for a oxide film to be protective it needs to remain adherent to the metal. If the generation of stresses induces cracking and spalling of the oxide the oxidation rate is dramatically increased and thus is an important factor that needs to be considered. These effects have been considered by Stringer (1970) and Birks and Meier (1983). There are two main sources that generate stress; growth and thermal stresses.

2.6.1. Growth stresses

Growth stresses arise during the isothermal formation of the scale and occur due to a number of causes.

(i) *Volume differences between the oxide and metal.*

The specific volume of the oxide is rarely the same as that of the metal, resulting in stress. The sign and magnitude of the stress is related to the Pilling-Bedworth ratio (PBR) (Pilling and Bedworth, 1923).

$$\text{PBR} = \frac{\text{Volume of oxide produced}}{\text{Volume of metal consumed}} \quad (2.8)$$

For values less than unity the oxide is in tension, which may cause oxide cracking, and oxidation will follow a linear rate law, governed by surface reaction kinetics. For

values of the PBR greater than unity the oxide is in compression and may be protective, and the oxidation will follow a rate law governed by the speed of transport of metal or environmental species through the scale. The PBRs of FeO, Fe₃O₄ and Fe₂O₃ on α -Fe are 1.68, 2.10 and 2.14 respectively. These stresses should only arise if new oxide forms at the metal-oxide interface, although in this case the stresses may be relieved by the movement of the metal lattice (e.g. shearing) or by metal ion mobility at the oxide-metal interface. Despite this, the PBR tends to give a fair indication of the stress sign.

Mitchell *et al.* (1982) have observed stresses in iron oxides particularly at 600° C, observing spalling and decohesion of the outer α -Fe₂O₃ layer and cracking of the magnetite layer. The compressive stresses in the haematite and tensile stresses in the magnetite were successfully explained by considering the PBRs of Fe₂O₃ on Fe₃O₄ and Fe₃O₄ on FeO respectively.

(ii) Epitaxial stresses.

Usually occur in thin films but constraints diminish as the oxide thickens.

(iii) Compositional changes in the alloy or scale.

This may arise due to selective oxidation in an alloy leading to a change in lattice parameter, or the dissolution of oxygen in metals of high oxygen solubilities.

(iv) Point defect stresses.

Scales with large deviations from stoichiometry such as FeO can develop a variation of lattice parameter across the scale due to a gradient of point defects.

(v) Oxide formation within the scale.

As a result of inward movement of oxygen through cracks and pores, forming new oxide within the scale in which only cations are usually mobile.

(vi) Specimen geometry.

Specimens featuring curved surfaces result in additional stresses in the growing film as the oxide surface area changes with scale thickness. Bruce and Hancock (1970) showed for iron, where the primary movement of ions is outwards, that adherent scales

on flat surfaces became non-adherent on cylinders and failure due to the compressive stresses showed as buckling.

2.6.2. Stress relief of growth stresses

Under normal conditions oxides cannot deform plastically under the glide of dislocations, as ceramics do not exhibit the five independent slip systems required for general plastic deformation. There is evidence to show that growing oxides do deform plastically rather than fracture as an oxide is formed (Stringer, 1970). Alternative mechanisms of stress relief generally involve diffusion, such as grain boundary sliding and dislocation climb processes.

2.6.3. Thermal stresses

Thermal stresses arise from a differential in thermal contraction between the substrate and the scale on changes of temperature, ΔT . The magnitude of this stress, σ , in the oxide may be expressed as

$$\sigma_{\text{ox}} = \frac{E_{\text{ox}} \Delta T (\alpha_{\text{ox}} - \alpha_{\text{m}})}{1 + 2 \left(\frac{E_{\text{ox}} t_{\text{ox}}}{E_{\text{m}} t_{\text{m}}} \right)} \quad (2.9)$$

where E is the elastic modulus, α is the coefficient of thermal expansion, t is thickness and the subscripts ox and m refer to the oxide and to the metal substrate respectively. The coefficient of thermal expansion for the oxide is generally less than that of the metal so compressive stresses will develop on cooling. If the stresses are large enough the scale will spall from the metal surface.

Chapter 3

Fluidized Bed Combustion

3.1. Introduction

A fluidized bed of particles is one where gas is flowing sufficiently fast to support the weight of the particles. The fluidized bed behaves in many ways like a liquid, the particles find their own level, objects can float or sink according to their density and rapid mixing of the particles occur. It is the property of rapid particle mixing that causes rapid heat conduction within the fluidized bed and has been exploited for the combustion of coal and other materials. This chapter first explains fluidized bed behaviour, then describes their use in the combustion of coal, then finally discusses wear problems associated with fluidized bed combustors.

3.2. Fluidized bed behaviour

A bed of particles offers resistance to gas flow through it. As the velocity of the gas flow increases the drag force on the particles increases and the particles rearrange themselves to offer less resistance to the gas flow resulting in an expansion of the bed of particles. As the velocity of the gas flow further increases expansion continues until the drag force supports the weight of the particles. At this stage the gas/particle system exhibits fluid like properties, where particles find their own level, and objects can float or sink according to their density. This is the point of incipient fluidization and the gas flow velocity required to achieve this is known as the minimum fluidization velocity, U_{mf} . The pressure drop across the bed increases linearly up to the point of incipient fluidization, remaining constant beyond it. This constant value may be exceeded prior to fluidization in order to overcome cohesive forces between particles and break down the residual packing and interlocking of particles and thus a pressure drop occurs at the point of fluidization. Further increasing the gas flow rate causes instabilities to develop, analogous to bubbles in a liquid, and it is these bubbles that are responsible for solids mixing in the bed. At high gas velocities material is thrown from the bed by pressure fluctuations before the gas velocity that is sufficient to entrain the bed particles

is reached (Botterill, 1983).

3.2.1. Effect of particle size and density

The different types of fluidized bed behaviour arise from different bubbling behaviour which is primarily governed by the size and density of the bed particles. Geldart (1973) classified bed materials into four main groups based on their fluidization behaviour (Fig. 3.1).

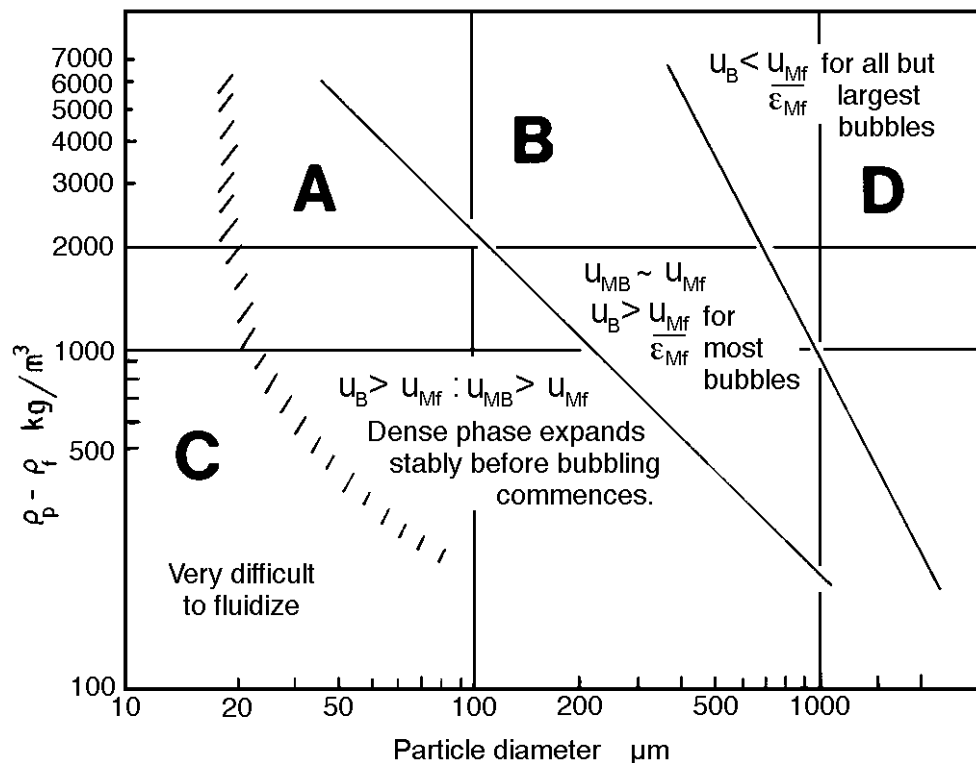


Fig. 3.1. Fluidized bed behaviour classified by particle diameter and difference between the particle density, ρ_p , and the density of the fluidizing medium, ρ_f , after Geldart (1973).

The region labelled A in Fig 3.1 (typically particles with densities below 1400 kg m^{-3} and diameter between $20 - 100 \mu\text{m}$) show a very stable bed expansion above U_{mf} where uniform fluidization occurs. At several times U_{mf} the bed collapses and bubbles form with a stable maximum size. The gas velocity at which the bed collapse occurs is referred to as the minimum bubbling velocity, U_{mb} .

Group B (typically particles with densities between $1400 - 4000 \text{ kg m}^{-3}$ and diameter between $40 - 500 \mu\text{m}$) show much less stable bed expansion and bubbling occurs at a

little above U_{mf} . Bubbles tend to grow until limited by the size of the bed.

In A and B particle beds, smaller slower bubbles coalesce with bigger faster rising bubbles and the bubble velocity, U_B , is greater than the interstitial gas flow rate, U_{mf}/ϵ_{mf} , where ϵ_{mf} is the voidage at minimum fluidization. Particles are carried upwards within the bubble wake and are continually being replaced by new particles. A downwards flow of particles elsewhere in the bed compensates for this upwards movement of material.

Unlike groups A and B, larger and/or denser particles (Group D) form bubbles which rise more slowly than the interstitial gas flow rate and there is no circulation of particles around the bubble which leads to less effective solids mixing.

Particles smaller than 30 μm diameter (Group C) tend to be difficult to fluidize as the interparticle forces are greater than the particle weight, and these systems are prone to channelling of air through the bed.

For group A and B bed particles, U_{mf} falls with increasing temperature as the gas viscosity decreases. However for group D particles in the turbulent flow regime gas density becomes important and U_{mf} increases with temperature.

3.2.2. Heat transfer in fluidized beds

Fluidized beds have an excellent gas to particle heat transfer due to their very large particle surface area. For example, 1 m^3 of 100 μm diameter particles have a surface area larger than 30,000 m^2 . As a result, the temperature of the incoming fluidizing gas quickly reaches the bed temperature.

The heat transfer between the bed and an immersed surface can be thought to consist of three additive components; the particle convective component caused by particles moving from the bulk of the bed to a region next to the heat transfer surface, the interphase gas-convective component where convective heat transfer occurs through the interphase gas and the radiant component. In most cases the particle convective component is the largest and is responsible for the marked increase in bed to surface heat transfer coefficient when the bed changes from incipient fluidization to a "bubbly state". An increase in bubbles increases the particle mixing and hence the heat transfer up to a point where this effect is countered by bubbles blanketing the heat transfer surface. Heat conducts through the gas phase between particle and surface as solid

contacts are too small and thus the heat transfer increases with increasing temperature due to the increase in gas thermal conductivity (Botterill, 1983).

3.3. Fluidized bed combustion (FBC)

The fluidized bed of a fluidized bed combustor is typically composed of inert solid particles (such as coal ash or silica) and are fluidized with a superficial gas velocity of at least 1.3 to 2 times the minimum fluidizing velocity. The fuel makes up less than 5% of the bed and operational temperatures are typically 850° C. Heat exchanger tubing carrying water (evaporator tubes) which have a metal surface temperature of between 200° - 450° C, may be within the bed. Superheater or reheater tubes carrying steam may be in-bed or above the bed and heated by the flue gases. The metal surface temperature of these tubes are generally 400° - 650° C (Rademakers and Kettunen, 1986).

3.4. Advantages of fluidized bed combustion

The fluidized bed combustor has a number of advantages over a conventional boiler;

- (i) The high heat transfer enables a reduction in the surface area of heat extraction tubes when compared to a similar output of a conventional boiler in spite of the much smaller temperature difference. This reduces the size and therefore the construction and maintenance costs of the boiler.
- (ii) A wide variety of fuels, both in type and quality, can be used in a single combustor design due to the low concentrations and rapid mixing of the fuel in the bed.
- (iii) The combustion efficiency is high (>96%)
- (iv) The emission of SO_x and NO_x gases can be reduced. SO_x can be retained within the bed with additions of limestone (CaCO₃) or dolomite (CaCO₃.MgCO₃) which react to form CaSO₄. This is cheaper than flue gas cleaning required on conventional boilers, the solid residue is easily disposed of as landfill and the efficiency of the combustor is not severely affected. NO_x emissions are inherently low because the operating fluidized bed temperature is too low to cause oxidation of atmospheric nitrogen. The NO_x emissions comes from the oxidation of organic nitrogen in the coal

and can be reduced by staged combustion* and/or injection of ammonia at the primary cyclone inlet (Minchener and Kelsall, 1990).

3.5. Types of combustor (NCB, 1985)

3.5.1. Atmospheric fluidized bed combustors (AFBCs)

3.5.1.1. Bubbling fluidized bed combustors

Bubbling AFBCs can be divided into industrial boilers, primarily used for heating applications, and larger utility boilers which are used for power generation. A typical superficial fluidizing velocity is $2 - 3 \text{ m s}^{-1}$, with a bed particle size of the order of $800 \mu\text{m}$.

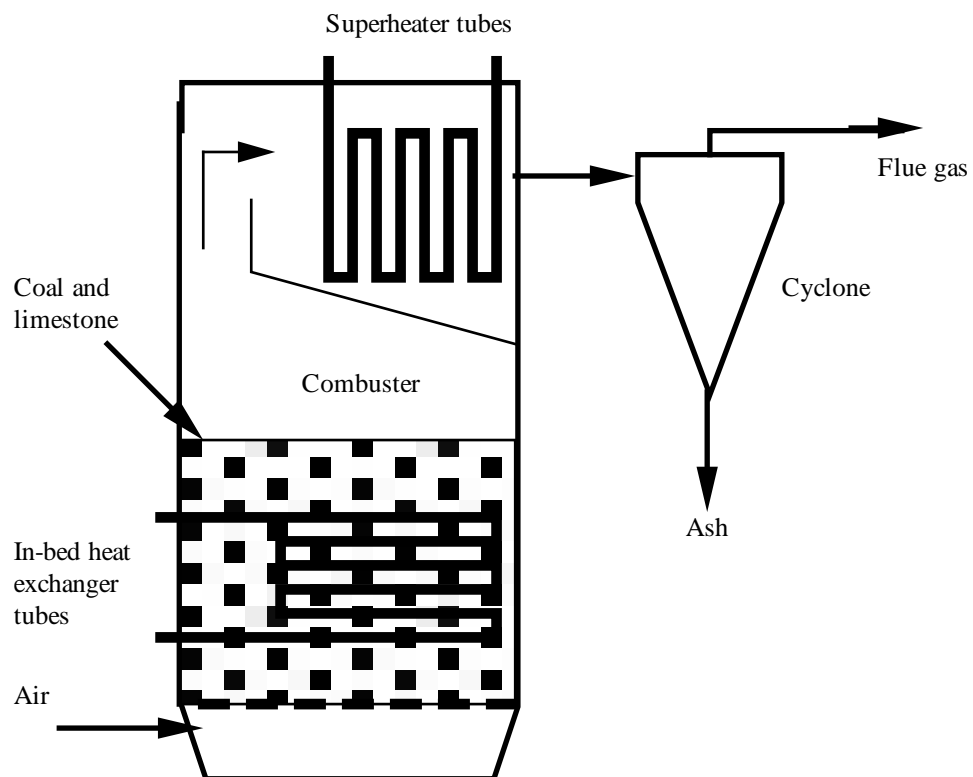


Fig. 3.2. A schematic diagram of a water tube industrial AFBC.

* where a portion of the total combustion air is added at some height above the primary air distributor.

(i) **Industrial boilers**

These boilers usually have shallow beds (0.15 to 0.3 m) where in-bed SO_x absorption is considered unimportant, and deeper beds (up to 1 m) where limestone or dolomite is used to reduce SO_x emissions. Hot water or low pressure steam is produced with outputs varying from 0.5 to 50 MWth.

The designs are either shell or water tube boilers. In a shell boiler, the water and steam are contained within a pressure vessel, which surrounds the bed, and hot gases from the bed pass through tubes immersed in the water. In a water tube boiler, the walls of the combustor are constructed with tubes through which water flows. Fig. 3.2 shows a schematic diagram of a water tube boiler. In both designs heat exchanger tubing may pass through the bed. The shell boiler is cheaper to manufacture but its output is limited to about 10 MWth (thermal output in MW) due to the high stresses within the pressure vessel.

(ii) **Utility boilers**

These boilers are designed for commercial power generation so have deeper beds (between 0.8 and 1.2 m) to allow efficient sulphur capture. The largest operating boiler has a power output around 160 MWe (electrical output in MW).

3.5.1.2. Circulating fluidized bed combustors (CFBCs)

In this system the fluidizing gas velocity is much higher than a bubbling fluidized bed ($5 - 8 \text{ m s}^{-1}$) so that solid particles become entrained in the gas and fill the combustion chamber. Material is recycled via an external fluidized bed heat exchanger, and the flue gases pass through a heat transfer boiler (Fig. 3.3). In more recent designs heat is also removed from the combustion chamber via tubes lining the upper combustor walls (water walls). The lower part of the furnace is usually refractory lined.

CFBCs show a number of advantages over the bubbling bed variety including the elimination of in-bed tubes (and associated wear), the ability to burn a wider range of fuels, improved sulphur absorption, cheaper manufacturing for large power outputs, and improved control. CFBCs have become widespread and conventional technology with around 200 units operating world-wide, with the largest soon to be 250 MWe at the Gardanne Mine in Provence, Southern France (Cooper, 1995).

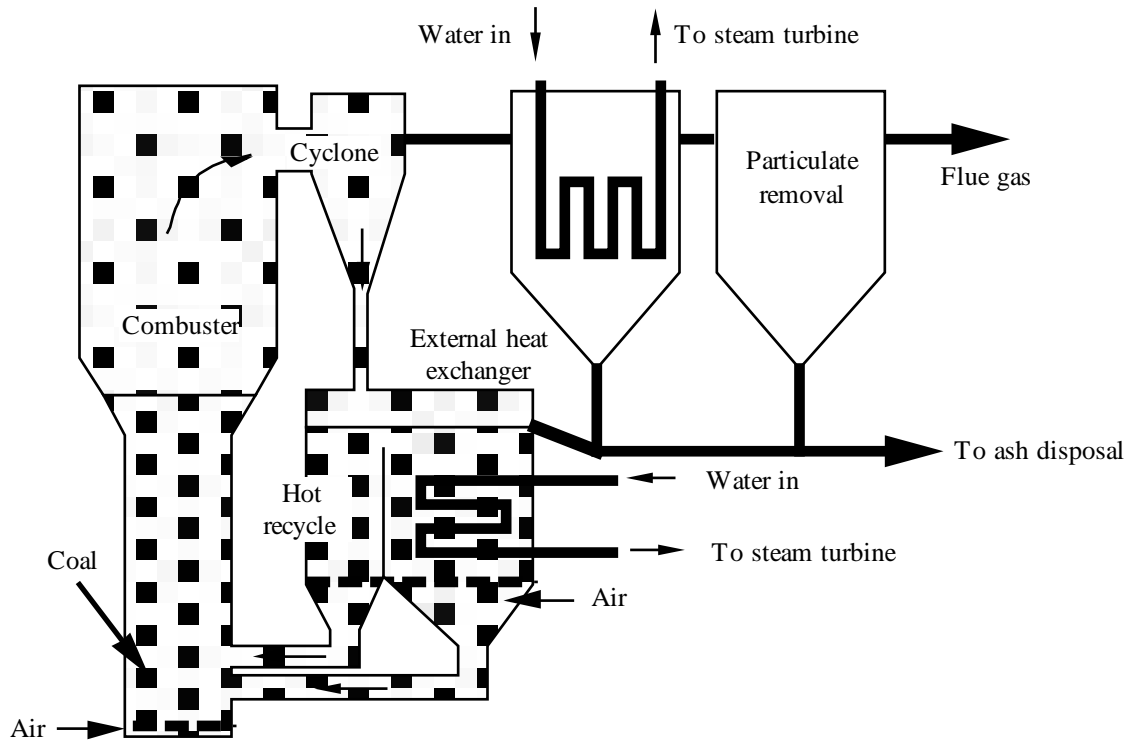


Fig. 3.3. A schematic diagram of a Circulating Fluidized Bed Combustor.

3.5.2. Pressurized fluidized bed combustors (PFBCs).

In a PFBC, steam from heat-exchanger tubing drives a steam turbine while the pressurized flue gases drive a gas turbine (Fig. 3.4). This combined-cycle operation can yield overall efficiencies of approximately 40% compared to 36.7% for conventional PC plant with flue gas desulphurization. Since the fluidizing air is at a high pressure the furnace size can be reduced to about one tenth of the size of an atmospheric pressure boiler of the same output, which reduces construction and maintenance costs. The most common PFBCs are based on a bubbling bed and have reached utility demonstration stage of development with a power output of around 70 MWe. The next stage in commercial development is to scale the technology up to 150 - 350 MWe (Burnard, 1995). PFBCs based on a circulating bed have potential advantages over pressurised bubbling beds, in the same way as do atmospheric CFBCs over bubbling AFBCs, but have yet to be demonstrated in a utility setting (EPRI, 1995).

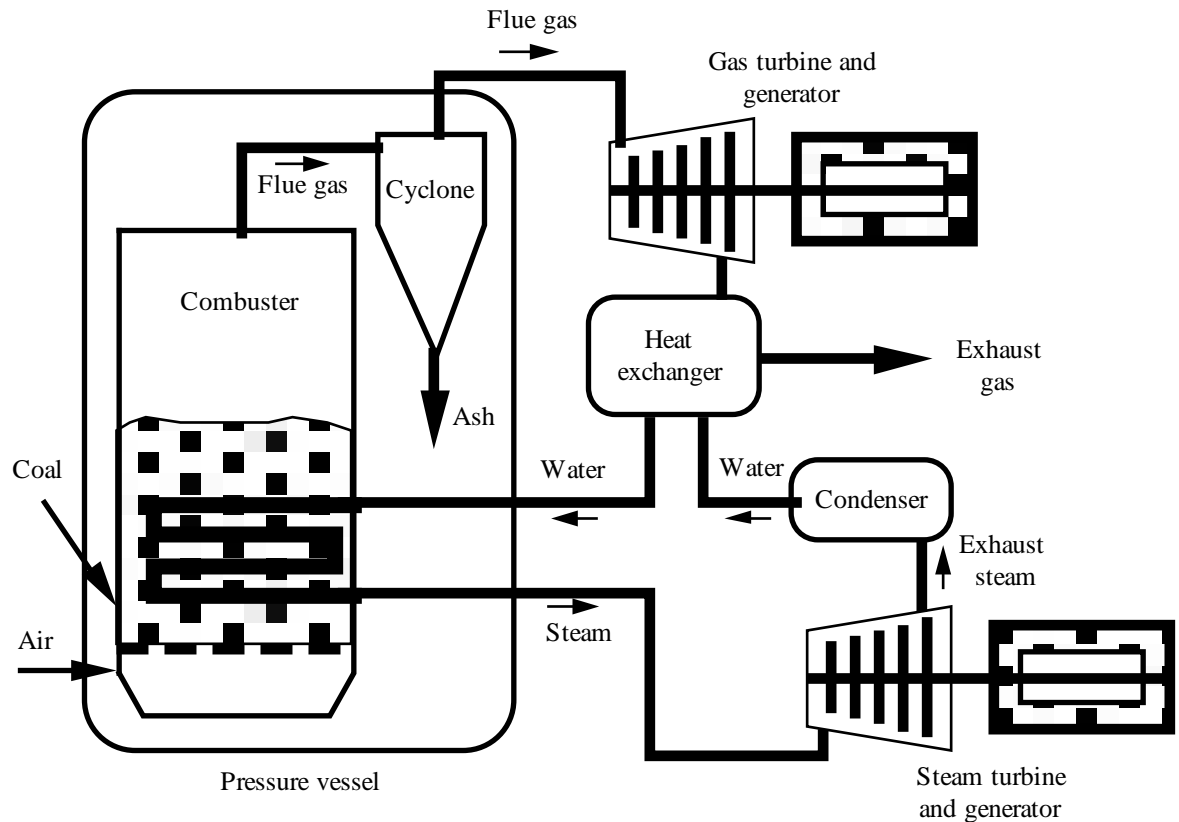


Fig. 3.4. A schematic diagram of a Pressurized Fluidized Bed Combustor

3.6. Wear problems experienced in FBCs

3.6.1. Introduction

This section briefly summarises the large amount of literature published about experience of wear problems in industrial FBCs. Most of the published papers reporting detailed results are from small scale pilot plant FBCs, notably the Tennessee Valley Authority's (TVA) 20 MWe AFBC utility pilot plant at Paducah, the TNO 4 MWth industrial boiler at Apeldoorn in The Netherlands, and the PFBC pilot plant at Grimethorpe, UK. Factors effecting wastage are outlined below, although identifying the causes responsible was often difficult as a change in wastage was accompanied by several changes to the combustor. Also results from similar FBCs operated under nominally identically conditions report very different material wastage rates.

3.6.2. Regions experiencing wear

(i) AFBCs and PFBCs

The main regions of wear in both AFBCs and PFBCs are on the underside of in-bed heat exchanger tubes. Two distinct wear patterns have been observed; one with maximum wear on the bottom, decreasing on either side to zero some 60 - 70° away from the vertical, and maxima on either side of the bottom of the tube approximately 35° from the vertical, with little or no wear on the bottom. These have been labelled Type A and B respectively by Stringer and Wright (1987). Explanations for the differing wear patterns have assumed a change in wear mechanism, e.g. from ductile metal erosion to brittle oxide erosion (Holtzer and Rademakers, 1991). However MacAdam and Stringer (1995) showed, by using a simple computer simulation, that type A behaviour associated with a highly constrained flow can change to type B behaviour with the introduction of a small degree of flow variability. Thus, type A behaviour might be expected to occur in a region of the bed experiencing a uniform flow of particles and type B where the direction of particle flow vary slightly.

Wear tends to be localised, with bends, sloping and vertical tubes particularly prone. In general, wastage in AFBCs is at a maximum on the lowest tubes in a tube bundle, decreasing on tubes further up in the bed. In PFBCs the reverse may be true as reported in the Grimethorpe pilot plant.

In many UK industrial boilers the wastage of containment walls above the level of the static bed was more severe than the in-bed tube wastage (Brain and Minchener, 1990).

(ii) CFBCs

Although CFBCs have no in-bed heat exchanger tubing, wastage problems have occurred, particularly wastage to the water walls. This consists of general water wall wear, wear in corners of the combustor and wear at the transition from the refractory lining of the lower part of the combustion chamber. Irregularities such as instrument penetrations, weld beads and tube bends around openings in the wall suffer significant localised wear (Stringer and Stallings, 1991).

3.6.3. Wear mechanisms

Wear is caused by the interaction of the inert bed particles and coal ash with a surface. The mechanisms by which this may occur were listed by Stringer and Wright (1986) and updated by Stringer (1995), a summary of which follows.

(i) Intrinsic wear

Erosion and three body abrasion of bed particles over a surface due the motion of normally behaved bed particles. Due to the low velocities involved the contribution to wastage by these mechanisms seems low.

(ii) Bubble induced wear

Bubbles may cause wear in several different ways; erosion from fast moving particles associated with rising bubbles and with bubbles tracking along inclined or vertical surfaces, and the abrasion of blocks of unfluidized particles (bubble wakes) thrown onto a surface by bubble collapse. The dominant mechanism is the latter and it is this bubble wake collapse that is responsible for the mechanical pulsing detected on tubes in AFBCs and cold models.

(iii) Long range flows

Erosion and abrasion associated with low range flow patterns in the bed. There is a general upwelling of particles in the centre of the bed and downwards flowing streams at the edge, or several related cells in larger beds. The evidence suggests that bubbles tend to flow along paths related to upward long range flows, so wear is effectively bubble related. Downwards flowing streams do exist and are probably responsible for wall wastage. In CFBCs due to the higher fluidizing velocities these downwards flowing particle streams are faster and denser giving rise to serious water wall wastage.

(iv) In-bed jets

Erosion by in-bed jets, which may be from coal or sorbent feed ports, particle reinjection ports, air distributor nozzles, expansion joints and cracks.

(v) **Local irregularities**

Local irregularities such as weld beads or probes induce local wastage. For example, a horizontal weld on a vertical tube causes wear on the upper surface of the weld and on the tube above the weld. Erosion by fast moving particles may be induced by local vortices generated by the irregularity. This type of wear is more serious in CFBCs due to the higher particle velocities.

3.6.4. Factors affecting wastage

Broadly two main factors determine the extent of wastage; the wear potential of the bed through combustor design and bed material erosivity/abrasivity, and the materials response.

(i) **Metal temperature**

General observations of in-bed tubes have indicated a reduction in wear where the surface metal temperature is high enough for a thick oxide to develop and provide some protection to the surface. For example, the cooler in-bed evaporator tubes rather than the hotter in-bed super-heater tubes experience the worse of the wear.

A detailed study over a range of metal temperatures in the TNO unit was carried out using venturi tubes (variable wall thickness) integrated into the heat exchanger and separate cooled test tubes (Holtzer and Rademakers, 1991). A transition from low wear at high temperatures to high wear at low temperatures occurred at around 270° C for mild and 2.25Cr - 1Mo steel. Staged combustion reduced the rate of oxidation and was accompanied by a reduction in the fluidization velocity and particle size. Under staged combustion the wastage of low alloy steels was reduced at low temperatures due to the changes in particle size and fluidization velocity, with a more gradual transition to enhanced wastage at high temperatures due to the formation of a less protective oxide (Fig. 3.5).

A similar AFBC in design at Renfrew, Scotland, has reported no major wastage problems but this may be due to differences in the minimum tube metal surface temperature, 280° C at Renfrew verses 230° C at TNO. From results shown in Fig. 3.5 a tube metal surface temperature of 280° C would just be hot enough to form a protective oxide.

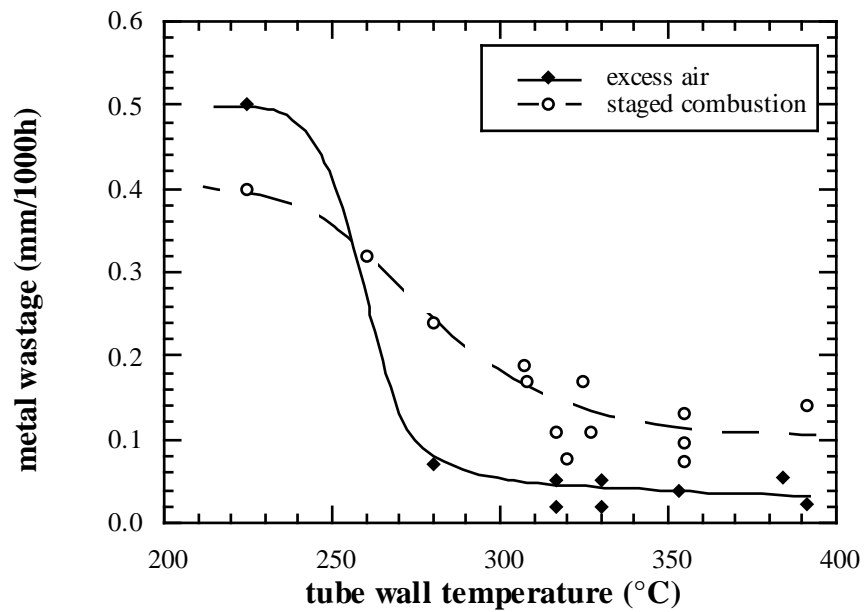


Fig. 3.5. Temperature effect on wastage of carbon steel in-bed tubes 4 MWth TNO FBC, after Holtzer and Rademakers (1991).

The 90 MWth AKZO AFBC boiler in Hengelo, with a minimum surface temperature of 350° C, showed very low wear rates on its low alloy tube bank after many 1000 hours although there was some severe localised wear which required shielding (Holtzer and Rademakers, 1991).

A similar transition has been reported in the Grimethorpe PFBC. On tube bank C the wastage decreased to low values at a steam temperature of 300° C (the surface metal temperature would be higher), and on tube bank C2 the transition occurred at around a surface metal temperature of 400° - 450° C (Stringer, 1995).

(ii) Coal and bed material

The first phase of testing at the TVA pilot plant resulted in low wastage of the in-bed tubes with a maximum wear rate of around 40 nm h⁻¹. A second tube bank was installed, of a slightly different design (a staggered arrangement of tubes rather than in line, and the distributor to bottom tube distance was increased from about 500 mm to 750 mm) and the coal was changed from South Hopkins to Pyro which had higher levels

of chlorine and quartz. After 4000 hours operation serious wastage had occurred, reaching a maximum rate of 1500 nm h^{-1} . Changing the coal to one similar to South Hopkins lowered the wastage rate considerably and further tube banks fired using these coals experienced wastage similar to the first tube bank. The most significant change which seemed to cause the order of magnitude increase in wastage was the change in coal (Wheeldon *et al.*, 1990).

The chlorine content was 10 times higher in the Pyro coal, but after small scale tests investigating the effect of a varying Cl content this was thought not to be responsible for such a large increase in wastage (Stencel *et al.*, 1990). Results from Grimethorpe also showed no variation in wastage rates for coals of differing Cl content (Stallings, 1990 referring to Meadowcroft). Analysis of the coal ash showed that the Pyro coal contained five times as much large ($+ 3.4 \text{ mm}$) quartz particles and unlike the Pyro ash the South Hopkins ash particles were covered with a continuous mineral deposit. The presence of large hard quartz particles and the absence of a mineral deposit coating, which at high temperatures would soften and reduce the particle angularity, was thought to be the primary reason for the large increase in wastage.

This example highlights the difficulty in determining the bed material erosivity, partly because changes in coal type are usually accompanied by other changes, such as the tube bank design, in a pilot plant. Also at operating bed temperatures coal ash softening occurs and coatings can develop on particles which may either round and soften particles or even increase their erosion potential.

(iii) *Fluidization conditions*

Cold bed studies have shown a linear increase in wastage with fluidization velocity for a constant particle size (Parkinson, 1987). The effect of fluidization velocity in fluidized bed combustors is less clear due to many other variables affecting wastage. However a substantial reduction in wastage was achieved in the TNO unit when the average fluidization velocity was reduced from 2.6 to 2.1 m s^{-1} and the peak velocities were suppressed by reducing the combustion air pressure fluctuations.

Brain and Minchener (1990) recommended a fluidization velocity below 2 m s^{-1} for industrial AFBCs as a three fold increase had been observed for a fluidization increase from 1.5 to 2.5 m s^{-1} .

(iv) Combustor design

Cold models have shown that wear was reduced as the in-bed tube packing density increased and that there was no difference in wear when using triangular or rectangular arrangement of tubes (Parkinson, 1987). Vertical tubes and tapered combustor walls increased wear quite significantly. This agrees with observations made in many industrial AFBCs where wear increased with tube inclination (Brain and Minchener, 1990).

The distributor to bottom tube distance was thought to be an important design variable in affecting wastage. As mentioned above an increase in this distance in the TVA unit was accompanied by a severe increase in wear, but the change in coal was thought to be responsible. The distance in the Renfrew unit was 114 mm compared to 178 mm in the TNO unit, but there was also a difference in metal temperatures. Brain and Minchener (1990) reported more wear on tubes in the second row of a triangular arrangement of tubes, i.e. tubes further from the distributor than those in the bottom row.

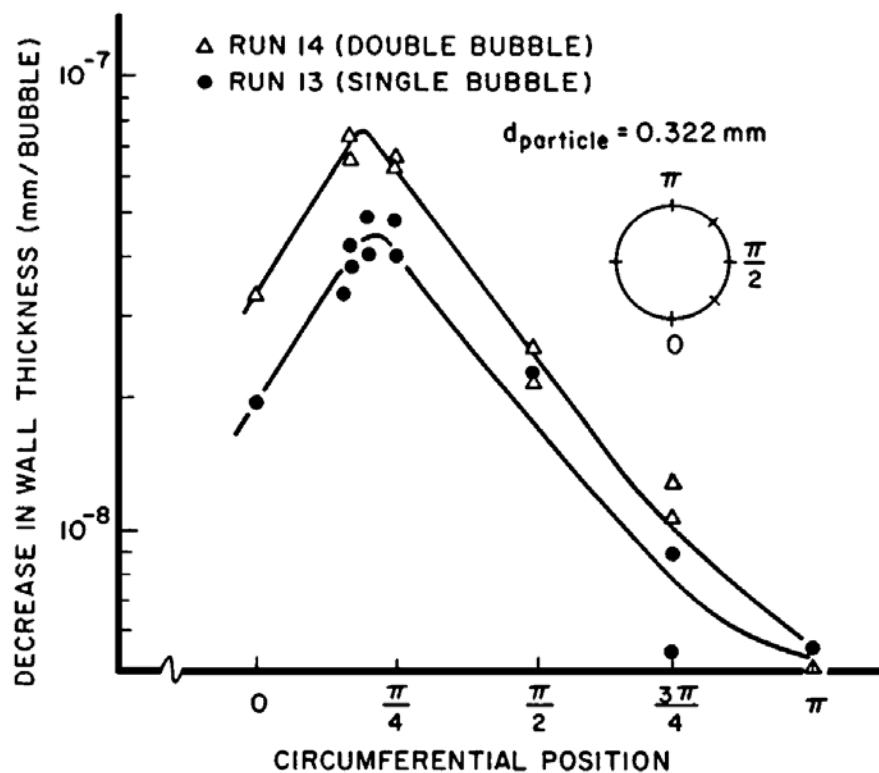


Fig. 3.6. Circumferential variation of material loss per bubble for single bubble and coalescing bubble pair (double bubble), after Levy and Bayat (1990).

Levy and Bayat (1990) showed that the impact of a bubble wake associated with two coalescing bubbles was approximately 2.3 times the velocity and as such caused more damage (Fig. 3.6). Modelling showed that as the distributor to tube distance increased the wear increased due to the increasing frequency of coalescing bubbles, and then decreased as coalescing bubbles became less frequent, as larger single bubbles formed from coalescing pairs.

Flow patterns in CFBCs seem very sensitive to changes in combustor geometry and imposed flows by air and solids injection, which in turn can lead to a dramatic increase in wastage. A CFBC at Chatham, New Brunswick experienced an increase in wear of its water walls just above the refractory lining from undetectable levels to 4800 nm h^{-1} with only a reduction in the cross-sectional area of the entry duct to the cyclone (Stringer, 1995)

(v) **Materials**

Generally at low metal temperatures no difference in wear behaviour between mild steel and low alloy steels is observed (e.g. Grimethorpe tube bundle E (Montrone, 1990) and TNO 4 MWth (Holtzer and Rademakers, 1991)), and stainless steels only show a slight improvement in wear resistance (e.g. TVA AFBC (Lewis *et al.*, 1990))

At higher temperatures wear is less of a problem as a thicker protective oxide forms. Corrosion resistance becomes the limiting factor to the lifetime of a tube so corrosion resistance metals such as stainless steels tend to be used.

3.6.5. Methods of combating wastage

(i) **Changing combustor design**

The initial tube bundle used in the Grimethorpe PFBC pilot plant (tube bundle designated A) suffered from severe wastage and to combat this the fluidizing velocity and the distributor to tube distance were reduced in the next tube bundles designated C and C2, both with limited success. Further tube bundles (D and E) at Grimethorpe were designed to test the hypothesis that raising the metal temperatures could decrease wastage, although results have not been published conclusions indicated that wastage can be controlled (Stringer, 1995).

(ii) External protection

Protective fins and studs have been widely used to combat wastage but with mixed results. There was no benefit of longitudinal fins on low alloy steels in Grimethorpe tube bank E (Montrone, 1990), although the use of studding eliminated wear on the underside of the tube. Fins may cause potential problems by running hotter than the tube itself and bending the tube by differential thermal contraction.

Shelves have been used successfully in industrial AFBCs to protect against wall wastage caused by the downwards flowing particle streams in the expanded region of the bed. The shelves collect a layer of unfluidized particles and disrupt particles flows close to the wall.

(iii) Wear resistant coatings and surface treatments

Chromizing appeared to be successful in eliminating wear on carbon steel and 2.25Cr - 1Mo steel on both finned and studded and bare tubes at low metal temperatures on tube bank E in the Grimethorpe PFBC (Montrone, 1990). In the TVA AFBC, chromizing, Extendalloy (powder metallurgy carbide containing abrasion resistant coating) and some thermal sprayed coatings all showed no wear after 6500 h compared with carbon steel on the bottom row which had worn an average of 1300 μm (Lewis *et al.*, 1990). Other coatings and surface treatments that have been used in other pilot plants include nitrided and aluminised steel and weld overlays.

(iv) CFBCs

Wastage of the water walls above the lower refractory lining in CFBCs have been tackled by all the methods described above; changing the angle of the refractory/wall interface to either a shallow angle or step, using weld overlays to protect the water walls and using metal shelves above the refractory. Shelves have had some success in reducing wastage but the other methods have been unsuccessful. Increasing the height of the refractory lining to a region of lower solids density or bending the water wall tubes to achieve a coplanar surface between the refractory lining and the unlined water wall have been suggested as alternative methods but are as yet untried (Stringer and Stallings, 1991).

(v) Summary

The wastage in AFBCs can be controlled with careful design and appropriate tube protection and the same is true for PFBCs. However, the fluidization velocity has to be severely reduced resulting in significant economic penalties. The system seems to be on a knife edge where small changes in operating conditions may cause a large increase in wastage (Stringer, 1995).

Chapter 4

Erosion - corrosion

4.1. Introduction

Erosion-corrosion refers to the simultaneous, synergistic interaction between solid particle erosion and corrosion. This may lead to a high wastage rate due to the continued removal of a protective oxide film. It is of considerable technical importance in several types of application including coal gasification, steam and gas turbines, and fluidized bed combustion (FBC) systems. Early studies simulated the environments of gas turbines or coal gasifiers which generally involved high velocities and high temperatures respectively.

High wastage rates of in-bed heat exchangers in FBCs encouraged further investigations of erosion-corrosion, although most studies still involved higher temperatures and velocities than experienced in a FBC. Sethi and Corey (1987) were the first to look at temperatures below 700° C and velocities of less than 10 m s⁻¹ using a drop tube apparatus. This however did not simulate the high particle flux experienced within a fluidized bed and so several investigators constructed test rigs using small fluidized beds. These studies are described below and then the mechanisms and models proposed, embracing the whole range of erosion-corrosion, are described and discussed.

4.2. Low temperature and velocity laboratory studies

4.2.1. Low flux

4.2.1.1. Sethi & co-workers

The arrangement used by Sethi & Corey (1987) is shown in Fig. 4.1. An impact velocity of between 1 and 10 m s⁻¹ was achieved by varying the length of the drop tube. Tests on a carbon steel, 2.25Cr - 1Mo and 9Cr - 1Mo steel and type 304 and 310 stainless steels were investigated using 1 mm alumina particles.

Three temperature regimes were observed; (1) at low temperatures the erosion rate was relatively independent of temperature, (2) increasing erosion rate with temperature at intermediate temperatures and (3) at higher temperatures there was a decrease of erosion rate with temperature (Fig. 4.2). The peak in wastage rate shifted to higher temperatures for higher velocities and for higher impact angles while in both cases the wastage rate increased, e.g. the temperature of the carbon steel peak at 2.7 m s^{-1} was $\approx 470^\circ \text{ C}$ at 30° and $\approx 540^\circ \text{ C}$ at normal incidence and $\approx 530^\circ \text{ C}$ for 4.3 m s^{-1} at 30° . The peak also shifted to higher temperatures with increasing chromium content.

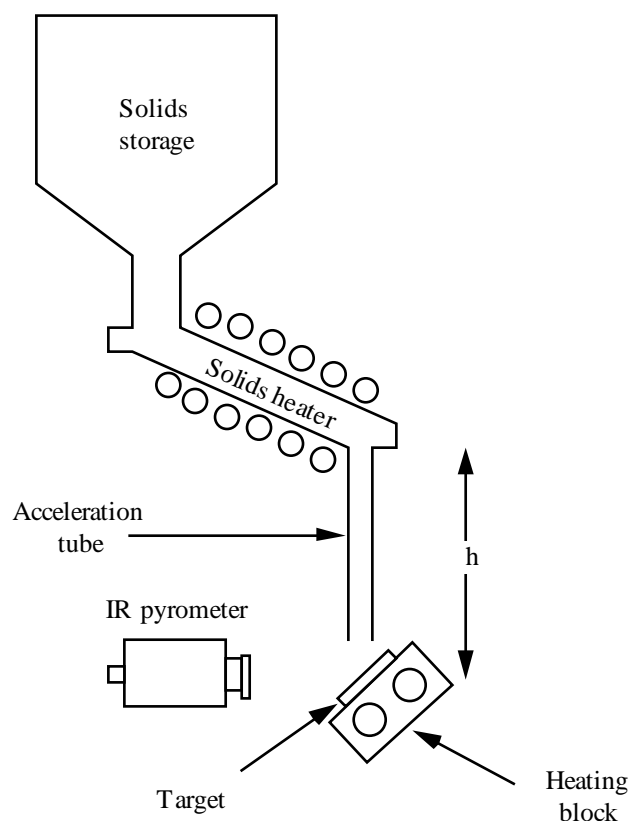


Fig. 4.1. A schematic diagram of the erosion-corrosion tester used by Sethi and Corey (1987).

It was proposed that the increase in wastage rate was due to the removal of the oxide film which increased in thickness with increasing temperature. Incomplete removal of the scale at higher temperatures was responsible for the decrease in wastage rate. This idea of oxide thickness was used to explain the observed effect of velocity and chromium content. At higher impact velocities, for example, the transition from

complete oxide removal to partial removal occurred at higher oxide thicknesses and hence at higher temperatures.

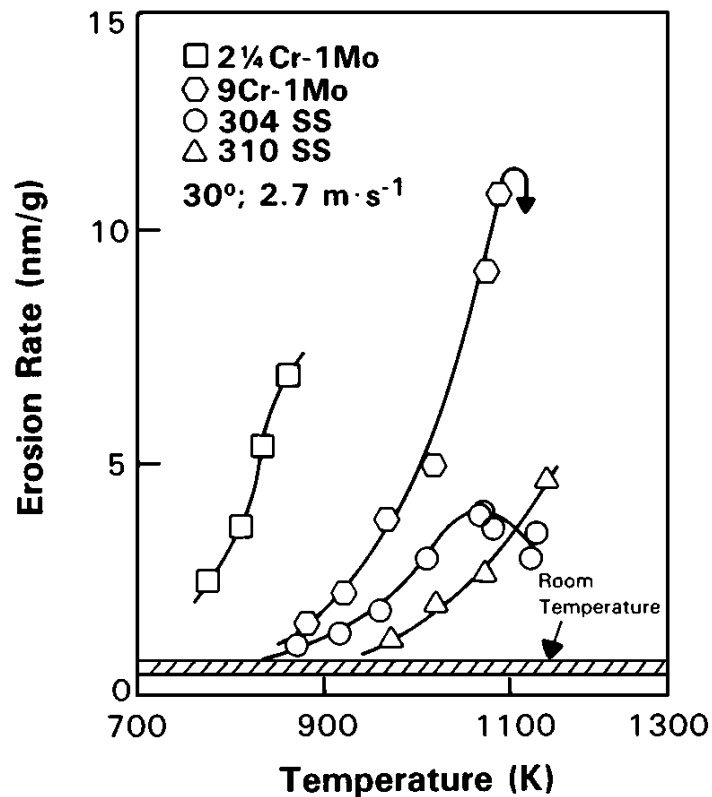
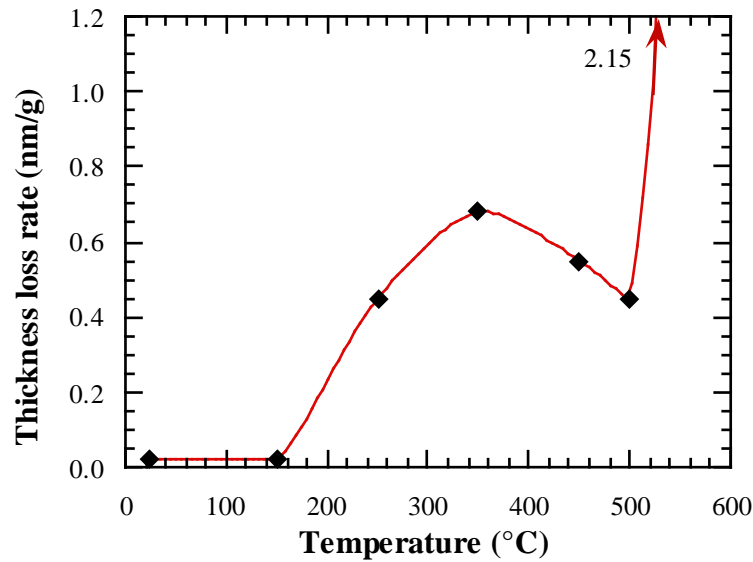


Fig. 4.2. High temperature erosion rates of alloys as a function of temperature, after Sethi and Corey (1987).

4.2.1.2. Levy & co-workers

A blast nozzle type erosion rig was used to study erosion-corrosion on a variety of materials, but usually 1018 plain carbon steel. Most tests were carried out at a particle loading of 75 g h^{-1} and a relatively high impact velocity, in the range $10\text{-}30 \text{ m s}^{-1}$ (Wang *et al.*, 1990), but a lower impact velocity of 2.5 m s^{-1} was also investigated (Wang *et al.*, 1991a). The effect of temperature for the erosion-corrosion of 1018 steel at 2.5 m s^{-1} by $250 \text{ }\mu\text{m}$ CFBC bed material particles is shown in Fig. 4.3a and shows the same temperature regimes observed by Sethi and Corey (1987) but with the addition of a fourth regime of high wastage at high temperatures (550° C) which was thought to be due to spalling of the thick scale developed by the 1018 steel at 550° C . At velocities of 10 m s^{-1} , wastage remained relatively constant up to 450° C and then increased rapidly (Fig. 4.3b).

(a)



(b)

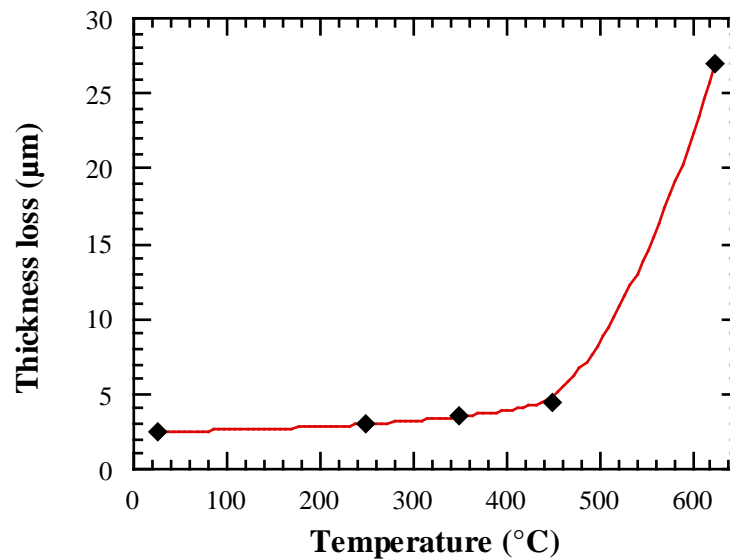


Fig. 4.3. Curves of test temperature vs. thickness loss of 1018 steel eroded-corroded at $\alpha = 30^\circ$, $250 \mu\text{m}$, CFBC bed material particles, (a) $V = 2.5 \text{ m s}^{-1}$, $t = 100 \text{ h}$, (b) $V = 10 \text{ m s}^{-1}$, $t = 5 \text{ h}$, after Wang *et al.* (1991a).

To explain this difference in wastage behaviour at moderate temperatures the idea of pseudoplasticity was proposed. At low velocity and strain rate microcracking of the oxide occurred simultaneously with crack healing to cause macroscopic plasticity of the oxide, which resulted in the reduction in wastage above 300°C . At higher velocity and

strain rate, crack healing could not occur, resulting in oxide spalling and chipping and no reduction in wastage was observed.

The erosion-corrosion of cooled 1018 steel was studied and is discussed in section 7.1 (Wang *et al.*, 1993a).

4.2.2. High flux

4.2.2.1. The Cambridge rig

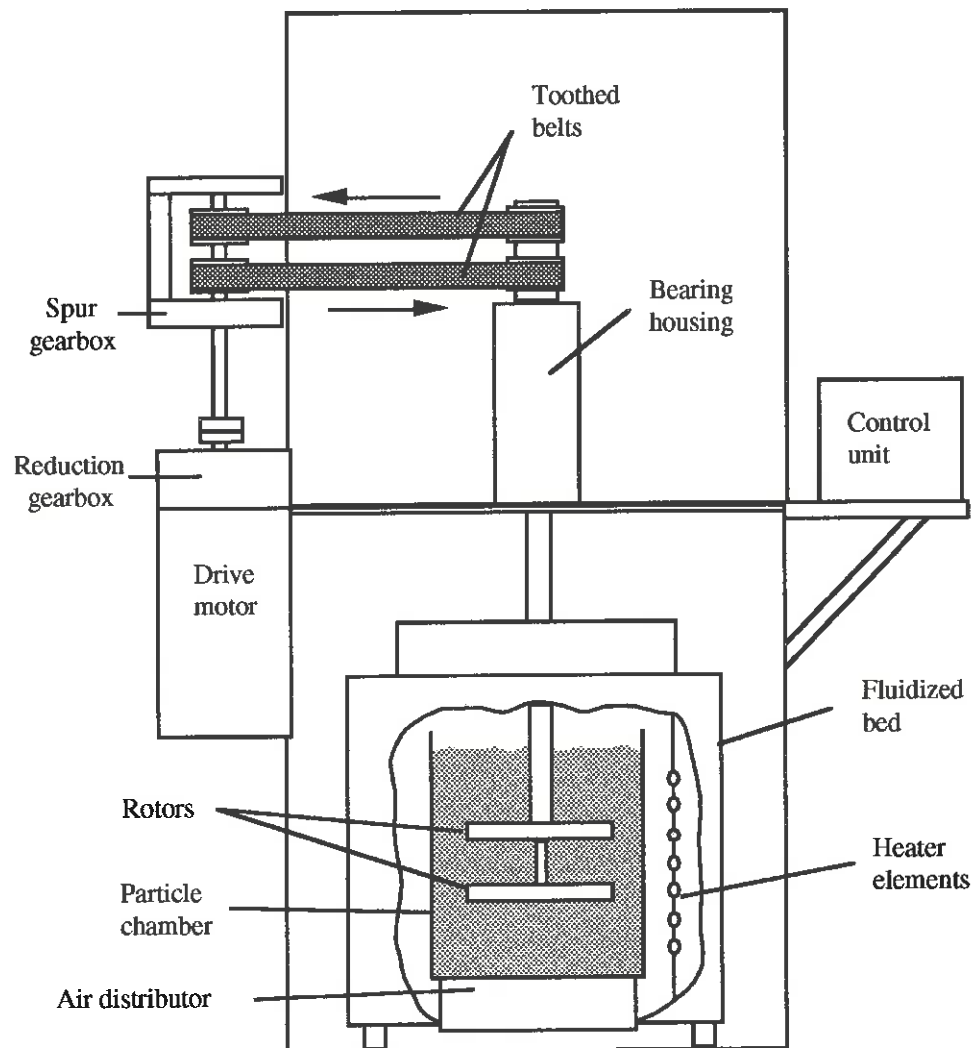


Fig. 4.4. Schematic diagram of the 'Cambridge' erosion-oxidation test rig, after Little *et al.* (1987).

The first laboratory test rig to investigate low velocities and high fluxes was described by Little *et al.* (1987). Four cylindrical specimens (80 mm long and 25 mm in diameter) were attached onto coaxial vertical shafts immersed in a fluidized bed, and rotated in a horizontal plane (Fig. 4.4). The pairs of specimens were counter rotated to minimise gross rotation of the bed particles, so that the impact velocity of the particles on to the specimens was due only to the motion of the rotors. The geometry of the specimens meant that they experienced a complete range of impact angles around their periphery while along their length the impact velocity increased with distance from the rotor axis, up to about 2.5 m s^{-1} . Specimen wastage was measured as thickness loss and measured by a linear variable displacement transducer placed against the specimen surface.

Two similar rigs were built; the first used by Entwisle (1990) which had a maximum temperature of 575° C , and the second, an improvement on the first, and used for this work was built around a smaller fluidized bed and had a maximum temperature of 800° C (Ninham *et al.*, (1989a);(1989b), Rogers (1992b)).

Initial quantitative characterisation was carried out at low temperatures with ABS polymer specimens (Entwisle *et al.*, 1987) and at elevated temperatures with high alloy steels (Ninham *et al.*, 1989a). $240 \mu\text{m}$ alumina particles were used for the majority of tests. The conclusions are summarised below.

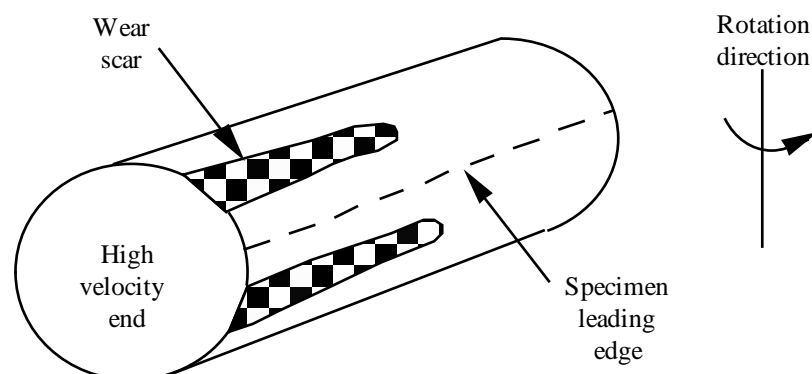


Fig. 4.5. Worn test specimen from the Cambridge rig.

(i) The greatest wear was found in two regions either side of the leading edge at angles between 0-30° and 150-180° where 90° was the leading edge of the specimen (Fig. 4.5). The width of the wear scar increased with increasing impact velocity. The absence of wear on the leading edge was attributed to the development of a 'dead' cap of defluidized particles at this point. Comparison of the results with abrasion and erosion models of the wear distribution did not show a dominant wear mechanism as both models predicted a similar wear distribution but with maximum wear at higher impact angles.

(ii) The wastage of the lower pair of rotors was 20-70% greater than the upper pair due to the slight increase in particle density within the bed.

(iii) For a fixed upper rotor position, the wear of the bottom rotor increased with decreasing specimen separation while the upper rotor wear was virtually unaffected. The explanation given was that bubbles developed with height, increasing the motion of the bed particles and that the lower rotor destroyed this bubble structure.

(iv) Use of only one rotor saw a drop in wastage by $\approx 30\%$ due to some gross rotation of the bed particles.

(v) An increase in fluidizing velocity resulted in a decrease in material wastage below $1.2 \cdot U_{mf}$, where U_{mf} is the minimum fluidizing velocity, and thereafter had a minimal effect.

(vi) The wear rate of specimens by the bed particles decreased with time due to particle attrition and reduction in angularity. To maintain a level rate of wear, 0.75 kg of bed material was replaced with new particles every 24 hours of use.

(vii) The wastage, W , increased with velocity according to:

$$W = k(v-v_0)^n \quad (4.1)$$

where n was found to be between 2 - 6. There was a threshold speed, v_0 , below which no wear was detected, and its value decreased with time.

(viii) After an initial incubation period the maximum wear increased linearly with time. Subsequent studies observed both positive and negative incubation times.

(ix) Wastage increased with particle size.

The temperature dependence of mild steel, 347 stainless steel and 800H Incoloy was studied by Ninham *et al.* (1989b). A peak in wastage at intermediate temperatures was observed (Fig. 4.6), the first results to reproduce similar findings by Sethi and Corey (1987). The explanation provided for this behaviour was similar to Sethi and Corey's argument except that the decrease at higher temperatures was suggested to be due to increased oxide plasticity. Unlike the prediction and observation made by Sethi and Corey that the peak wastage temperature increased with increasing particle velocity, these results appeared to show no increase. This was explained by the nature of the apparatus, where higher velocities also mean higher particle fluxes. Observation of unworn areas of the specimen suggested that tribological enhancement of the oxidation occurred, where by an increased flux increases the oxidation rate. This in turn would reduce any shift in peak temperature.

Similar results were found by Entwisle (1990) for mild steel, 9Cr - 1Mo steel, and 410 stainless steel in quenched, annealed and tempered forms. The temperature-wastage peak for mild steel was narrower than that measured by Ninham and occurred at 400° C rather than 300° C. The differences were explained by apparatus differences and that Entwisle's tests were interrupted. It was noted that the alloy content of the steel affected the magnitude and position of the peak wastage rate and also the wastage behaviour at temperatures above the peak wastage (Fig. 4.7).

Variations in the microstructure of 410 stainless steel caused changes in the wastage behaviour. The wastage increased in the order of: ferritic steel (152 H_v), tempered martensite (231 H_v) and untempered martensite (465 H_v), and in line with short term oxidation kinetics. This emphasised the importance of oxidation kinetics rather than mechanical behaviour (Hutchings *et al.*, 1991).

The increase in wastage rates with increasing temperature was again attributed to increasing oxidation and removal of oxide, but the decrease was believed to be due to the development of an oxide thick enough to confer a high degree of wear resistance (Entwisle, 1990).

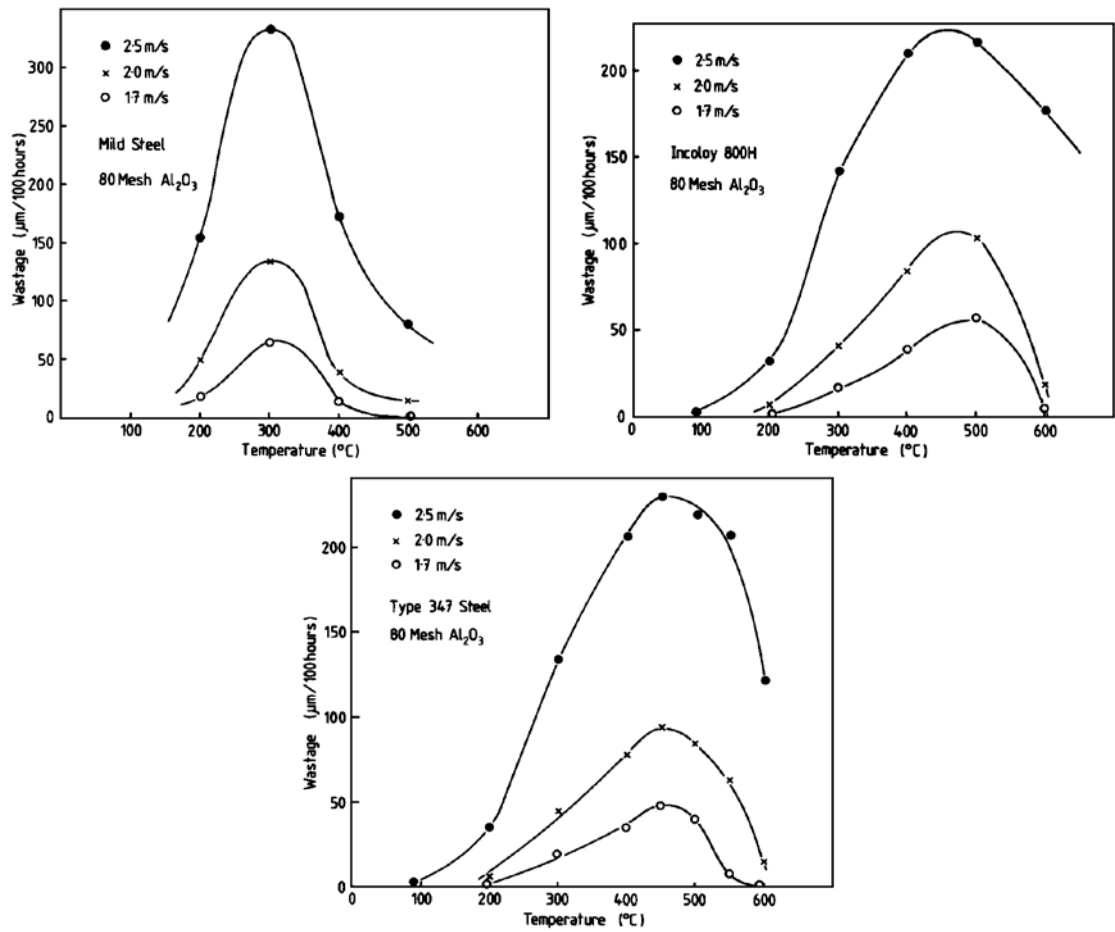


Fig. 4.6. Erosion-corrosion of steels in a fluidized bed environment, after Ninham *et al.* (1989b).

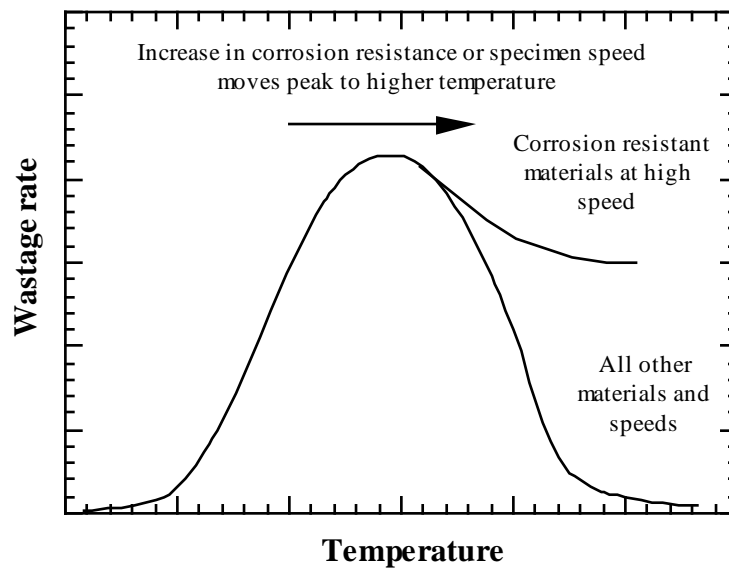


Fig. 4.7. Schematic diagram showing the typical variation of wastage rate with temperature for high alloy and stainless steels, after Entwisle (1990).

Examination of the oxide scales supported this view. A more recent study by Rogers *et al.* (1992c) on the wear scars of the low alloy steel 722M24T illustrates the point (Fig. 4.8). At temperatures below 300° C a layer of embedded abrasive fragments covered much of the specimen; no measurable wear occurred at 100° C but at 200° C some wastage occurred at oblique angles. At 300° C and 400° C corresponding to the increasing and maximum wastage rates, the wear scars were covered with very thin oxides which exhibited interference colours and traces of alumina fragments were detected. This suggested that the oxides were continually being formed and removed resulting in the high wastage rates. At velocities too low to cause wear, a region of deposited abrasive particle fragments again formed. At 500° C the wear scar formed at high velocities was covered by a thin coloured oxide film, while a thicker grey protective oxide formed at lower velocities corresponding to a significant drop in wastage. At higher temperatures a thick oxide covered the whole worn surface. Under these conditions wear of the oxide occurred rather than its complete removal.

2.25Cr - 1Mo and 1Cr - 0.5Mo steels were also studied (Rogers, 1992b; Rogers *et al.*, 1995). The wastage-temperature behaviour for 2.25Cr - 1Mo was similar to 722M24T (3Cr) but with a broader peak and its maximum wastage at around 450° C rather than 400° C. At 600° C both steels exhibited low wastage rates due the formation of a thick protective oxide. The 1Cr - 0.5 Mo steel behaved more like mild steel with the formation of a thick mechanically protective oxide at 500° C. The wastage rate against temperature for these three low alloy steels at an impact velocity 2.5 m s⁻¹ is shown in Fig. 4.9.

The effect of a temperature gradient on erosion-corrosion wastage rates was investigated by Ninham *et al.* (1991) and later by Rogers (1992b) and is discussed with the present work in Chapter Seven.

Rogers (1992b) also studied the effect of surface treatments and coatings on erosion-corrosion behaviour.

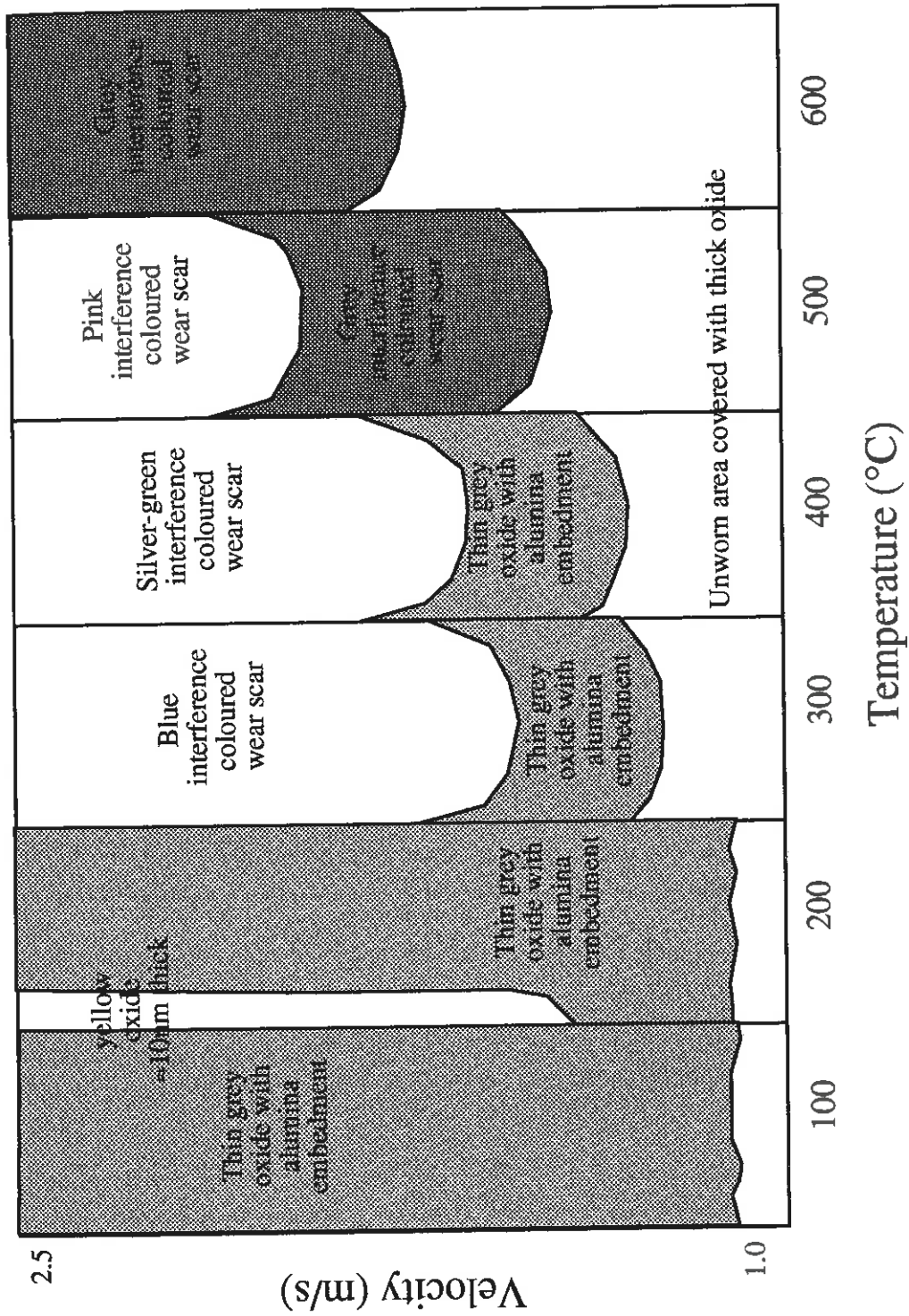


Fig. 4.8. Wear scars on 722M24T alloy after exposure in the fluidized bed for 72 h, after Rogers *et al.* (1992c).

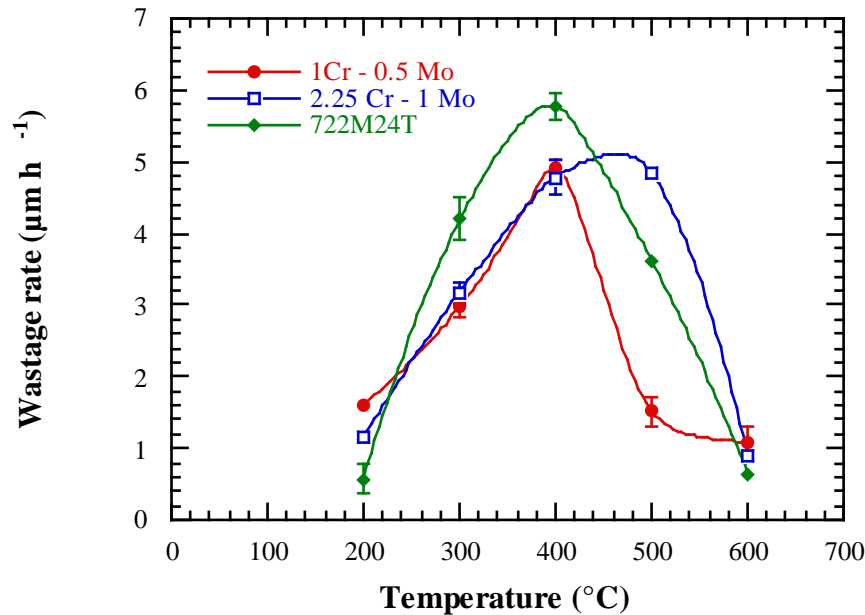


Fig. 4.9. Wastage rate against temperature for three low alloy steels exposed on the upper rotor of the 'Cambridge' rig, after Rogers (1992b).

Nitrocarburizing 722M24T steel (Rogers, 1990) increased the surface hardness from 300 H_v to nearly 1000 H_v . The wastage rates generally decreased, but the wastage after 72 hours at 200° C was higher than the untreated metal. The improvement in wastage was thought to be due to the greater surface hardness and oxide adhesion of the nitrocarburized steel. The higher wastage at low temperatures was attributed to the higher oxidation rate of the nitrocarburized steel degrading its mechanical properties. The temperature of maximum wastage decreased from 400° to 300° C and this was thought to be due to the higher oxidation rate of the diffusion layer relative to the untreated steel.

TiN coatings (Rogers *et al.*, 1992c) on 722M24T steel and mild steel reduced the wastage rate to around 3% of the uncoated steels, especially at temperatures below 400° C. This was attributed to the high coating hardness and its low oxidation rate. The increase in wastage observed between 200° and 400° C was due to a decrease in the coating hardness. A significant increase in wastage was observed at higher temperatures due to an increase in the oxidation rate of TiN.

Vacuum plasma sprayed alumina coatings significantly reduced the wastage to below $20\ \mu\text{m}$ at all temperatures for 72 hours exposure. The coating proved to be wear resistant and provided a good oxidation barrier to the substrate.

4.2.2.2. The UMIST rig

The experimental rig used by Stott *et al.* (1989) rotated two small cylindrical rods in a vertical plane through a fluidized bed and is shown in Fig. 4.9b. The specimens only enter the bed at the bottom of each cycle, spending approximately 20% of the time in the bed and thus for the majority of the test period the specimens can undergo oxidation in the absence of wear. The reason for this arrangement is not fully explained although it perhaps simulates wear of material in the splash zone of a fluidized bed. The specimens were 25 mm long and 3 mm in diameter, and the wastage of material was measured by weight changes.

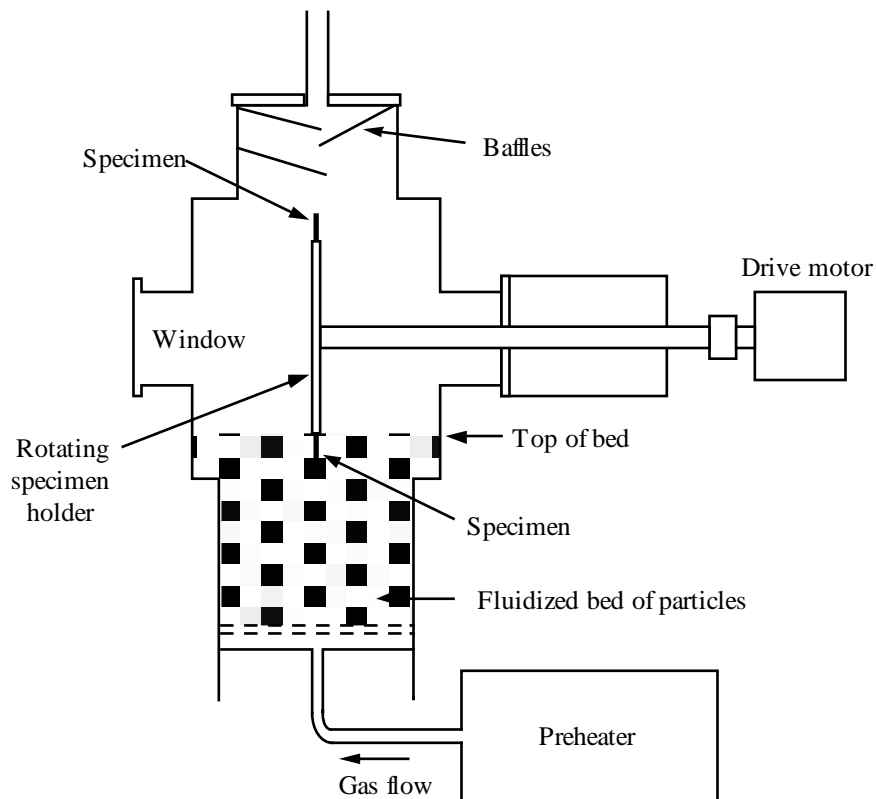


Fig. 4.9b. A schematic diagram of the fluidized-bed rig (side elevation) used by Stott *et al.* (1989).

Initial studies (Stott *et al.*, 1989) were conducted on mild steel, 2.25Cr - 1Mo and Fe - 12Cr steel, and 310 stainless steel, using two sizes of abrasive, coarse $800\ \mu\text{m}$ and

fine 100 - 150 μm silica particles. After 5 hours exposure, two types of wear versus temperature behaviour were observed depending on impact velocity and particle size (Fig. 4.10). For the large particles and at an impact velocity of 5 m s^{-1} the weight loss remained low below 300°C and rapidly increased with increasing temperature similar to the behaviour observed by Wang *et al.* (1990) at 10 m s^{-1} (Fig. 4.3b). The increase was more rapid with decreasing chromium content. At lower velocities, no rapid increase in weight loss was observed. However, the behaviour between 100° and 500°C was not measured.

Examination of the eroded surfaces showed most damage occurred at the leading edge of the rod. Below 300°C only very thin oxides were observed while at 500° and 600°C thicker oxides were evident. These were significantly cratered where high wear rates were measured and deformed in the low wastage areas. These deformed oxides were similar in appearance to the protective 'glaze' oxides developed during sliding wear investigated by Stott *et al.* (1987).

A further study by Stott *et al.* (1991) (Fig. 4.11) showed the wastage of mild steel decreasing with temperature, the wastage of 321 stainless steel increasing with temperature and the Fe-Cr steels showing maximum wastage at intermediate temperatures. As with the previous study specimen surfaces were relatively featureless at 250°C . At 450° and 650°C important differences were observed. The maximum wastage occurred at either side of the leading edge, erodent debris was embedded in the oxides and oxide spalling occurred increasingly at the higher wastage rates. It was assumed that each metal showed a peak in wastage behaviour against temperature although, due to the lack of temperatures investigated, the temperatures at which the peaks occurred were not established. It was suggested that an accumulation of a critical strain caused scale detachment. The results were also consistent with the trend of an increasing peak wastage temperature with increasing chromium content. However, the unusual result of the 321 stainless steel showing the highest mass loss was not explained.

The erosion-oxidation behaviour of Incoloy 800H was intensively studied by Stack *et al.* (1991, 1992) using rectangular specimens and $200 \mu\text{m}$ silica particles. A peak in weight loss occurred at around 500°C and, at this temperature, weight loss rapidly increased above a specimen velocity of about 1.4 m s^{-1} with a velocity exponent of 3.5.

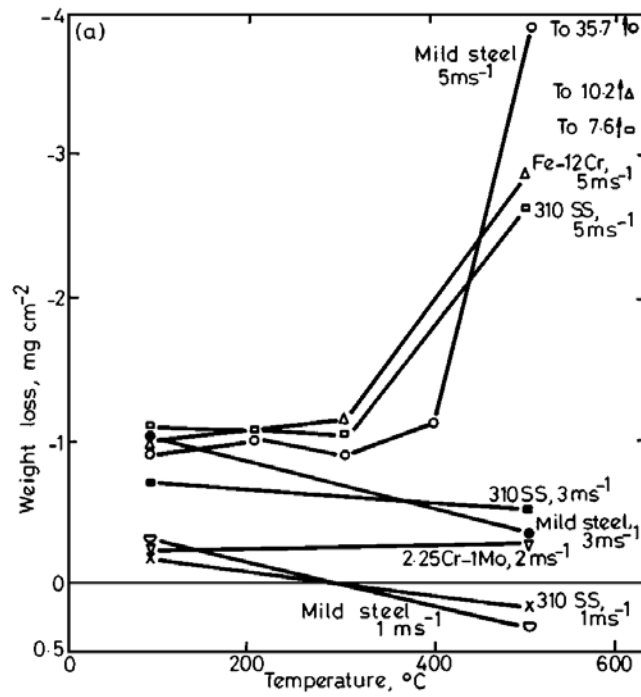


Fig. 4.10. Weight loss against temperature after 5 h exposure to erosion-corrosion with coarse silica, after Stott *et al.* (1989).

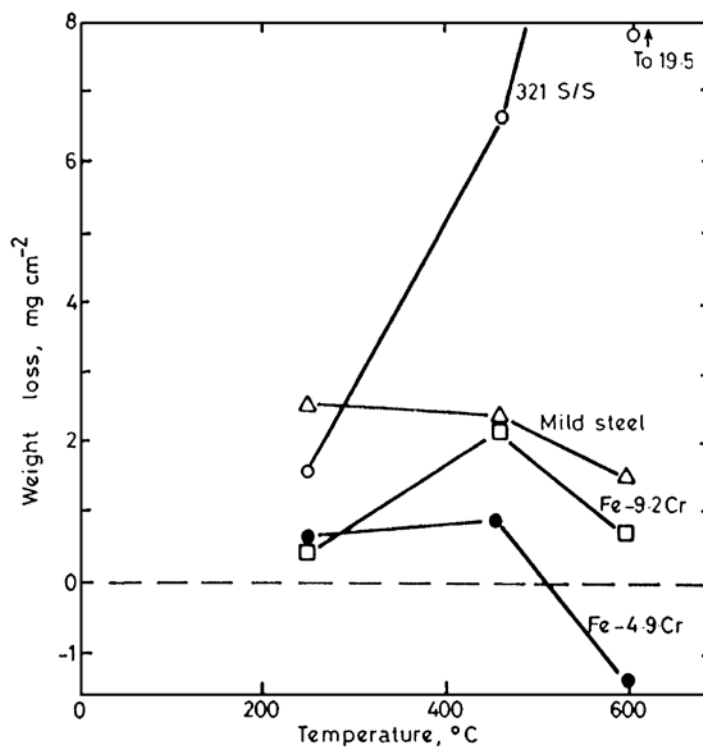


Fig. 4.11. Plots of weight loss against temperature for various alloys after 24 h exposure to erosion-corrosion at 5 m s⁻¹, after Stott *et al.* (1991).

Pre-oxidation of Incoloy 800H and other high temperature alloys was studied in an attempt to improve their erosion-oxidation behaviour. Generally pre-oxidation gave some early protection, then the mass loss behaviour approached that of the untreated specimens once the pre-oxidised scale had been penetrated (Fig. 4.12). The protection was most effective for scales pre-oxidised in an H_2/H_2O atmosphere due to superior adhesion of the scales. The proposed mechanisms for pre-oxidised scale removal were initial scale deformation followed by crack initiation and growth.

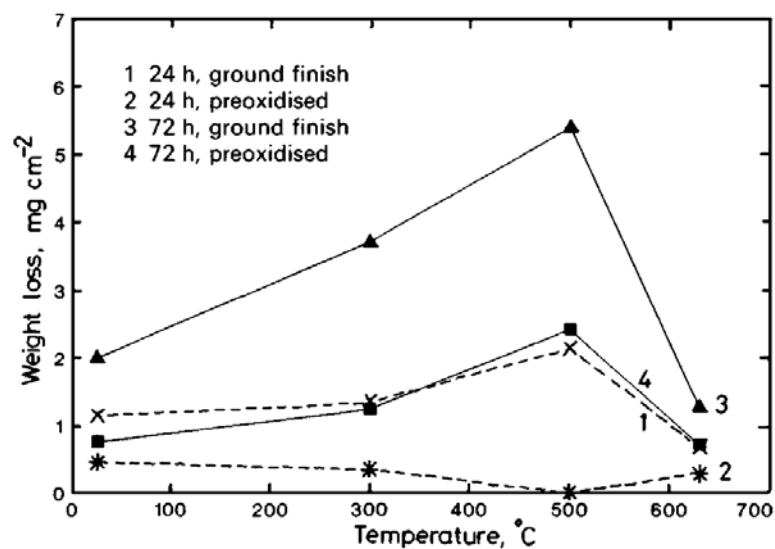


Fig. 4.12. The effect of temperature on the erosion-corrosion of pre-oxidised and ground Incoloy 800H in 200 μm silica and at 1.9 m s^{-1} , after Stack *et al.* (1991).

4.2.2.3. The Berkeley rig

A significant source of wear in a fluidized bed has been attributed to the wakes of rising bubbles and the collapse of 'teardrop' like voids which form periodically beneath horizontal or inclined tubes. In an attempt to investigate this aggregate, hammering process MacAdam and Stringer (1987) designed and built a rig at the Lawrence Berkeley Laboratory, University of California (Fig. 4.13). A horizontal specimen rod was oscillated 10 mm vertically within a fluidized bed, with a rapid downstroke and a slow upstroke. The velocity ($1 - 2 \text{ m s}^{-1}$) of the downstroke and frequency of the oscillation (1 Hz) was chosen to match the velocity and frequency of rising bubbles and

voids. Most experiments were carried out at room temperature and with 800 μm diameter impure quartz bed particles (30% clay). Wear was measured by mass changes and thickness loss.

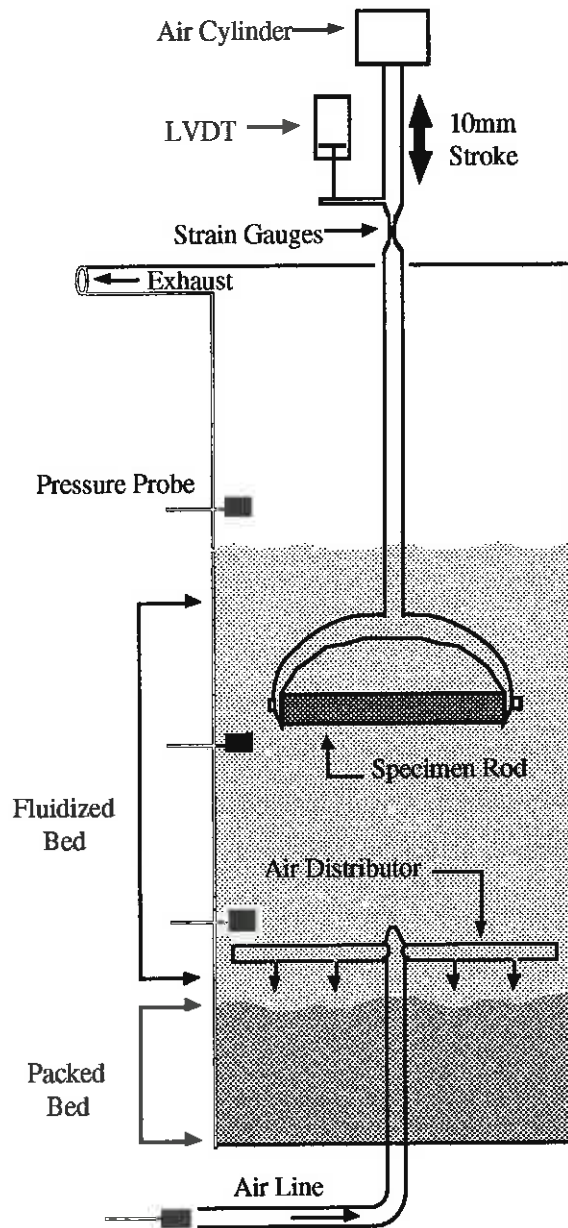


Fig. 4.13. A schematic diagram of MacAdam and Stringer's fluidized bed wear rig (MacAdam and Stringer, 1987)

Tests on several types of metal and plastic were initially undertaken (MacAdam and Stringer, 1987, 1989). Metals and plastics both showed steady state wear loss, the metals after an incubation period. These wear rates were shown to be comparable with industrial cold fluidized bed studies and the magnitude of wear relatively mild when

compared with abrasion and erosion studies (MacAdam and Stringer, 1991a). An inverse relationship between hardness of annealed metals and wear rate was shown.

The general distribution of wear was similar to results from the 'Cambridge' rig, but with a maximum wear rate at 145° and 215° (0° being located at the rod top) closer to the specimen's leading edge. At 180° plastics and pure aluminium typically showed 25 to 30% of the maximum wear. Other metals showed virtually no loss at this location and even a slight increase in thickness in some cases. This increase was shown to be due to the deposition of quartz bed material as a semi-continuous conglomerate layer. Little damage occurred on the specimen sides and top surfaces. Again some metals showed a build up of the conglomerate quartz layer on the top surfaces which was significantly less deformed than that on the bottom.

The worn surface regions of all metallic specimens consisted of a composite containing highly strained thin metal foils sandwiched between layers of agglomerated micron and sub-micron sized quartz bed particles.

To investigate the nature and distribution of particle impacts some short duration experiments were carried out (MacAdam and Stringer, 1991b). A PMMA and 6061-T6 aluminium rod were gold coated and exposed in the rig for 30 and 5 seconds respectively. Where an impact had occurred the gold coating had been removed and the impact site could thus be observed. The PMMA rod showed the impact density and distribution of the impacts. The impact density and aspect ratio of the scars increased from the 180° position to a maximum at 120° to 135° and then decreased to almost zero at 90°. The aspect ratio of the wear scars indicated normal particle erosion at 180°, impingement erosion at 145°, and abrasion at 120° to 135°. Examination of single impacts on the aluminium rod explained the different positions in maximum wear rate and impact density. Two types of impact were identified, damaging and non-damaging; a quarter of all impacts were damaging. The greatest density of damaging impacts occurred at 145° resulting in the maximum wear loss. It was also calculated that the abrasion track widths were typically 1 to 5% of the mean particle diameter, and that the time interval between impacts at a given location ranged from 4 to 19 minutes for damaging impacts.

Due to the surface morphology of the worn region, the infrequency and size of impacts, the wear mechanism was suggested to involve multiple impacts leading to removal by cutting or fracture.

The effect of different bed materials were studied using quartz, olivine and silicon carbide, with hardnesses of 820, 750, and 2480 kg mm⁻² respectively (MacAdam and Stringer, 1993a). Quartz was the most erosive, followed by silicon carbide and then olivine, and the wear scar width decreased down the order; silicon carbide, quartz then olivine. From observations on the top of the samples silicon carbide appeared to have no threshold loading below which no loss occurred unlike quartz and olivine. These results were explained by differences seen in the extent and nature of particle embedment. Both quartz and olivine formed fine debris which became embedded as an agglomeration. Whilst individual silicon carbide fragments (of size near 5µm) embedded in the metal. The lack of an agglomeration of silicon carbide increased the size of the wear scar and also enabled lips of metal to be rewelded to the base metal on subsequent impacts thus reducing the wear rate when compared with quartz.

Wang *et al.* (1993b) used the rig to investigate the effect of microstructure of 1018 steel on material wastage at room temperature. Four microstructures were studied; annealed, normalised, cold drawn and as quenched. It was found that the wear resistance was linearly related to the steel hardness, while no relationship with hardness was found with higher velocity impacts (>10 m s⁻¹) under a blast nozzle tester (Wang *et al.*, 1991b). It was suggested that under the mild wear conditions of the bed, particle impacts did not result in high strain rate and severe work hardening of the surface, so that thermal and work induced hardness was able to influence the wear behaviour of the steel.

A similar heated rig was used to expose mild steel at temperatures up to 550 °C (MacAdam and Stringer, 1993b). The temperature dependence of material thickness loss for two mixing conditions, high dust and low dust, are shown in Fig. 4.14. Below 350° C wastage was predominantly due to abrasion and showed only a small temperature dependence. Above 500 °C the removal of oxide caused a rapid increase in wear rate. At intermediate temperatures a high concentration of sub-micron dust enabled a protective deposit to form reducing the wear rate to zero.

A recent paper (Zhang *et al.*, 1996) describes modification to the heated rig to allow cooling of the specimen in order to investigate erosion-corrosion in a temperature gradient. Preliminary results were presented for a specimen at a metal temperature of 190° C with the fluidized bed at 700° C. These results are described and discussed in Chapter Seven.

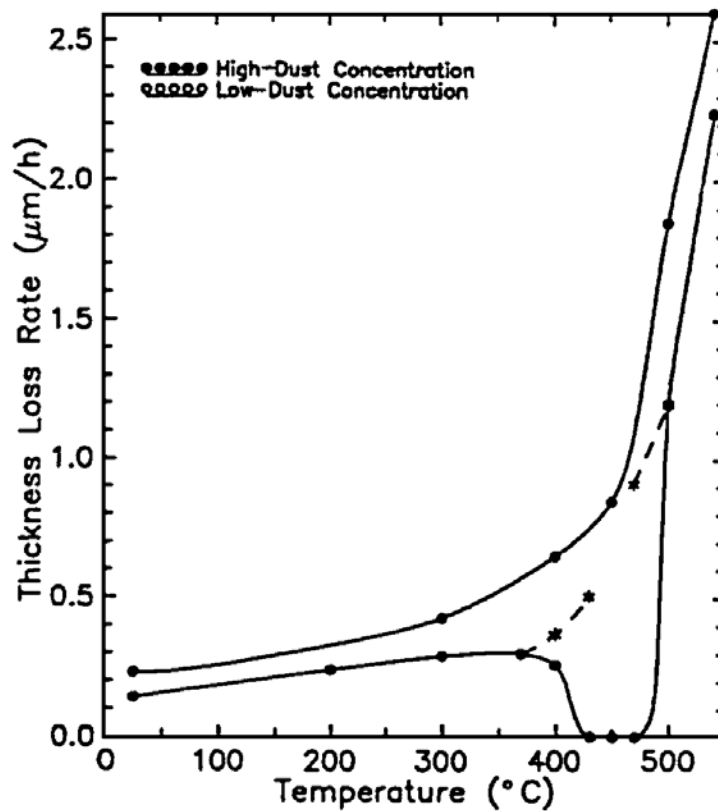


Fig. 4.14. Temperature dependence of maximum wastage rate for the high- and low-dust test series, after MacAdam and Stringer (1993).

4.2.2.4. The NPL rig

The rig used at the National Physical Laboratory, Teddington, by Hall and Saunders (1990) was very similar to the 'Cambridge' rig, but with a non-fluidized bed of abrasive particles. The specimens were also shorter so that only a single impact velocity was studied for each test. Mild steel, chromium-molybdenum ferritic steels and type 310 and 347 stainless steels were exposed to an impact velocity of 2 m s^{-1} in a bed of $< 300 \text{ }\mu\text{m}$ diameter alumina particles between temperatures of 250° and 550° C . Wear was measured by thickness loss.

Maximum wear again occurred at intermediate temperature, with the temperature of maximum wastage increasing with chromium content. Comparing these results with data from the 'Cambridge' rig shows the peak wear temperatures to be similar but the wear rates were approximately double due to the slumped nature of the bed. Greater wastage occurred on the lower wear scar of the specimen where compression of the

erodent between specimen and container base produced higher frictional forces.

At lower temperatures the exposed specimen surfaces were rippled, and at higher temperatures small cracks were observed on mild steel. These started at the surface and penetrated the into the substrate in the direction parallel to particle impingement.

4.3. Mechanisms and modelling

In the simplest terms erosion-corrosion can be separated into two regimes, dominated by erosion or corrosion depending on which process occurs at a greater rate under the conditions of interest. In between the two extremes of pure erosion and pure corrosion, important synergistic interactions can increase the metal loss rate significantly beyond that due to either erosion or corrosion alone, as illustrated by the laboratory studies. From observations made during a study of the erosion-corrosion of nickel and cobalt, Kang *et al.* (1987) suggested two broad synergistic regimes, (1) erosion-enhanced corrosion in which the dimension of the impact damage zone is confined within the scale thickness, and (2) corrosion affected erosion in which the damage zone includes both scale and metal. The relative ratio of erosion and corrosion rates determine the dominant regime. For example, for a fixed erosion rate a transition from erosion, corrosion affected erosion, erosion enhanced corrosion and corrosion will occur on increasing temperature. Rishel *et al.* (1991) extended this classification, subdividing the erosion enhanced corrosion regime to include scale spalling. The classifications are shown schematically in Fig. 4.15.

Pure erosion. This occurs when the corrosion rate is negligible when compared with the erosion rate, as in the case of severe erosion or in non-corroding conditions.

Corrosion-affected erosion. With an increasing corrosion rate, a thin film develops, but the stress field introduced by an impacting particle has dimensions greater than the scale thickness so that both scale and metal is deformed. The metal loss rate increases over pure erosion and a surface composite layer consisting of intermixed metal, scale, and embedded erodent particle fragments is typically produced.

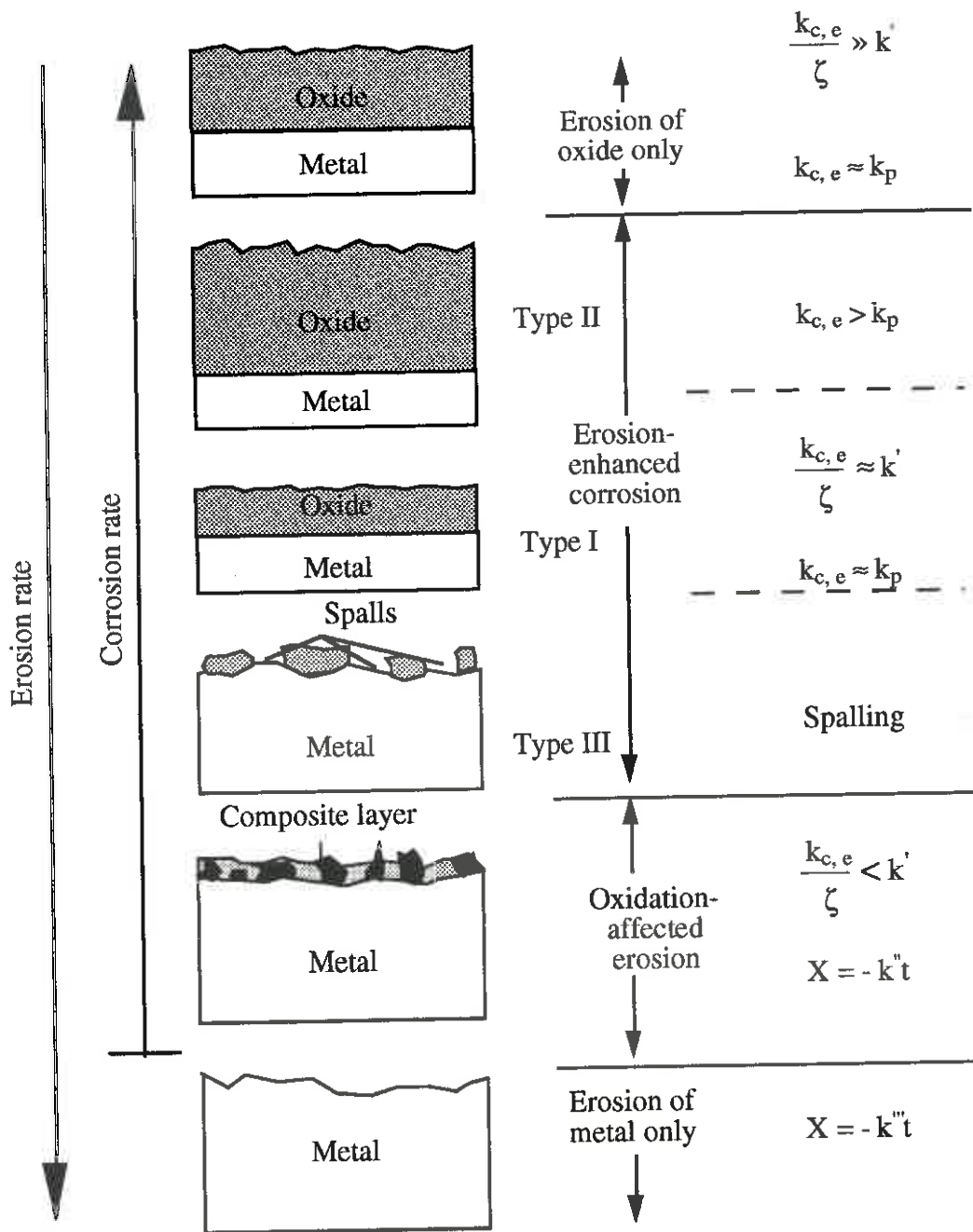


Fig. 4.15. Erosion-corrosion mechanisms, after Rishel *et al.* (1991).

Erosion-enhanced corrosion was broken up into 3 categories. The first two involved a continuous steady state thickness, ζ_{ss} , the third involved spalling.

Parabolic oxidation was assumed so that the thickness of the oxide film was expressed as:

$$\frac{\partial \zeta}{\partial t} = \frac{k_p}{\zeta} \quad (4.2)$$

where k_p is the parabolic rate constant and ζ is the oxide thickness. If the scale is maintained without spalling, scale is removed from the outer surface at the rate k' (which depends on the erosion conditions). The net growth rate will then be:

$$\frac{\partial \zeta}{\partial t} = \frac{k_{c,e}}{\zeta} - k' \quad (4.3)$$

where k_p is replaced by $k_{c,e}$, the applicable parabolic rate constant during erosion-corrosion. A steady state thickness is possible when $\partial \zeta / \partial t = 0$ to give

$$\zeta_{ss} = \frac{k_{c,e}}{k'} \quad (4.4)$$

If a specimen is exposed to erosion-corrosion a scale builds up to the thickness ζ_{ss} ; if it has been pre-oxidised to a thickness $\zeta > \zeta_{ss}$, then net erosion will occur until ζ_{ss} is reached.

Type I erosion enhanced corrosion was defined with $k_{c,e} = k_p$, i.e. the scale rate was unaffected by erosion. Good agreement (Chang *et al.*, 1990) has been found between literature values of k_p and those calculated from measured values of ζ_{ss} and k' for the erosion-corrosion of cobalt.

Type II erosion enhanced corrosion was defined by $k_{c,e} > k_p$, that is, an enhancement of the scaling rate occurs in the presence of erosion. This was observed for the erosion corrosion of Ni-270 in sulphidising conditions, where a thicker scale developed than under corrosion only. It was thought that the presence of erosion increased the proportion of nickel sulphides in the scale which provides a faster route for ionic transport than nickel oxide thus increasing the scale growth rate. Similar behaviour was noted by Levy *et al.* (1986) for low-chromium steels in methane/air mixtures. Generally the presence of cracks or dislocations introduced by erosion of the oxide provide fast diffusion paths for ions.

Type III erosion enhanced corrosion was described as the case in which erosion induced spalling of the scale adds to further material loss, resulting in a very thin or absent scale and a high corrosion rate. Spalling was classified as erosion enhanced corrosion; it is the mechanism of discontinuous scale thinning that leads to an enhanced corrosion rate.

Pure corrosion. This was defined as a regime where the ratio of corrosion to erosion rate was very high, resulting in effectively pure corrosion and parabolic rate thickening. Unless $k' = 0$ a steady state thickness will exist although it will be very large.

4.3.1. Comparison with other erosion-corrosion classifications

Other researchers have tended to use different nomenclature for essentially the same erosion-corrosion processes, although in many cases the criteria used to define the transition between regimes was different. Stack *et al.* (1995a) recently reviewed the range of erosion-corrosion regime nomenclature; a summary is shown in Fig. 4.16.

Hogmark (1983)	erosion-dominated	erosion of corrosion product and substrate	flaking of the corrosion product	erosion of the corrosion product without flaking	erosion affected corrosion	corrosion
Rishel, Kang, Birks (1991)	erosion	oxidation affected erosion	erosion enhanced oxidation Type III Type I Type II			erosion of oxide only
Nicholls and Stephenson (1995)	substrate dominated	scale modified	scale-dominated			
Sethi <i>et al.</i> (1990)	erosion-dominated	erosion-corrosion dominated	corrosion-dominated			
Sundararajan (1990)	metal erosion	oxidation affected erosion	oxidation controlled erosion			
Stack <i>et al.</i> (1993)	erosion-dominated	erosion-corrosion-dominated	corrosion-dominated 1		corrosion-dominated 2	

Fig. 4.16. Summary of erosion-corrosion regimes, after Stack *et al.* (1995a).

An earlier study by Hogmark *et al.* (1983) discussed a mechanism classification similar to that of Rishel *et al.* (1991). In order of increasing relative corrosion rate, they listed (1) pure erosion, (2) simultaneous damage of metal and scale (equivalent to corrosion affected erosion), (3) flaking (spalling) of scale at individual impacts, (4) erosion of scale without flaking, (5) erosion-affected corrosion, and (6) pure corrosion. Pure corrosion was treated as involving a periodic flaking due to stress build-up, and erosion affected corrosion was attributed to the effects of erosion on the critical thickness for flaking or spalling. The regime of erosion of scale without flaking was not treated in terms of steady-state scale thickness as in the work of Rishel *et al.* (1991).

Sundararajan (1990, 1991) classified erosion-corrosion regimes in a similar manner to Rishel *et al.* (1991) but with one main difference. Type III erosion enhanced corrosion was split into two separate cases of 'oxidation controlled' erosion: (1) continuous oxide removal, in which all oxide is removed down to bare metal within each impact site, and (2) intermittent spalling of the oxide when the scale builds up to a critical thickness, Z_c , only after several impacts. Stephenson *et al.* (1983) provided evidence of a critical scale thickness. Ductile-to-brittle transitions were observed on oxide scales of nickel-based superalloys and impacts went from ductile to brittle behaviour above a critical scale thickness. Sundararajan determined the conditions required for each regime to be dominant, and produced erosion-corrosion regime maps for temperature and velocity variations (Fig. 4.17). The ratio between the depth of plastic deformation in the metal, L_m or oxide, L_o , and steady state scale thickness, Z_{ss} , was used to determine the transitions between regimes. The proposed conditions were:

$$\frac{Z_{ss}}{L_m} < 0.1 \quad \text{- metal erosion}$$

$$0.1 L_m < Z_{ss} < L_o^* \quad \text{- oxidation-affected erosion}$$

$$Z_{ss} > L_o \quad \text{- oxide erosion}$$

* From Sundararajan (1991), $2 L_o$ is used in Sundararajan (1990)

and for the spalling mechanisms the oxide thickness grown between impacts, Z_b , was considered, so that:

$$Z_b < Z_c < Z_{ss} \quad - \text{oxidation controlled erosion (spalling)}$$

$$Z_{ss} > Z_b \text{ and } Z_{ss} > Z_c \quad - \text{oxidation controlled erosion (continuous)}$$

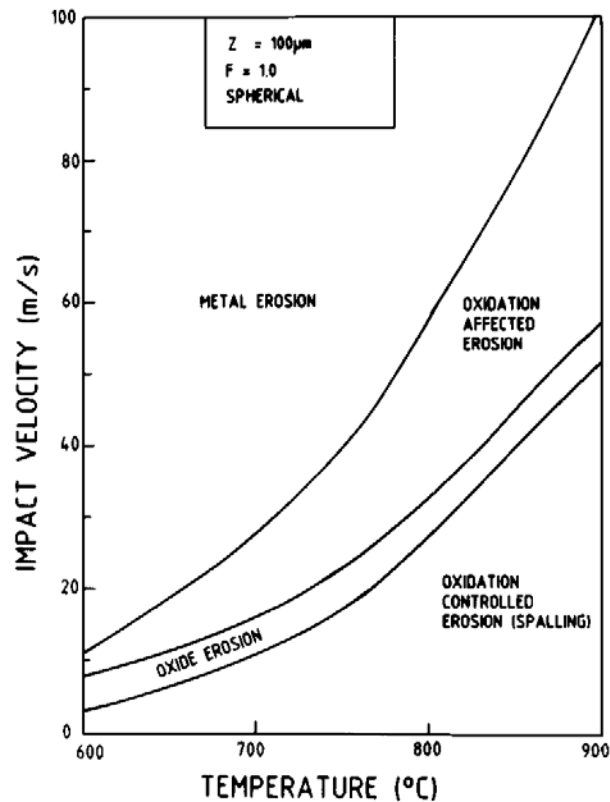


Fig. 4.17. Erosion-corrosion regime map of impact velocity against temperature for a spherical particles impacting mild steel, after Sundararajan (1991).

Nicholls and Stephenson (1995) have suggested three regimes; substrate dominated, scale modified and scale dominated, with similar criteria to determine the dominant mechanism as Sundararajan, by considering the ratio of scale thickness, z , to contact area, a_s on the substrate and a_c , on the scale:

$$\frac{z}{a_s} < 0.1 \quad - \text{substrate dominated}$$

$$1 < \frac{z}{a_s} \text{ and } \frac{z}{a_c} < 0.1 \quad - \text{scale modified}$$

$$\frac{z}{a_c} > 1 \quad - \text{scale dominated}$$

These criteria were part of a sophisticated computer erosion-corrosion model, which has been gradually developed and improved. Monte Carlo methods were used to calculate impact variables and the effect of each individual impact on an array of points. In the substrate and scale dominated regimes the material was considered to behave as either a substrate or scale of infinite thickness, respectively. In the scale modified regime the contact area and effective surface modulus was calculated for the combined scale/substrate composite.

Sethi and Wright (1990) proposed three regimes based on their experimental results (section 4.2.1.1); metal erosion at low temperatures, erosion-corrosion dominated regime over the region of increasing wear with increasing temperature, and corrosion dominated at the transition from increasing to decreasing wear. This was modified by Stack *et al.* (1993) who subdivided the corrosion dominated regime into two, the transition from corrosion dominated 1, to corrosion dominated 2 occurred when the weight change was zero, i.e. the weight gain from corrosion was equal in magnitude to the weight loss from erosion. Erosion-corrosion maps examining the effect of many variables were constructed, using essentially the same criteria and assumptions as Sundararajan (1991) but without the spalling mechanisms, and with the addition of the third transition from corrosion dominated 1 to 2, described above (Stack and Bray, 1995b).

4.3.2. Modelling wastage for different regimes

4.3.2.1. Erosion enhanced corrosion

The simple model of parabolic oxidation and linear erosion used by Rishel *et al.* (1991) for the erosion enhanced corrosion regime was used by Markworth *et al.* (1991) and Liu *et al.* (1988) as a basis for computer models. Both authors found that the oxide thickness generally showed an asymptotic behaviour with time to a steady state thickness. Also under some circumstances an initial mass increase was observed followed by a decrease to a constant mass loss.

Liu *et al.* (1988) defined the point of zero mass loss as the 'cross-over' point which they suggested signalled the transition from erosion-dominated to oxidation-dominated behaviour. They derived a series of plots showing the cross-over time for Al_2O_3 and Cr_2O_3 forming alloys given the oxidation and erosion rate constants.

To verify the model, results from Kang *et al.* (1987) of the erosion-oxidation of cobalt and nickel were simulated by adjusting the erosion rate to fit the experimental data. The model was then used to examine the early stages of oxide growth to explain the observed surface morphology. For example, an early stage of thin oxide coverage allowed erosion-corrosion within the corrosion affected erosion regime to occur, causing plastic deformation of the substrate leading to the formation of the observed moguls. However no mention is made of the fact that the assumptions behind the model break down at thin oxide thicknesses.

Markworth *et al.* (1991) represented the erosion rate as a function of the oxide thickness thus:

$$\dot{Y} = \frac{ac}{S^k} - bS \quad (4.5)$$

where S is the oxide thickness, k denotes the order of the oxidation kinetics ($k=0$ linear kinetics, $k=1$ parabolic kinetics), a is the oxidation rate constant, c is the Pilling-Bedworth ratio and b is a constant. As was mentioned this has a limited validity, perhaps only for small S , but it enabled the equation to be solved for the oxide thickness, thus:

$$S^{k+1} = \frac{ac}{S^k} (1 - e^{-(k+1)bt}) \quad (4.6)$$

To improve this model in order to account for discrete erosion events, a statistical approach to model erosion was used rather than the an empirical one (Markworth, 1992). Scale was assumed to be removed over an erosion footprint down to the metal scale interface, and so this was, effectively, a spalling model (section 4.3.2.2) similar to models proposed by Sundararajan.

An important point regarding this type of model, which does not seem to have been made by any of the authors mentioned, is the implications for the temperature dependence of the metal thickness loss rate. At the steady state thickness (equation 4.4) the metal thickness loss is proportional to the scale loss rate through appropriate density factors and despite the oxidation rate varying with temperature it is the erosion rate that determines the material loss rate. Therefore, within this regime any change in the material loss rate with temperature is due to a temperature dependence of the erosion rate (Kosel, 1992).

4.3.2.2. Scale Flaking or Spalling

Scale spalling is included by most authors as an important mechanism but there is a general lack of agreement whether it belongs to the corrosion affected erosion or erosion enhanced corrosion regime, or where it falls with respect to the temperature of maximum wastage. This may be partly due to the relative ease of modelling complete scale removal, as the corrosion history of the specimen is lost once spalling occurs.

Sethi and Wright (1990) proposed a scale removal model which was considered a mechanism of their corrosion affected erosion regime. They assumed parabolic oxidation kinetics, and that the oxide was removed down to the base metal over the erosion 'footprint' of an impact when the oxide was below a critical oxide thickness. Using this model they showed that a four-fold increase in flux led to a doubling in the wastage rate (Fig. 4.18). As the flux increases the time between impacts decreases; although the oxide thickness is reduced the average rate of oxidation is higher, therefore more oxide is removed in unit time.

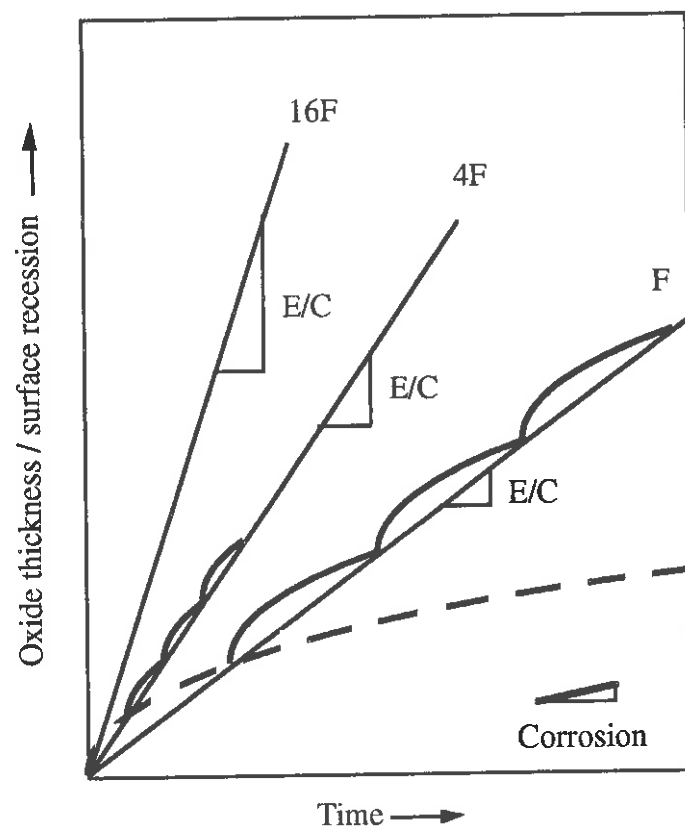


Fig. 4.18. The effect of flux on the wastage rate, after Sethi and Wright (1990).

Modelling the scale modified erosion regime Nicholls and Stephenson (1995) used fracture mechanics. The maximum stress induced by an impact in a coating or scale was calculated and compared with its fracture stress to determine whether fracture occurred, if so the scale was removed to the scale-substrate interface. If not then possible damage to the substrate was calculated which could cause material removal through accumulated substrate damage. A similar approach was taken with the scale dominated regime, where if the scale fracture stress was exceeded, an appropriate amount of scale was removed relating to the crack depth.

Sundararajan (1991) proposed basic models for his two spalling mechanisms assuming parabolic growth kinetics and removal of the scale to the scale-substrate interface. Oxidation controlled erosion by continuous mode was modelled by considering the time between impacts given the particle flux and contact area. The oxide thickness growth within this time was removed by a subsequent impact. The normalised mass erosion rate, E , for a spherical particle was derived as:

$$E = \frac{1.56\alpha\rho_o}{H_m^4\sigma_p^4} \left(\frac{K_p V}{Fr} \right)^{1/2} \quad (4.7)$$

where ρ is the density, H is the hardness, K_p is the parabolic rate constant, F is the particle flux, V is the impact velocity, r is the particle radius and the subscripts m , o and p refer to the metal, oxide and particle respectively. Note that a low velocity exponent is predicted, there is a strong temperature dependence through K_p and that the dependence on flux is negative rather than positive due to the mass normalised basis of the erosion rate. For the oxidation controlled erosion by spalling, a critical thickness Z_c was defined at which spalling occurred. Thus the time between impacts, t_c , was

$$t_c = \frac{Z_c^2}{2K_p} \quad (4.8)$$

and, following a similar argument, the erosion rate was derived as

$$E = \frac{2\rho_o K_p}{FZ_c} \quad (4.9)$$

No dependence on impact velocity and particle size is predicted.

4.3.2.3. *Corrosion affected erosion regime*

There is a general lack of agreement on the mechanisms of corrosion affected erosion and the process appears difficult to model, particularly as the formation and removal of the composite layer is a multiple impact process and no satisfactory erosion model has been developed for multiple impact erosion. The oxidation behaviour of the composite layer is likely to be rapid and uneven due to short-circuit diffusion along metal/scale fragment and metal/embedded erodent fragment interfaces. Sundararajan (1991) estimated the range of conditions over which corrosion affected erosion should be dominant in the development of his erosion-corrosion maps. He estimated that the scale thickness was between one-tenth and twice the deformation depth of an impact. This led to the conclusion that for a given velocity the correct steady state thickness for corrosion affected erosion to be dominant was over a narrow temperature range of about 100° C.

4.4. Summary

Despite the nature of fluidized beds where the predominant wear process is open three-body abrasive wear there are many similarities between high temperature fluidized bed studies and erosion-oxidation studies.

The effect of temperature on wastage seems to be the most consistent behaviour and the most understood. Most results show a peak in wastage at intermediate temperature with the peak moving to higher temperature and wastage rates with increasing particle impact energy (particle size or velocity) and higher temperature with increasing oxidation resistance.

From surface observations the peak marks a transition from corrosion affected erosion to erosion enhanced corrosion. Below the peak the increase in wastage is due to the continued removal of the unprotective oxide film/composite layer which increases in thickness as the temperature increases. Above the peak the oxidation kinetics increase to such an extent to allow a continuous protective oxide scale to form causing a transition to erosion enhanced corrosion. The decrease in wastage occurs as the oxide becomes more protective.

Higher impact energies remove a greater thickness of oxide, and therefore a larger oxide thickness, and hence a higher temperature is required to achieve a transition from

corrosion affected erosion to erosion enhanced corrosion. Thus the peak wastage shifts to higher temperatures for higher velocities.

Improving the oxidation resistance of an alloy decreases the oxidation kinetics at a given temperature, therefore the critical oxide thickness required for a transition from corrosion affected erosion to erosion enhanced corrosion occurs at higher temperatures.

The same power law relationship between erosion rate and velocity used for pure erosion can be used to describe erosion-corrosion behaviour, although the velocity exponents are considerably more varied, ranging from 2 to 10 (Rogers, 1992b). This however assumed that $v_o = 0$ in equation 4.1, and an increase in v_o would reduce the velocity exponent. The reason for the particularly high exponents may be due to transitions between mechanisms, such as a change from no wear to increasing wear at a velocity greater than zero, or where flux increases with velocity, which would raise the exponent by 1.0 when compared to a fixed flux.

Most fluidized bed studies show maximum erosion rate at shallow angles (type A), with little or no wear at normal impacts. However this may be the result of the high flux environment preventing high erosive condition at steeper angles (i.e. a dead cap), as Sethi and Corey (1987) reported higher erosion at normal impact angles. Also unlike Sethi and Corey's results most results from fluidized beds are not normalised which would increase the relative erosion rate of shallower angles. MacAdam and Stringer (1995) have shown that the difference between type A and type B wear is simply that type A wear arises from a constrained particle flow, which can develop into type B if a small degree of freedom in the particle flow is introduced. Laboratory studies generally have a fixed pattern of particle flow, hence usually show type A rather than type B wear which is often observed in FBCs where there is likely to be much more variability in particle impact directions.

Particle properties are less well characterised than other variables in erosion-corrosion research. Particle parameters such as flux has been shown to be more important in erosion-corrosion than erosion due to oxide fracture and time of regrowth. An increase in flux would also reduce the thickness of an oxide film which may lead to a change in mechanism.

Particle hardness on the effect of erosion-corrosion may be more complicated than for pure erosion. In oxidation dominated regimes the ratio of particle to scale hardness

may have more significance than the particle to substrate hardness ratio and, as MacAdam and Stringer (1991a) showed, additional factors such as fracture toughness and the nature of fragments produced have to be considered as a protective layer of particle embedment may form.

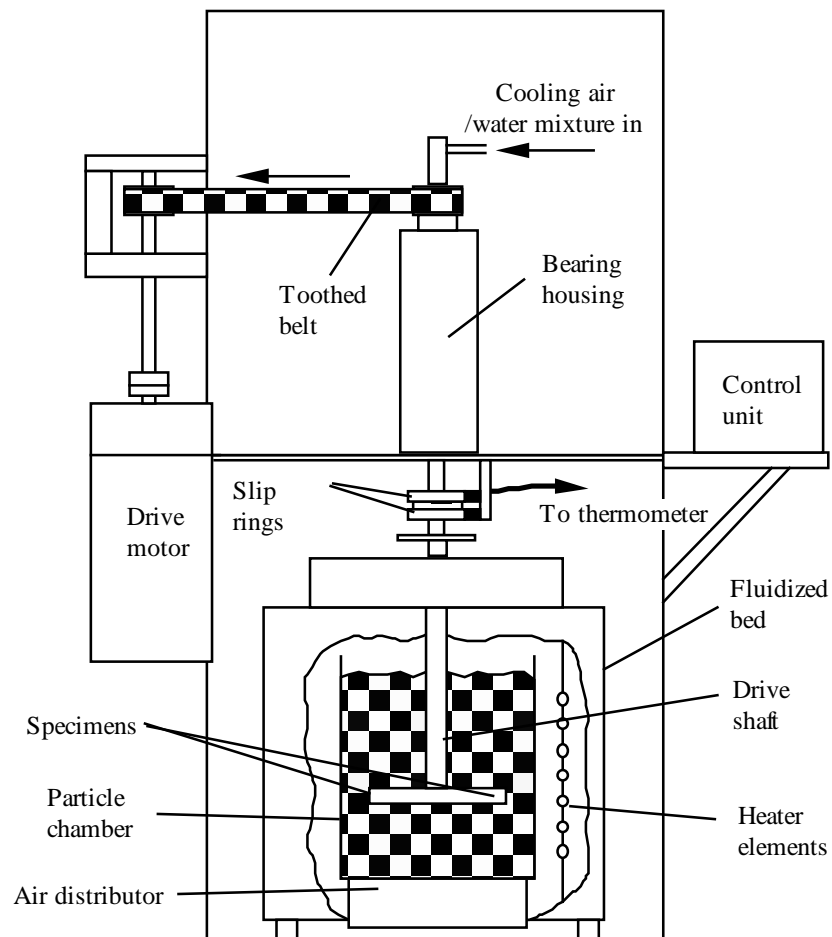
Chapter 5

Experimental Methods

5.1. Introduction

The low-velocity erosion-oxidation apparatus and main experimental methods have been described in greater detail by Rogers (1992b). This chapter therefore summarises the essential features and will concentrate on the modifications made to the apparatus and differences in experimental methods primarily associated with cooled specimen tests.

5.2. Erosion-corrosion apparatus



The erosion-oxidation apparatus is shown in Fig. 5.1. The apparatus consists of a small, electrically heated fluidized bed, within which tubular specimens are rotated in a horizontal plane by a rotor assembly and motor.

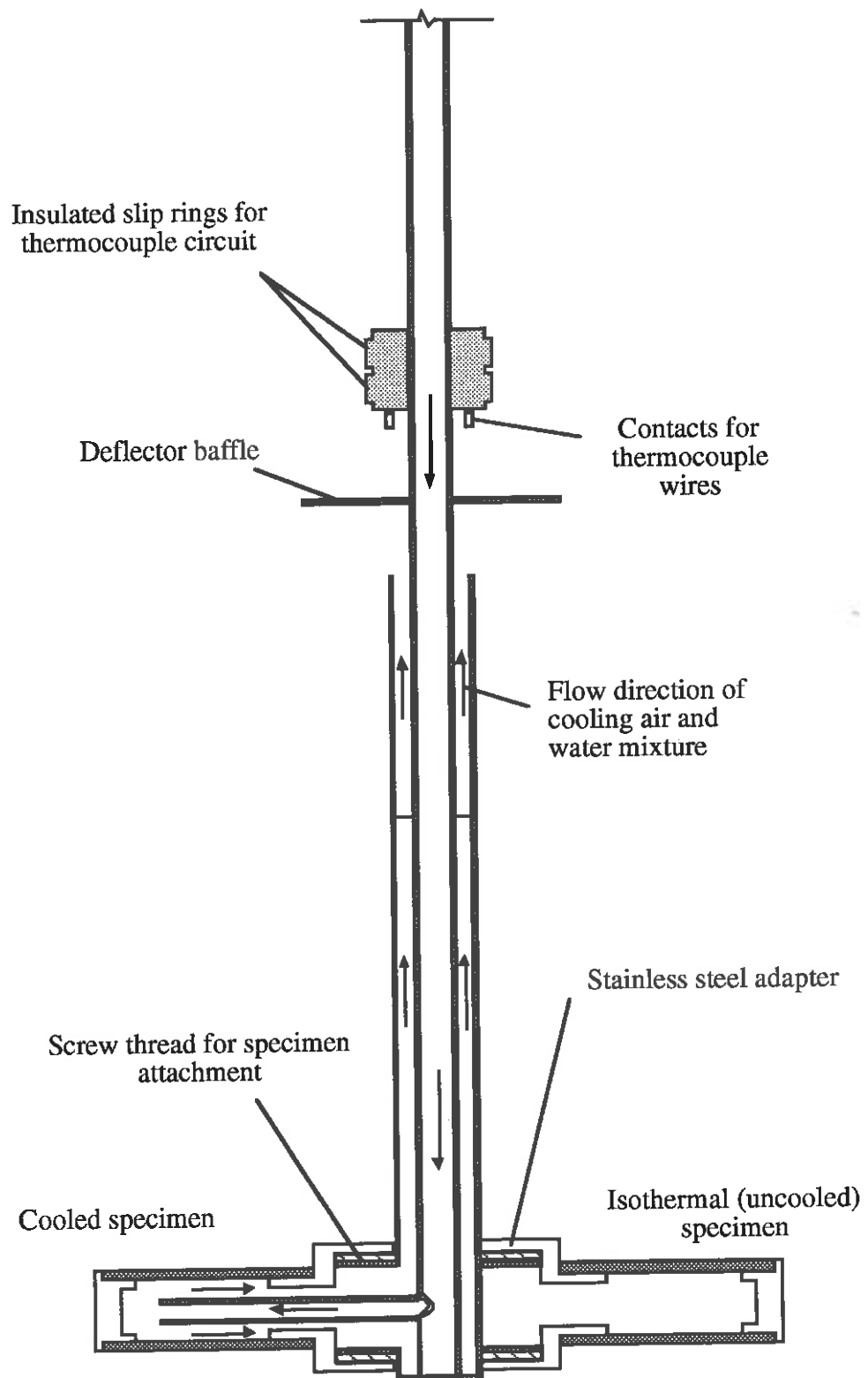


Fig. 5.2. Schematic diagram of the cooled specimen rotor.

Fig. 5.2. Schematic diagram of the cooled specimen rotor.

The rotor assembly shown in Fig. 5.2 is the same as that used by Rogers (1992b), designed to allow cooling of one of two specimens. An air/water mixture enters at the top of the rotor, passes down a central shaft into the specimen, then along the outside of the rotor shaft to be vented at the top of the bed. The inclusion of insulated slip rings allowed continuous temperature measurements during a test.

5.2.1. Bed particles

80 mesh brown alumina grit* was used for the bed particles. These were angular and had a mean diameter of 240 μm as measured by laser granulometry, with 97% in the range 100 - 500 μm . The alumina was used in a conditioned state, achieved by replacing 0.75 kg of bed particles from the ≈ 28 kg in the particle chamber with new particles every 24 hours of testing. Fig. 5.3 shows micrographs of both new and conditioned particles. Conditioned particles had rounded asperities and smoothed surfaces, and also the amount of dust on the particle surface was reduced.

5.2.2. Test specimens

The test specimens were machined from one inch diameter bar to the dimensions shown in Fig. 5.4, which also shows the dimensions of the adapter and endcap. The first batch of specimens used a 7/8" BSF screw thread and were machined at British Coal. Further specimens, machined in this department, were threaded with a shallower 7/8" UNF which was easier to tap. The specimen diameter was machined down from 1 inch to 25 mm on a lathe about 60° centres. This minimised the eccentricity of the surface about the centres which increased the accuracy when measuring the thickness loss of the specimen (see section 5.3). The surface was finished to a rough polish using 6 μm diamond paste.

* obtained from Abrasive Developments Ltd.

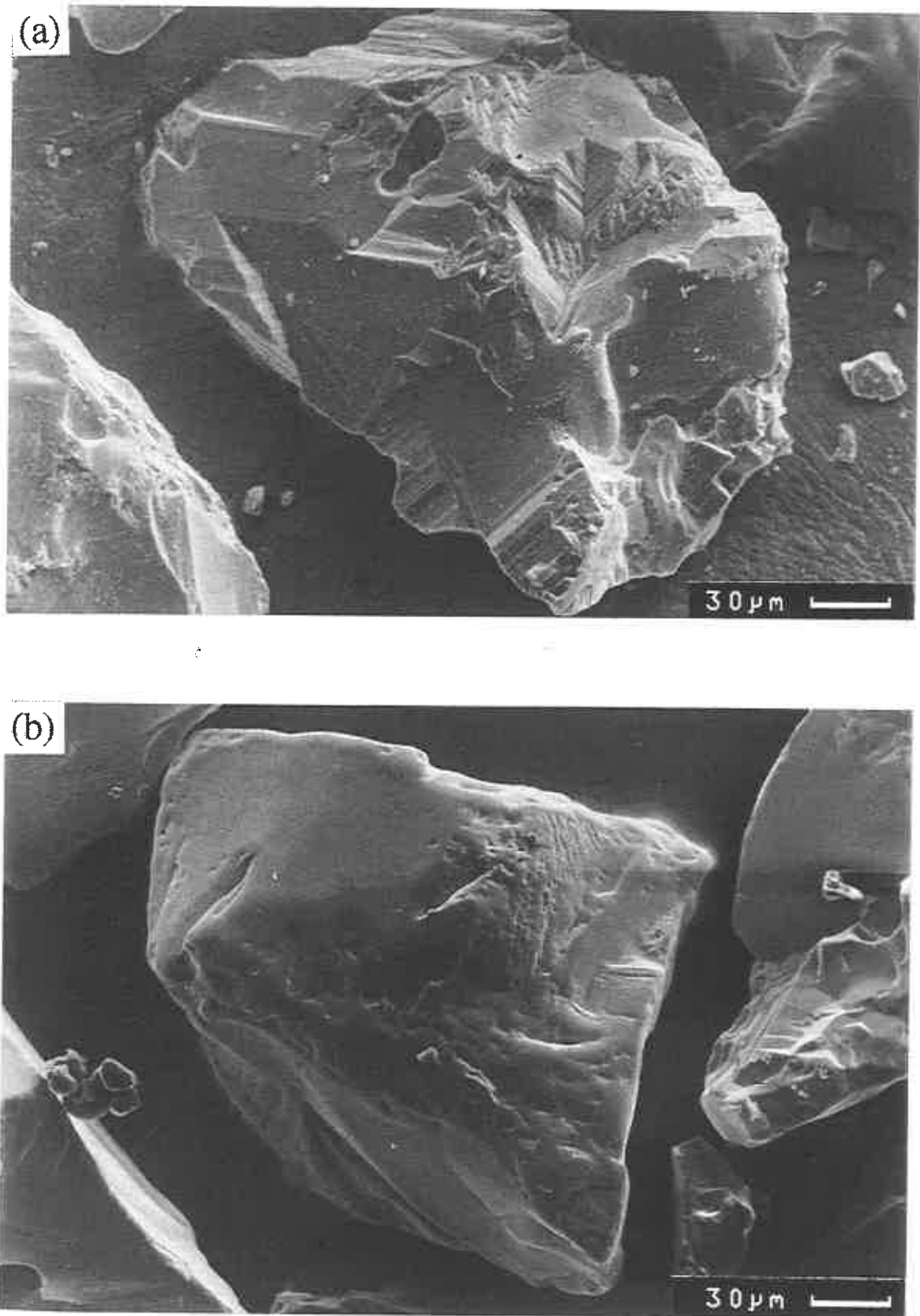


Fig. 5.3. Micrographs of (a) new and (b) conditioned 80 mesh brown alumina particles.

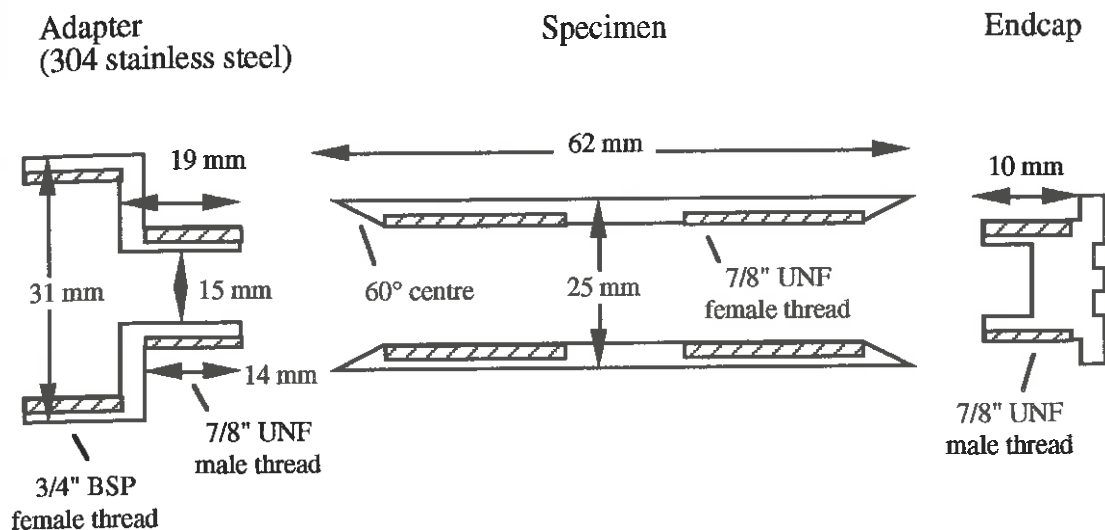


Fig. 5.4. Dimensions of the erosion-oxidation test specimen, endcap and adapter for the rotor.

5.2.3. Rig modifications

To achieve a greater temperature difference between the cooled specimen and the fluidized bed temperature than previously obtained, a water/air mixture was used as a coolant rather than solely air. Water was injected into the air line using a peristaltic pump to control the flow rate (Fig. 5.5). A thin diameter tube aligned parallel to the air flow reduced the back pressure from the compressed air. Distilled water was used to reduce scaling within the rotor and was fed from a storage container.

To compensate for the extra heat removed by the improved cooling, the insulation surrounding the fluidized bed was increased and the fluidizing air was preheated. The insulation was increased by adding an external layer of porous furnace brick and lining with insulating board to protect the fragile refractory. Preheating the fluidized air was achieved by passing the compressed air, via stainless steel tubing, first through the dust extraction outlet and then a tube furnace before entering the air distributor at the base of the fluidized bed. This is shown in Fig. 5.6 for one of the two air lines feeding the air distributor. To prevent excessive oxidation the inlet tubes of the air distributor were replaced with stainless steel.

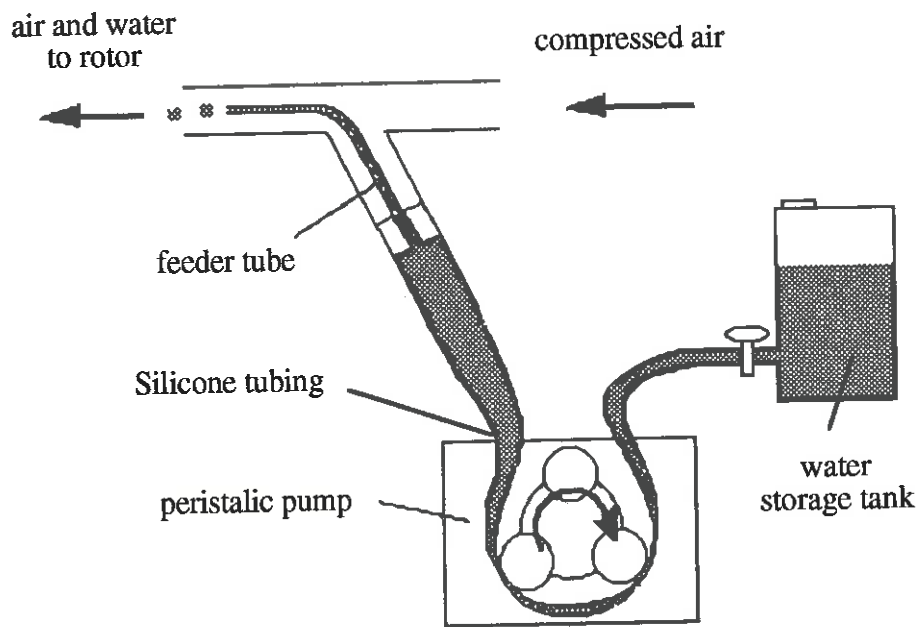


Fig. 5.5. Schematic diagram showing the cooling water fed into the compressed air line.

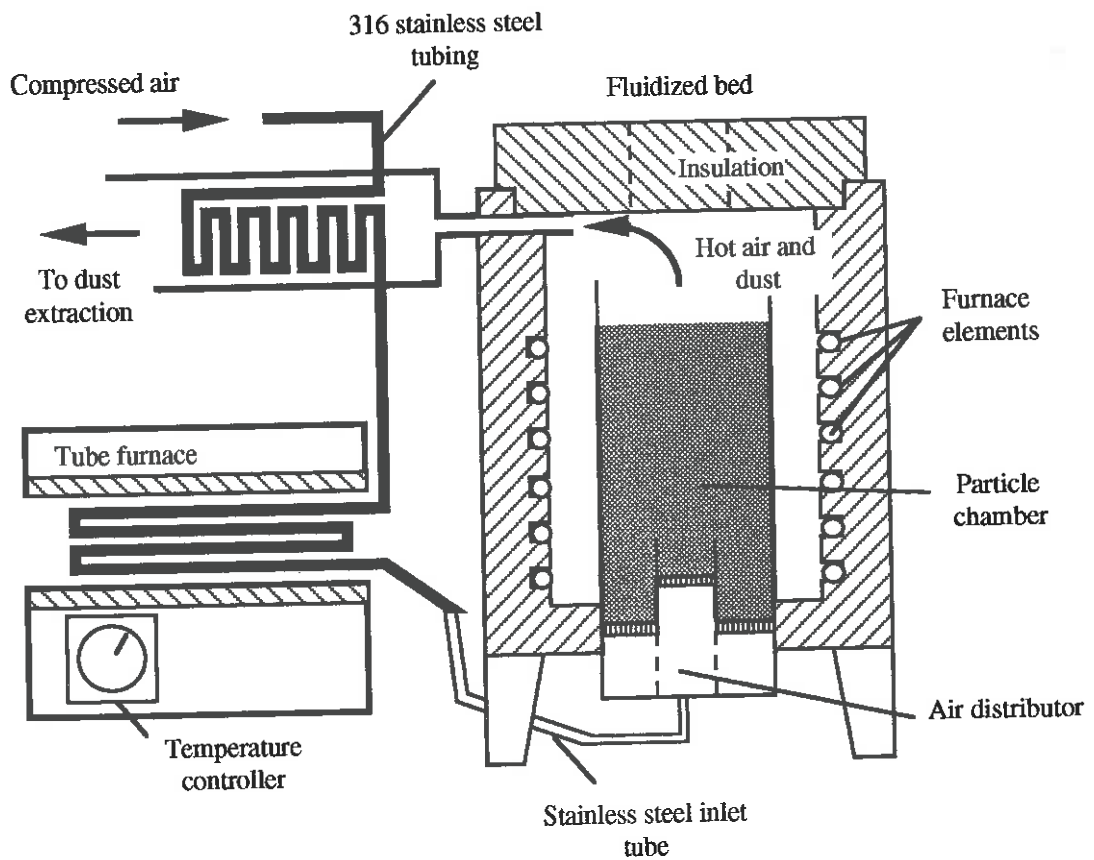


Fig. 5.6. Schematic diagram showing the inlet route for the fluidizing air for the fluidized bed. Extra insulation surrounding the fluidized bed not shown.

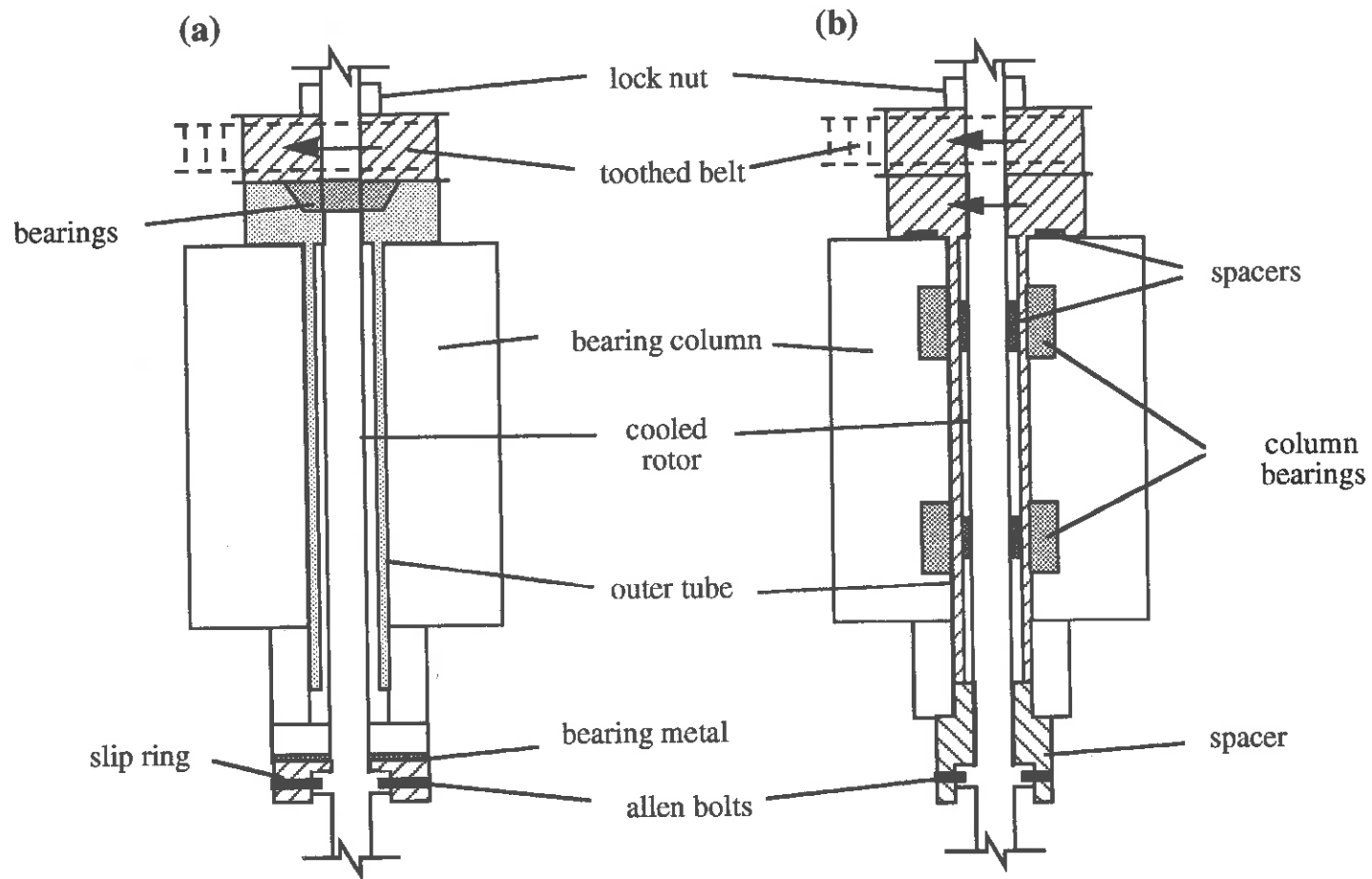


Fig. 5.7. Schematic diagram of the bearing column, (a) before and (b) after modifications.

The bearing column was initially designed for two counter rotating rotors (used by Ninham and Rogers, 1992b). The cooled specimen rotor replaced the inner shaft of the double rotor which ran on the bearings at the top of the column, and held in place by a slip ring at the base of the column. The bearings within the column originally used by the outer rotating shaft remained stationary during operation (Fig. 5.7a). This arrangement proved unsatisfactory after prolonged use as the bearing metal on the slip rings became fouled with particles, resulting in wear at the base of the column and leading to lateral movement of the rotor. The slip rings were replaced with a spacer which pinched the rotor shaft against the outer tube within the column thereby using the bearings within the column (Fig. 5.7b).

5.2.4. Experimental procedure

The experimental procedure for running the erosion-oxidation test rig is described below. It is essentially the same method as used by Rogers (1992b) for isothermal tests but with additional operations when internally cooling a specimen.

(i) Preliminaries

1. The two specimens were screwed into position on the rotor and a scratch was made along the back of the specimen (the specimens rotated clockwise during a test). The scratch was needed as a reference for the measuring rig and enabled repositioning during interrupted tests. Prior to testing, the initial radius profile of the specimens was measured on the specimen measuring rig (section 5.3). An anti-seize compound was brushed onto the screw threads to aid specimen removal. A thermocouple was spot welded to the back of the cooled specimen and attached to the contacts of the slip rings on the rotor with crocodile clips. The thermocouple was held in place with stainless steel wire tied around the rotor shaft.

2. The dust extractor, refrigeration dryer, compressor, fluidized bed furnace and fluidizing air preheating furnaces were switched on. The fluidized bed furnace temperature controller was set 50° to 100° C above the desired bed temperature (sometimes to higher temperatures for tests involving large amounts of cooling). The temperature of the fluidizing air preheating furnaces was set as high as 650° C

depending on the amount of cooling. Pre-heating the air reduced the excess temperature required by the fluidized bed furnace. The fluidizing air velocity was increased until the bed was lightly bubbling, with the flow rate to the outer distributor set at four times that to the inner distributor.

3. As the bed heated up the fluidizing air velocity was reduced to maintain a lightly bubbling bed, as excess air caused vigorous bubbling and loss of bed particles to the space between the furnace and the particle container. The bed was usually switched on at least a day before testing to allow the furnace to reach equilibrium temperatures. It was also useful to switch on the motor control unit and the peristaltic pump about an hour before a test to allow the motor and pump to warm up.

(ii) Starting a test

4. The air/water cooling line was attached to the rotor and the cooling air was turned up high. The furnace was opened and the rotor lowered into the bed. The cooling line was momentarily disconnected to allow the toothed drive belt to be fitted, and the rotor was bolted into position and the drive belt tensioned. The water lines for the cooling coil at the base of the bearing column were fitted and the re-circulating water switched on (this was not necessary for a cooled specimen test).

5. The drive motor was switched on and its speed adjusted to 250 revs min⁻¹. The peristaltic pump was switched on and its speed and the air pressure was adjusted to give the required cooled specimen temperature. The furnace temperature controller was adjusted to an appropriate value such that the bed temperature close to the specimens was at the required test temperature (this was measured with an external thermocouple placed manually into the bed).

6. The gas flow into the bed was adjusted to give a lightly fluidized bed, with the flow rate through the outer chamber of the distributor four times that of the inner. After the gas preheating modifications were made to the rig the standard gas feed pressure of 15 psi was usually insufficient to provide a high enough gas flow rate, so the pressure was increased to provide enough air.

7. The furnace temperature controller, the water flow rate and the cooling air pressure were adjusted again once the bed had reached equilibrium to give the required

bed and specimen temperatures. Equilibrium was sometimes reached as long as an hour after the start of a test if the initial bed temperature was not sufficiently hot, requiring the bed to heat up while a great deal of heat was removed as part of the specimen cooling process.

(iii) Shutting down

8. After the required exposure time the rotor was stopped and removed from the fluidized bed. The water was turned off just before the rotor, and the air pressure increased to reduce static oxidation during the rotor removal which took several minutes. Slumping the fluidized bed at this point further reduced the temperature of the cooled specimen. Once removed from the bed the specimens were allowed to cool and removed from the rotor, and the radius profiles of the worn specimens were measured. For interrupted tests the specimens were repositioned on the rotor and exposed in the test rig for a further time period.

9. During a test, bed particles were thrown out of the particle chamber and fell between the particle chamber and the furnace. These covered some of the furnace elements which reduced the furnace's heating capacity. Periodically these particles were removed, sieved to remove large pieces of furnace refractory and returned to the bed.

5.3. Specimen measurement

The amount of specimen wear was determined by measuring its radius profile around its circumference. The specimen was rotated about centres using a stepper motor via a pair of gear wheels while the radius was measured with a linear variable displacement transducer (Fig. 5.8). The process was controlled by a BBC microcomputer running a program called TRANS written by Entwisle (1990), which recorded and stored 400 radial measurements for each rotation of the specimen. The high velocity end of the specimen was 98 - 96 mm from the centre of rotation when attached to the erosion-oxidation test rig. Adjustment of length was difficult as both the adapter and specimen had to be screwed on tight to prevent water leaking from the cooled specimen and rotation of the specimen during a test. Prior to measuring, this distance was recorded and the measuring scale on the rig set to this value with the LVDT positioned at the high

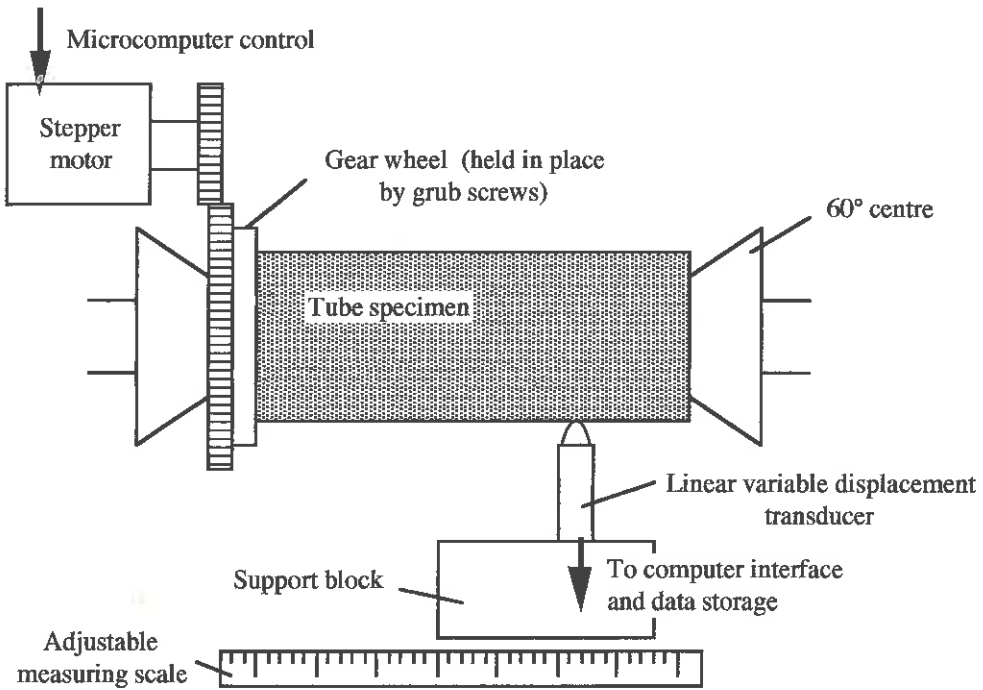


Fig. 5.8. Schematic diagram of the specimen measuring rig.

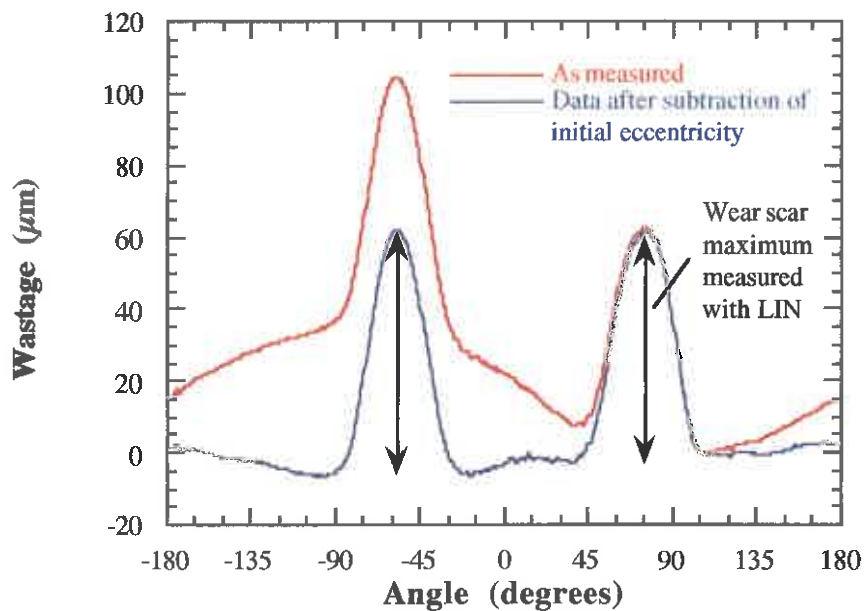


Fig. 5.9. Graph of wastage against angle recorded by the specimen measuring rig, and the result of subtracting the specimen profile wear.

Fig. 5.9. Graph of wastage against angle recorded by the specimen measuring rig, and the result of subtracting the specimen profile wear.

5.3.1. Analysis of data

Data measured and recorded using the measuring rig and the program TRANS was analysed by the program LIN. The use of both programs is described in detail by Rogers (1992b). LIN gave the option of subtracting the data measured before exposure from that measured afterwards to remove the specimen eccentricity caused during machining (Fig. 5.9). The eccentricity was measured as a sinusoidal curve of one wavelength and made analysis much less accurate for poorly machined specimens whose amplitude was often over 100 μm . LIN was used to measure the magnitude and angle of the two wear scar maxima and the angular width of each wear scar. The average of the two wear scar maxima was calculated and this value was used as the wastage at that position on the specimen.

5.3.2. Analysis techniques

The erosion-oxidation specimens were observed in a Camscan S2 SEM using both secondary and backscattered electron detectors. A special holder was used to allow a whole specimen to be placed within the SEM specimen chamber.

Chapter 6

Isothermal erosion-oxidation of mild and 316 stainless steel

6.1. Introduction

This chapter describes the isothermal behaviour of mild steel (070M20) and 316 stainless steel on the single rotor arrangement in the fluidized bed test rig. Although isothermal tests of mild steel have been carried out in previous work (Rogers, 1992b; Ninham *et al.*, 1989b; Entwisle, 1990), accurate interrupted tests on the single rotor were required to compare directly to the cooled mild steel tests described in Chapter Seven. 316 stainless steel was used as an uncooled specimen material on later cooled tests at 500° C bed temperature and was tested isothermally with the mild steel. The experimental procedures for the fluidized bed test rig are described in Chapter Five.

The composition of mild steel and 316 stainless steel are shown in Table 6.1.

		Composition (wt %)								
		Fe	C	Si	Mn	P	S	Cr	Mo	Ni
Mild steel 070M20	Balance	0.15	0.23	0.75	0.017	0.080	-	-	-	-
316 stainless steel	Balance	0.014	0.58	1.34	0.025	0.018	16.59	2.05	11.17	

Table 6.1. Composition of the mild steel and 316 stainless steel.

Specimens were machined from one inch diameter bar to the dimensions shown in Fig. 5.3. The mild steel had been hot rolled at 800° C and subsequently pickled and cold drawn. The microstructure of ferrite and pearlite shown in Fig. 6.1 was elongated in the longitudinal direction of the bar. The 316 stainless steel had been solution annealed and Fig. 6.2 shows the microstructure of equiaxed austenite grains.

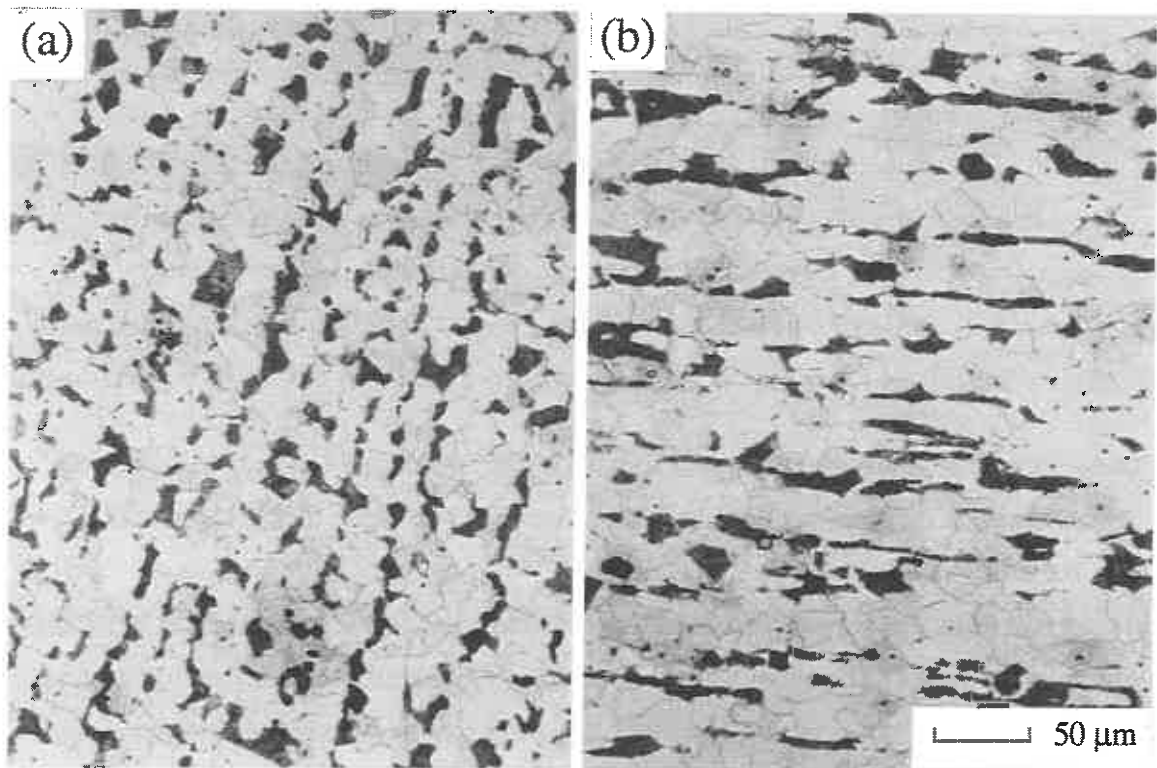


Fig. 6.1. Microstructure of the mild steel, (a) cross section of bar, (b) longitudinal section of bar. Etch: 2% Nital.

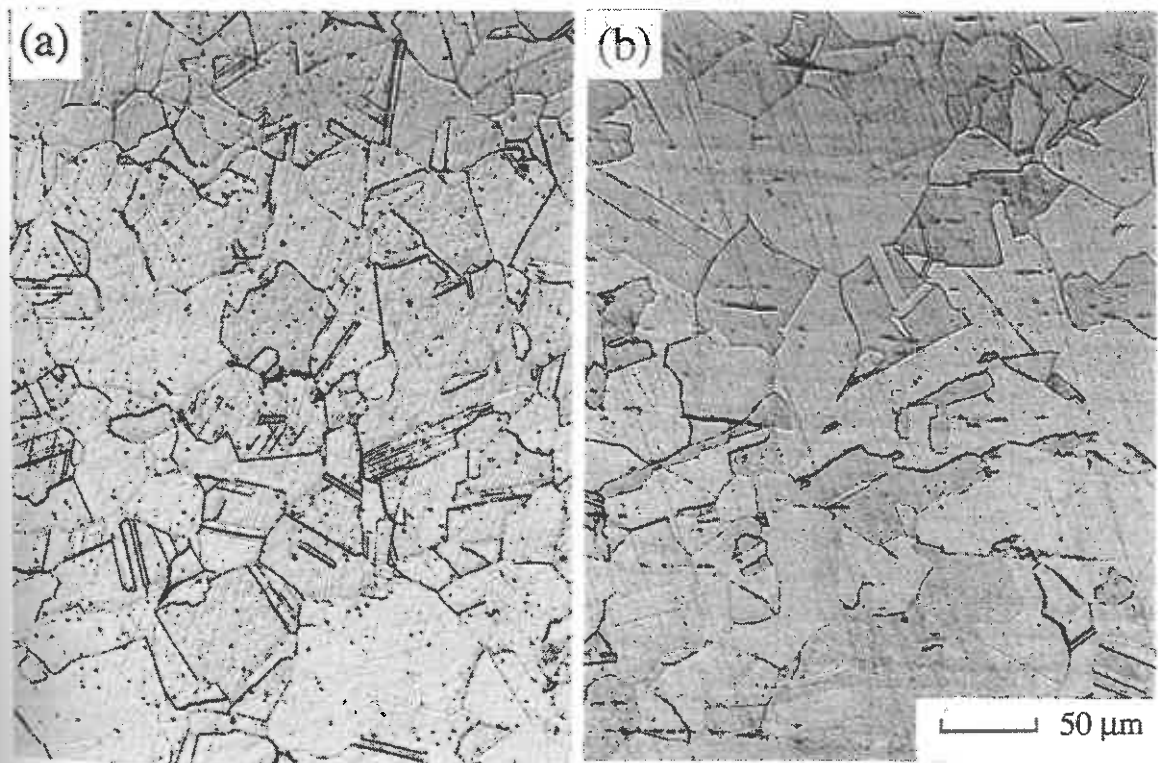


Fig. 6.2. Microstructure of the 316 stainless steel, (a) cross section of bar, (b) longitudinal section of bar. Etch: 2 parts HCl, 2 parts glycerol and 1 part HNO₃.

6.2. Specimen Appearance

The visual appearance of the mild and stainless steel specimens after exposure in the fluidized bed test rig is shown in Figs. 6.3 and 6.4 and shown schematically in Figs. 6.5 and 6.6 respectively. Typically the wear scar was covered with a coloured interference oxide which did not change with exposure time, while the front and back of the specimen were covered with a uniform oxide which thickened during exposure. Table 6.2 shows the relationship between the colour of an interference oxides and their thickness.

The mild steel specimens exhibited a thin interference oxide over all of the wear scar up to 400° C increasing in thickness with temperature. At 400° C a thicker oxide developed at lower impact velocities while at 500° C the whole of the wear scar was covered with a thick oxide scale. At 200° C the wear scar was covered in a grey coloured layer formed from deposited bed particle fragments at high impact angles and particularly at lower impact velocity. A similar region formed at low impact velocity at 300° and 350° C and to a greater extent at 400° C.

The wear scar of 316 stainless steel at 200° C was similar in appearance to the mild steel specimen exposed at 200° C, metallic in colour and with a deposit layer over the front of the wear scar. At low velocity the alumina deposit formed a continuous layer while at higher velocities the surface consisted of small 'islands' of discontinuous deposit. The specimens exposed at 300°, 350° and 400° C had very thin interference oxides covering most of the wear scar with colours changing from pale straw to golden brown, and a smaller region of discontinuous alumina deposit at low velocity. At 500° C a dark red and brown wear scar oxide formed over most of the wear scar while a thicker more continuous brown deposit developed at the low velocity end of the specimen. At 600° C the deposit layer covered the width of the wear scar at low velocities with a thin grey brown oxide at higher velocities.

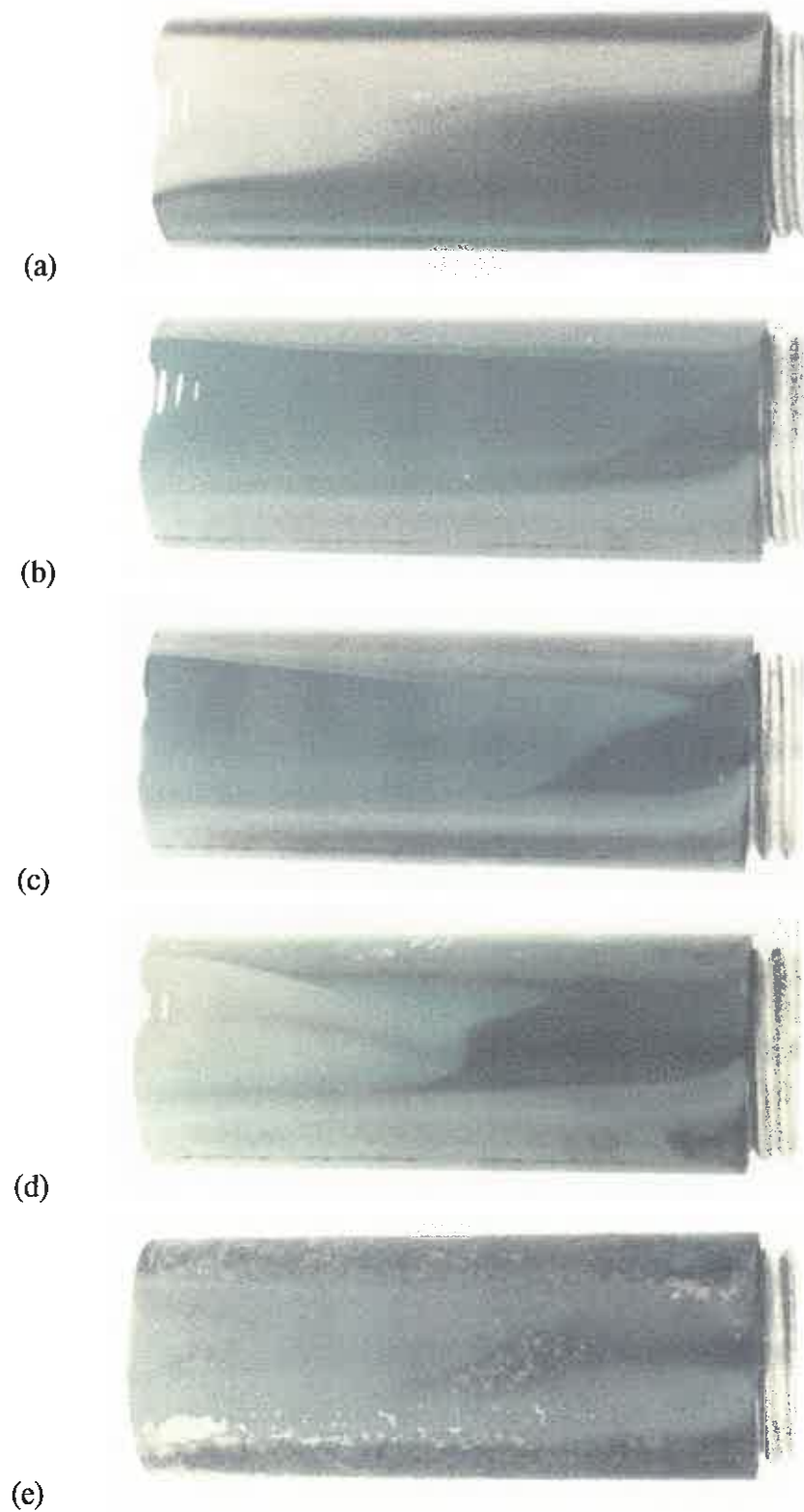


Fig. 6.3. The lower wear scar of isothermal mild steel specimens with the specimen leading edge at the bottom and the high velocity end on the left; (a) 200° C (265 h), (b) 300° C (130 h), (c) 350° C (104 h), (d) 400° C (129 h) and (e) 500° C (235 h).

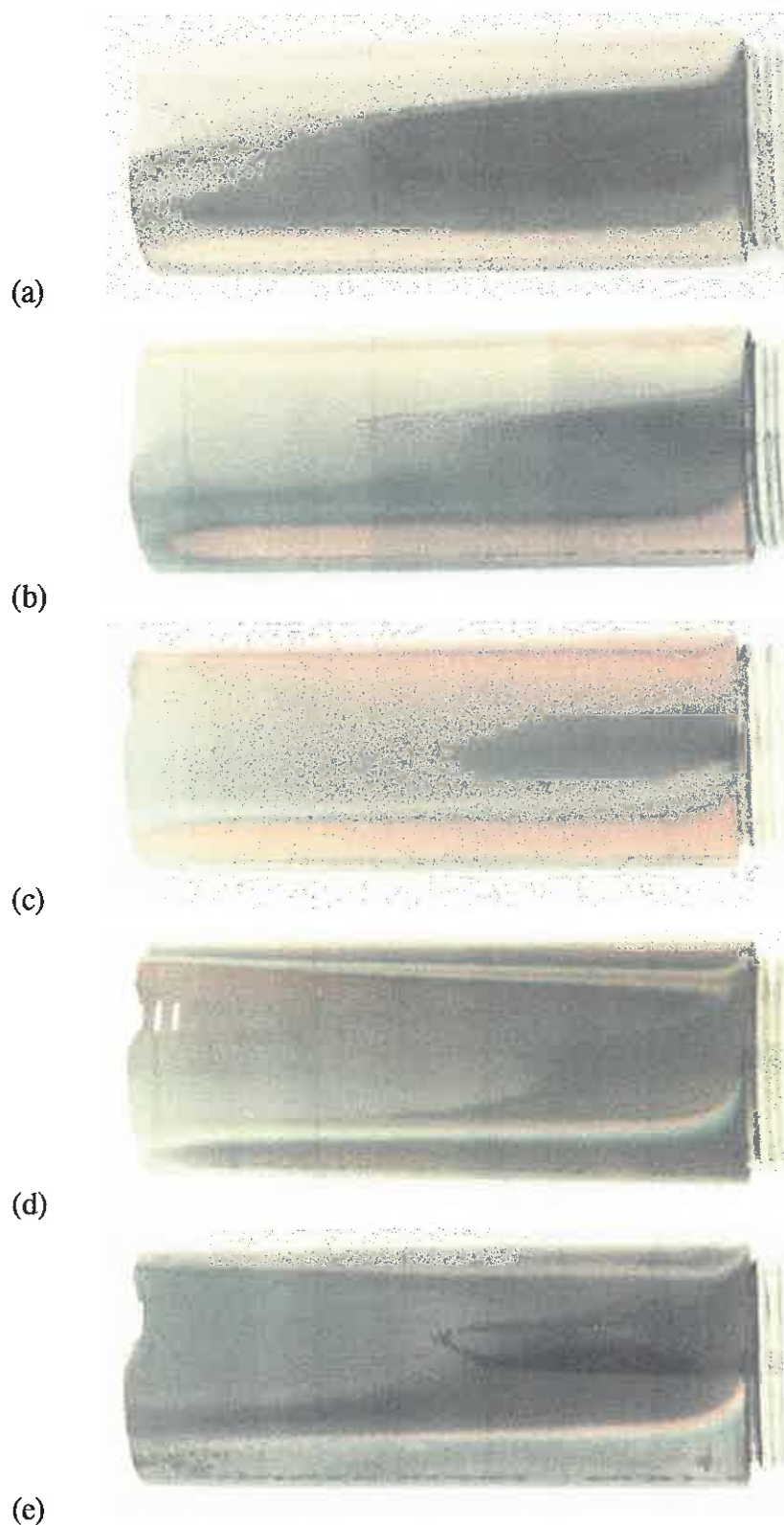


Fig. 6.4. The lower wear scar of isothermal 316 stainless steel specimens with the specimen leading edge at the bottom and the high velocity end on the left; (a) 200° C (240 h), (b) 300° C (130 h), (c) 400° C (129 h), (d) 500° C (189 h). and (e) 600° C (131 h).

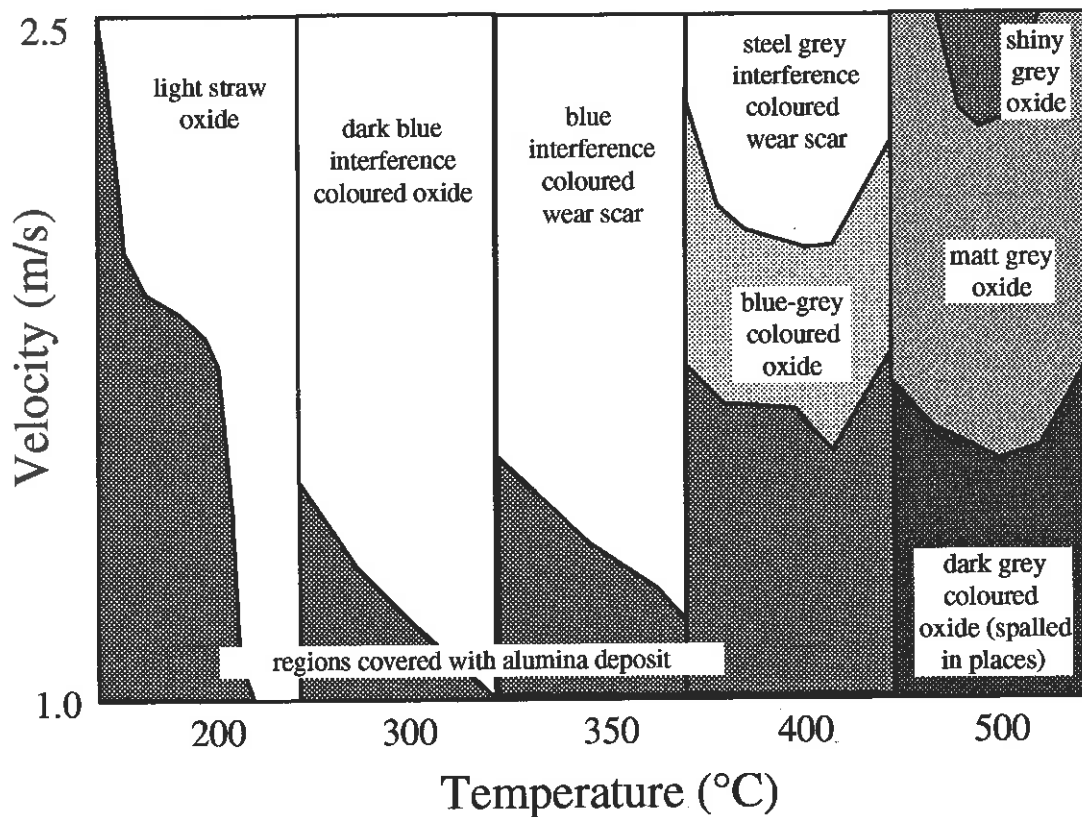


Fig. 6.5. Schematic diagram showing the lower wear scars on mild steel after exposure in the fluidized bed test rig, the leading edge is on the left of the diagram.

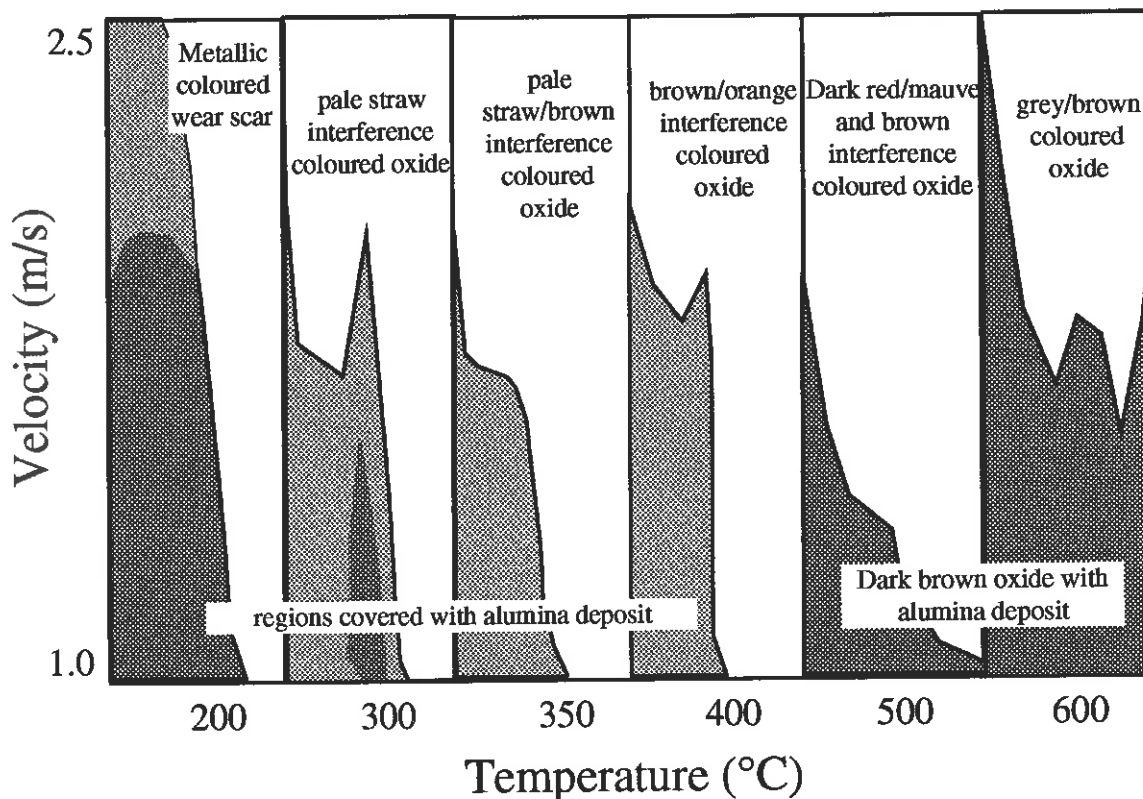


Fig. 6.6. Schematic diagram showing the lower wear scars on 316 stainless steel after exposure in the fluidized bed, the leading edge is to the left of the diagrams.

Oxide colour	Haematite thickness (nm)	Magnetite thickness (nm)	Total oxide thickness (nm)
Pale straw	7.7	0	7.7
Golden brown	10.3	0	10.3
Reddish brown	13.2	0	13.2
Red	15.2	0	15.2
Deep red	15.9	0	15.9
Purple	18.4	0	18.4
Violet	21.0	3.6	24.6
Blue	22.4	6.8	29.2
Greenish-blue	24.4	17.0	41.4
Greenish-silver	30.3	24.1	54.4
Greenish-straw	35.0	28.8	63.8
Straw	38.0	38.5	76.5
Greyish-brown	52.1	46.3	98.4
Greyish-pink	60.6	57.4	118.0

Table 6.2. Relationship between the oxide thickness on iron and its interference colour, after Davies *et al.* (1954).

6.3. Wastage behaviour

The wastage rates of both mild steel and stainless steel were linear with time after an initial incubation period at all temperatures. The incubation period was either positive or negative depending on whether the initial wear rate was greater or less than the steady state wear rate. Fig. 6.7 shows a graph of wastage against time for mild steel at 300° C where the incubation periods at the three velocities shown were negative.

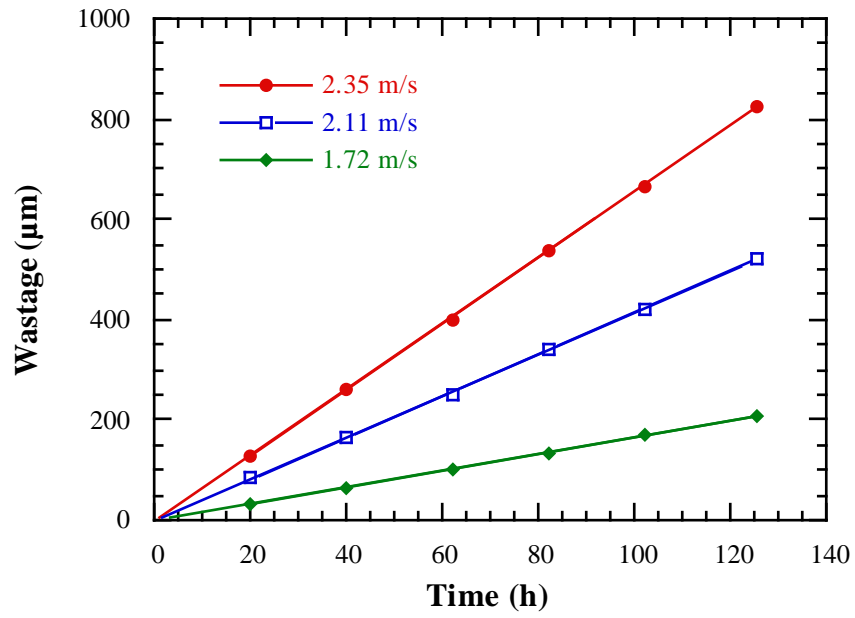


Fig. 6.7. Wastage against time for mild steel at 300° C

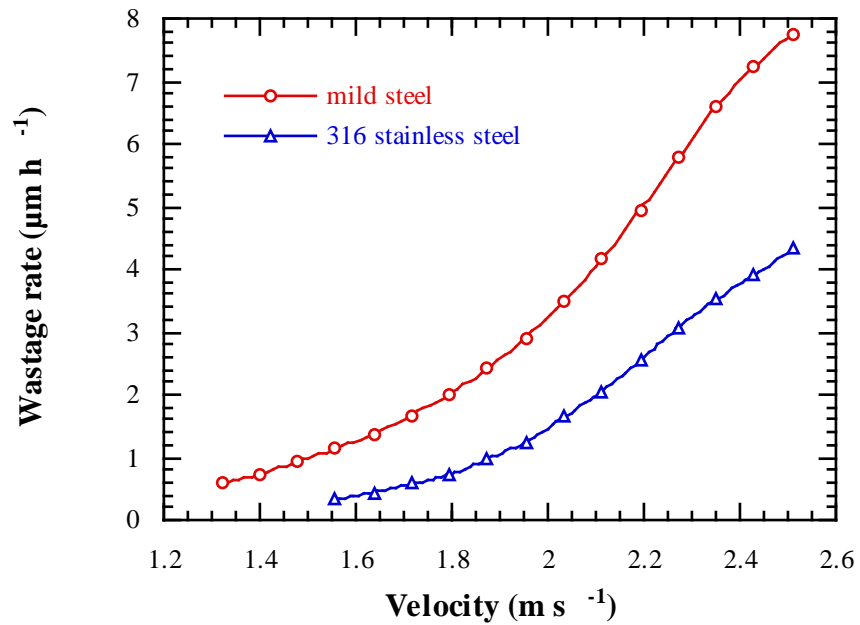


Fig. 6.8. Variation of wastage rate with velocity for mild and 316 stainless steel at 300° C.

The incubation period varied between 40 and -25 hours but was typically between ± 5 hours, and no overall trend was observed with changes in temperature or velocity. Earlier studies by Rogers (1992b) on several low alloy steels including mild steel showed larger incubation periods at high and low temperatures where the steady state morphology differed from the unworn surface, with an alumina deposit layer forming at low temperatures and a thick oxide at high temperatures. It was also noted that repeat tests under nominally identical conditions had different incubation periods indicating a sensitivity to the initial specimen surface condition.

Fig. 6.8 shows the variation of wastage rate with impact velocity for mild and stainless steel at 300° C. The wastage rate increased with increasing velocity and a power law relationship was observed at all temperatures as with earlier tests (section 4.2.2.1). There tended to be a slight decrease in wastage rate from this relationship at high velocity due to an end effect caused by presence of the endcap and a change in particle flow around the end of the specimen.

The variation of the velocity exponent, n , with temperature for both mild steel and 316 stainless steel is shown in Fig. 6.9. The velocity exponent was calculated by using a power law curve fit to the wastage rate velocity data without the two highest velocity data points to exclude the end effect. Very similar results were observed by Rogers (1992b) for mild steel with high velocity exponents at 200° and 400° C and lower values at 300° and 500° C. The high velocity exponents were caused where the wastage at lower impact velocities was reduced by a change in the wastage mechanism; a layer of particle deposit and a thicker mechanically protective oxide at 200° and 400° C respectively. At 300° and 500° C the wear scars had a relatively uniform morphology over their whole length and the velocity exponents have lower values closer to those observed in erosion studies (section 1.1.2). It must be noted that in the current experimental arrangement where particle flux increases with velocity, the velocity exponent is 1.0 greater than when the flux is constant. The 316 specimens showed the same trend with the highest velocity exponents at 200° and 600° C where low wastage occurred at low impact velocities where an deposit layer had covered the wear scar.

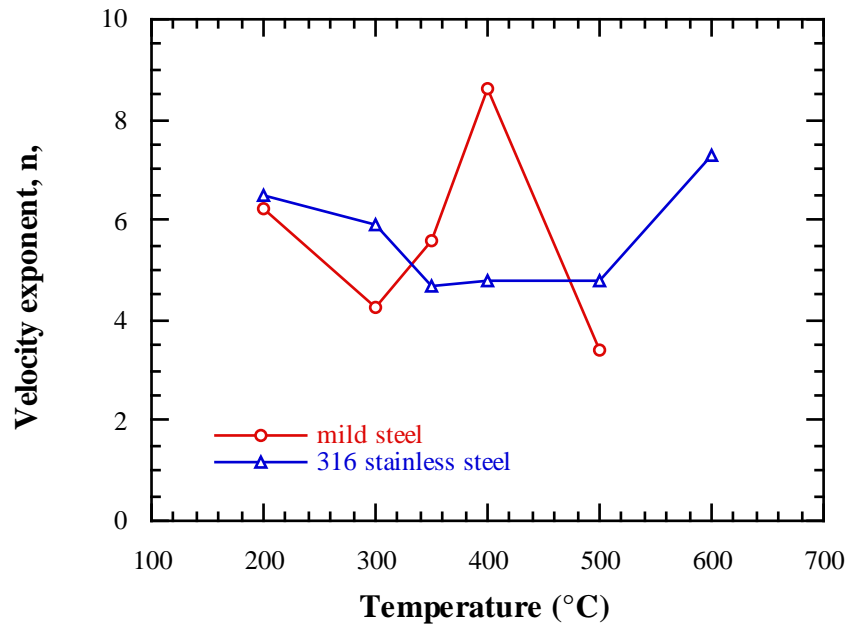


Fig. 6.9. Variation of velocity exponent with temperature for mild and 316 stainless steel.

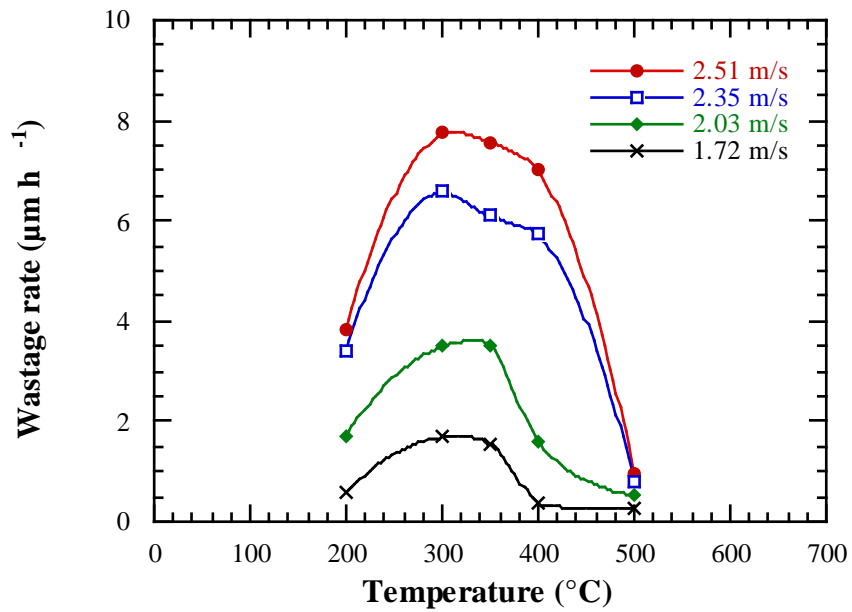


Fig. 6.10. Variation of wastage rate with temperature for mild steel.

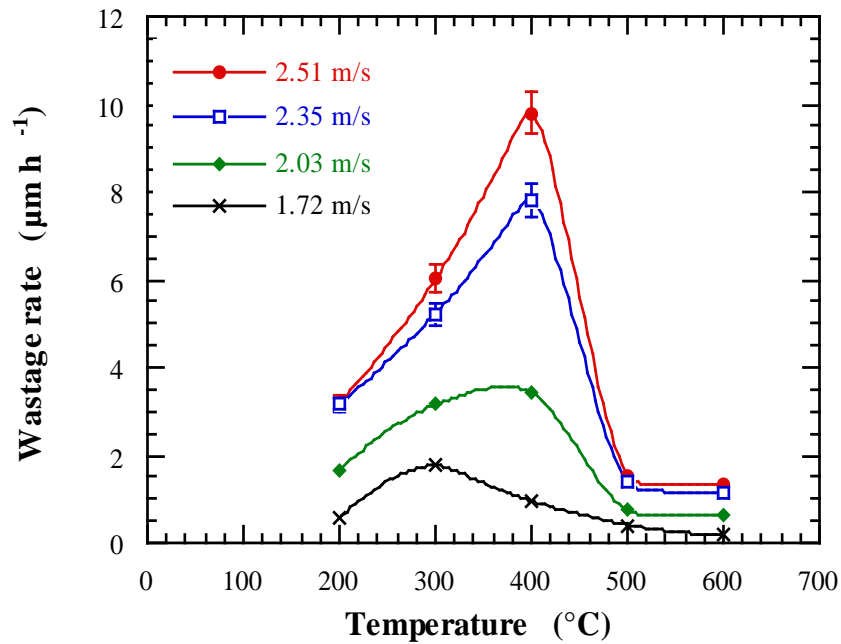


Fig. 6.11. Variation of wastage rate with temperature for mild steel exposed on the lower rotor of the double rotor arrangement, after Rogers (1992b).

Fig. 6.10 shows the variation of wastage rate with temperature for mild steel and Fig. 6.11 shows a similar graph from an earlier study from the lower rotor of the double rotor arrangement. The wastage temperature behaviour of mild steel measured on the single rotor was similar, but not identical to the results obtained from the double rotor arrangement used in earlier tests (Rogers, 1992b; Ninham *et al.*, 1989b). Both showed the characteristic bell shaped curve, although, the magnitude of the wastage rates was slightly less than those from the lower rotor of the double rotor arrangement, and the temperature of the maximum wear rate was slightly lower, 350° - 300° C rather than 400° - 350° C. The higher wastage rates and the higher temperature of maximum wastage from the earlier study both indicate a more severe wear environment.

Although specimens were not tested at 100° C previous studies have measured very low wear rates on mild steel (Entwisle, 1990) and 722M24T (Rogers, 1992b) due to the formation of an alumina deposit up to 5 μm thick over the whole of the wear scar.

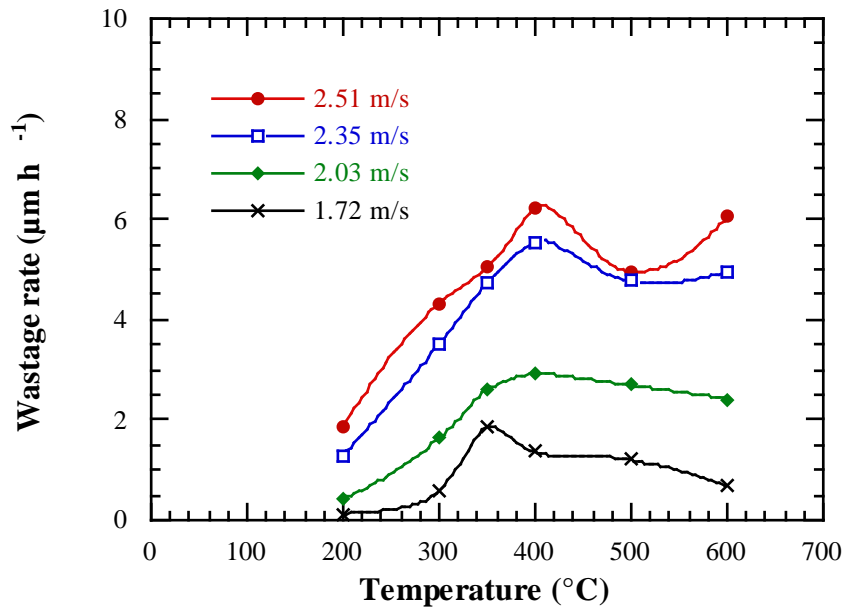


Fig. 6.12. Variation of wastage rate with temperature for 316 stainless steel.

Fig. 6.12. shows the variation of wastage rate with temperature for 316 stainless steel. The temperature of maximum wastage was higher than mild steel at around 400° C as a higher temperature was required for the formation of a thicker wear scar oxide to provide some mechanical protection and thereby reduce the wastage rate. Unlike mild steel the wastage remained high at temperatures above the peak wastage and the wear scar oxide was still very thin. It might be expected that a thicker more protective oxide might form above 600° C as the oxidation rate increases. The behaviour is similar to earlier work on stainless steels (Entwisle, 1990) described in Fig. 4.7, where a bell shaped curve was observed but the wastage remained high at high temperatures and high velocities. The increase in wastage at 2.51 m s⁻¹ from 500° to 600° C was probably caused by an end effect.

6.4. Microscopic observations

The mechanism of wastage proposed by earlier studies was that the increasing wastage with temperature was caused by the increasing oxidation and removal of oxide. The decrease at higher temperatures was due to the formation of a mechanically protective oxide. General observations of the wear scar have shown that for mild steel the

formation of a thicker wear scar oxide at 500° C and at low velocities at 400° C was associated with a low wastage rate. The 316 stainless steel with its superior oxidation resistance still showed a thin wear scar oxide at 600° C and the wastage remained high.

(i) Interference coloured oxide covered wear scar

At lower temperatures where the wastage mechanism is thought of as formation and removal of oxide, the wastage rate increased with increasing temperature as the oxidation rate increased. The microscopic appearance of the interference oxide covered wear scars (200° - 350° C for mild steel and all the stainless steel specimens to 600° C) was very similar for both alloys. The surface consisted of a combination of numerous impact craters caused by individual impacts indicating a degree of plastic deformation to the metal substrate (Fig. 6.13a). Each crater was approximately two microns in diameter elongated slightly in the direction of specimen rotation. The backscattered detector showed that the wear scar was covered with discrete alumina particle fragments (darker regions) and areas richer in alumina where a composite of metal and alumina has formed (Fig. 6.13b and 6.14). These regions appeared to resist particle impacts better than the surrounding metal as they were slightly raised and less cratered. The areas richer in alumina seemed to increase in density with temperature for both mild steel and stainless steel so that these regions became more prominent as they were slightly raised. The area covered by the alumina rich regions also increased towards the leading edge of the wear scar (Fig. 6.15).

Wear ripples were a common feature on both alloys, usually very prominent at high impact velocities and at the back edge of the wear scar where the ripples were approximately 300 µm. Smaller more closely spaced ripples were sometimes observed in the middle of the wear scar, for example stainless steel at 200° C (Fig. 6.16). The ripples became more defined at higher temperatures so that mild steel above 300° C and stainless steel above 500° C had ripples easily visible to the naked eye. Fig. 6.17 showed ripples on stainless steel exposed at 600° C at the high velocity end and back of the wear scar. The backscattered detector showed alumina rich areas on the down flow side of the ripples (Fig. 6.17b).

(ii) Alumina deposit

These areas rich in alumina on the wear scar differed from the almost continuous

alumina deposits which covered the wear scar and usually formed towards the leading edge and at low particle impact velocities. The alumina formed a hard surface coating which protected the underlying metal from wear. Fig. 6.18 shows a region of the deposit layer at the low velocity end of mild steel exposed at 400° C which has fractured off probably caused by the measuring transducer running over the surface. The layer is approximately 1 μm thick and the edges appears to show brittle failure. A continuous deposit as shown in Fig. 6.18 was observed in some areas, in others a less continuous deposit was observed usually at the boundary between the alumina embedment and the bare wear scar but also on large areas of the wear scar at higher velocities (Fig. 6.19). Observations suggest that the embedded layer of alumina formed early on in a test as an imprint of the initial surface scratches was sometimes observed (vertical lines in Fig. 6.20).

(iii) Thicker wear scar oxides

The wear scar of the mild steel specimen exposed at 400° C resembled that of lower temperatures but was covered with a thin oxide scale (Fig. 6.21). It was likely that this grew once the test had stopped as the metal was at 400° C for several minutes.

At 500° C the wear scar had a significantly different appearance. The wear scar was covered with an oxide scale which was compacted and rippled. The scale was also cratered in places where oxide had been removed and regrown (Fig. 6.22). Despite the formation of a thick protective scale on the wear scar, alumina embedment 'islands' were observed at the low velocity end of the specimen (Fig. 6.23).

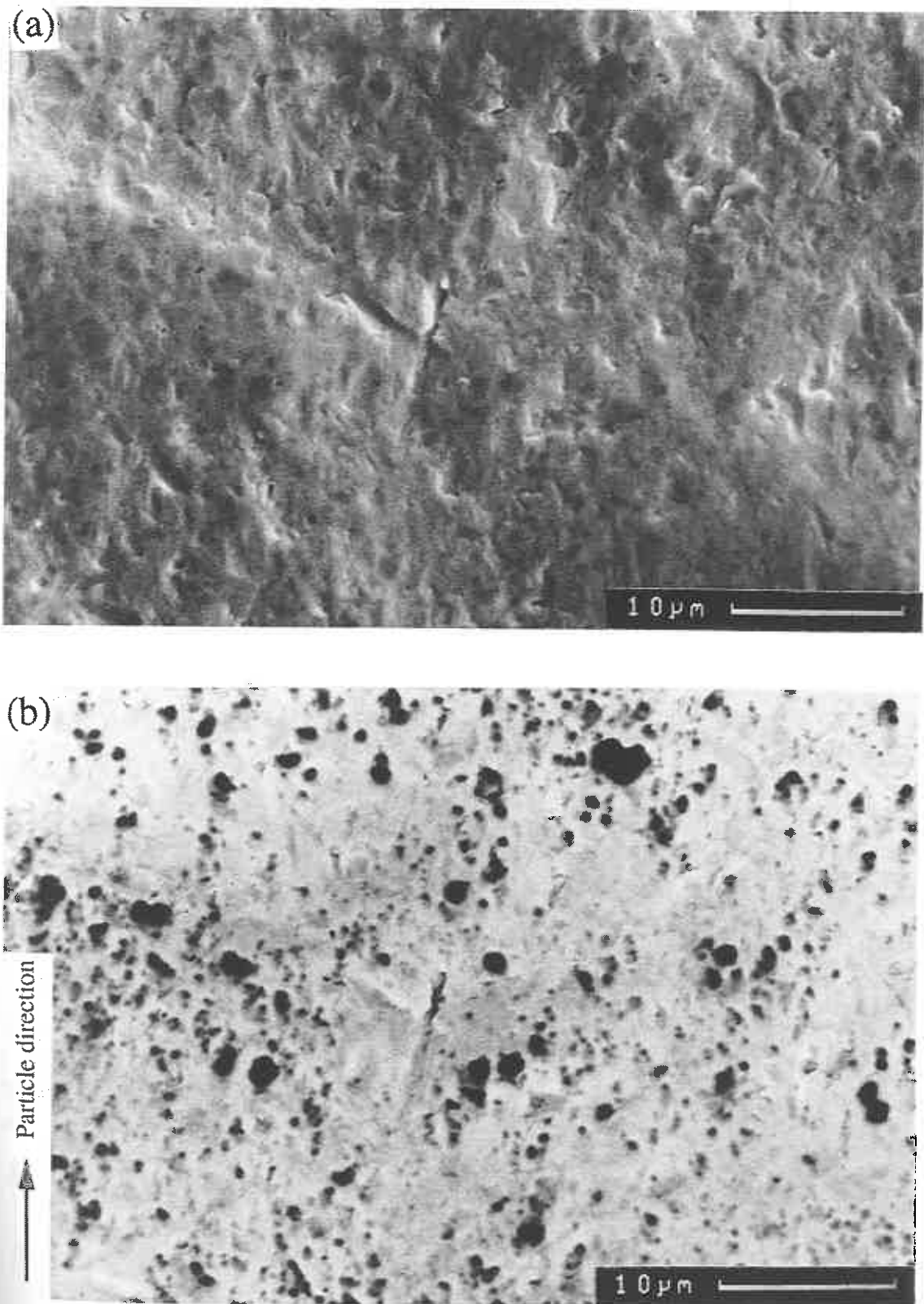


Fig. 6.13. (a) SEM secondary electron and (b) backscattered electron micrograph of the wear scar of mild steel exposed at 200° C.

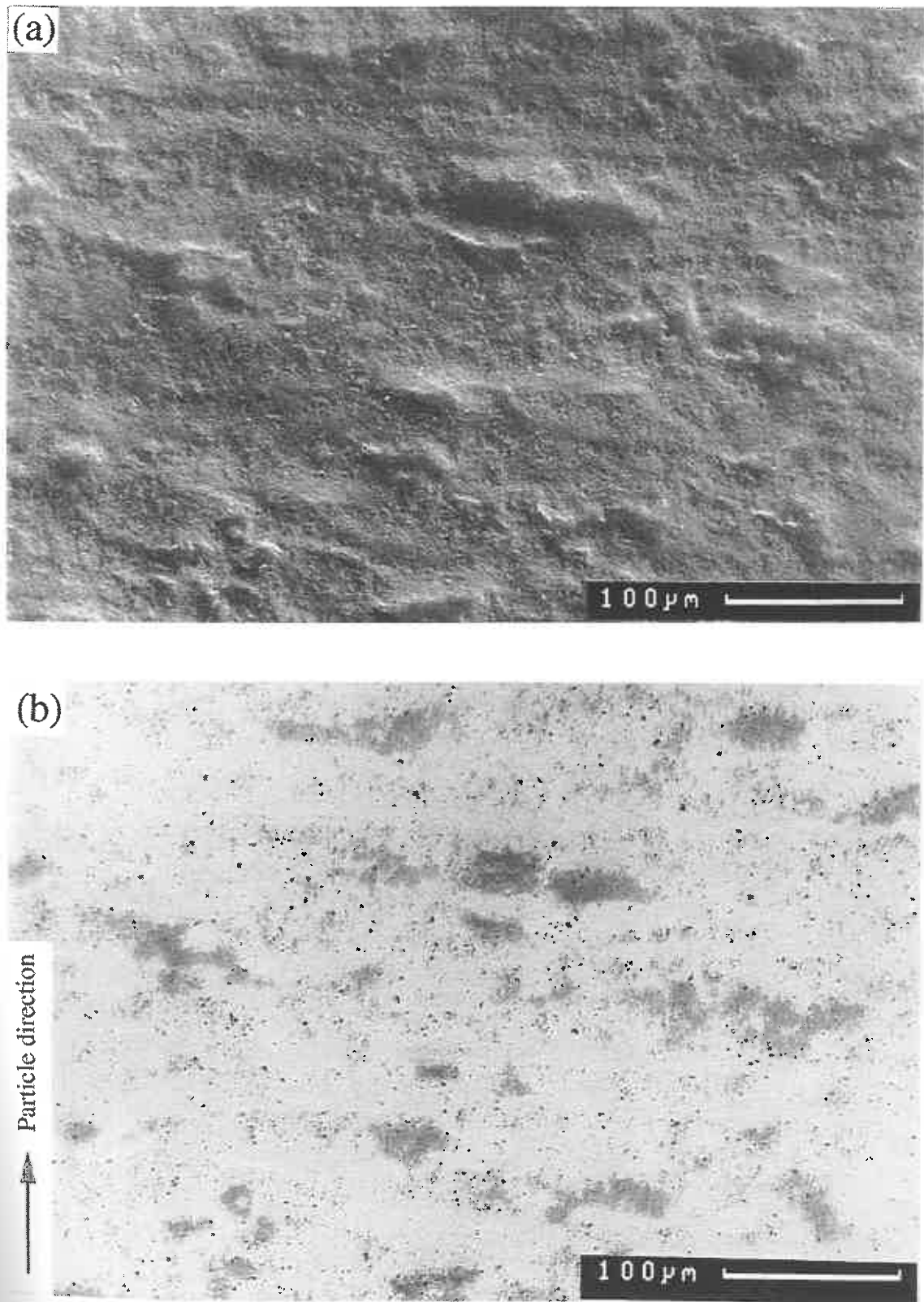


Fig. 6.14. (a) SEM secondary electron and (b) backscattered electron image of the bottom wear scar of mild steel at high impact velocity, mid impact angle and exposed at 300° C.

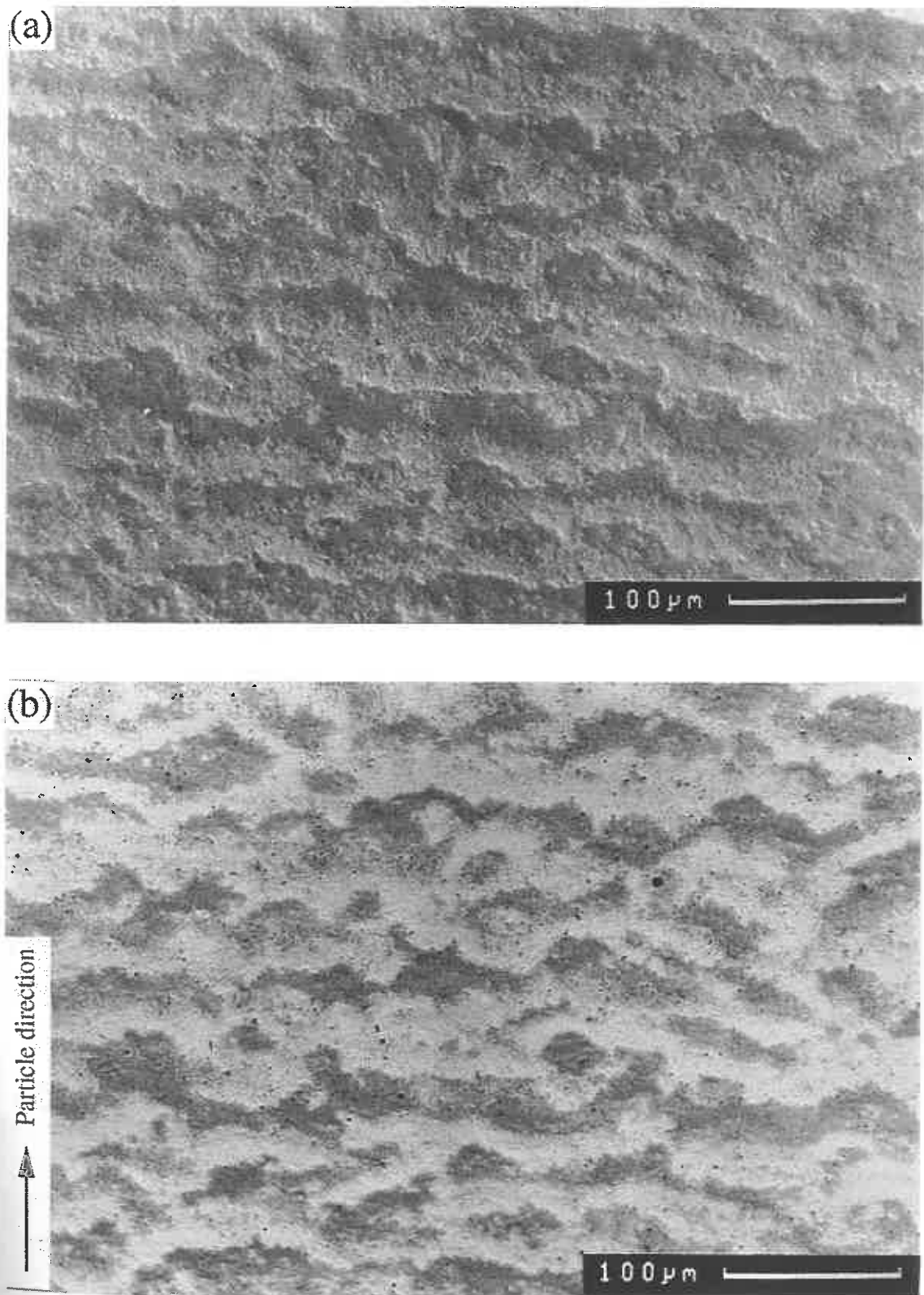


Fig. 6.15. (a) SEM secondary electron and (b) backscattered electron image of the bottom wear scar of mild steel at high impact velocity, high impact angle (close to the specimen leading edge) and exposed at 300° C.

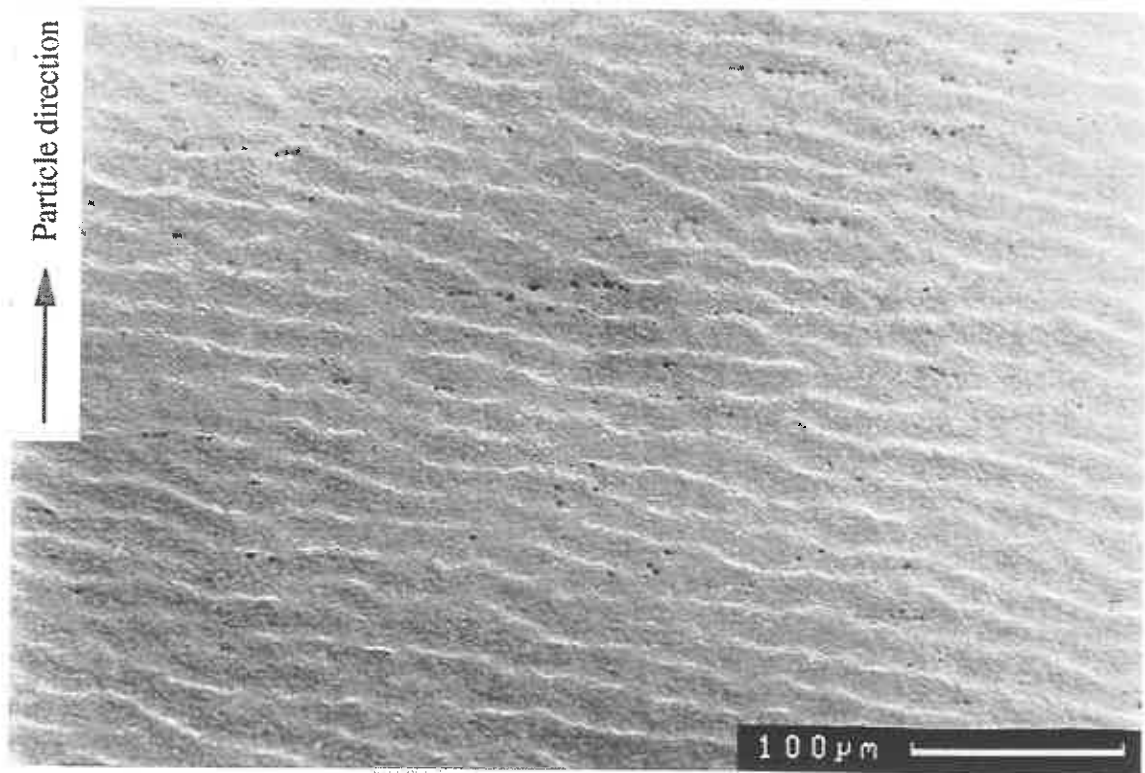


Fig. 6.16. SEM secondary electron image of the bottom wear scar of stainless steel, at high impact velocity, medium impact angle and exposed at 200° C.

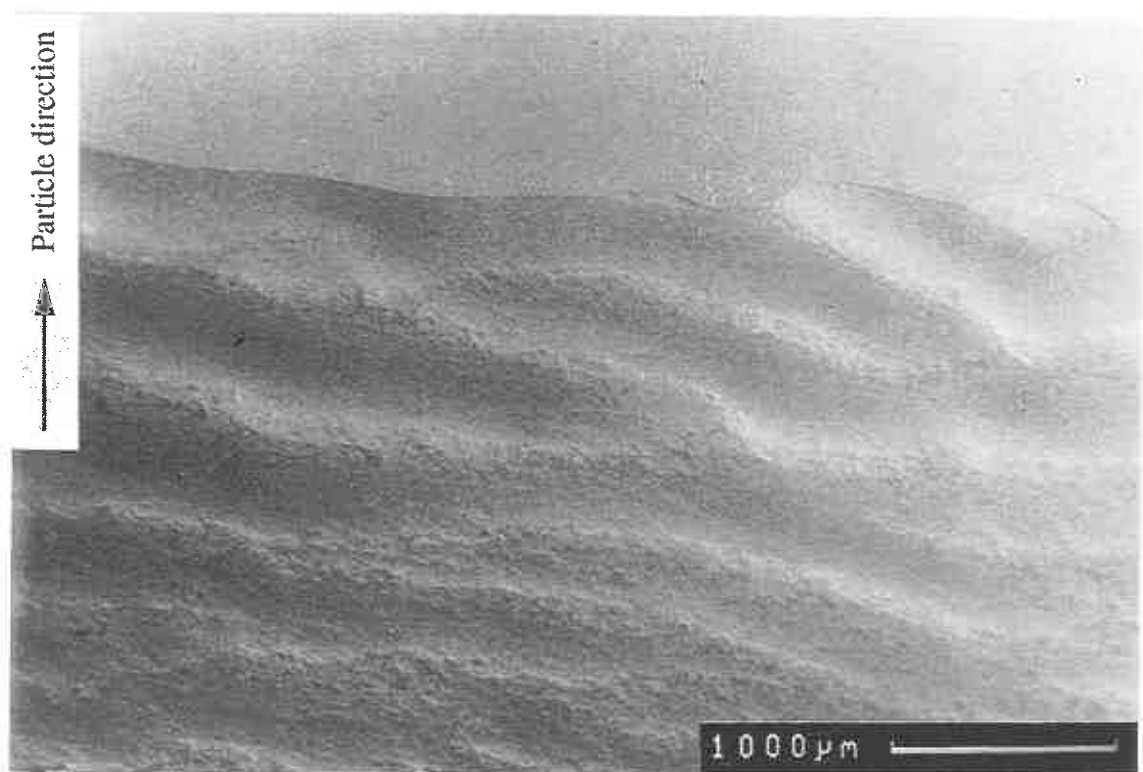


Fig. 6.17. (a) SEM secondary electron of the back edge of the bottom wear scar at high impact velocity of stainless steel exposed at 600° C.

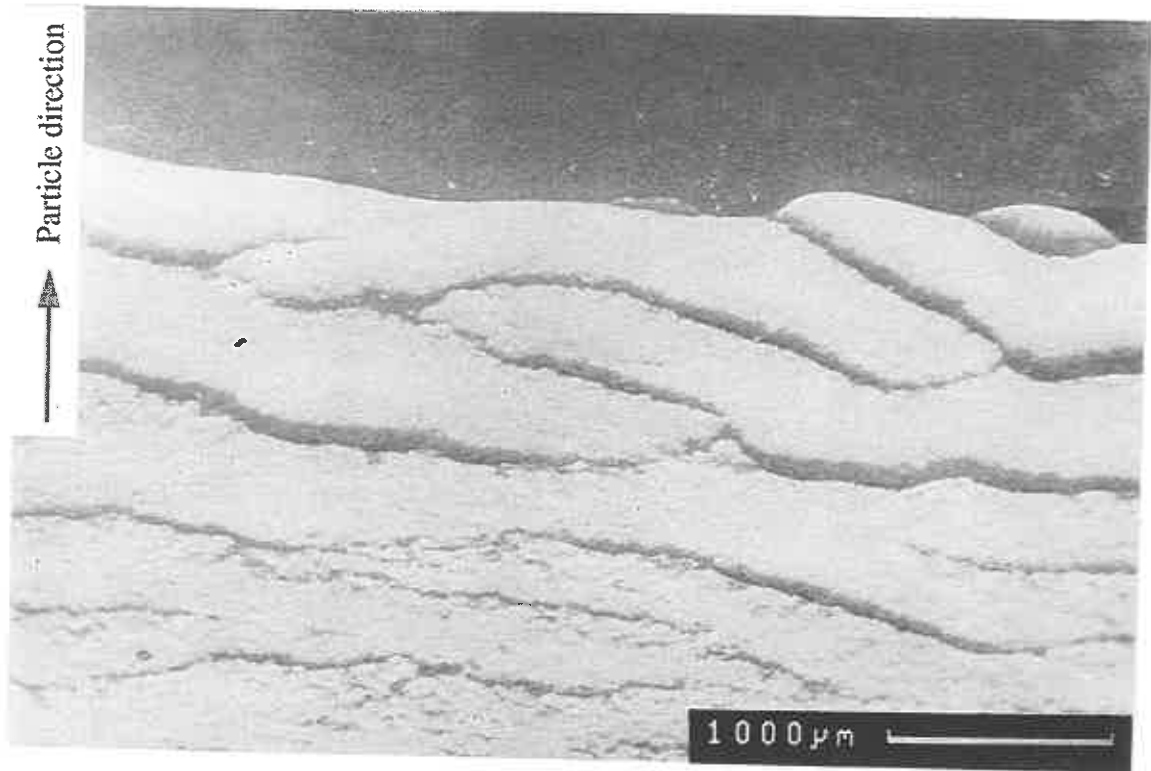


Fig. 6.17. (b) SEM backscattered electron image of the back edge of the bottom wear scar at high impact velocity of stainless steel exposed at 600° C.

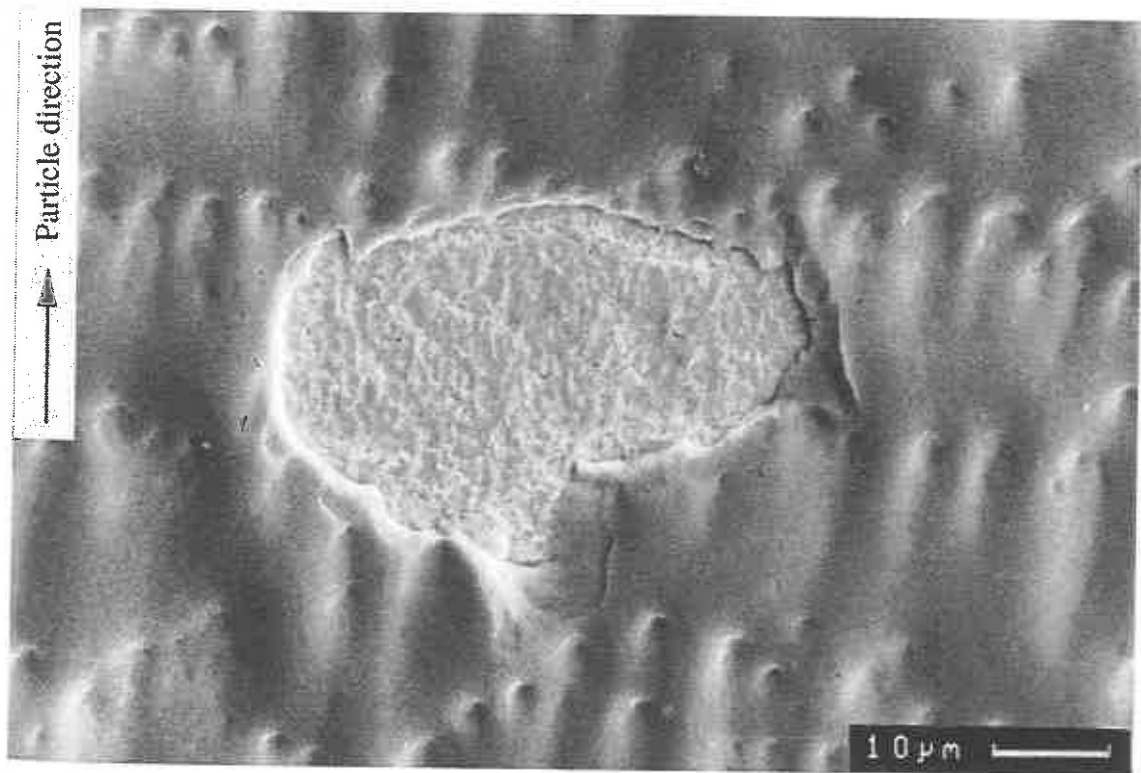


Fig. 6.18. SEM secondary electron image of fractured area of the alumina deposit at low impact velocity on mild steel exposed at 400° C.

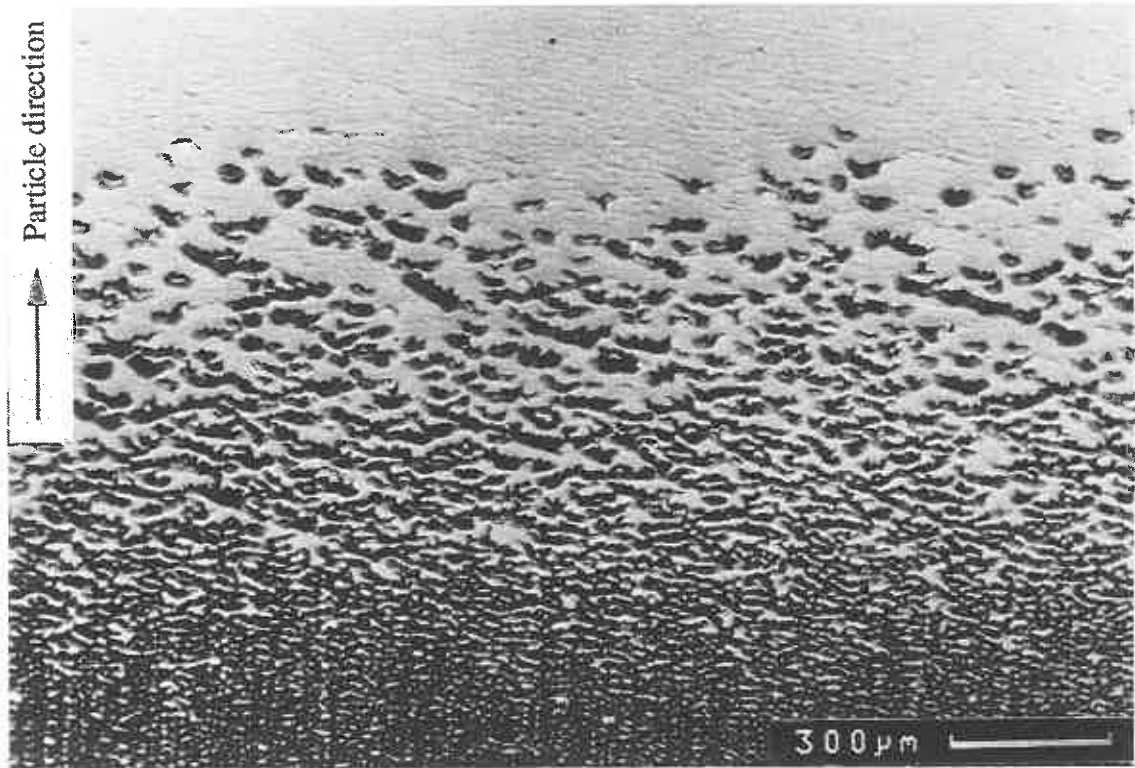


Fig. 6.19. SEM backscattered electron image of the boundary of the alumina embedded region on stainless steel exposed at 200° C.

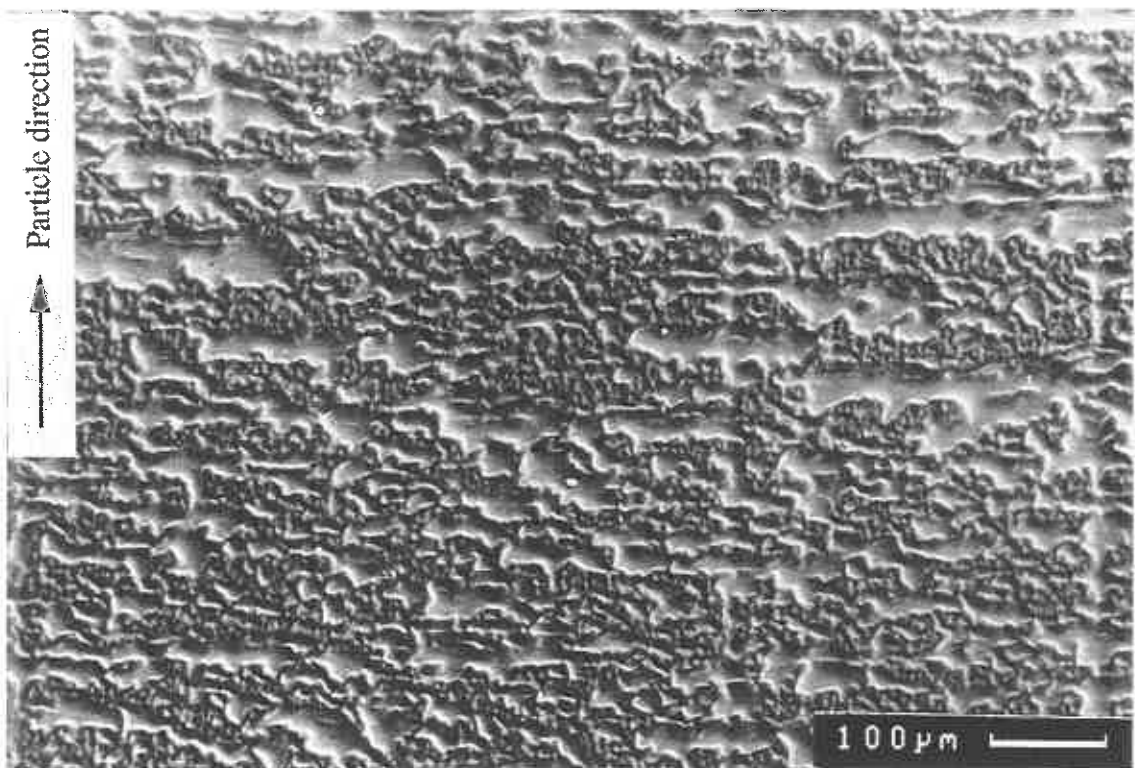


Fig. 6.20. SEM secondary electron image of alumina embedded region on the bottom wear scar of mild steel exposed at 200° C.

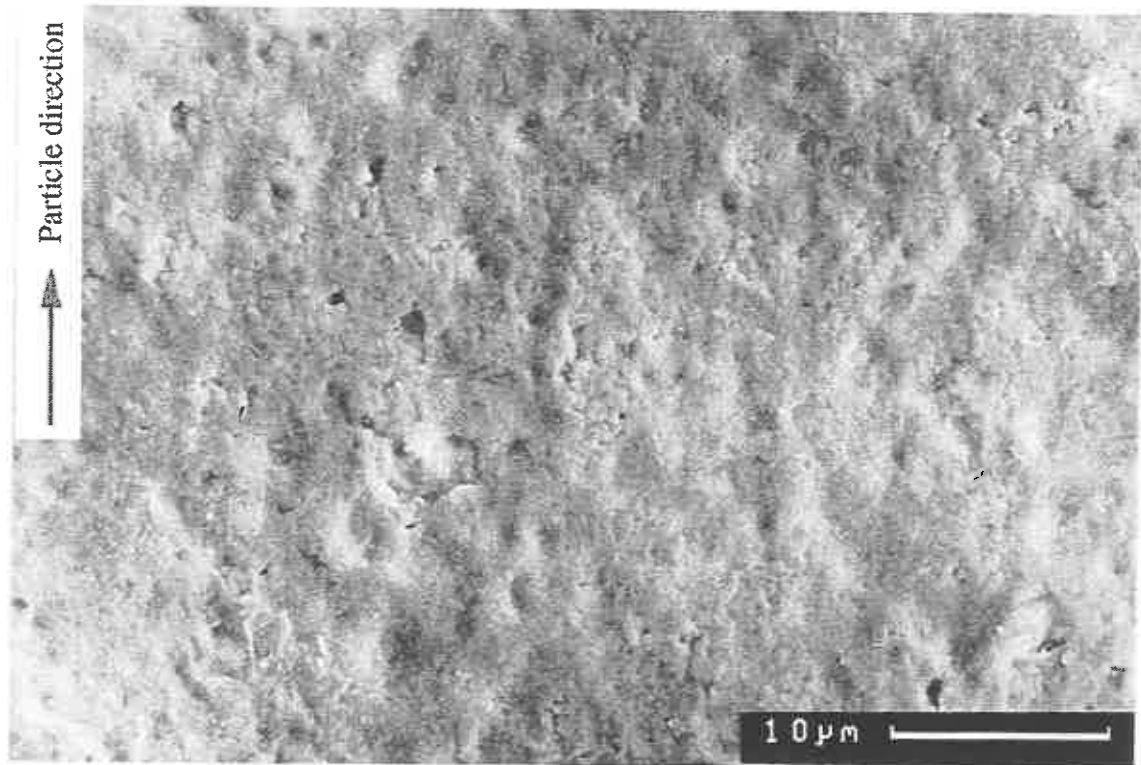


Fig. 6.21. SEM secondary electron image of the wear scar on mild steel exposed at 400° C.

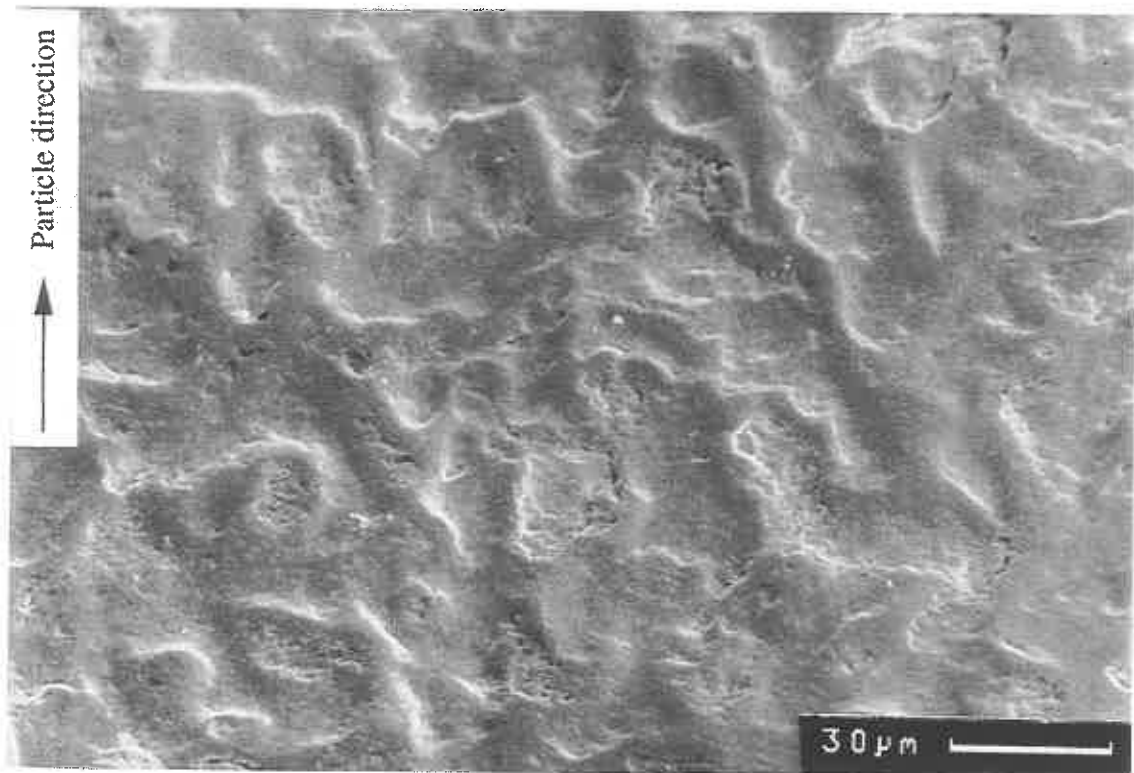


Fig. 6.22. SEM secondary electron image of the wear scar on mild steel exposed at 500° C.

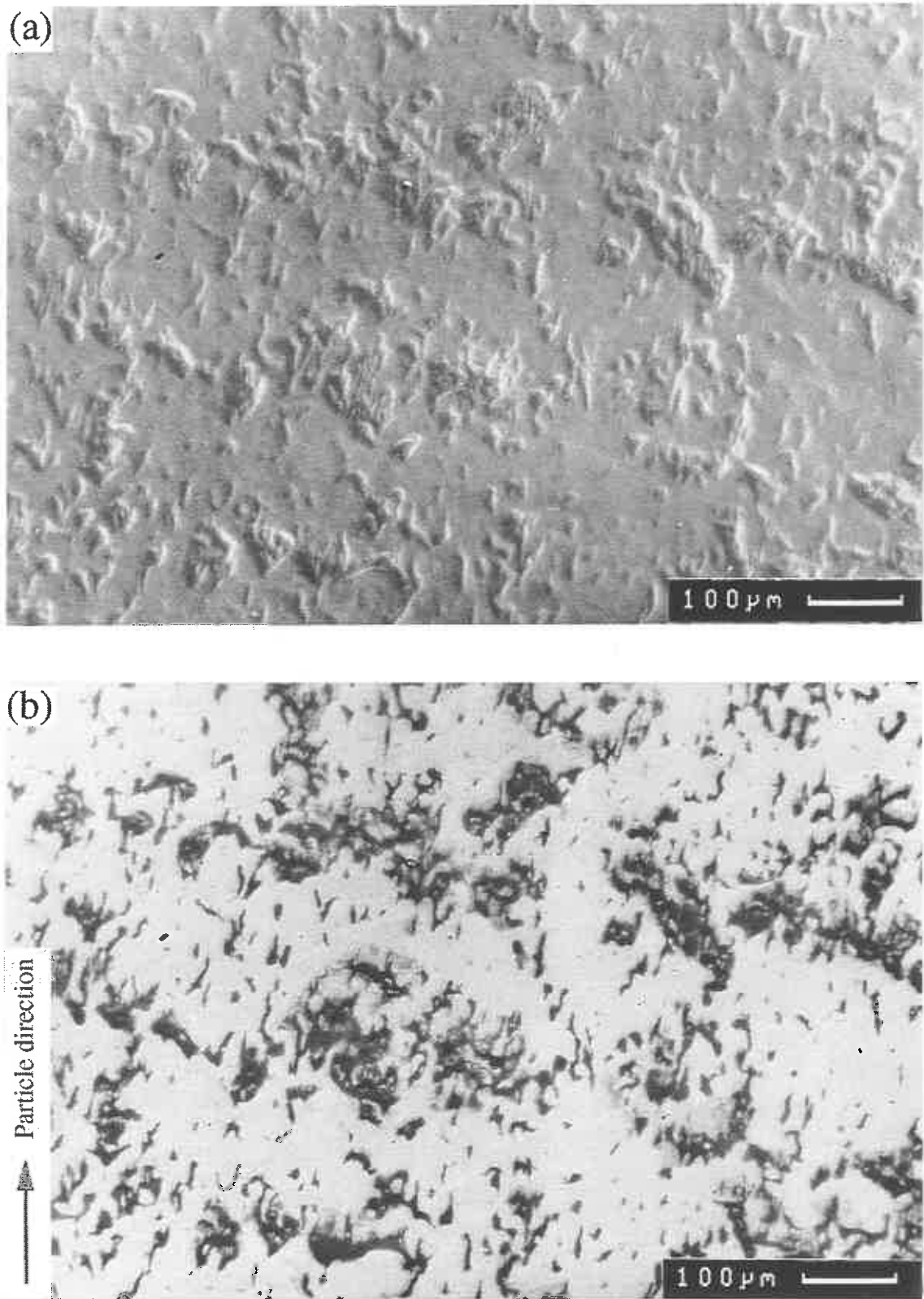


Fig. 6.23. (a) SEM secondary electron and (b) backscattered image of alumina deposit islands on mild steel exposed at 500° C.

6.5. Conclusions

The isothermal behaviour of mild steel measured with the single rotor arrangement and using tube specimens was similar but slightly different to earlier studies using bar specimens on a double counter rotating arrangement. The wastage rates were between those previously observed on the upper and lower rotor, and the temperature of maximum wastage was a slightly lower. This highlighted the need to obtain accurate isothermal wastage behaviour to directly compare to the cooled specimens described in Chapter Seven.

Chapter 7

Erosion-oxidation of mild steel in a temperature gradient

7.1. Introduction

Chapter Three described the erosion-corrosion problems in industrial fluidized bed combustors, and Chapter Four the results from laboratory scale test rigs attempting to simulate this behaviour. Both high flux and low flux studies have generally shown the same temperature dependence of metal wastage, that of an increase to a maximum value around 300° to 500° C then a decrease at higher temperatures as a mechanically protective oxide film develops. Wastage-temperature behaviour of in-bed heat exchanger tubing in FBC boilers differ from the laboratory studies by not decreasing at low temperatures, the low temperature evaporator tubing experiencing the maximum wastage as shown by Holtzer and Rademakers (1991) (Fig. 3.5).

A major difference between FBCs and laboratory studies which may explain this discrepancy is that the FBC bed temperature is typically 800° to 900° C while the surfaces of in-bed evaporator tubes, internally cooled by water and steam, are between 200° and 450° C. In contrast, most laboratory tests are conducted isothermally with the same bed and specimen metal temperature.

A few experimental and theoretical studies have investigated the influence of a heat flux on the oxidation behaviour of metals (Griess *et al.*, 1978; Glover, 1980; Malik, 1990). Results suggest that under these conditions a more porous, less adherent oxide may form and high rates of oxidation could occur. It should be noted however that in these studies the oxidation rate increases because of a temperature gradient across a scale sufficiently thick that its growth was diffusion controlled. Under conditions of high wastage in a FBC boiler however, the surface oxide is very thin.

There have also been few laboratory studies of erosion-corrosion in a temperature gradient. Preliminary experiments were conducted on the 'Cambridge' rig using a

single rotor, similar but simpler in design than the rotor used in the present study. This also allowed air/water cooling of one of two cylindrical specimens, but the outlet for the coolant was via an external copper tube clamped to the rotor (Fig. 7.1). Specimen temperature measurements were not accurate, since they could not be made while the specimens were rotating.

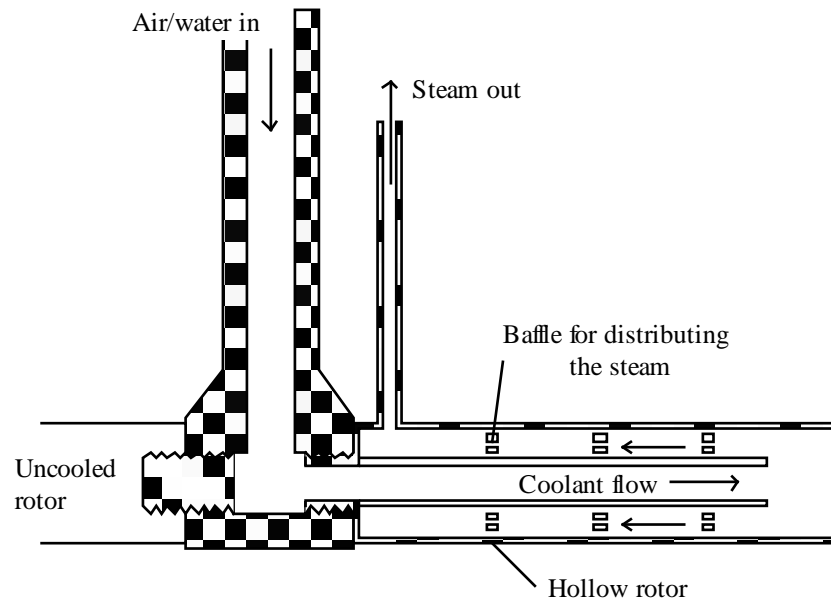


Fig. 7.1. Schematic diagram of the rotor design for early cooled tube studies (Entwisle *et al.*, 1990)

Results showed a large increase in the wastage of the cooled specimens when compared to the isothermal results, although only the isothermal results at the cooled metal temperatures were conducted on the same single rotor, while at other temperatures results obtained from the double rotor arrangement were used. Comparison of isothermal results from the two rotor arrangements seemed to show that the single rotor arrangement was more aggressive which may partially explain the high values of wastage of the cooled specimens. The cooled specimen was partially insulated by ceramic tubes which may have modified the particle flow over the specimen and the tests were of short duration (< 20 h) so that errors arising from the incubation period may have been significant. Without comprehensive isothermal results on the same rotor and accurate temperature measurements it is difficult to assess the effect of cooling.

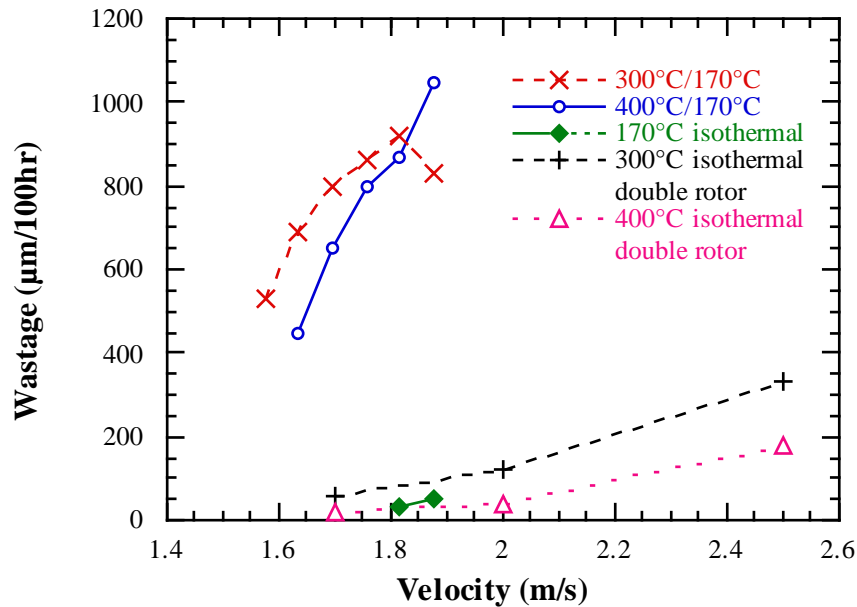


Fig. 7.2. Wastage against velocity for cooled and isothermal specimens, after Ninham *et al.* (1991).

Rogers (1992b) used a single rotor of a new design which allowed internal cooling of one of two tube specimens and continuous temperature measurements during a test. This rotor is described in Chapter Four and was used for all current tests on the erosion-corrosion test rig. Specimens were exposed for 50 hours and air cooled at bed temperatures of 500°, 400°, 300° and 200° C. The cooled specimen temperature was measured with an external thermocouple current discharge welded to the back of the specimen. It has since been shown that the temperature over the wear scar was significantly greater than that measured at the back. These tests are listed in Table 7.1 with a calibration of the wear scar temperatures, and the results are presented and discussed in this chapter together with further tests.

Wang *et al.* (1993a) carried out a series of erosion-corrosion tests on cooled 1018 carbon steel, using a gas blast apparatus to propel 250 µm silica sand particles at 20 m s⁻¹. Test conditions were similar to isothermal tests described in section 4.2.1.2. Specimens were cooled from behind with water and the specimen temperature was measured with a thermocouple inserted into a blind hole drilled in the back of the specimen. The environment temperature was measured by a second thermocouple above the specimen protected from particle impacts by a shelter. Environment

temperatures of 450° and 550° C were used with the specimen cooled to as low as 25° C. The metal thickness loss for both gas temperatures increased with cooling, reaching a maximum at a specimen temperature of 50° - 90° C then decreasing at 25° C (Fig. 7.3). The behaviour was quite different for isothermal tests in similar conditions where an increase in wastage was measured with increasing temperature (Figs. 7.3 and 4.3b). The thickness loss at 25° C in a gas temperature of 450° C was twice that of a specimen eroded isothermally at 25° C. It was also observed that particle deposition increased as the specimen temperature and environment temperature increased.

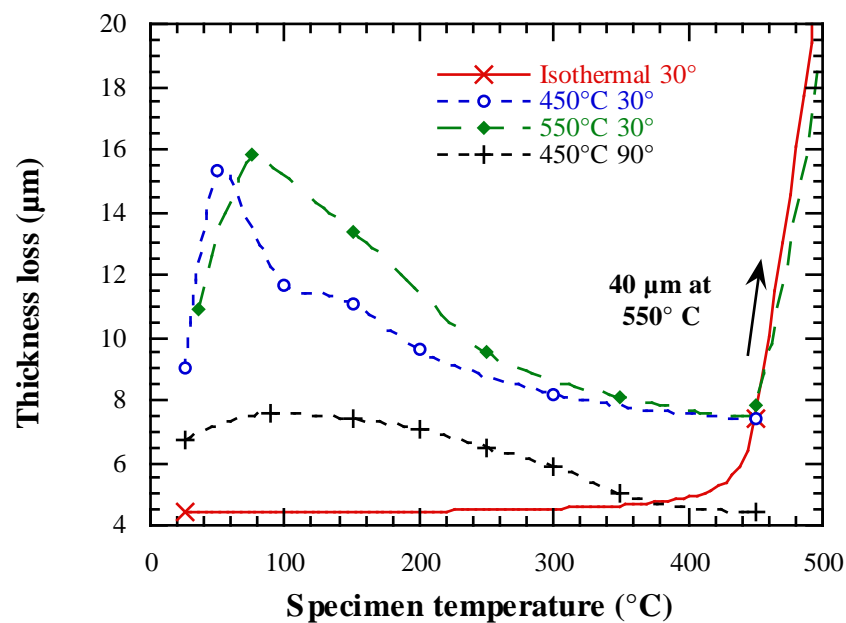


Fig. 7.3. Specimen temperature against thickness loss for cooled 1018 steel at environment temperatures of 450° and 550° C, after Wang *et al.* (1993a).

The gradual decrease in thickness loss with increasing temperature was explained by an increase in metal ductility and also by the greater protection of the surface by particle deposition. The authors suggested that local heating caused by plastic deformation during particle impacts increased the surface metal ductility, and that this heat was conducted away from the surface more quickly in a cooled specimen than an isothermal one at the same temperature. The ductility of the cooled specimen was therefore lower than in the isothermal case and thus the thickness loss was greater. This, however, does not explain why, for the isothermal tests and at low temperatures for the cooled tests, the wastage increases, as the ductility increases and the wastage mechanism was essentially

bare metal erosion. This was also the reason given for an increase in thickness loss at the higher gas temperature as the temperature gradient in the specimen was higher, despite observing more particle deposition at a gas temperature 550° C. No mention was made of the possible effect of heat conduction from the hotter particles to the cooler specimen on impact and that, as the specimen temperature was measured below the surface, the temperature at the surface was likely to be higher. Therefore the cooled specimen may be expected to behave in a more ductile manner.

A recent paper by Zhang *et al.* (1996, as yet unpublished) presented preliminary results from a cooled specimen exposed in the Berkeley erosion-corrosion fluidized bed test rig (section 4.2.2.3). The specimen metal temperature was 190° C in a fluidized bed at 700° C, with the specimen metal temperature measured at the top (back) of the specimen. The maximum wastage rate was about five times higher than an isothermal specimen at 200° C (Fig. 7.4). The mechanism of wear was unchanged but the amount of particle deposition was significantly less for the cooled specimen, and this was thought to be the main cause for the increase in wear.

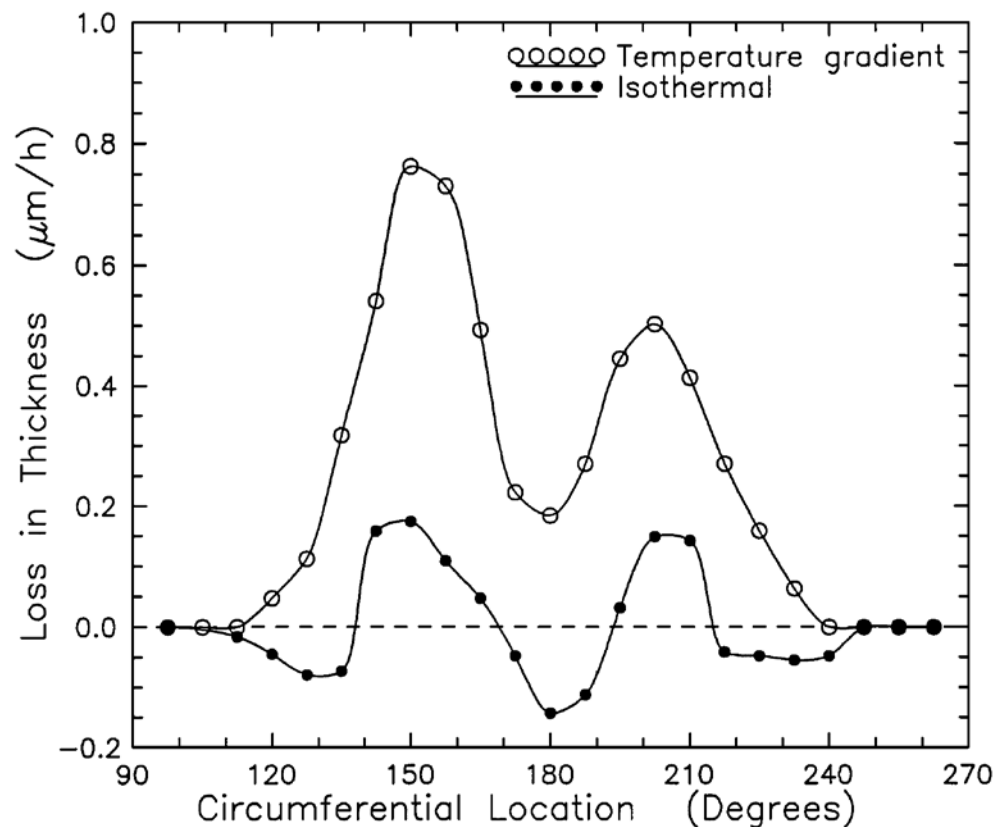


Fig. 7.4. Circumferential material loss for a cooled (190° C / 700° C) and isothermal (200° C) 1018 steel specimen, after Zhang *et al.* (1996).

7.2. Test History

7.2.1. First Phase

As a continuation of the tests by Rogers (1992b) (Table 7.1), single exposure 50 h tests on mild steel specimens were conducted at bed temperatures of 300°, 400° and 500° C using water cooling and the test rig modifications, described in Chapter Five, to achieve cooler metal temperatures. Mild steel was used as the uncooled specimen in all these tests.

7.2.2. Second Phase

Results from the first phase showed large variations in the wastage of the uncooled specimens at 300° and 400° C, while at 500° C, due to the development of a thick oxide, measurements were not accurate enough to determine any variations in wastage. The wastage of these isothermal (uncooled) specimens was lower than the uncooled specimens in tests by Rogers (1992b) which may have been due to differences in fluidization and changes to the bed behaviour as a result of increased cooling (section 7.4.3.1).

As a result, more accurate, interrupted tests of mild steel at 500° C bed temperature were conducted using 316 stainless steel uncooled specimens. Complimentary, interrupted, isothermal data of both mild steel and 316 stainless steel were measured on the same rotor, as previous isothermal data had been obtained from the double rotor arrangement. Results of the isothermal tests have been described in Chapter Six. Interrupted tests allowed the determination of a wear rate without an error caused by an incubation period.

During these tests, a variation in the interference oxide over the back and wear scar was noticed. Measuring temperatures with thermocouples showed that the wear scar was significantly hotter than the back of the specimen. As described in the experimental methods the temperature during a test was measured at the back of the specimen and it was initially assumed that the temperature was relatively uniform over the specimen. Therefore, it was necessary to calibrate the temperature of the wear scar relative to the temperature at the back.

7.2.3. Calibration of wear scar temperatures

Calibration of the wear scar temperature was made at 32 and 47 mm from the low velocity end of the specimen, corresponding to impact velocities 1.7 and 2.1 m s⁻¹ respectively. Fig. 7.5 shows the positions of these thermocouples relative to the internal features of the specimen; at 47 mm, the thermocouple was positioned between the end cap and the cooling air/water inlet, and was approximately on the coolest part of the specimen, while at 32 mm it was located at the centre of the specimen between the water/air inlet and outlet. Thermocouples were positioned towards the back of the wear scar so as to minimise any disruption to the particle flow over the specimen, and routed up the drive shaft in the usual way (Fig. 7.6). During calibration two thermocouples were attached to the upper wear scar with one also at the back, although only one thermocouple could be monitored at any given time. To change the thermocouple the rotor was stopped, connections changed at the slip ring and the rotor restarted.

A suitable length of time was allowed before a temperature measurement was taken to enable the temperatures of the bed and specimen to reach equilibrium. The thermocouples on the wear scar lasted typically 5 - 10 hours before the wires wore through and needed to be replaced.

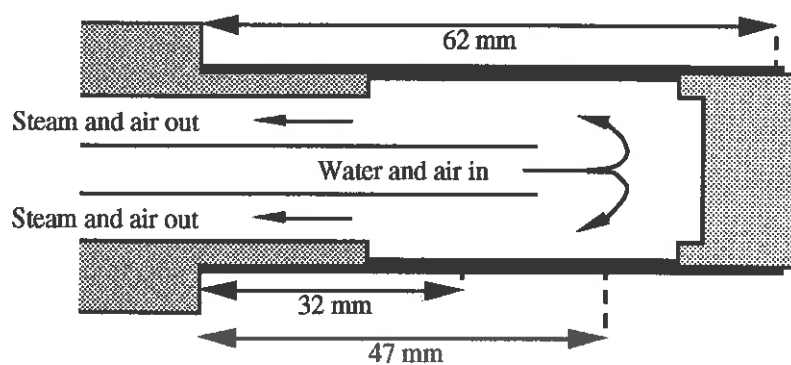


Fig. 7.5. Positions of thermocouples for wear scar temperature calibrations.



Fig. 7.6. Photograph showing the position of the thermocouple on the wear scar at an impact velocity of 2.1 m s^{-1} , the back of the specimen is at the top of the picture.

Figs. 7.7 and 7.8 show some of the calibration results; Fig. 7.7 shows the temperature differences between the wear scar and the specimen back (at 32 mm) for a bed temperature of 400° C , and Fig. 7.8 shows the differences between the wear scar temperature, the front and the back of the specimen for a 500° C bed temperature and with internal baffles.

The temperature measurements made on the upper and lower wear scar were similar, and the temperature at 1.7 m s^{-1} was generally hotter than at 2.1 m s^{-1} , although, the presence of the baffles reduced this difference. The front of the specimen was usually hotter than the back but still cooler than the wear scar. In Fig. 7.8 no data points are shown between a back temperature of 280° and 170° C as a small increase in water flow rate caused a sudden drop in temperature from around 260° to 180° C . This might have been due to an increase in the flow of water over the back of the specimen.

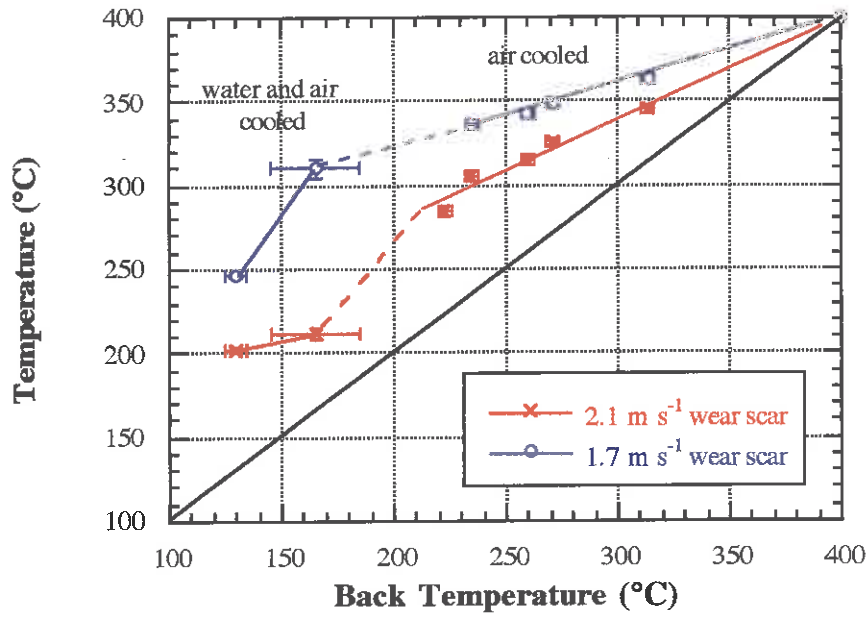


Fig. 7.7. Temperature of cooled specimen upper wear scar relative to the back at 400° C bed temperature and with no internal baffles.

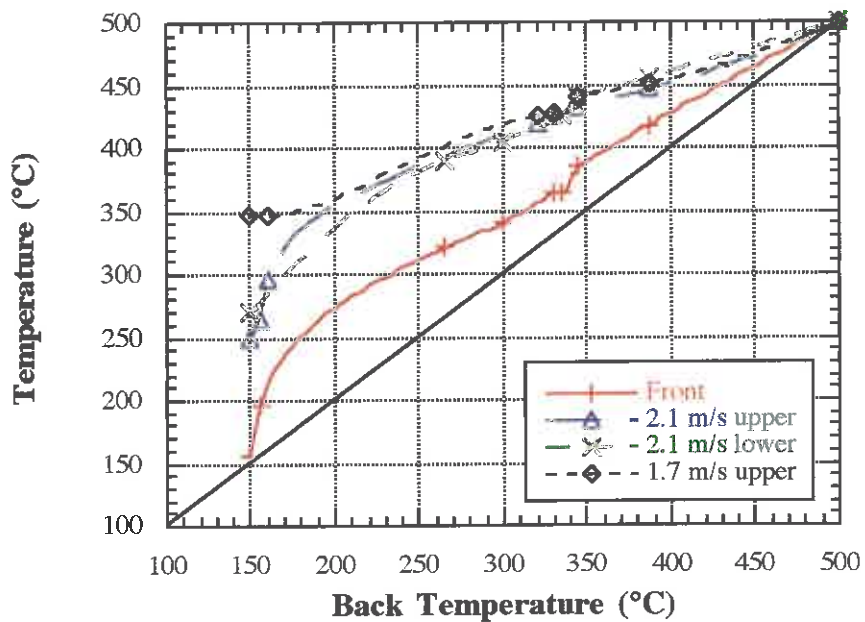


Fig. 7.8. Temperature of specimen front and wear scar relative to the back, at 500° C bed temperature and with internal baffles.

The wear scar temperatures for all the cooled specimen are shown in Table 7.1.

Number of Tests	Cooling conditions	Time (h), (number of interruptions)	Material (uncooled)	Temperature (°C)			
				Bed	Back	Wear scar 1.7 m s ⁻¹	Wear scar 2.1 m s ⁻¹
Tests after Rogers (1992b)							
1	air	50	MS (MS)	200	125	-	-
"	"	"	"	300	215	267	253
"	"	"	"	300	175	250	230
"	"	"	"	400	330	372	357
"	"	"	"	400	280	355	328
"	"	"	"	400	215	335	280
"	"	"	"	500	425	478	468
"	"	"	"	500	360	445	445
"	"	"	"	500	300	407	407
"	"	"	"	500	250	-	400
1st phase							
2	air/water	50	MS (MS)	300	115	203	175
3	air/water	50	MS (MS)	400	175	310	210
3	air/water	50	MS (MS)	400	120	245	202
1	air/water	50	MS (MS)	500	185	375	325
2nd phase							
2	air/water and baffles	85 (4) 105 (5)	MS (SS)	500	150	345	250
1	air/water	105 (5)	MS (SS)	500	300	412	415
1	air	150 (4)	MS (SS)	500	380	450	450
1	air/water and new baffles	108 (5)	MS (SS)	500	210 (front)	326	280

Table 7.1. Summary of cooled specimen tests and calibration results.

7.3. Results

7.3.1. Specimen appearance

The general appearance of the exposed cooled specimens are shown in Figs. 7.9 and 7.10 (colour photos) and described in Tables 7.2 - 7.4 for bed temperatures of 500°, 400°, and 300° C respectively, with the specimens tested by Rogers (1992b). The front and back of the specimens were similar in appearance, although the temperature at the front was measured to be slightly hotter than the back. Specimens cooled with both water and air usually showed a variation of oxide colour along the length of the specimen due to large variations in temperature.

Back metal temperature (°C)	Appearance of specimen front and back	Wear scar temperature (°C) 2.1 / 1.7 m s ⁻¹	Appearance of specimen wear scar
500	Thick grey oxide scale which spalled on cooling	500	Continuous silver / grey oxide scale
*425	Grey/brown oxide with some spalling	468/478	Shiny grey oxide at high velocities with a continuous silver oxide at low velocities
380 (150h)	Grey/brown oxide with some spalling	450	Shiny dark blue / grey oxide, with areas of particle embedment
*360	Continuous matt grey oxide	445	Shiny dark blue / grey oxide
300 (105h)	blue grey oxide	412/415	Blue/grey oxide. dark blue, purple and light straw at the coolest part.
*300	Continuous grey / brown oxide	407	Blue interference colour (straw coloured in places)
*250	Matt blue / grey oxide, with some variation of colour along the specimen length	400	Blue interference coloured wear scar which became straw coloured over the circular metal clip
185	Blue/straw interference coloured oxide	325/375	Straw, purple and blue interference coloured oxide
210 front (108h)	Shiny multicoloured, from straw to light blue and purple	280/326	metallic, straw and blue
150 (105h)	purple red and blue	250/345	metallic and light straw

Table 7.2. Appearance of specimens exposed at a bed temperature of 500° C, *after Rogers (1992b).

(a)



(b)



(c)



(d)



Fig. 7.9. The lower wear scar of cooled specimens at 500° C bed temperature ; (a) back temperature 150° C, total exposure time 85 h, (b) 185° C, 50 h, (c) 300° C, 108 h, and (d) 380° C, 188 h. The specimen leading edge is at the bottom.

Back metal temperature (°C)	Appearance of specimen front and back	Wear scar temperature (°C) 2.1 / 1.7 m s ⁻¹	Appearance of specimen wear scar
400	Continuous matt grey / blue oxide	400	Blue/grey interference colour, with black embedment layer at low velocities and edge of wear scar
*330	Continuous matt grey / blue oxide	357/372	Blue interference colour
*280	Blue and brown oxides	328/355	Blue interference oxide which became straw coloured over the circular metal clip
*215	Blue / purple interference colour	280/335	Wide straw interference coloured oxide
175	Orange, purple and blue interference coloured oxide	210/310	Wide light straw interference coloured oxide
120	Straw interference coloured oxide	202/245	Wide straw and metallic coloured wear scar

Table 7.3. Appearance of specimens exposed at a bed temperature of 400° C, *after Rogers (1992b).

Back metal Temperature (°C)	Appearance of specimen front and back	Wear scar temperature (°C) 2.1 / 1.7 m s ⁻¹	Appearance of specimen wear scar
300	Matt grey / brown oxide	300	Blue interference coloured oxide
*215	Purple, blue and straw interference coloured oxides	253/267	Light straw interference coloured oxide
*175	Straw interference coloured oxide, but blue coloured at the interface with the wear scar	230/250	Wide metallic / silver coloured wear scar
115	Bronze interference coloured oxide	175/203	Wide metallic / silver coloured wear scar

Table 7.4. Appearance of specimens exposed at a bed temperature of 300° C, *after Rogers (1992b).

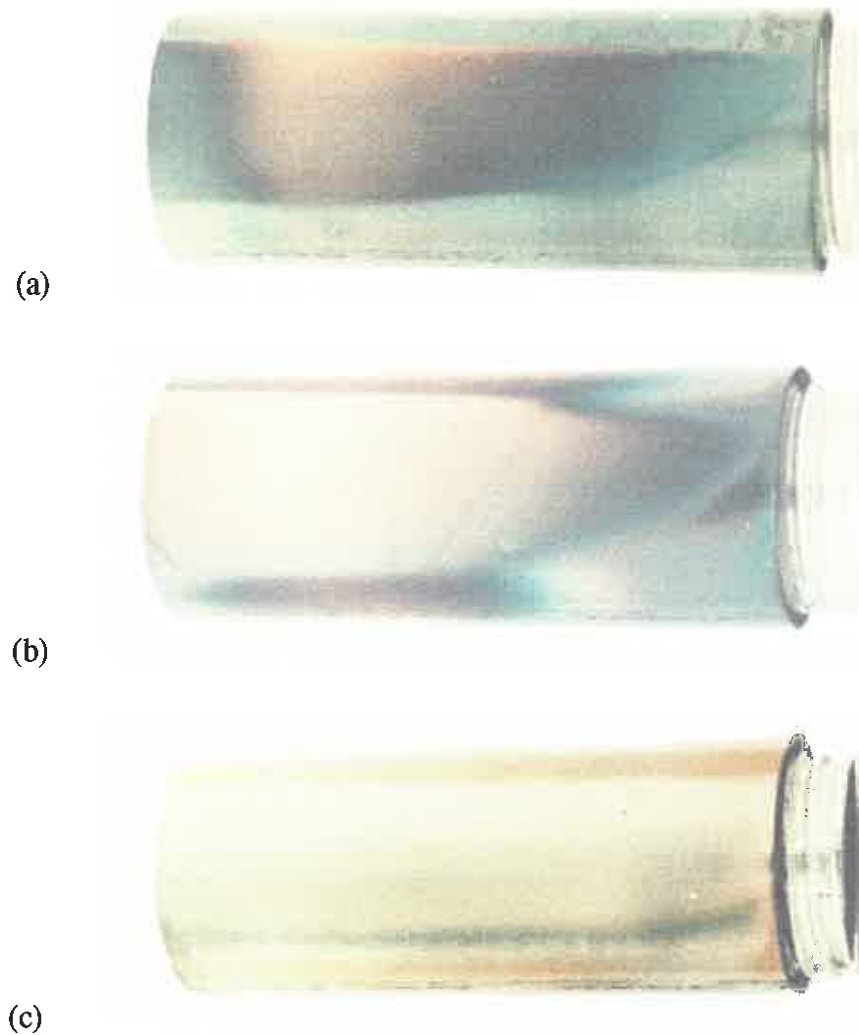


Fig. 7.10. The lower wear scar of cooled 50 h specimens, (a) 500/185° C (bed temperature/back temperature), (b) 400/175° C (similar to 400/125° C), and (c) 300/115° C. The specimen's leading edge at the bottom.

7.3.2. Specimen wastage behaviour

Graphs of wastage against impact velocity for the interrupted tests at a bed temperature of 500° C are shown in figures 7.11 to 7.14. The temperature measured on the wear scar at the impact velocities 2.1 and 1.7 m s⁻¹ are marked on the graphs. Fig. 7.15 shows the wastage at these two velocities against the wear scar temperature plus the isothermal wastage against metal temperature. Similar graphs of wastage against temperature for earlier tests at the bed temperatures of 500°, 400° and 300° C are shown in figures 7.16 to 7.18 respectively.

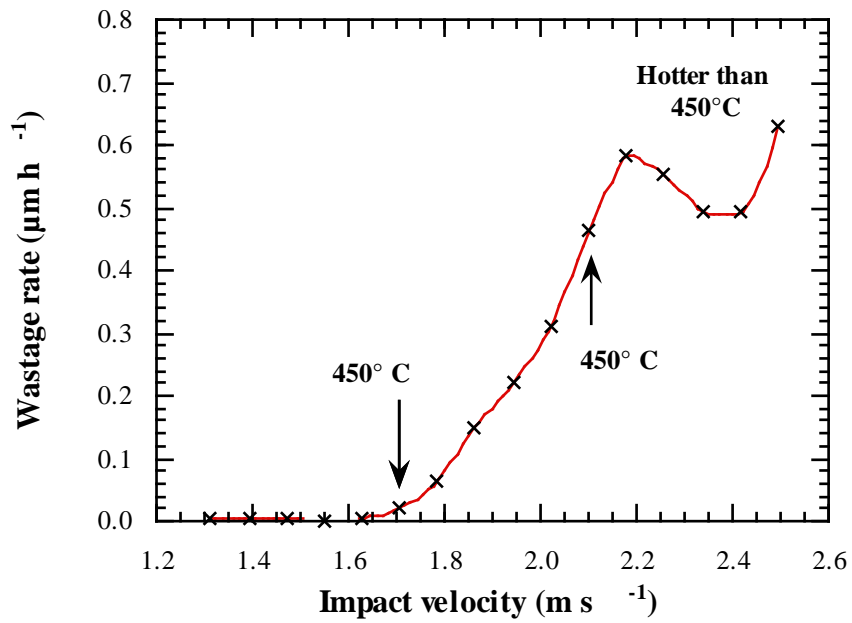


Fig. 7.11. Wastage rate against velocity for cooled mild steel at 380° C back and 500° C bed temperature.

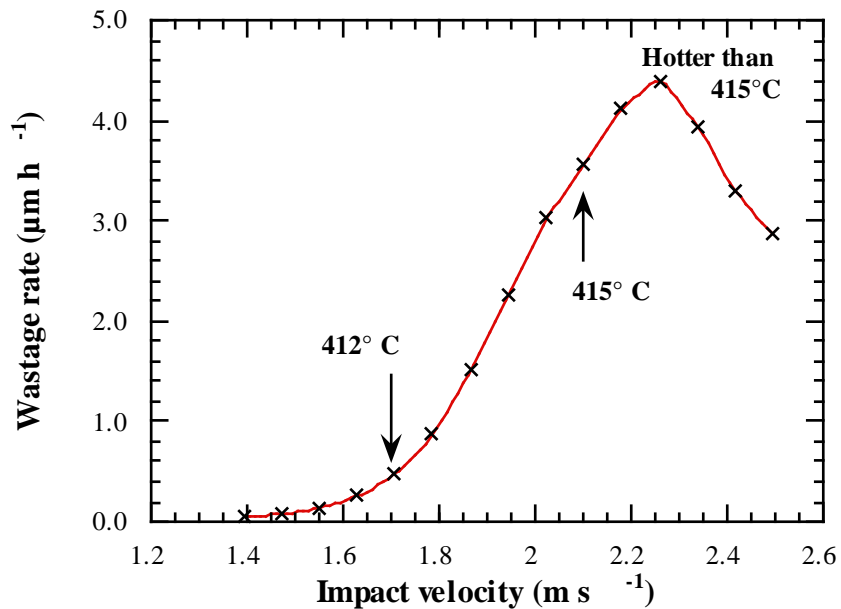


Fig. 7.12. Wastage rate against velocity for cooled mild steel at 300° C back and 500° C bed temperature.

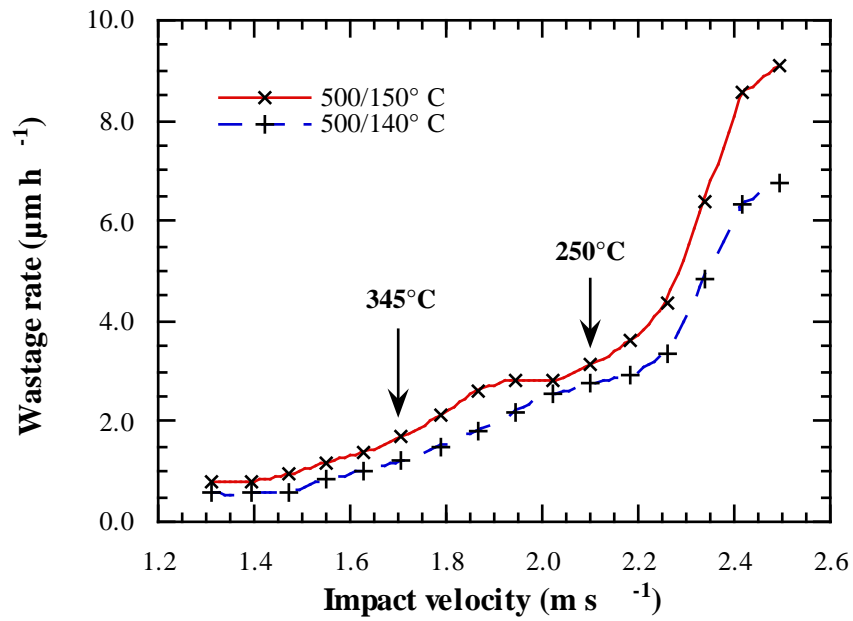


Fig. 7.13. Wastage rate against velocity for cooled mild steel at 150° C and 140° C back and 500° C bed temperature.

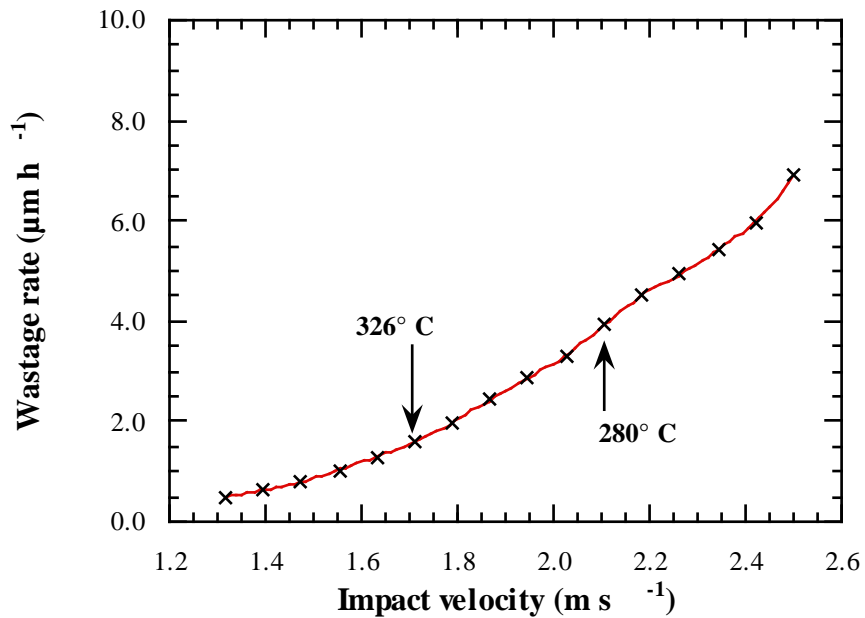


Fig. 7.14. Wastage rate against velocity for cooled mild steel at 210° C front and 500° C bed temperature (with internal baffles).

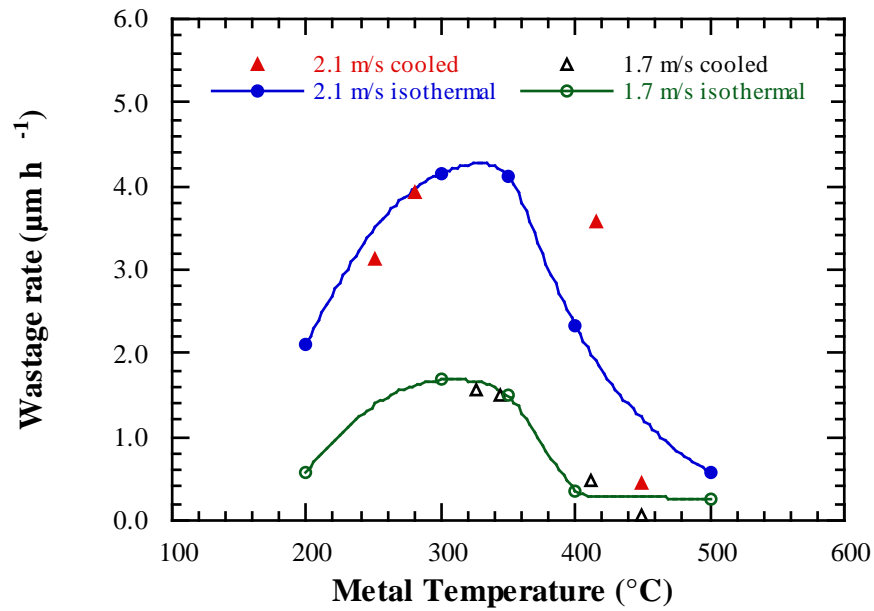


Fig. 7.15. Wastage rate against wear scar metal temperature for cooled mild steel at 500° C bed temperature and impact velocities 2.1 m s⁻¹ and 1.7 m s⁻¹.

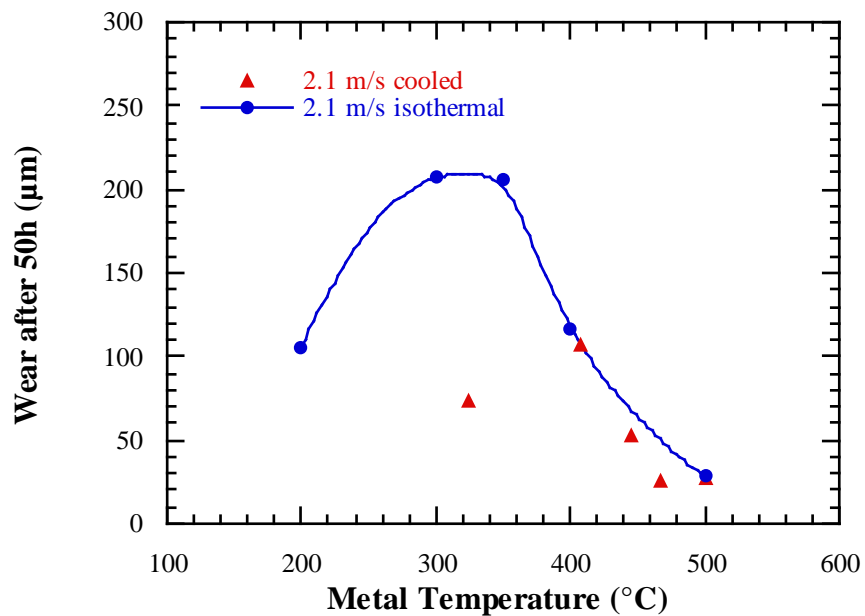


Fig. 7.16. Wastage after 50 hours against wear scar metal temperature for cooled mild steel at 500° C bed temperature and impact velocities 2.1 m s⁻¹.

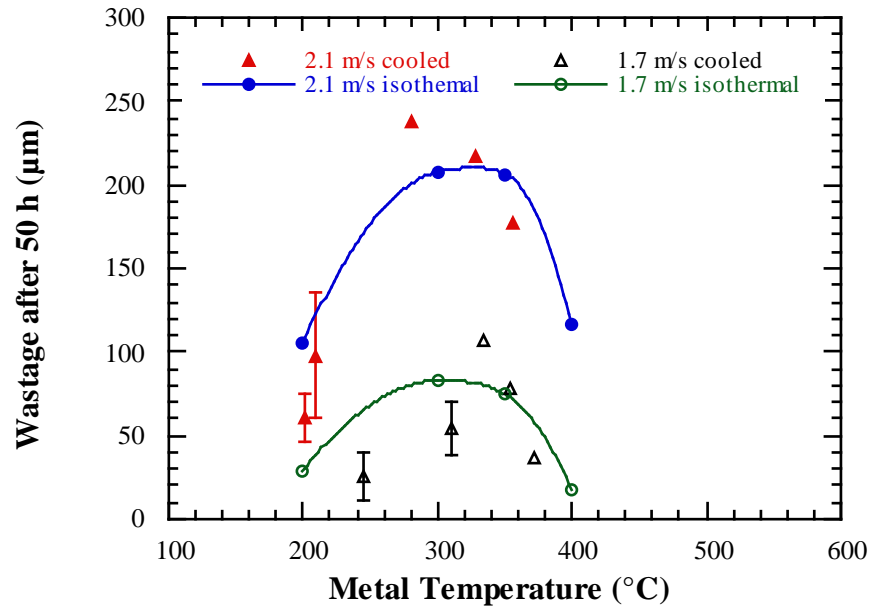


Fig. 7.17. Wastage after 50 hours against wear scar metal temperature for cooled mild steel at 400° C bed temperature and impact velocities 2.1 m s⁻¹ and 1.7 m s⁻¹.

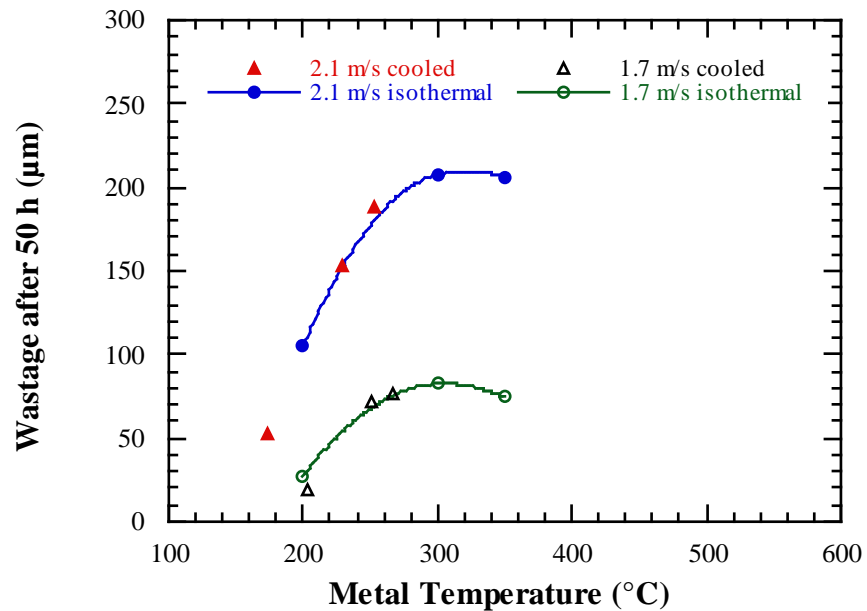


Fig. 7.18. Wastage rate against wear scar metal temperature for cooled mild steel at 300° C bed temperature and impact velocities 2.1 m s⁻¹ and 1.7 m s⁻¹.

7.4. Discussion

7.4.1. Wastage - velocity behaviour

The wastage - velocity behaviour of the cooled specimens was more complicated than that of the isothermal specimens because the specimen temperature varied with specimen position and therefore impact velocity.

The specimen cooled to 380° C at the back (450° C on the wear scar) wasted at a lower rate at both 2.1 and 1.7 m s⁻¹ than the 500° C isothermal specimen, despite not forming a thick grey oxide scale on the wear scar. The test conducted by Rogers (1992b) which was cooled to around 470° C also had wasted at a lower rate than the 500° C isothermal specimen but had a thick wear scar oxide. A black alumina embedment layer had formed on the wear scar which appeared to have been worn off in places, so this could have been a transient effect which reduced the wastage by protecting the metal early on in the test. The wastage velocity graph (Fig. 7.11) showed a gradual increase in wastage with velocity and then a decrease above about 2.2 m s⁻¹ as the surface temperature increased due to the presence of the end cap. This suggested that the wastage may be further reduced at temperatures above 450° C. The appearance of the wear scar oxide at high impact velocities resembled the wear scar oxide on the 400° C isothermal specimen at medium velocities, which roughly agreed with the temperature measurements.

The specimen cooled to 300° C at the back (415° C on the wear scar) wasted at a much higher rate than the 500/380° C* specimen. The wear scar temperature calibration at 2.1 m s⁻¹ for this specimen was probably inaccurate. The cooling was achieved by using a high air pressure and a small amount of water. This gave rise to an uneven temperature distribution with the region close to the water/air inlet and towards the specimen back visibly cooler as indicated by the surface oxide colours. Unlike other specimen calibrations, the temperature measured at 2.1 was hotter than 1.7 m s⁻¹ which suggests that the thermocouple was not measuring the coolest part of the specimen or the cooling pattern was perhaps slightly different during calibration. As with the 500/380° C specimen at velocities above 2.2 m s⁻¹ the wastage decreased at the hotter metal temperature over the endcap (Fig. 7.12). The appearance of the wear scar more

* refers to the specimen cooled to 380° C at its back and at a bed temperature of 500° C

closely resembles that of the 350° C isothermal specimen rather than the 400° C isothermal specimen in terms of its wear scar oxide colour and with less alumina embedment at lower velocities.

Fig. 7.13 shows the wastage-velocity behaviour of two specimens with back temperatures of 150° and 140° C. During testing the back temperatures of both specimens varied significantly ($\pm 20^\circ \text{C}$), but the calibration tests suggested that the wear scar temperatures were slightly more stable especially at 1.7 m s⁻¹. These two specimens gave an indication of the degree of error for nominally the same test, which in this case was fairly large because of the difficulty in maintaining consistent cooling conditions. The effect of the temperature difference along the length of the specimens on the wastage can also be seen in Fig. 7.13 with a reduction in wastage at the coolest point when compared to the wastage - velocity behaviour of an isothermal specimen. This is shown schematically in Fig. 7.19.

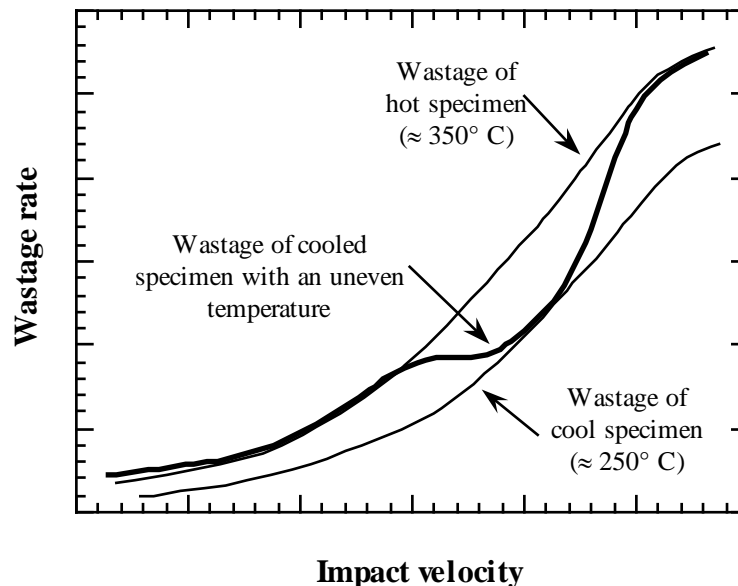


Fig. 7.19. A schematic diagram illustrating the shape of the wastage rate - velocity behaviour shown in Fig. 7.13.

This was the inverse effect to that seen on the hotter specimens (Figs. 7.11 and 7.12) where the wastage decreased at the end of the specimens as the metal temperature increased due to the presence of the endcap. Despite the large temperature differences measured along the specimen, the wear scar had a fairly uniform metallic colour similar to the 200° C isothermal specimen, changing to light straw at either ends.

In an attempt to reduce further the temperature of the wear scar, once it was discovered that the coolest temperature reached was around 250° C, a different set of baffles were made to channel the cooling air and water across the front half of the specimen. This did not reduce the minimum temperature of the wear scar but reduced the temperature variations along the length of the specimen. Unlike the other cooled specimens the wastage rate against velocity behaviour (Fig. 7.14) increased uniformly with velocity and showed no large increase or decrease towards the end of the specimen. The appearance of the upper wear scar was similar to the 500/150° C specimen, although the lower wear scar shown in Fig. 7.9 had regions covered in straw and blue oxide indicating hotter regions, perhaps where the baffle restricted the flow of water.

7.4.2. Wear scar appearance and temperature

7.4.2.1. Visual appearance

Comparing the wear scar oxide colours of all the cooled specimens described in Tables 7.2 - 7.4 with the oxide colours of the isothermal specimens seemed to indicate that the cooled specimens experienced a lower metal temperature than suggested by the wear scar oxides. For example, an isothermal specimen at 300° C had a blue interference wear scar, whereas the cooled specimens with wear scar metal temperatures measured above 300° C had wear scar oxides of a thinner, straw colour.

A major source of error when comparing the wear scar oxide colours was that, at the termination of a test, it took several minutes to remove the specimens from the bed and, unlike the isothermal tests, the cooled specimens continued to be cooled minimising any oxide grown on the wear scar while the rotor was stationary. To assess the effect of cooling after the test, two mild steel specimens were exposed isothermally for several hours and one was cooled during removal. The actions of stopping the rotor and cooling the specimen were carried out as simultaneously as possible, as the timing of the cooling, relative to the rotor stopping, was quite important; if the specimen was cooled before the rotor was stopped then a thin equilibrium oxide could be worn off but, if the rotor was stopped much before the specimen was rapidly cooled a thin interference oxide might grow on the bare metal surface. Table 7.5 describes the appearance of these cooled specimens.

By rapidly cooling the isothermal specimens with water and air as the rotor stopped, a

blue/red wear scar was observed at 350° C rather than the grey/blue oxide, and a straw coloured oxide developed at 300° C in contrast to the blue interference coloured oxide without cooling. In general the oxide colours on the cooled specimens described in Tables 7.2 - 7.4 agreed with these observations, a straw or metallic wear scar developed below 300° C and a blue oxide developed above 350° C.

Isothermal Temperature (°C)	Appearance of specimen wear scar (uncooled)	Appearance of specimen wear scar (cooled)
400	blue/grey oxide	blue oxide
350	blue interference coloured oxide	blue/red interference coloured oxide
300	dark blue interference coloured oxide	light straw interference coloured oxide
250	light straw interference coloured oxide	metallic

Table 7.5. Appearance of mild steel specimen wear scars exposed isothermally in the fluidized bed test rig but rapidly cooled once the rotor had stopped.

Despite general agreement, there were still several inconsistencies between the wear scar oxides and the temperature measurements. The appearance at low velocity of the coolest specimens perhaps indicated a cooler metal temperature than that measured. For example, the oxide colour of the 500/150° C specimen at 1.7 m s⁻¹ was light straw but the wear scar temperature was measured as 345° C. Also the colour of regions on different specimens of similar metal temperature was not always consistent. For example, as expected the 400/280° C test had a blue coloured wear scar at 1.7 m s⁻¹ with a measured surface temperature of 355° C, but the 400/215° C test at 1.7 m s⁻¹ had a light straw coloured wear scar with a surface temperature of 335° C.

There was also a noticeable difference in the amount of alumina deposition between the cooled and uncooled specimens. The specimens cooled to around 200° C at bed temperatures of 400° and 300° C showed very little or no alumina deposit as opposed to the significant area of the wear scar covered on the 200° C isothermal specimen. At higher temperatures the 500/380° C specimen had alumina embedment at high impact velocity. This was not seen on the isothermal specimens although no similar temperature was tested (450° C) and it may also have been a transient effect.

7.4.2.2. *Microscopic appearance*

Microscopic observations of the cooled specimen wear scars showed similar features to the isothermal specimens of comparable visual appearance. The wear scar features did not give a good indication of the wear scar temperature because, as observed on the isothermal specimens, there was not a significant change in the microscopic appearance of the wear scar until a thick equilibrium scale developed at 500° C.

SEM micrographs of the 500/380° C specimen (wear scar temperature of 450° C) showed that the wear scar was quite featureless over the interference oxide covered areas (Fig. 7.20 a and b) and was similar in appearance to the wear scar of 400° C isothermal and 500/300° C specimens at lower impact velocity. This agreed with the general visual appearance of the wear scars. The difference between the 500/380° C and the isothermal 400° C surface was that the 400° C specimen showed more erosion features and the presence of further oxidation in the form of oxide nodules (Fig. 7.21 a and b). It is likely that these formed once the test had stopped as they would probably be easily removed by particle impacts. The difference during the cooled test was that the metal temperature was quickly reduced once the rotor stopped.

The 500/300° C specimen had a measured wear scar temperature of around 410° C, but the wear scar at the coolest point most closely resembled the appearance of the 350° C isothermal specimen with alumina rich regions on the wear scar near the leading and trailing edge (Figs 7.22 - 7.24). As discussed above the coolest part of the specimen by the water/air outlet may have been cooler than measured by the calibration thermocouple. Away from the coolest part of the 500/300° C specimen the ripples close to the trailing edge of the wear scar were similar in appearance to those on the 400° C isothermal specimen with thicker alumina rich regions on the down-flow side of the erosion ripples (Fig. 7.25).

The 500/140° C specimen with a wear scar temperature between 250° and 350° C showed a typical low temperature wear scar of discrete impact craters over the whole of the wear scar. When compared with the closest isothermal specimen at 300° C, there were fewer regions of alumina rich areas on the wear scar (Fig. 7.26) and it more closely resembled the worn region on the 200° C isothermal specimen (area not covered with alumina deposit).

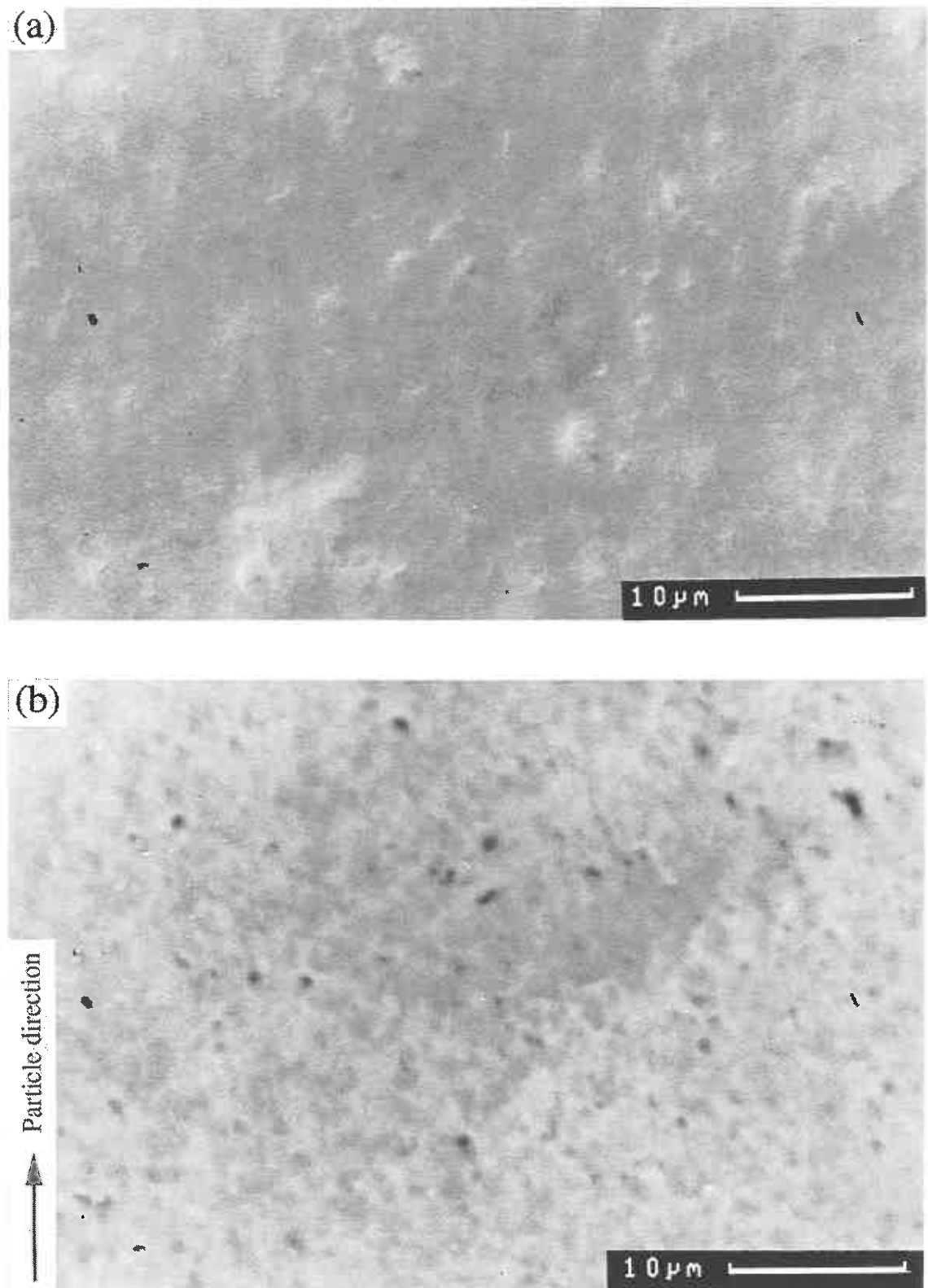


Fig. 7.20. (a) SEM secondary electron and (b) backscattered electron micrograph of the wear scar of mild steel exposed at 500/380° C and at the high velocity end of the specimen.

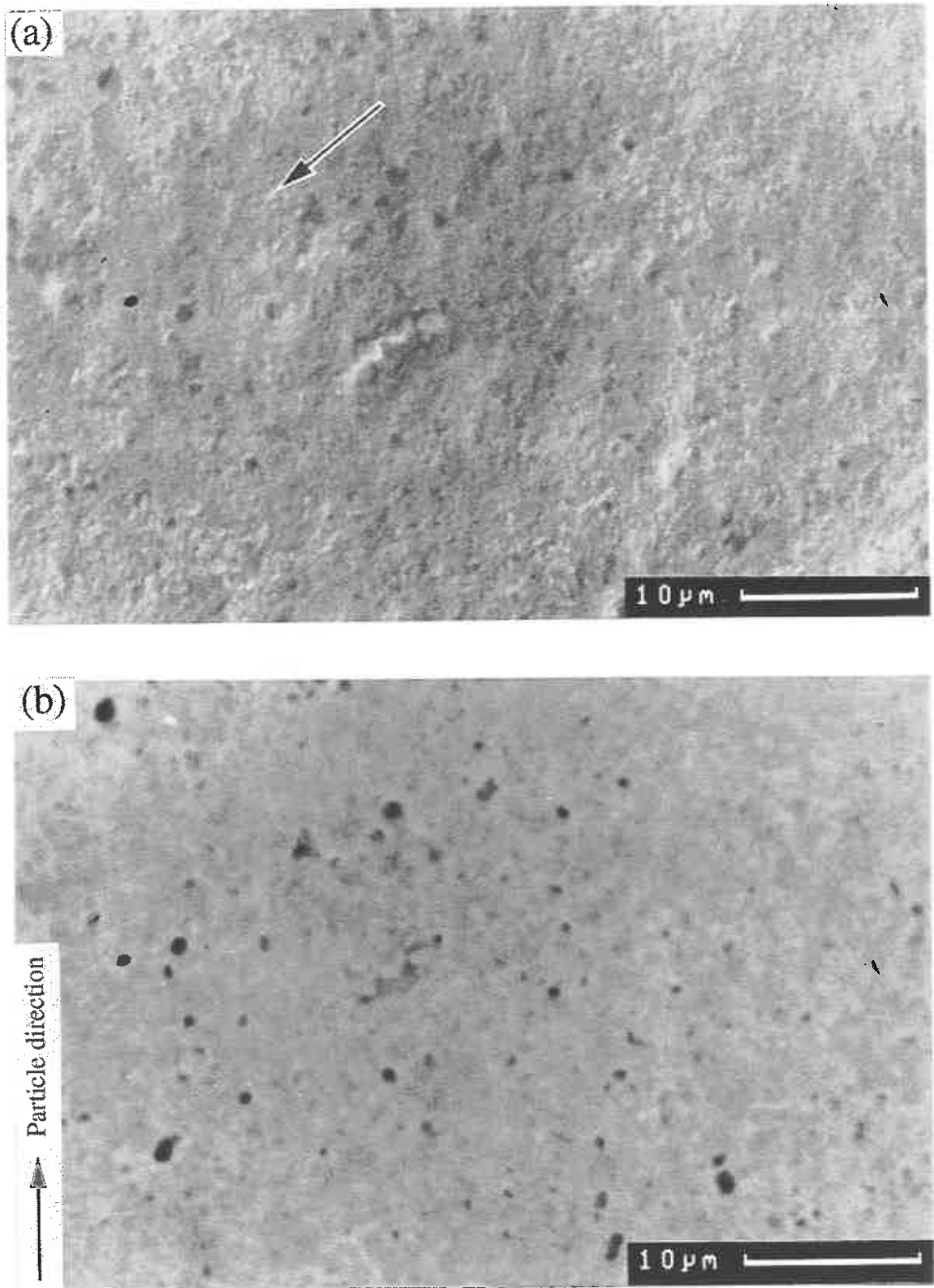


Fig. 7.21. (a) SEM secondary electron and (b) backscattered electron micrograph of the wear scar of mild steel exposed at 400° C and at low impact velocity (arrow shows oxide nodule).

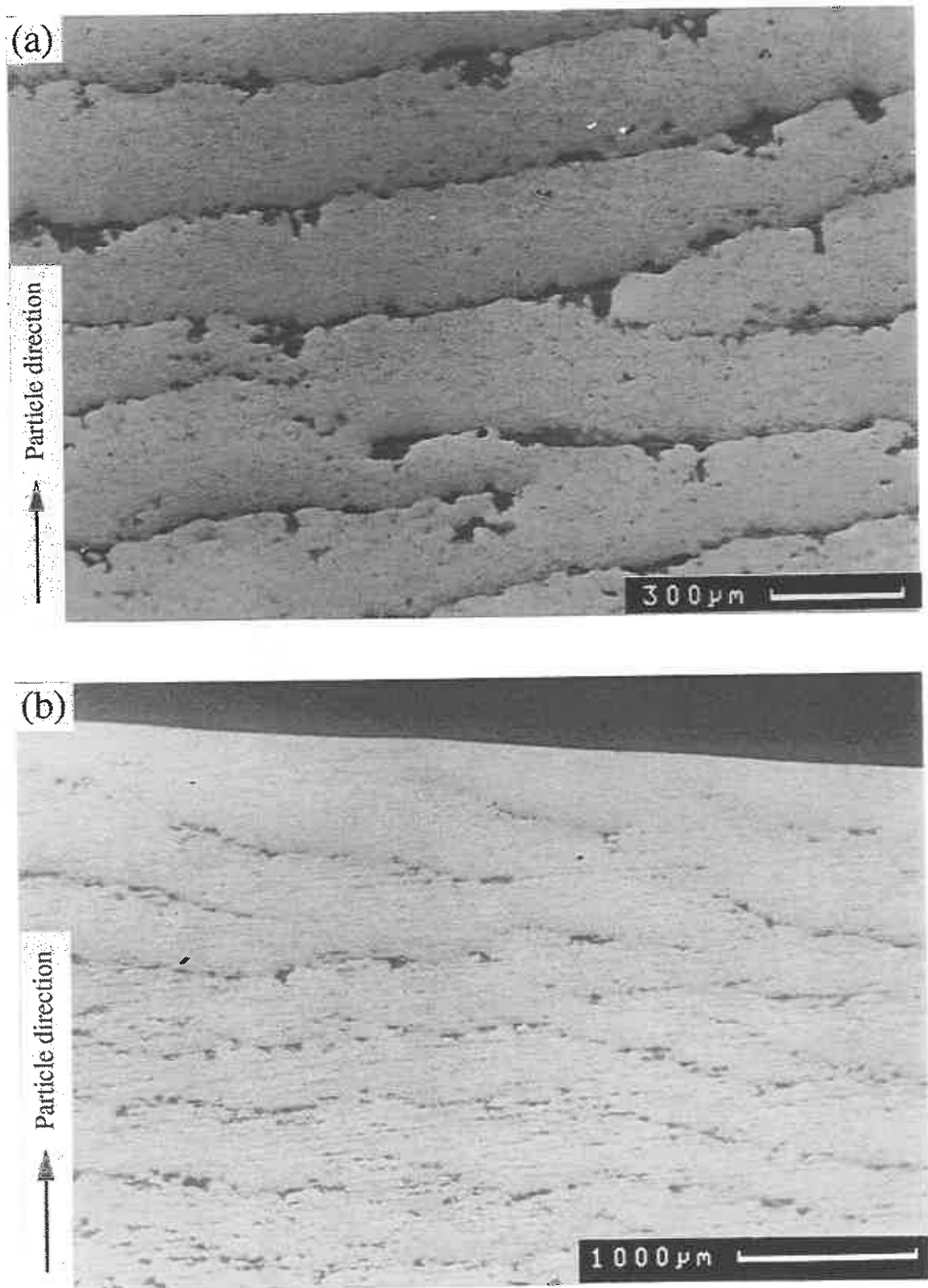


Fig. 7.22. SEM backscattered electron micrographs of (a) the coolest part of the 500/300°C specimen upper wear scar and (b) 350°C isothermal specimen lower wear scar at low impact angle and medium velocity.

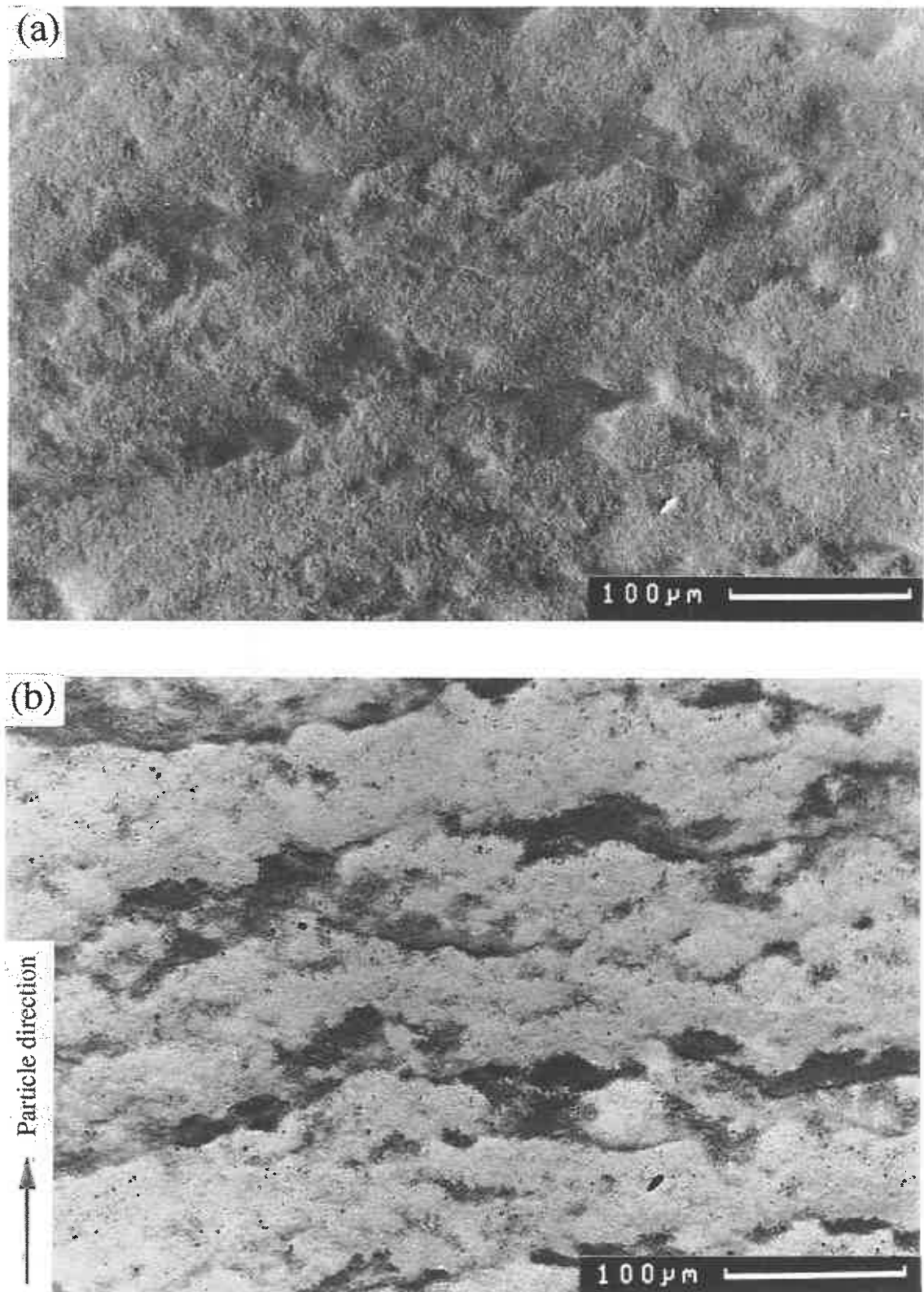


Fig. 7.23. (a) SEM secondary electron and (b) backscattered electron micrograph of the wear scar of mild steel exposed at 500/300° C at high velocity and close to the specimen leading edge (high impact angle).

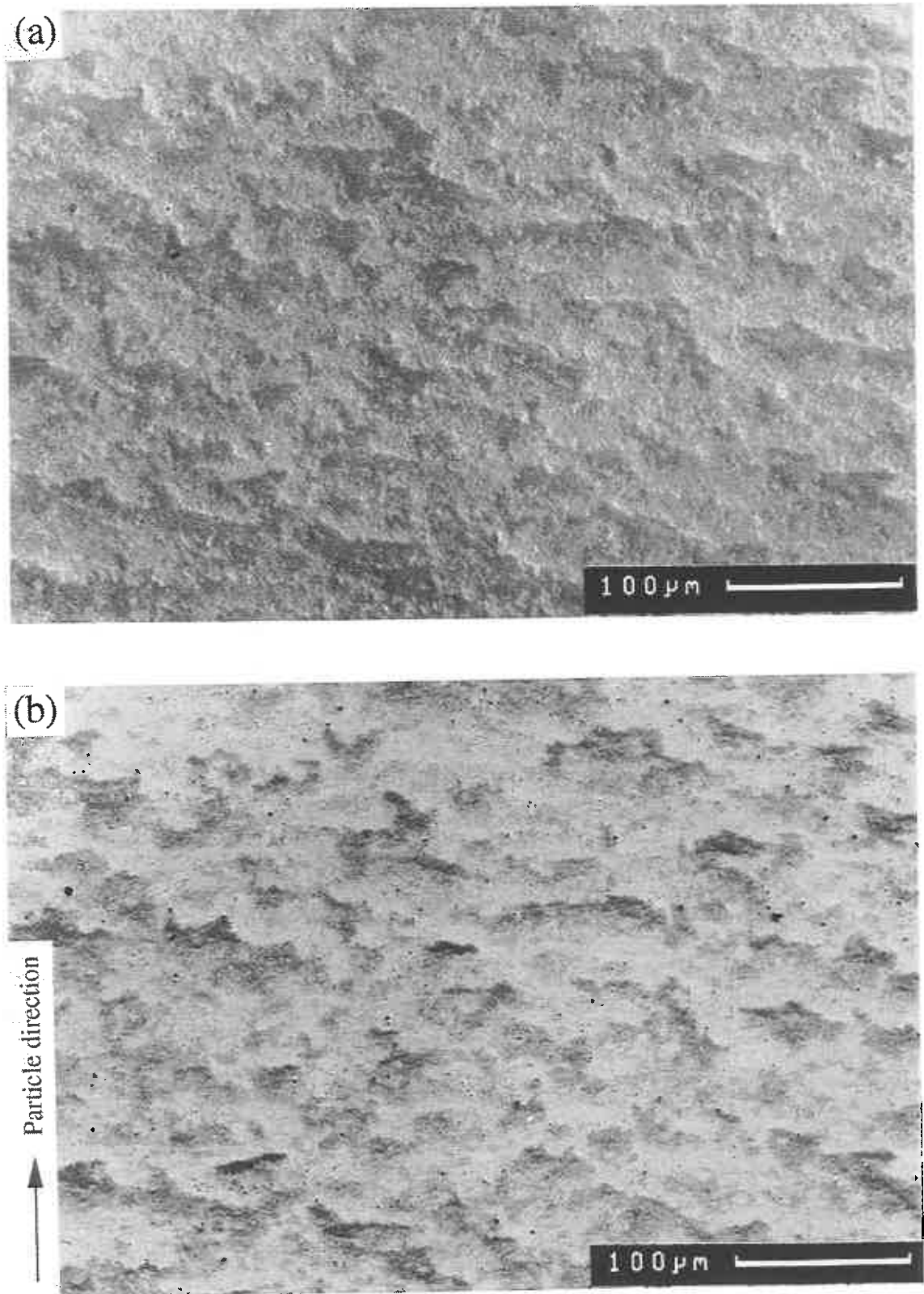


Fig. 7.24. (a) SEM secondary electron and (b) backscattered electron micrograph of the wear scar of mild steel exposed isothermally at 350° C at high velocity and close to the specimen leading edge (high impact angle).

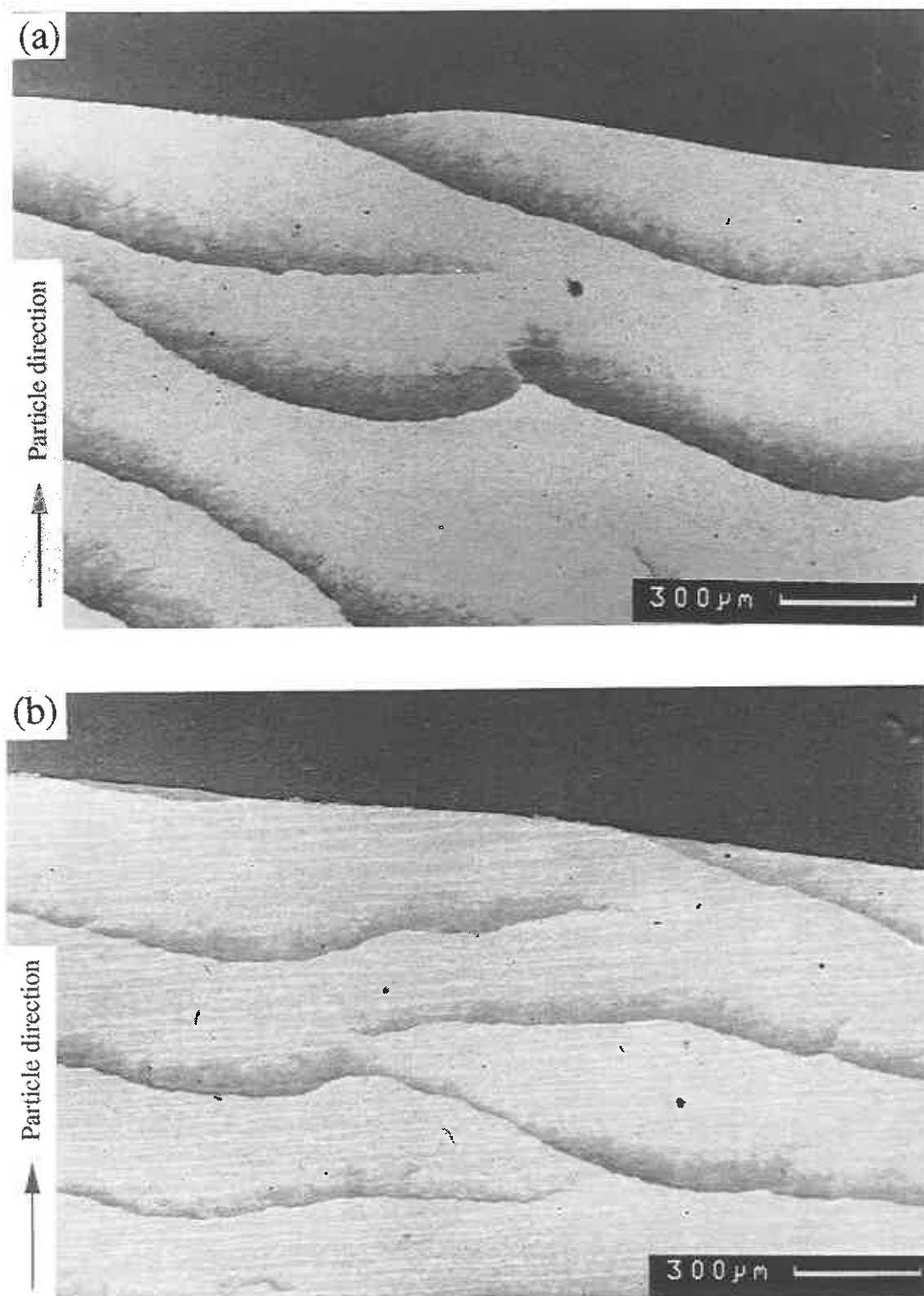


Fig. 7.25. SEM backscattered electron micrographs of (a) 500/300° C specimen and (b) 400° C isothermal specimen wear scar at low impact angle and high velocity.

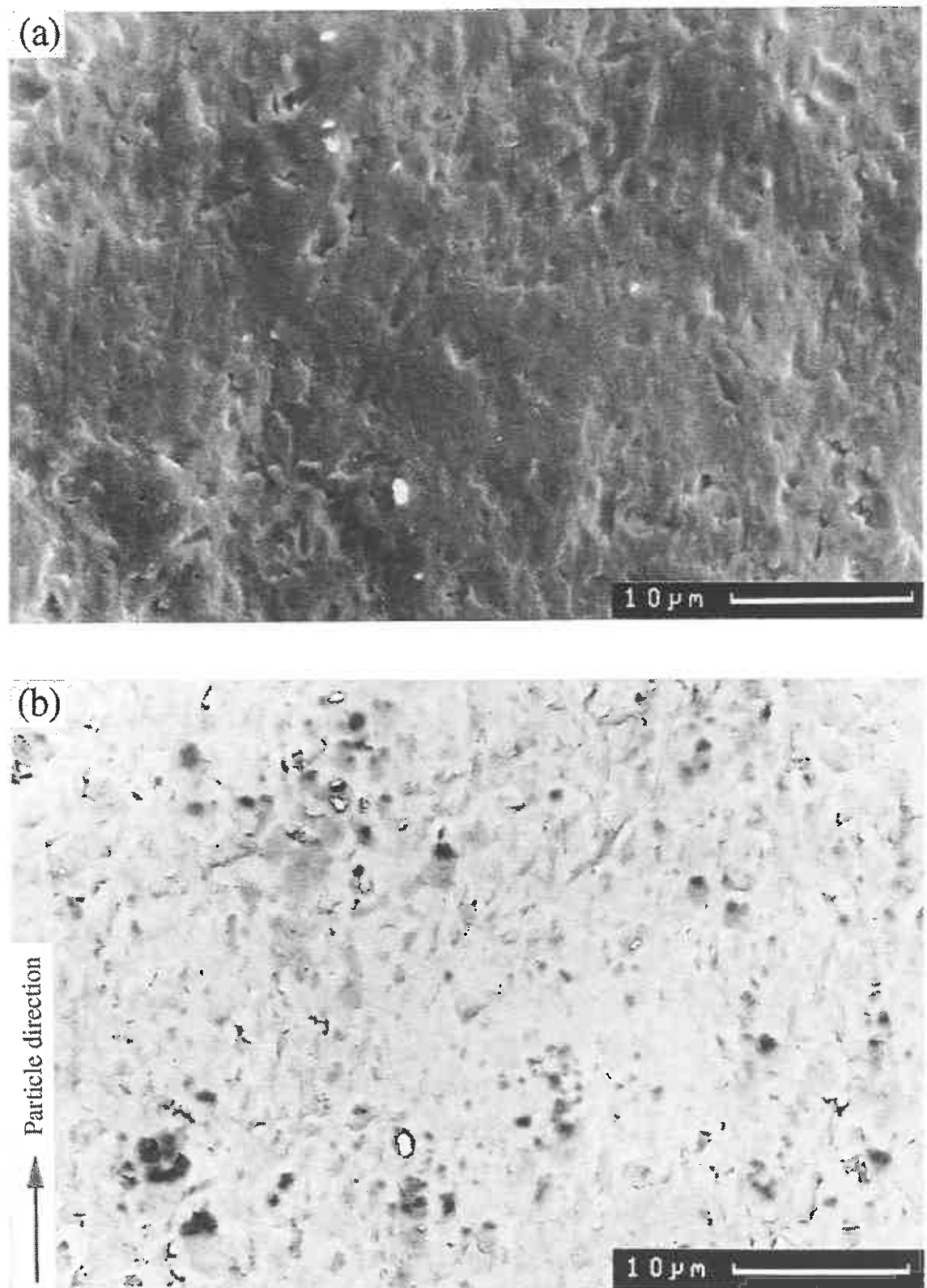


Fig. 7.26. (a) SEM secondary electron and (b) backscattered electron micrograph of the wear scar of mild steel exposed at 500/140° C at high impact velocity.

7.4.3. Wastage - temperature behaviour

Fig. 7.15. shows the wastage of the interrupted cooled specimens at the impact velocities 2.1 and 1.7 m s⁻¹. Assuming the measurements of the wear scar temperatures were accurate then the wastage values of the cooled specimens agree with the wastage of an isothermal specimen at the same metal temperature. As indicated by the wastage against velocity graphs, it seems clear that the cooled specimens showed the bell shaped wastage-temperature behaviour with the 500/380° C and 500/300° C specimens on the high temperature side showing a decrease in wastage with increasing metal temperature, whereas the 500/150° C specimen was on the low temperature side and showed an increase in wastage with increasing metal temperature. The 500/210° C specimen appeared to be close to the maximum of the bell shaped curve as the wastage remained high despite changes in temperature along its length.

The results of calibration from previous tests at bed temperatures of 500°, 400° and 300° C are shown in figures 7.16 to 7.18. Despite the presence of incubation errors on all these measurements the results also showed a fair agreement between the wastage of the cooled specimens and the isothermal specimens at the same metal temperature. The water cooling of the 500/185° C specimen (325° C at 2.1 m s⁻¹) was less stable than the later 500/150 tests which might partly explain its particularly low wastage and, with only one exposure, it was difficult to determine if the wastage was representative.

7.4.3.1. *The effect of cooling on the fluidized bed*

Cooling seemed to effect the wastage behaviour of the bed. With increased cooling the temperature of the bed furnace needed to be increased in order for the bed temperature to be constant near the specimens. This gave rise to a temperature gradient in the bed, with the top of the bed hotter than the temperature close to the specimens and this temperature gradient increased as the cooling increased. Fig. 7.27 shows the wastage rates of the uncooled stainless steel specimens of the interrupted cooled tests plotted against the furnace temperature required to maintain the bed temperature at 500° C close to the specimens. A slight reduction of wastage occurred with a large temperature gradient in the bed, perhaps because the overall density of the bed was reduced.

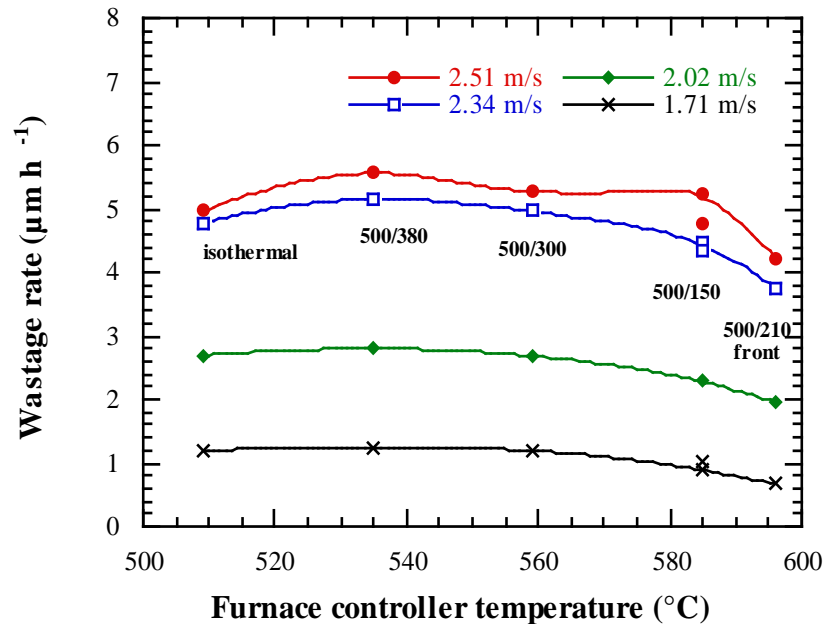


Fig. 7.27. Variation of wastage rate of the uncooled 316 stainless steel specimens against the fluidized bed furnace controller temperature required to maintain a bed temperature of 500° C close to the specimens.

Taking the effect of cooling on the wastage potential of the bed into account, the relative wastage of the coolest specimens would be increased slightly. For the interrupted tests the wastage at lower metal temperatures would be slightly higher than the isothermal wastage rate but, for the tests conducted at 400° C bed temperature, the wastage rate would be closer to the isothermal wastage rate.

7.4.3.2. Alumina embedment

Embedment of fragments from alumina particles seems to be an important part of the erosion-oxidation process. In some places the deposit layer probably formed initially as a transient effect, and then was subsequently worn through and removed leaving small islands topped with alumina deposit. On other specimens and temperatures the embedment layer formed and remained a permanent feature on the wear scar with little or no associated wear.

The cooled specimens, particularly at low metal temperatures, had little or no areas of the wear scar covered in protective alumina deposit. The most striking example was the specimen cooled to around 200° C (115° C back) at 300° C bed temperature, which

was free of alumina deposit unlike the isothermal 200° C specimen.

A possible explanation for this behaviour was the change in the particle 'brittleness' in the fluidized bed at different bed temperatures. Observations during the tests suggested that the particle attrition at 200° C was greater than at higher temperatures as a larger amount of particle fines were observed at the top of the bed. Therefore, at lower bed temperatures, there was probably a higher amount of particle fines in the bed and during impact, particle fragmentation occurred more readily, both of which effects may have encouraged the formation of an alumina deposit.

The wastage of the 300/115° C specimen was very similar to the wastage of the 200° C isothermal specimen and was much lower than the maximum wastage observed at higher temperatures (Fig. 7.18). Therefore, the cause of decreased wastage at low temperatures may not be due to the formation of a protective alumina layer but rather that the alumina layer formed because the wastage rate was low and assuming other conditions were suitable for the deposit to form.

In most cases the alumina deposit formed in regions where the wastage rate was inherently low, such as at the low velocity end of the specimen. Also it seemed that the tube specimens were more likely to have alumina embedment at their low velocity end than the bar specimens tested in previous studies. This may have been due to the presence of the larger diameter adapters effecting the particle flow over the specimen at low velocities.

Zhang *et al.* (1996) reported that in the Berkeley erosion-corrosion fluidized bed test rig a cooled specimen at 190° C had about five times the wear of a isothermal 200° C specimen because of the reduction in silica bed particle deposition. Their specimens were exposed to a much more aggressive environment and particle attrition and deposition played a more important role in influencing wastage. For example, Fig. 4.14 showed that during high dust conditions the wastage was reduced to zero at intermediate temperatures due to the formation of a bed particle deposit. This highlighted the fact that the conditions for particle deposition are complex and not well understood. In the current tests the alumina deposit formed on most of the isothermal specimens and did not form on the cooled tube specimens at low metal temperatures which also experienced a low wastage. This also indicated that the conditions required for the formation of deposit were more complex than the reasons suggested, i.e. a low bed temperature and regions of low wear.

7.4.4. Origin of temperature increase over the wear scar

It seems likely that the temperature gradient between the bed particles and the specimen extended part way into the bed, and the local temperature gradient over the wear scar would be much steeper than over the front or back as hot bed particles were continually replaced over the wear scar. At the front and back of the specimen particles were replaced less frequently and thus would be cooled, extending the temperature gradient further into the bed of particles.

If the temperature gradient over the wear scar was particularly steep, then this may increase the errors involved in measuring the temperature by using an external thermocouple. If the thermocouple was measuring the temperature above the specimen then the temperature difference between the surface and the measured value would be greater than at the back of the specimen where the temperature gradient was lower. Despite this, increasing the size of the fused ends of the thermocouple to a relatively large 'ball' increased the temperature on the wear scar by no more than about 10° C. The temperature measurements were made at the back of the wear scar and it was likely that the temperature also varied across the width of the wear scar.

This work has highlighted a potential error in the temperature measurements made in previous experiments investigating erosion-oxidation in a temperature gradient. In the experiments by Wang *et al.* (1993a) the specimen temperature was measured below the surface of the specimen and, in experiments by Zhang *et al.* (1996) the specimen temperature was measured at the top of the specimen (equivalent to the back of the specimen in the 'Cambridge' rig). In both cases the temperature of the worn surface might be higher than that measured due to the contact of the hotter bed particles.

The same error may apply to temperature measurements of in-bed heat exchanger tubes in FBCs as in many of the published papers it was not clear how or where the tube temperature measurements were taken. As temperature of the bed in FBCs was typically 850° C, hotter than the bed temperature in the fluidized bed test rig, the metal surface temperature difference between areas of the tube in particle contact and unworn regions may well be larger than the difference measured in these experiments. This may partly explain why major differences between the wastage behaviour in FBCs and fluidized bed laboratory studies have been observed, although other factors such as the differences in particle size, impact variables, and corrosion environment are probably more important.

7.4.5. Summary

Despite some doubt about the accuracy of the wear scar temperature measurements the wastage behaviour of the cooled mild steel specimens was similar to the isothermal specimens of the same metal temperature. This was contrary to earlier tests, where the back temperature was considered to be representative of the whole specimen. This was perhaps not so surprising as the only major difference was that for the cooled specimens the particle temperatures were hotter and so the mechanical behaviour of the particle may have changed a little. Otherwise the oxidation behaviour was governed by the surface metal temperature which was the same in both cases. The presence of a temperature gradient across the specimen has been shown to increase the oxidation rate of a metal by other studies (Griess *et al.*, 1978; Glover, 1980; Malik, 1990) but only in case of thick scales where ionic diffusion is the main transport mechanism. In this case the oxide was very thin and so the temperature drop across it would be minimal. The effect of cooling the specimens seemed to reduce the amount of alumina deposit on the specimens, particularly at low metal temperatures but this did not seem to effect the maximum wastage rate.

7.5. Conclusions

Mild steel specimens were exposed in the fluidized bed test rig and cooled relative to the temperature of the fluidized bed. The temperature difference between the cooled specimen and bed temperature was increased from an earlier study by increasing the furnace insulation, preheating the fluidizing air and using water to cool the specimens.

The temperature measurements were initially taken at the back of the specimen, but it was later discovered that the temperature of the wear scar was significantly hotter than this due to the flow of hotter bed particles over the wear scar.

The wastage against temperature behaviour of cooled specimens appeared to be similar to the isothermal specimens at the same metal temperature, in that the wastage values were similar in value and that a bell shaped curve behaviour was observed.

The position of the bell shaped curve also agreed with isothermal tests, however it is unclear how accurate the wear scar temperature measurements were as wear scar oxide colours perhaps indicated slightly cooler metal temperatures. This was complicated

due to the time interval after the completion of a test when the rotor was removed from the fluidized bed which meant that the wear scar appearance might not be the same as the equilibrium oxide formed during erosion-oxidation.

Bed particle deposition occurred on many specimens, particularly at low temperatures, although the cooled specimens at low metal temperature were free of deposit. Although the deposit on the 200° C isothermal specimen protected most of the wear scar the narrow region of wear close to the specimen's trailing wasted at a similar rate to the maximum wastage of a cooled specimen at the same metal temperature.

Chapter 8

Short term oxidation

8.1. Introduction

In an attempt to understand the erosion-oxidation mechanisms that occur in the fluidized bed test rig, experimental results must be compared to predictions of simple erosion-oxidation models. In order to achieve this, the models need to have data that is applicable to the erosion-oxidation environment. The synergistic nature of erosion-corrosion makes obtaining suitable data for erosion-oxidation models very difficult as some studies have shown the presence of erosion may enhance the oxidation rate of an alloy. However, some experiments were conducted to obtain more applicable data, the most important of which was oxidation kinetics.

Most of the erosion-oxidation models proposed to date have used parabolic oxidation kinetics mainly for mathematical simplicity. Parabolic rate constants are usually calculated from thermogravimetric data measured over several hours and thus do not compare to the time intervals between particle impacts in the fluidized bed test rig which are typically an order of seconds. To obtain temperature dependent kinetic data over a more appropriate time scale an accurate thermogravimetric analyser was used.

8.2. Experimental methods

8.2.1. Experimental procedure

Short term oxidation studies were carried out on a Perkin Elmer Series 7 Thermogravimetric analyser (TGA) with an balance accuracy of 0.1 μg and a furnace capable of reaching 1000° C. To use the high accuracy range of the balance samples were required to be less than 130 mg, so a typical sample was approximately 5 x 7 x 0.2 mm with a surface area between 0.5 and 1.0 cm^2 . Samples were cut from 1 mm cross sections of the bar stock and then thinned by wet grinding on SiC grit paper and polished with diamond paste to a surface finish of 1 μm on all surfaces. Before

preparation a 1.2 mm diameter hole was drilled into the top of the specimen to allow it to be hung from a silica hook within the TGA (Fig. 8.1).

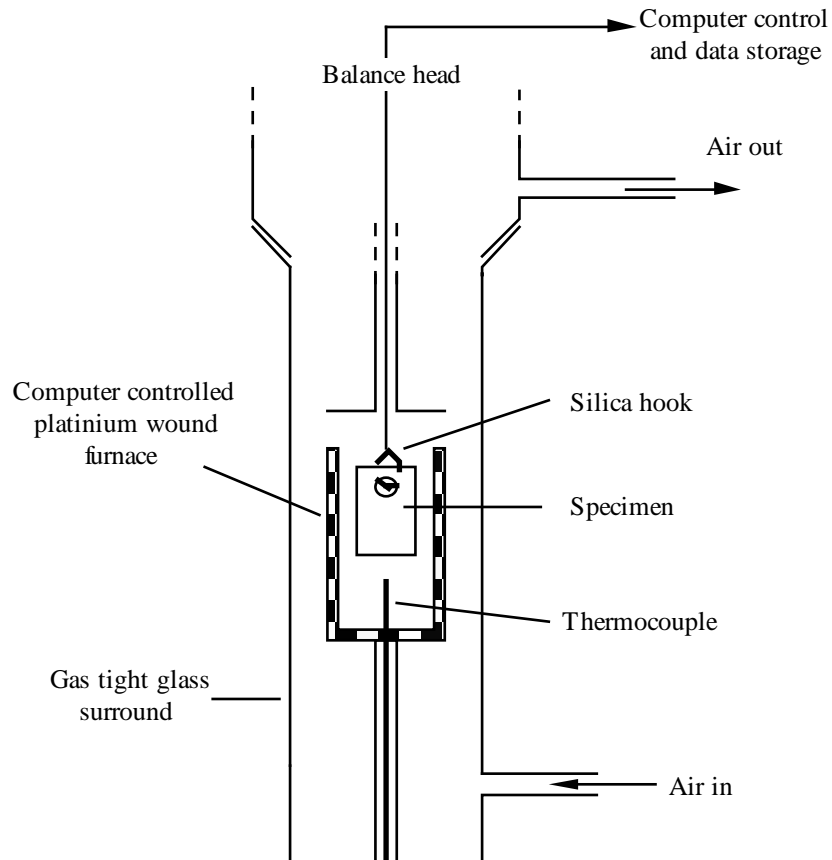


Fig. 8.1. The specimen arrangement in the Perkin Elmer Series 7 Thermogravimetric analyser (TGA).

Tests were conducted in air, started at room temperature and ramped to the desired test temperature at $200^{\circ}\text{C min}^{-1}$ (the maximum rate), and then held at the test temperature for the test duration. One thousand data readings were taken for each test, so for a one hour test readings were taken every 3.8 s.

Tests of 1 h and 15 h duration were conducted on mild steel specimens over the range of temperatures 350° - 600°C . Similar tests were conducted on 1Cr, 2.25Cr - 1Mo, and 3Cr (722M24T) steels specimens at fewer temperatures.

The effect of surface preparation on mild steel was investigated in order to assess the effect of plastic deformation and cold work on the initial oxidation rate. 1 h tests on 1 and $6\ \mu\text{m}$ polished and 1200 ($6\ \mu\text{m}$), 400 ($25\ \mu\text{m}$), 180 ($60\ \mu\text{m}$) SiC grit finishes were compared with a specimen eroded with the fluidized bed particles at $2.5\ \text{m s}^{-1}$ using a

drop tube (section 9.2).

8.2.2. Analysis of data

8.2.2.1. *Errors and calibration of temperature ramp*

The ramp in furnace temperature, from room to test temperature, caused additional weight changes of the specimen other than that associated with oxidation. Although it was possible to heat the furnace and specimen up in an inert atmosphere, and then switch to air once the test temperature was reached, the experimental set-up made the timing of such a switch of gases imprecise. (The weight gain of a mild steel specimen was in fact greater in nitrogen or argon either due to the effect of low partial pressure of oxygen or to water vapour in the gas). The test arrangement also causes the initial oxide to form at a temperature lower than the test temperature, which may cause transient effects, and these effects are not discussed further.

The magnitude and behaviour of any weight changes associated with the ramp in temperature was initially investigated with platinum foil specimens. After an increase of weight over the first minute a general decrease in weight with time was observed as the temperature increased then, once the test temperature had been reached, the weight decreased more slowly to a constant value after about ten minutes (Fig. 8.2). The initial behaviour of the platinum specimens did not appear to replicate the initial behaviour of steel specimens which usually showed a sudden sharp drop in weight at the start of the test. A preoxidised steel specimen was oxidised and its weight gain against time is shown in Fig. 8.3. The specimen suddenly lost weight when the furnace was switched on and then gained a similar weight once the furnace had stopped ramping. This was probably due to interactions between the magnetic specimen and the electromagnetic field surrounding the furnace at a high furnace current. During an oxidation test the sudden increase in weight at reaching the test temperature was usually obscured by the weight gain caused by oxidation. These effects are shown schematically in Fig. 8.4.

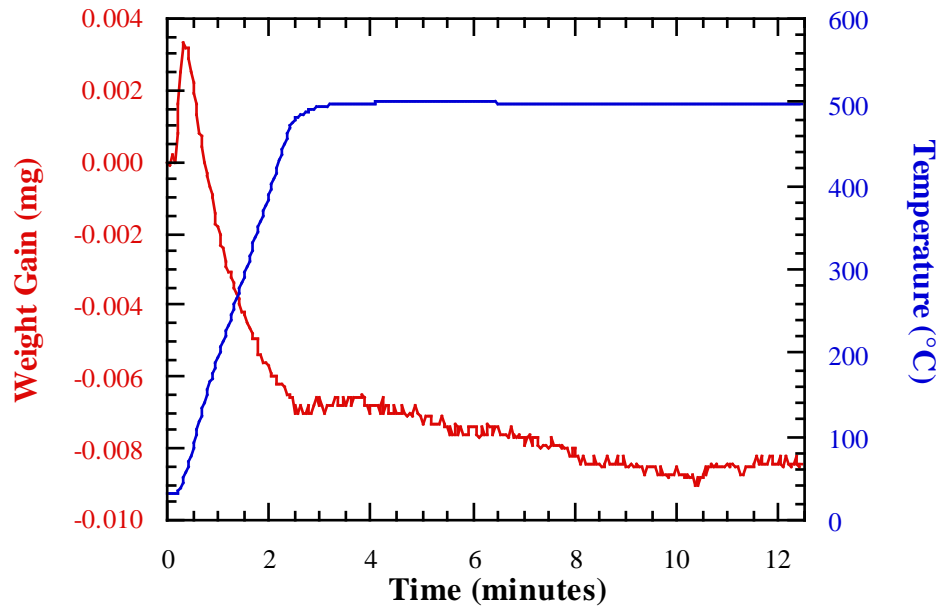


Fig. 8.2. The initial weight change of a platinum foil specimen heated to 500° C.

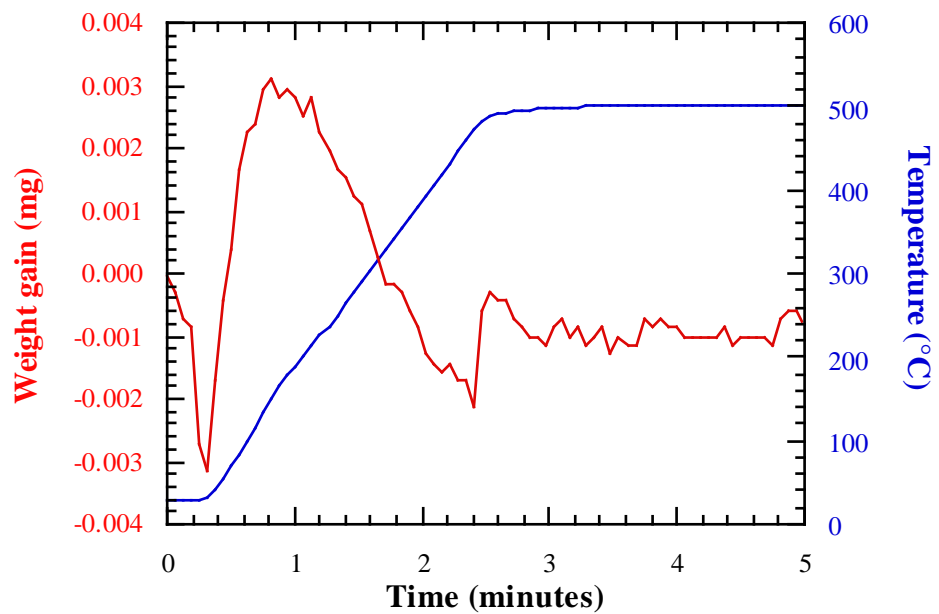


Fig. 8.3. Initial weight change of a preoxidised 2.25Cr - 1Mo steel specimen heated to 500° C.

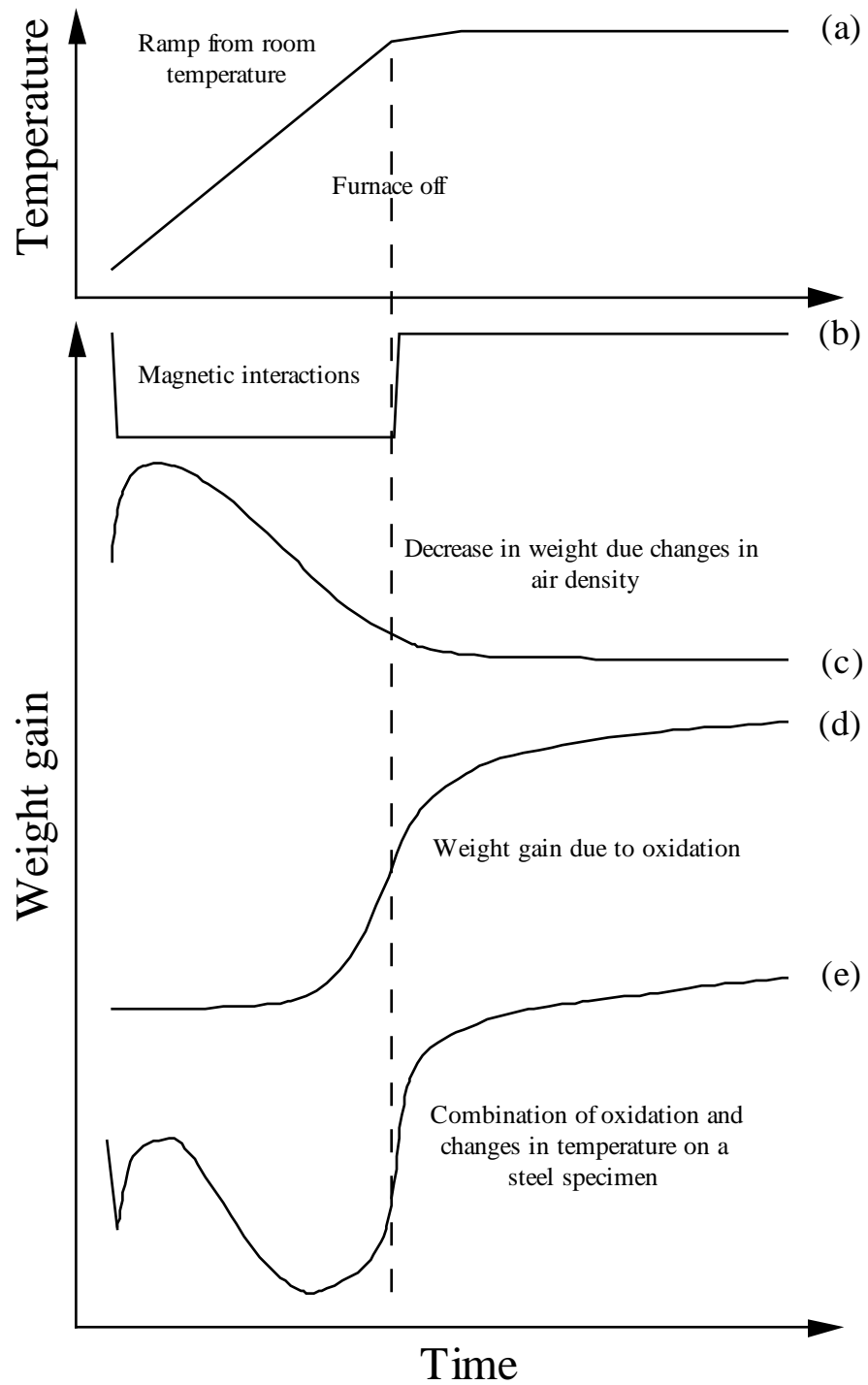


Fig. 8.4. Schematic diagram showing the effect of ramping the temperature on the weight of a test specimen; (a) temperature against time, (b) magnetic interactions, (c) air buoyancy, (d) oxidation and (e) as measured, i.e. (b) + (c) + (d).

To correct for the changes in weight associated with these two effects the data was adjusted by subtracting an approximation of the effects based on the initial weight changes. The magnitude of the increase in weight caused as the furnace switching off was approximated by the initial decrease in weight at the start of the test. The effect of the change in buoyancy was approximated by assuming a linear decrease in weight with time during the temperature ramp and then a gradual decay to a constant weight afterwards. The rate of weight loss with time was estimated from the initial part of curve where the weight started to decrease. These corrections on a sample test are shown in Fig. 8.5.

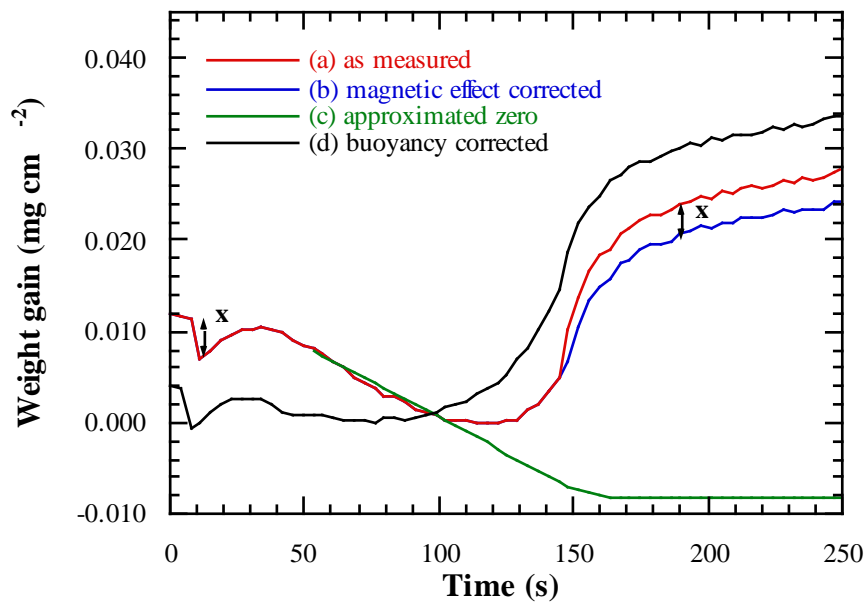


Fig. 8.5. Correction of weight gain data for a mild steel specimen heated to 500° C; (a) as measured, (b) removal of the magnetic interaction, x, (c) the approximation of the weight loss due to the buoyancy effect based on the initial weight loss and (d) the buoyancy correction applied to b.

8.2.2.2. Calculation of rate constants

For parabolic oxidation the weight gain, W , can be expressed as a function of time, t , as:

$$W^2 = K_p t + C \quad (8.1)$$

where K_p is the parabolic rate constant and C is a constant. In order to calculate the rate constant from equation 8.1 the constant, C , is assumed to be zero, as $W = 0$ at $t = 0$, and the K_p is assumed to be constant with time.

Differentiating equation 8.1 gives:

$$K_p = 2W \frac{dW}{dt} \quad (8.2)$$

This removes the zero constant and an apparent parabolic rate constant can be calculated at any point in time. A rate constant can be calculated even if the oxidation behaviour does not follow the parabolic oxidation kinetics.

8.3. Results

8.3.1. Effect of temperature

Fig. 8.6 shows the weight gain against time for 1 h tests on mild steel, while Fig. 8.7 shows longer term tests over 15 h. The data over 1 h was corrected for buoyancy and magnetic effects as described in 8.2.2.1 while the sampling rate over 15 h was too infrequent to provide enough detail over the first few minutes for the data to be corrected.

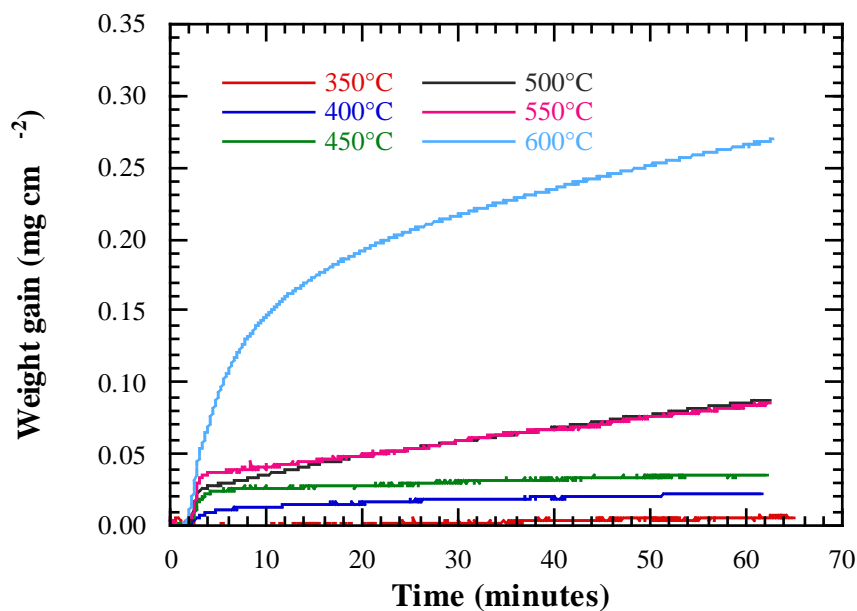


Fig. 8.6. The effect of temperature on the weight gain against time for mild steel with surface finish of 1 μm , corrected for buoyancy and magnetic effects.

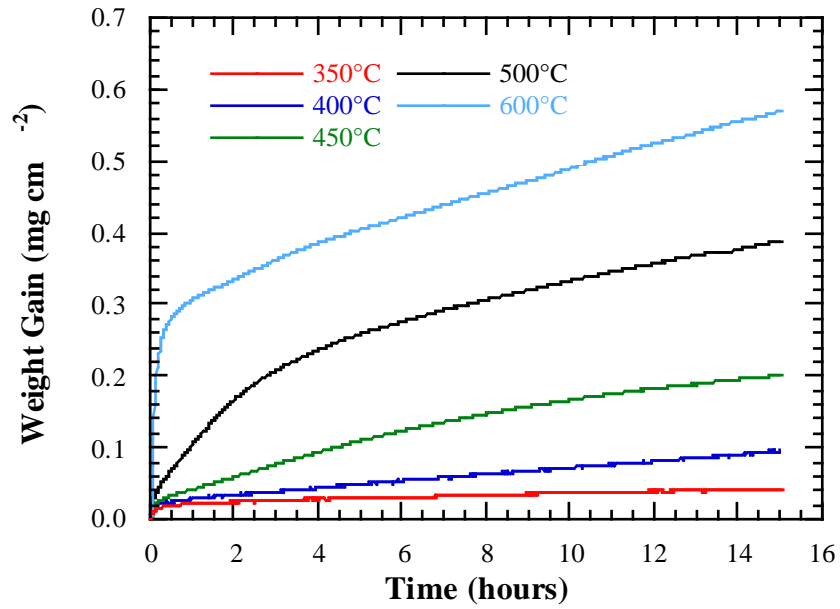


Fig. 8.7. The effect of temperature on the weight gain against time for mild steel with surface finish of 1 μm , uncorrected.

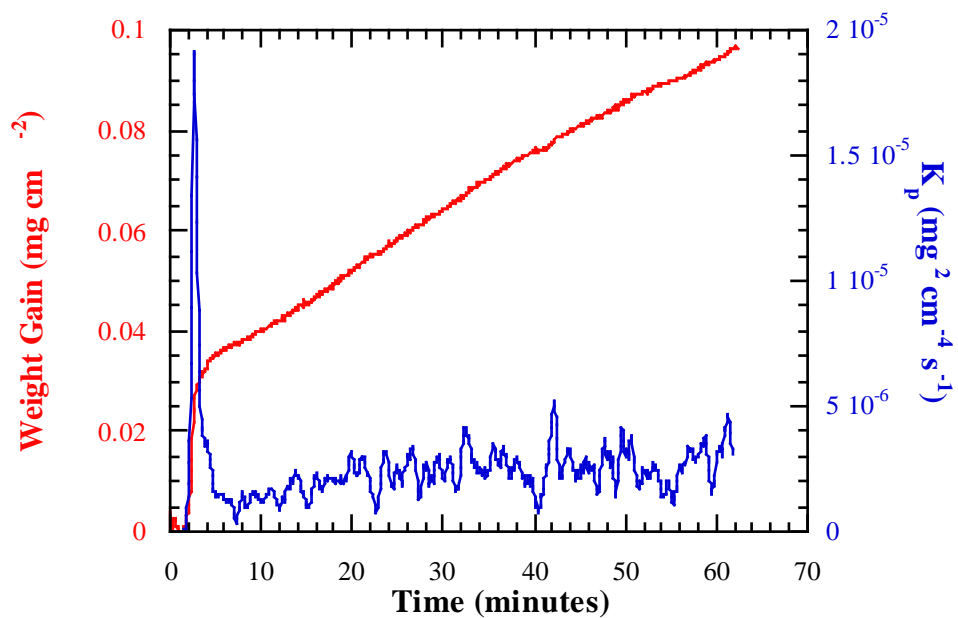


Fig. 8.8. Weight gain and smoothed parabolic rate constant against time for mild steel at 500° C for a 1 hour test.

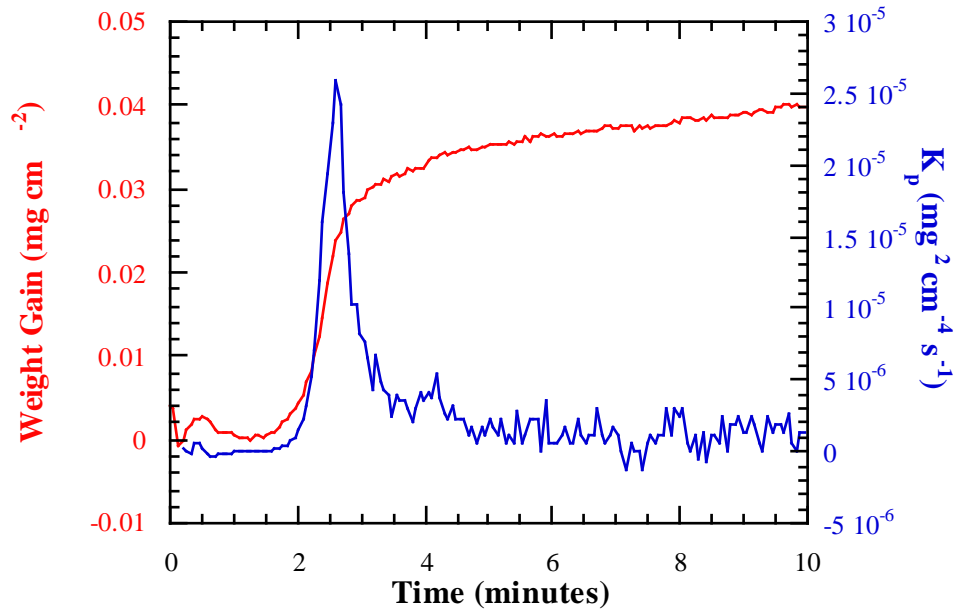


Fig. 8.9. Variation of weight gain and unsmoothed parabolic rate constant with time for mild steel at 500° C over the first 10 minutes of a 1 hour test.

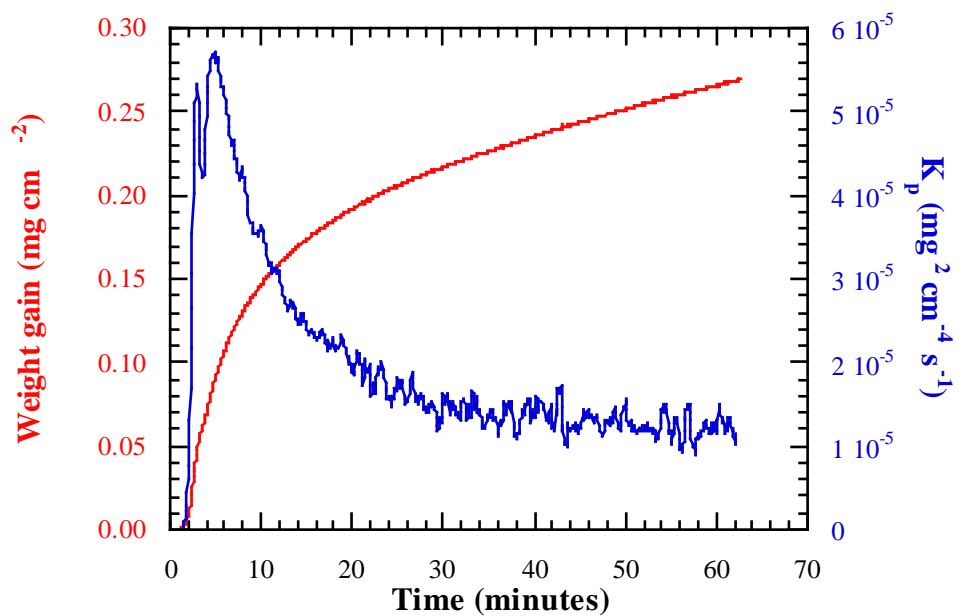


Fig. 8.10. Weight gain and smoothed parabolic rate constant against time for mild steel at 600° C for a 1 hour test.

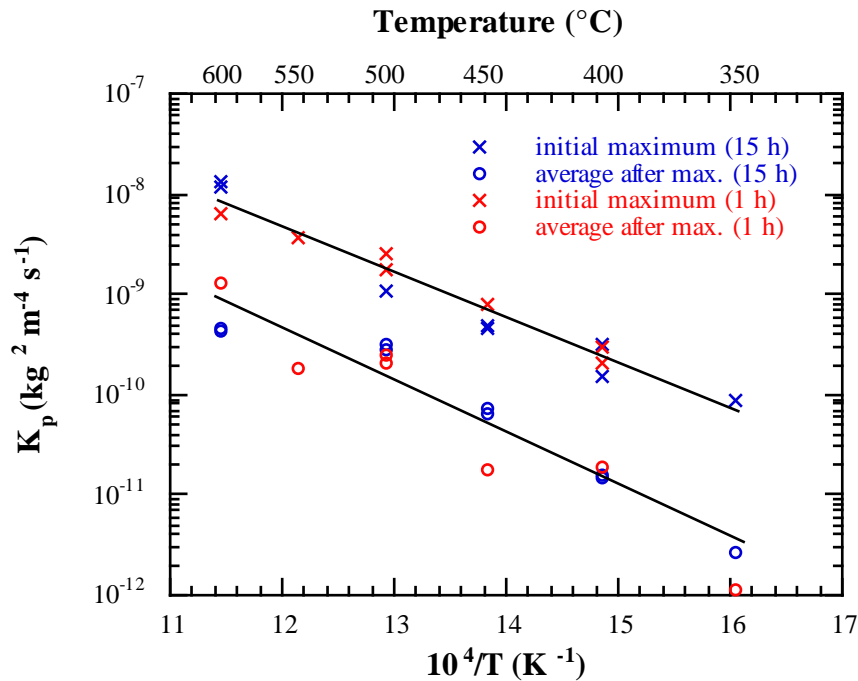


Fig. 8.11. Arrhenius plot for mild steel showing the initial maximum and average at later time for the corrected 1 h tests and the uncorrected 15 h tests.

The weight gain of mild steel increases with temperature, although the weight gain at 550° C over the first 1 h was similar to that at 500° C. The initial weight gain at 350° C was less than the changes caused by the temperature ramp, so any weight gain over the first 10 minutes, due to oxidation, was not determined.

Fig. 8.8 shows a plot of K_p and weight gain against time for mild steel at 500° C for a 1 h test. The rate constant increased rapidly to a peak as the temperature reached 500° C (at approximately 2.5 minutes) and then dropped to a value approximately an order of magnitude lower at longer time. The initial peak in rate constant is shown more clearly in Fig. 8.9 which shows the first 10 minutes of the test. A very narrow initial peak in the rate constant was observed at other temperatures except 600° C, and again the rate constant decreased to a value an order of magnitude less than the initial maximum. At 600° C the initial peak was observed but the rate constant remained high and decreased more slowly over about 20 minutes instead of about 1 minute for the lower temperatures (Fig. 8.10).

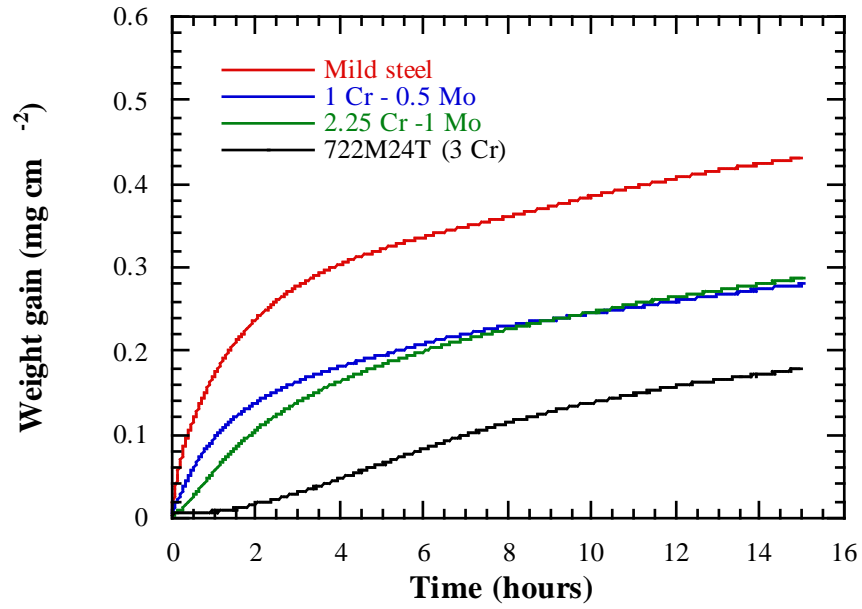
An Arrhenius plot of the initial maximum rate constant and the average rate constant at later time for both the 1 h and 15 h tests are shown in Fig. 8.11. The initial maximum rate constants from the 1 h tests were more accurate due to the higher sampling rate and the corrections made to the data for the temperature ramp. The average rate constant after the initial peak from the 15 h tests were more representative of a longer term behaviour. The activation energy for the initial and average sets of rate constants were approximately 81 and 93 kJ mol⁻¹ respectively.

The weight gain of the low alloy steels were less than that of mild steel at the same temperature. The weight gain against time over 15 h for the 3 steels at 500° and 600° C is shown in Fig. 8.12.

The initial weight gain of the low alloy steels over the first few minutes at 400° C and below was too low to be distinguished from the weight changes caused by the temperature ramp.

The weight gain of 722M24T at both 500° and 600° C showed a sigmoidal shaped curve with a small initial increase, a region of low weight gain then a increase in the rate of weight gain which reduced with time. At 500° C the weight gain over 1 h was very small and the initial weight gain was difficult to determine. The other low alloy steels also showed this sigmoidal behaviour but to much less of an extent. For example, Fig. 8.13a shows the weight gain and rate constant of 2.25Cr - 1Mo steel at 500° C over 1 h. After the initial weight gain and associate spike in rate constant, the rate constant dropped to a low value and then gradually increased. A test over 15 h showed that the rate constant reached a second maximum at around two hours and then slowly decreased over a number of hours (Fig. 8.13b, the first peak in the rate constant in not shown due to smoothing of the data). The time of the second maximum in rate constant decreased with a reduction in alloy content and an increase in temperature, so that 1Cr steel at 600° C behaved in the same way as mild steel and no second maximum was observed (Fig. 8.14).

(a)



(b)

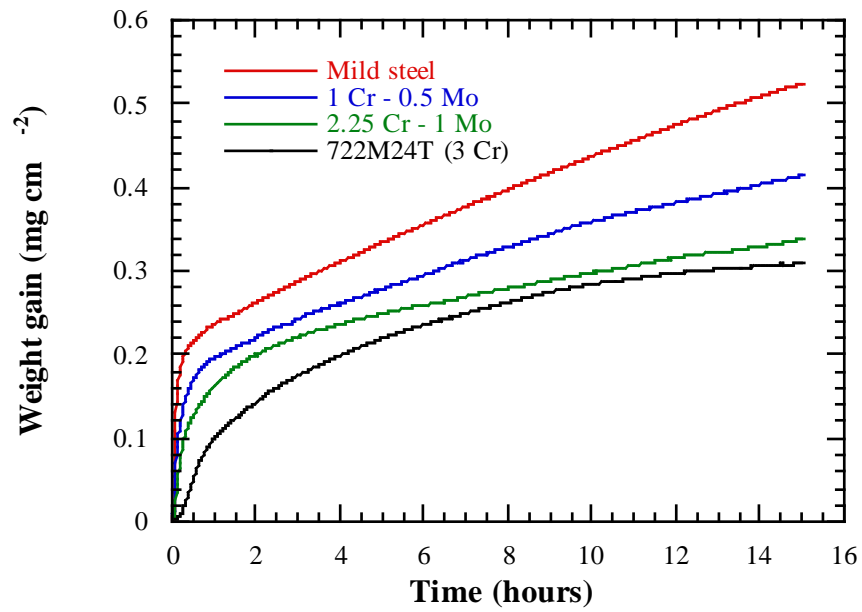
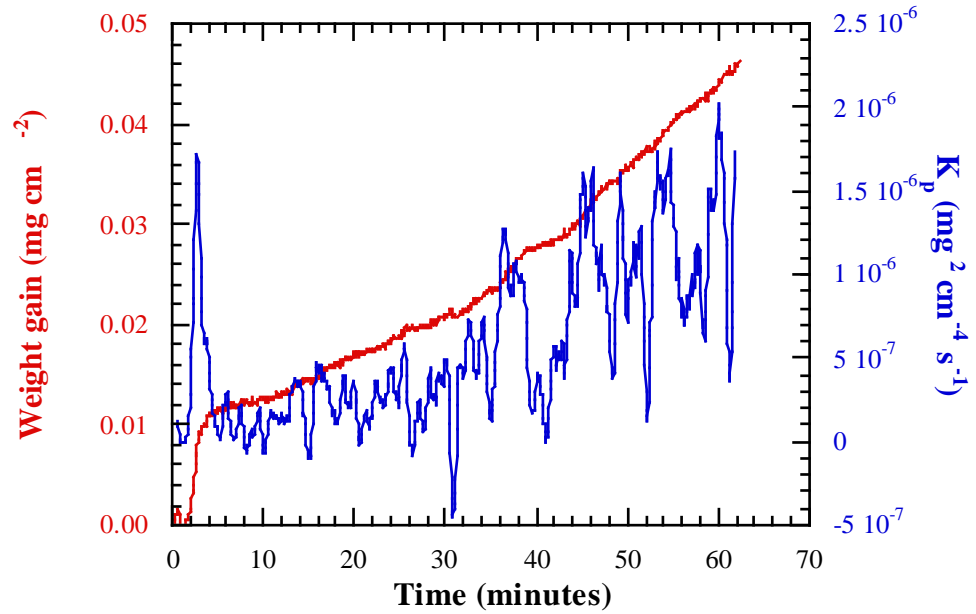


Fig. 8.12. Variation of weight gain with time for mild steel and three low alloy steels, (a) 500° C and (b) 600° C.

(a)



(b)

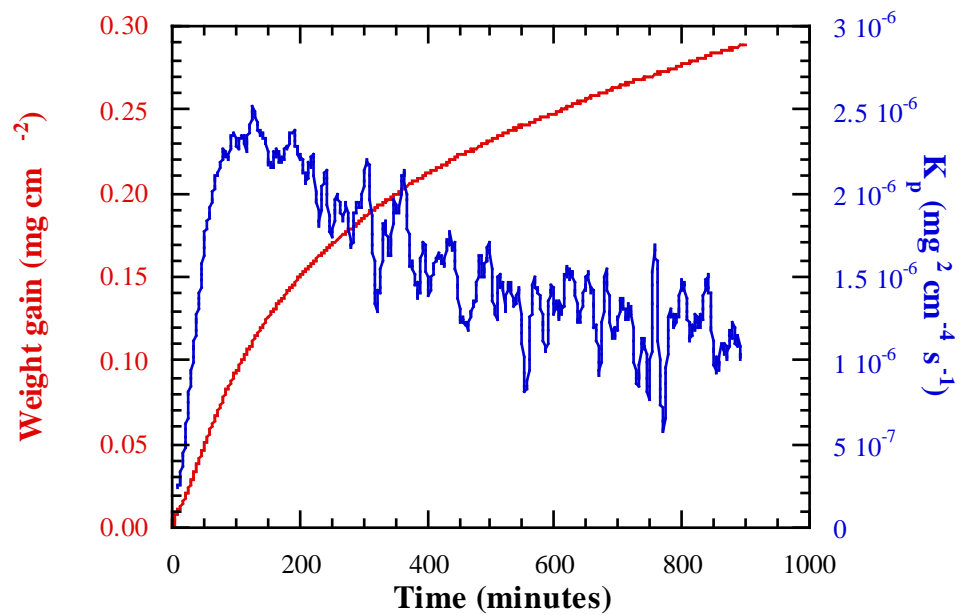
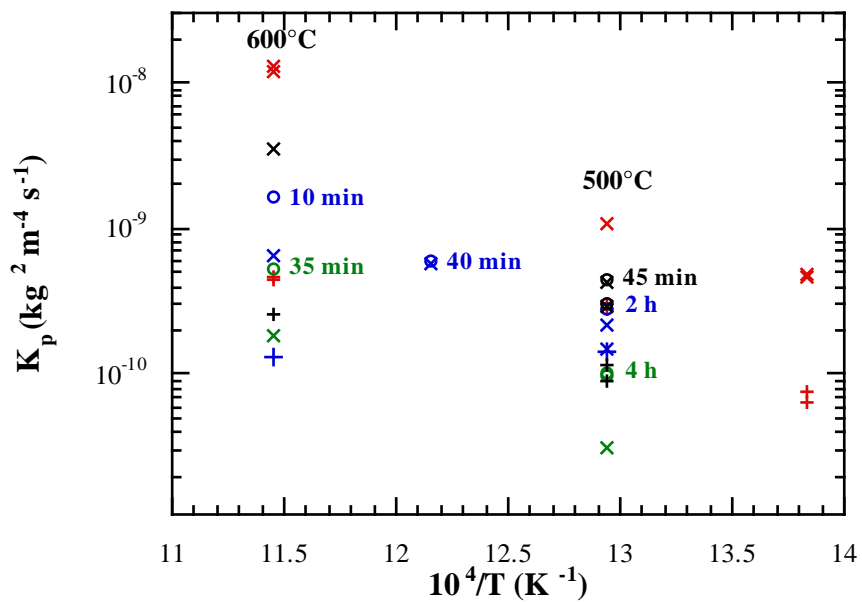


Fig. 8.13. Graphs of weight gain and apparent parabolic rate constant against time for 2.25Cr - 1Mo steel at 500°C over (a) 1 h and (b) 15 h.

An Arrhenius plot for the three low alloy steels and mild steel are shown in Fig. 8.14. Where applicable the time of the second maximum is given on the graph, and the rate constants have been calculated from uncorrected 15 h tests, except the 2.25Cr - 1Mo tests which include some corrected 1 h tests.



Key

	initial max (15 h)	2nd max (15 h)	average 4-15 h
Mild steel	x		+
1 Cr	x	o	+
2.25Cr - 1Mo	x (1 h)	o	+
722M24T	x	o	+

Fig. 8.14. Arrhenius plot of the low alloy steels compared to mild steel, showing the initial maximum rate constant, the second maximum and the time at the second maximum and the average rate constant between 4 and 15 h.

8.3.2. Effect of surface preparation

Fig. 8.15 shows the effect of surface finish on the oxidation behaviour of mild steel at 500° C. The initial weight gain of the diamond polished and SiC grit finishes was very similar, but after the initial rapid weight gain the polished finishes gained less weight than the grit finishes. A change in particle size of the SiC paper had very little effect on the weight gain whereas a difference was observed between 1 and 6 μm diamond paste, the 6 μm finish gained less weight just after the initial rapid weight gain. The change of rate constant with time of the 1 μm diamond surface finish was shown in Fig. 8.8 and the other surface finishes showed a very similar behaviour with time. As indicated by the weight gain against time curves there was no significant difference between the initial maximum rate constants for all of the specimens, and the average rate constant after the initial maximum for the grit finishes was higher than the two polished finishes (Fig. 8.16).

The higher weight gain of the grit finishes compared to the polished finishes was due to the higher degree of surface cold work. Caplan and Cohen (1966) showed that cold work increased the oxidation rate of iron as the larger number of dislocations prevented the formation of voids at the metal-oxide interface, although the difference in oxidation behaviour between different abraded surfaces was less than the difference between an abraded and annealed surface (Fig. 2.5). It is unclear why the 6 μm gained less weight than the 1 μm diamond finish as the 6 μm polish would have a higher cold worked surface, although as the difference arises in the first 15 minutes this may be due to differences in oxide nucleation.

The weight gain of an eroded specimen is shown, its weight gain was less than the other surface finishes. Fig. 8.17 shows a micrograph of the eroded surface using a backscattered electron detector. The surface was partially covered by embedded alumina particle fragments (darker regions), reducing the effective surface of the specimen. So the weight gain of the eroded surface cannot be compared directly the other surface finishes.

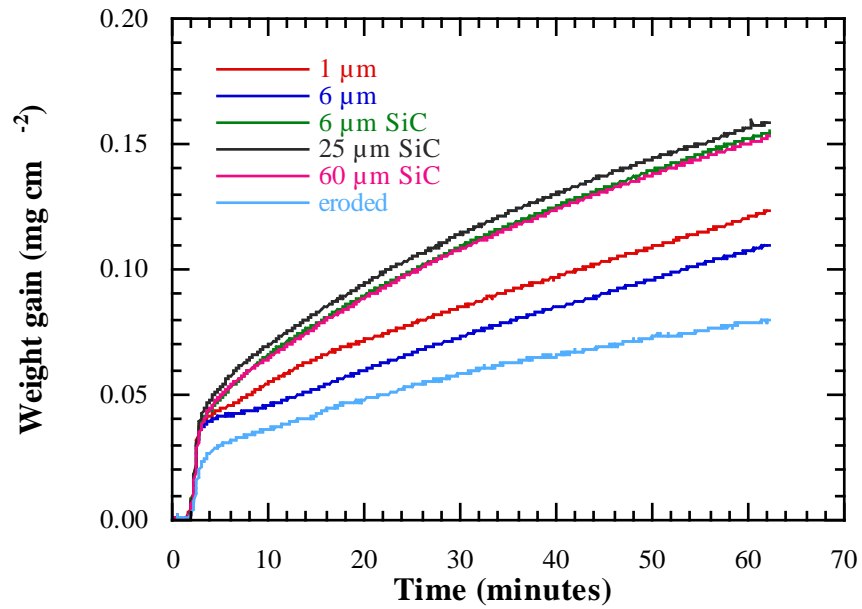


Fig. 8.15. The effect of surface finish on the oxidation behaviour of mild steel at 500° C. An average of two tests, corrected for buoyancy and magnetic effects.

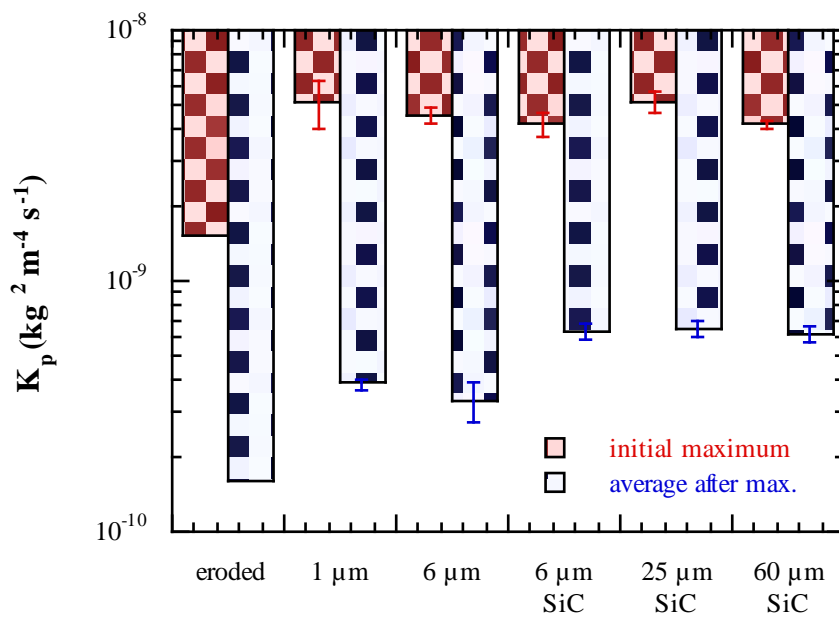


Fig. 8.16. Initial maximum and average after the initial maximum apparent rate constant for mild steel of various surface finishes.

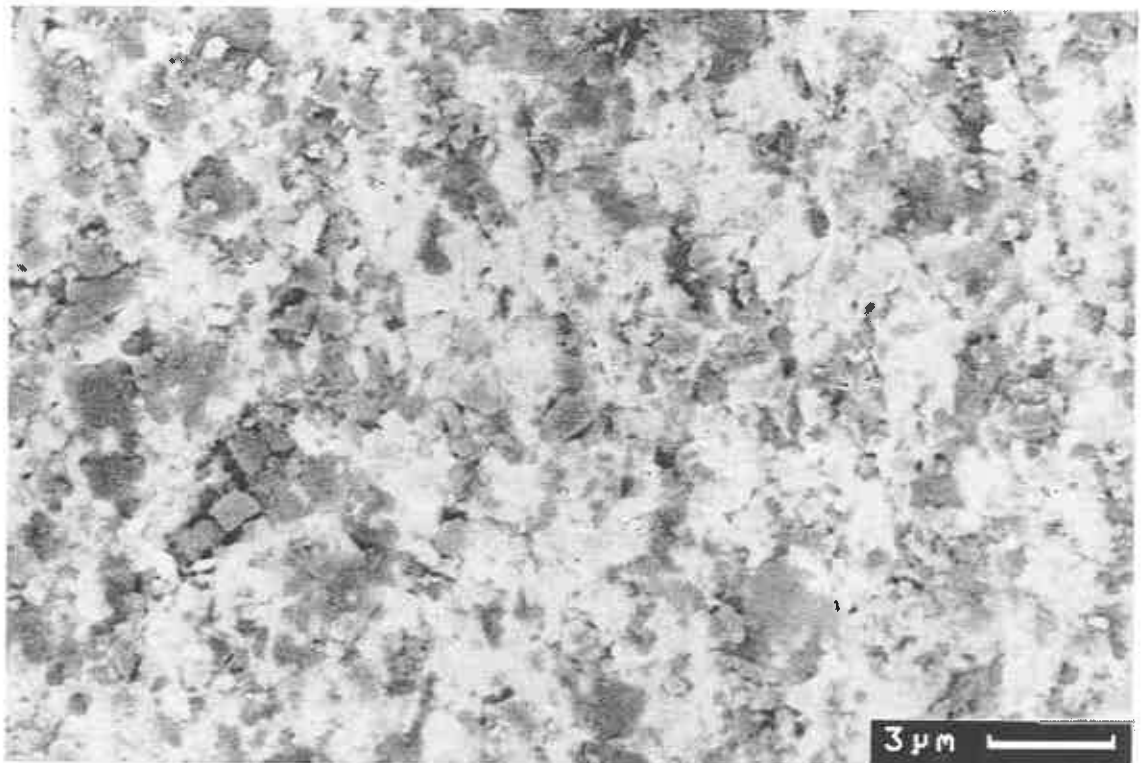


Fig. 8.17. SEM backscattered electron micrograph of the surface of the eroded specimen prior to oxidation.

8.4. Discussion

The effect of correcting the initial weight gain for the effect of buoyancy and magnetic effects did not have a great effect on the initial maximum rate constant. This is partly due to the two effects having approximately equal and opposite effect on the weight gain over the temperature range that could be accurately measured by the balance. At low temperatures where the initial weight gain was of the same magnitude as these effects the correction was too imprecise to accurately gauge the magnitude of the weight gain, due to oxidation, in the first few minutes.

Similar tests over 1 h at the same temperature gave significantly different weight gains. These errors were usually larger than the errors caused by ramping from room temperature. The largest differences tended to occur between tests conducted at different times, so where comparison was important the tests were conducted in a single batch. The furnace thermocouple was calibrated and the accuracy of the balance was cross checked with a static balance of similar accuracy. The systematic errors may have been due to position of the specimen in the furnace which may have been significant as the specimen was of comparable size to the furnace. It was difficult to maintain a consistent specimen arrangement between batches of tests as the TGA was used by many other users and the furnace height may have been adjusted by other users (the furnace was replaced twice, for instance) and it was difficult to view the specimen with the furnace raised. Other errors may have arisen due to slight differences in specimen preparation.

For mild steel the apparent parabolic rate constant over the first few minutes of oxidation was larger than that at later time, with the maximum typically an order of magnitude larger. The rate constant was an apparent parabolic rate constant as it is unlikely that the oxidation was obeying the parabolic rate law which was only usually the case when oxidation is limited by diffusion through an oxide scale. Initially the oxidation kinetics may have followed a logarithmic rate law during nucleation and early growth of a thin oxide film. A typical time in the fluidized bed test rig between successive particle impacts is of the order of several seconds so if it is assumed that the oxide is removed and regrown in that time then the initial oxidation is of relevance.

The values of the average rate constants of mild steel measured are very similar to values reported by Pinder (1977) and lower than rate constants reported for iron (e.g.

Païdassi, 1956) (Fig. 8.18). The activation energy calculated of around 90 kJ mol^{-1} is low when compared to reported values of around 150 kJ mol^{-1} . However, this tends to be for specimens reduced in hydrogen to remove the thin air grown oxide prior to the oxidation test. For iron not hydrogen reduced Païdassi (1956) measured an activation energy of 66 kJ mol^{-1} between $450^\circ - 600^\circ \text{ C}$. The effect of surface deformation introduced in surface preparation also has the effect of reducing the activation energy. This increases the oxidation rate generally while at higher temperatures annealing of the surface occurs more rapidly and reduces the work hardening with time so that the increase in temperature is reduced with temperature.

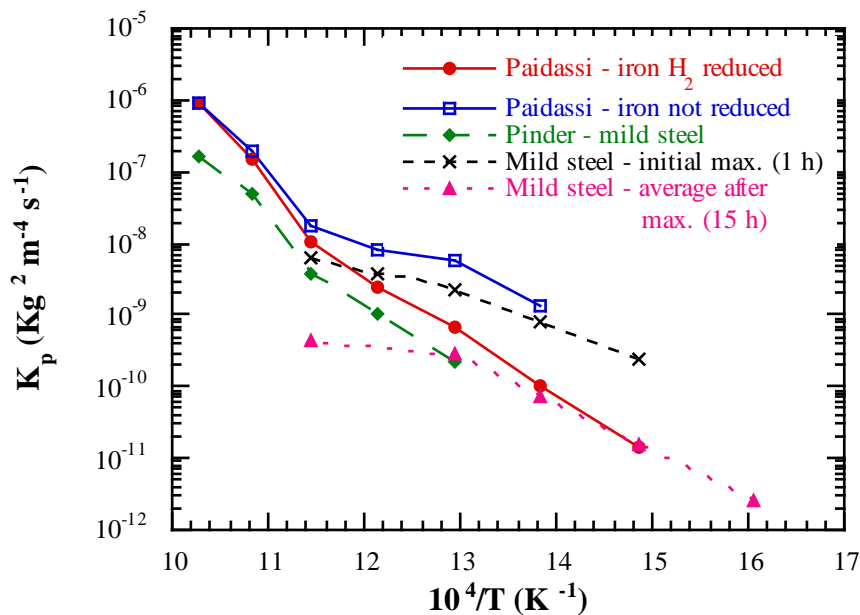


Fig. 8.18. Arrhenius plot comparing mild steel with reported rate constants for mild steel and iron.

It must be noted that due to the accuracy of the balance the oxidation kinetics were measured above 400° C , whilst erosion-oxidation of mild steel was studied over the temperature range $200^\circ - 600^\circ \text{ C}$. Thus, in order to model erosion-oxidation over this temperature range the oxidation kinetics need to be extrapolated to lower temperatures. This may result in errors in the rate constants at lower temperatures if the activation energy changes due to changes in the oxidation mechanism.

The low alloy steels also exhibited an increase in rate constant initially. However, as

shown by the sigmoidal shaped weight gain, the rate constant increased again reaching a maximum rate constant at a later time. An increase in chromium content and a decrease in temperature increased this time. The initial increase may be due to the formation of a rapidly grown chromium rich oxide which reduced the oxidation rate and was then overgrown by a faster growing iron rich oxide causing an increase in the oxidation at a longer time.

The effect of surface preparation on the oxidation behaviour of mild steel is of importance to erosion-oxidation processes as during steady state erosion the surface is continuously work hardened by impacting particles. No measurable difference of the oxidation rate over the first few minutes was observed between the polished and grit finishes, but this compared surfaces, work hardened to a different extent. Measuring the oxidation rate of rough polished specimens (where the surface was work hardened) rather than electropolished or annealed and reduced specimens was more relevant to the erosion-oxidation environment studied.

Several observations indicate that the oxidation kinetics of mild steel in the fluidized bed may be greater than those measured on specimens oxidised in air. The oxidation rates measured by Entwisle (1990) in the fluidized bed were higher than in a furnace and this was suggested to be caused by the interaction of particles with the surface. TEM observations of thin oxide films formed during erosion-oxidation have shown they consist of very fine grains which would enhance grain boundary diffusion and hence the oxidation rate (Kara *et al.*, 1996). Also during erosion-oxidation a freshly exposed area of metal over an impact crater is surrounded by oxide which is likely to increase the nucleation of new oxide.

These results are discussed further in Chapter Ten with reference to the results of simple erosion-oxidation models.

8.5. Conclusions

During static oxidation of mild steel the initial apparent parabolic rate constant was an order of magnitude larger than measured at a later time. For modelling erosion-oxidation in the fluidized bed test rig, where the time between successive impacts is typically several seconds, the higher initial rate constants are more applicable to the models which considered oxide removal with each impact.

Increasing the surface work hardening of mild steel increased the oxidation rate at longer time but caused no measurable difference over the initial period of rapid oxidation. This may be one of several factors that could increase the oxidation rate of mild steel in the fluidized bed when compared to the experimentally obtained oxidation kinetics.

Chapter 9

Erosion Studies

9.1. Introduction

In addition to the investigation of pure oxidation, erosion at low impact velocity was investigated using a drop tube apparatus, and short exposure, room temperature studies were carried out in the fluidized bed test rig. The aim of such experiments was to compare impact morphologies in the erosion-oxidation rig with pure erosion impacts and to measure, quantitatively, the particle flux in the erosion oxidation test rig.

9.2. Erosion drop tube experiments

9.2.1. Experimental methods

Fig. 9.1 shows the erosion drop tube apparatus used to impact specimens with particles at impact velocities comparable to those experienced in the fluidized bed test rig. The particle feeder consisted of a rotating drum which fed particles into a silica drop tube of 11.2 mm internal diameter. The tube length was 34 cm long which, for spherical alumina particles under free fall in a vacuum over this distance, produces a velocity of $\approx 2.6 \text{ m s}^{-1}$. If air resistance is considered the terminal velocity of the alumina particle is approximately 3 m s^{-1} (Weast, 1976-1977) and thus an impact velocity slightly less than 2.6 m s^{-1} was achieved.

The particle flow rate could be adjusted by changing the rotational speed of the drum and was set to a constant 5 g min^{-1} . The target was an approximately $7 \times 8 \text{ mm}$ section of mild steel cut from 1 inch bar stock and its surface was prepared to a $1 \mu\text{m}$ diamond polish finish. The specimen wear was measured by its weight change on a Sartorius electronic balance which had an accuracy of $0.1 \mu\text{g}$. The specimen area was limited by the size of the weighing pan on the electronic balance which was suspended from the balance head and caused any larger specimens to slide off.

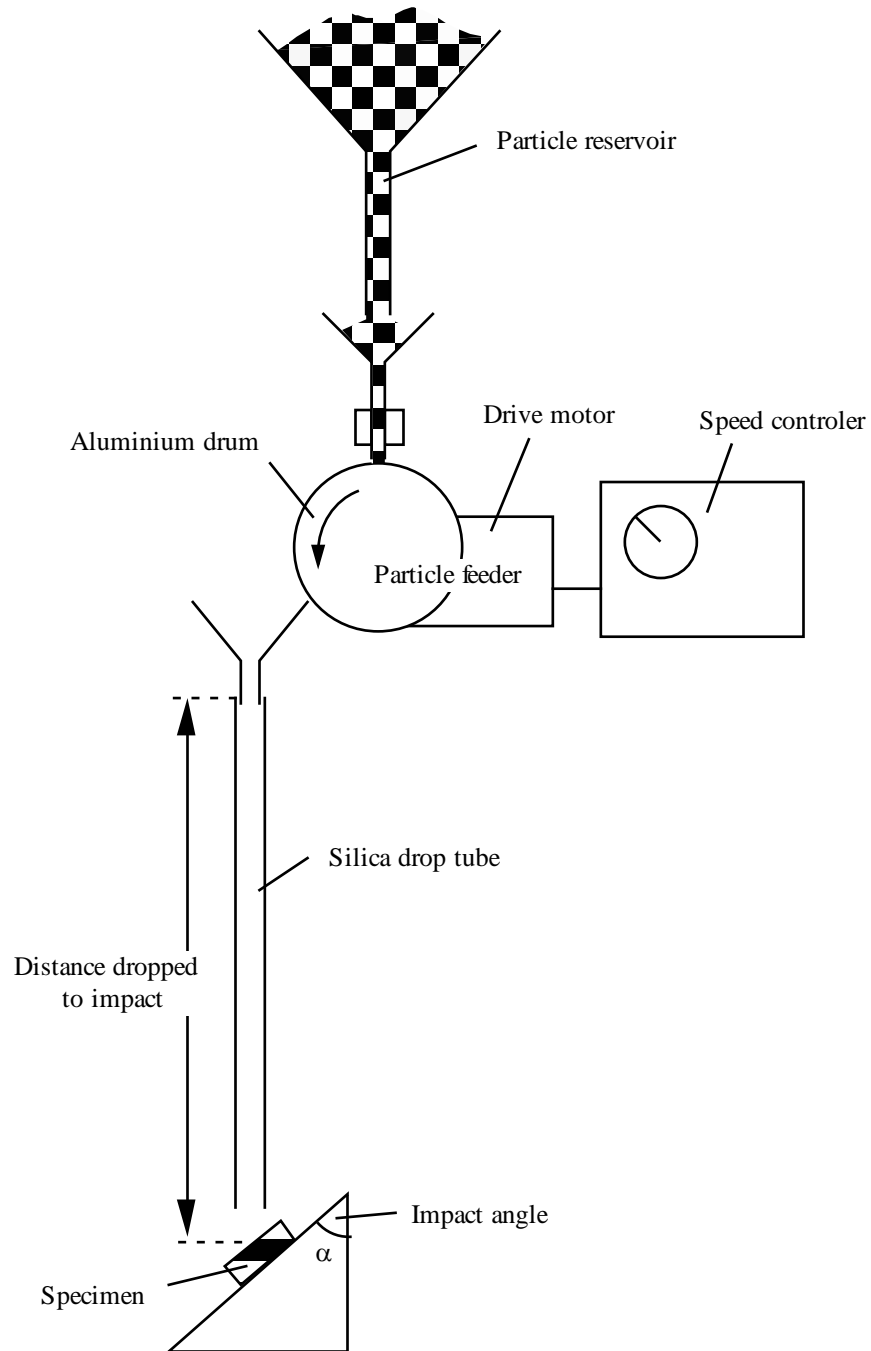


Fig. 9.1. Schematic diagram of the erosion drop tube apparatus.

This meant that the specimen was smaller than the area of the drop tube which was not ideal for quantitative measurements.

These results were compared with a similar flat specimen exposed in the fluidized bed test rig. The tests were conducted at 50° C rather than at room temperature which helped to fluidize the bed. The specimen was mounted on a cylindrical holder (Fig. 9.2) with high temperature wax and the holder was positioned on the rotor so that the

specimen was tilted at 30° to the horizontal. The specimen was positioned at the high velocity end of the holder and was exposed in the rig for 15 minutes at $250 \text{ revs min}^{-1}$ so that the particle impact velocity over the specimen was approximately 2.5 m s^{-1} .

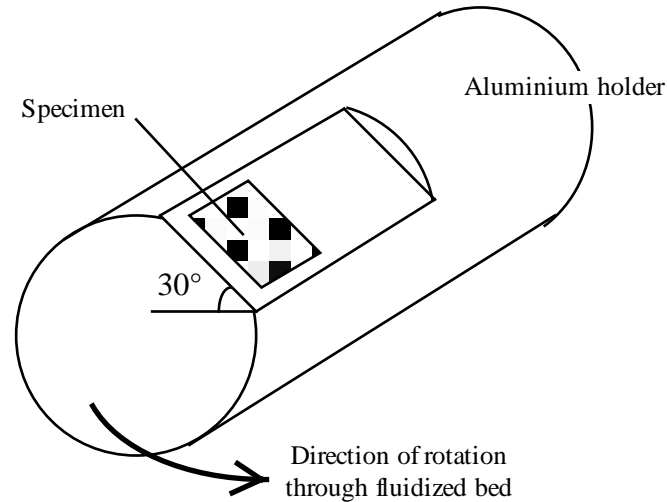


Fig. 9.2. Diagram of the specimen holder for the fluidized bed test rig.

9.2.2. Results and discussion

(i) Drop tube specimens

Fig. 9.3 shows the weight loss of mild steel against the weight of erodent for the impact angles, 30° , 45° and 60° . An initial incubation period was observed at all impact angles, during which time the specimen gained weight and this was followed by a constant mass loss rate. The incubation time period and the magnitude of the initial mass gain both increased with impact angle. The steady state erosion rates of the three impact angles were not significantly different and varied between 0.016 and $0.027 \mu\text{g g}^{-1}$.

A quantitative comparison of the wear rates of the specimens at different impact angles was difficult due to a number of factors; the drop tube specimen was smaller than the erosion footprint which would cause a systematic error at the different impact angles as the density of particles over the erosion footprint varied slightly. The particle flux also varied slightly with time due to wear of the funnel and changes in the speed of the motor. This was periodically corrected for by measuring the particle flow rate and then adjusting the speed of the rotating drum. Any change in flux would have caused a random error as the wear rate per weight of erodent decreased as the flux increased due to increased

particle-particle interactions.

Figs. 9.4 - 9.6 show SEM micrographs of the steady state surfaces of 30°, 45° and 60° specimens respectively. All the specimen surfaces consisted of a composite of deformed metal and alumina particle fragments. The alumina fragments are shown as dark areas on the backscattered electron micrographs. The percentage of alumina fragments increased with impact angle, and this correlated with the larger initial weight gain in the specimen at greater angles shown in Fig. 9.3.

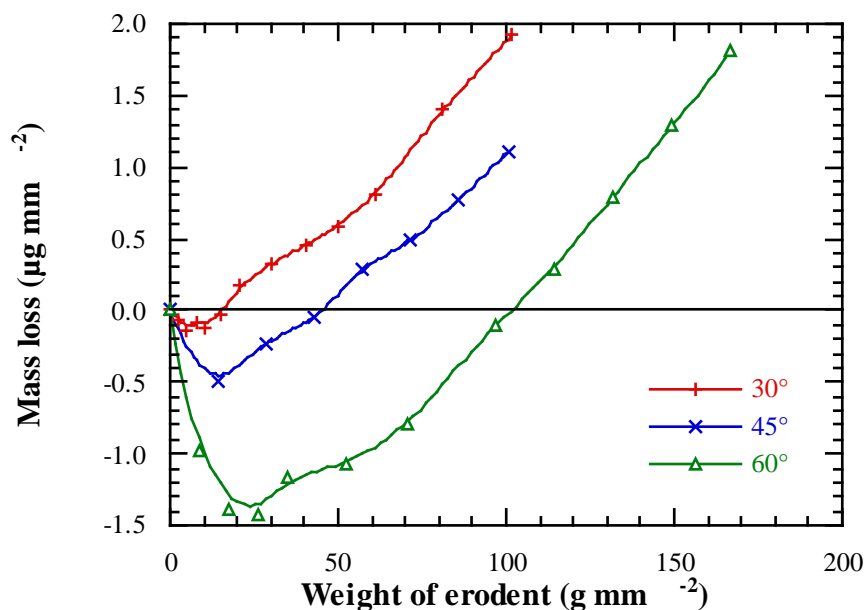


Fig. 9.3. Mass loss against weight of erodent for 80 mesh alumina impacting mild steel for impact angles of 30°, 45° and 60°.

Fig. 9.7 shows mild steel impacted with 100 g of alumina at an impact angle of 45° with individual impact craters of up to 3 µm in diameter. This was significantly smaller than the particle diameter of around 240 µm. Some impacts indented the surface while others ploughed into the surface causing significant plastic deformation and lip formation. The SEM backscattered image (Fig. 9.7b) shows a single particle fragment on the edge of an impact crater. Fig. 9.8 shows a higher magnification of a sample impacted with more particles. Several particle fragments, located with a backscattered electron detector, each about 1 µm across (marked with arrows) are shown embedded into the steel by subsequent impacts.

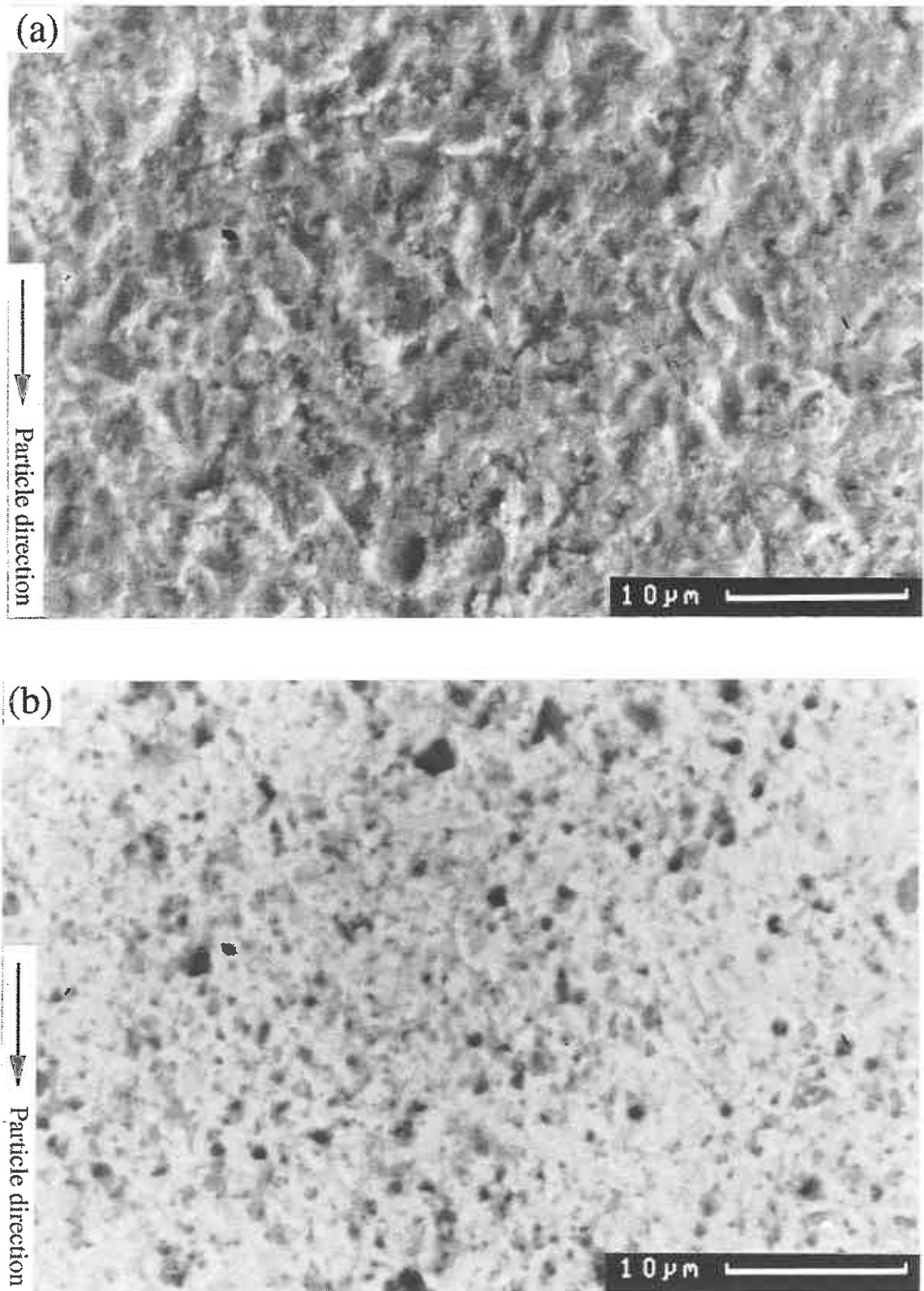


Fig. 9.4. (a) SEM secondary electron and (b) backscattered electron micrographs of the steady state eroded surface of mild steel impacted with 80 mesh alumina at 30° and around 2.5 m s^{-1} .

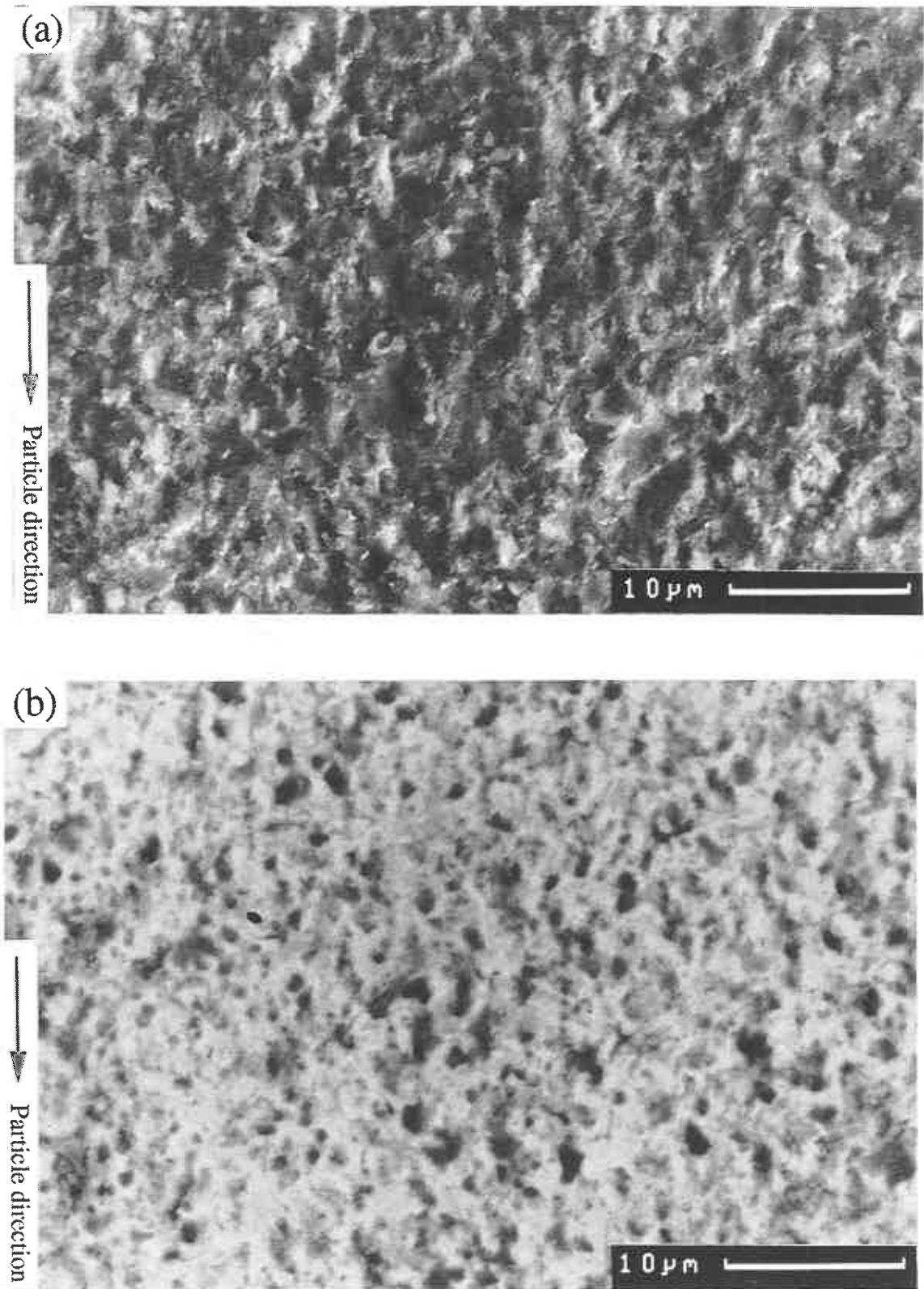


Fig. 9.5. (a) SEM secondary electron and (b) backscattered electron micrographs of the steady state eroded surface of mild steel impacted with 80 mesh alumina at 45° and around 2.5 m s^{-1} .

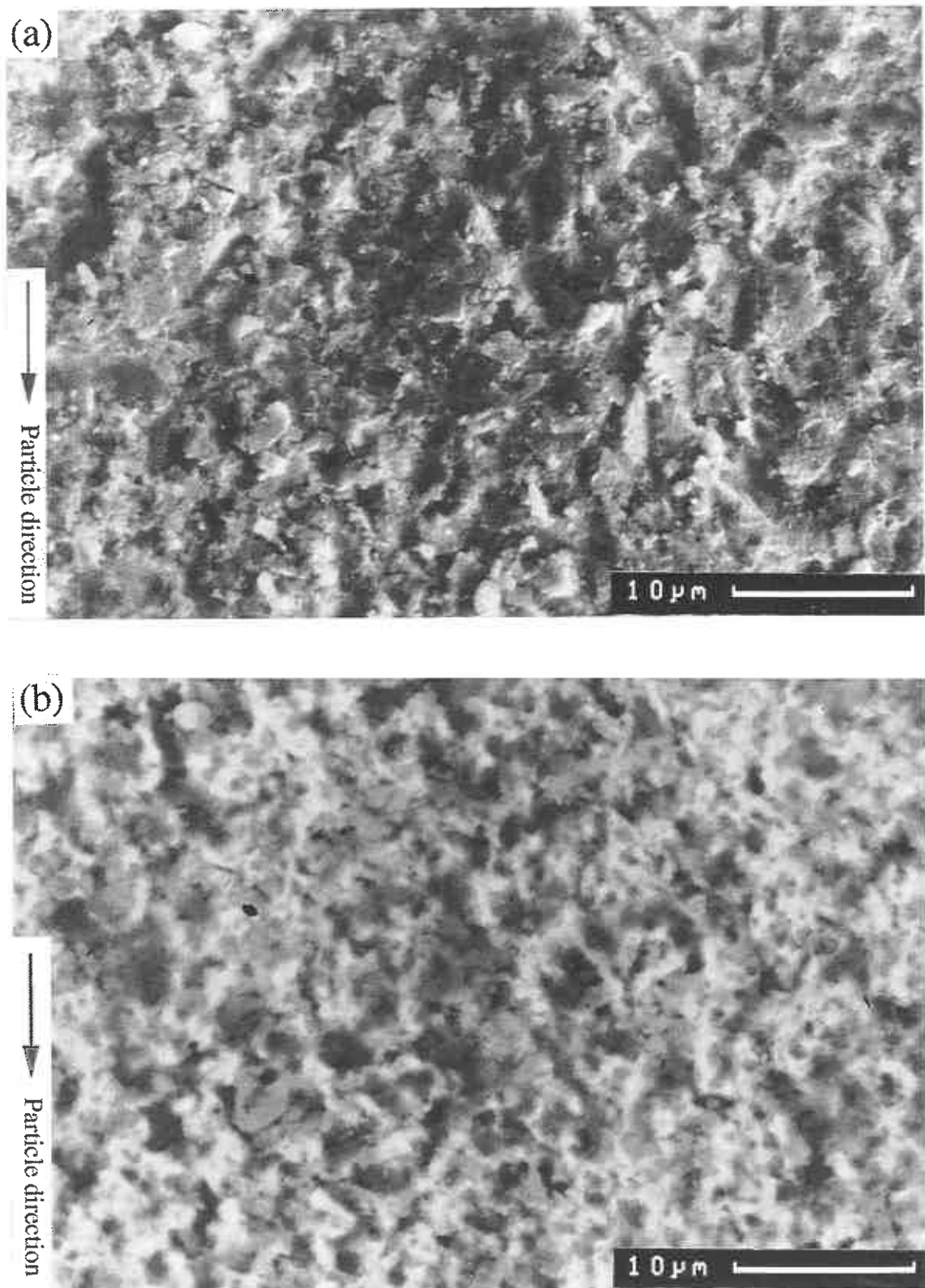


Fig. 9.6. (a) SEM secondary electron and (b) backscattered electron micrographs of the steady state eroded surface of mild steel impacted with 80 mesh alumina at 60° and around 2.5 m s^{-1} .

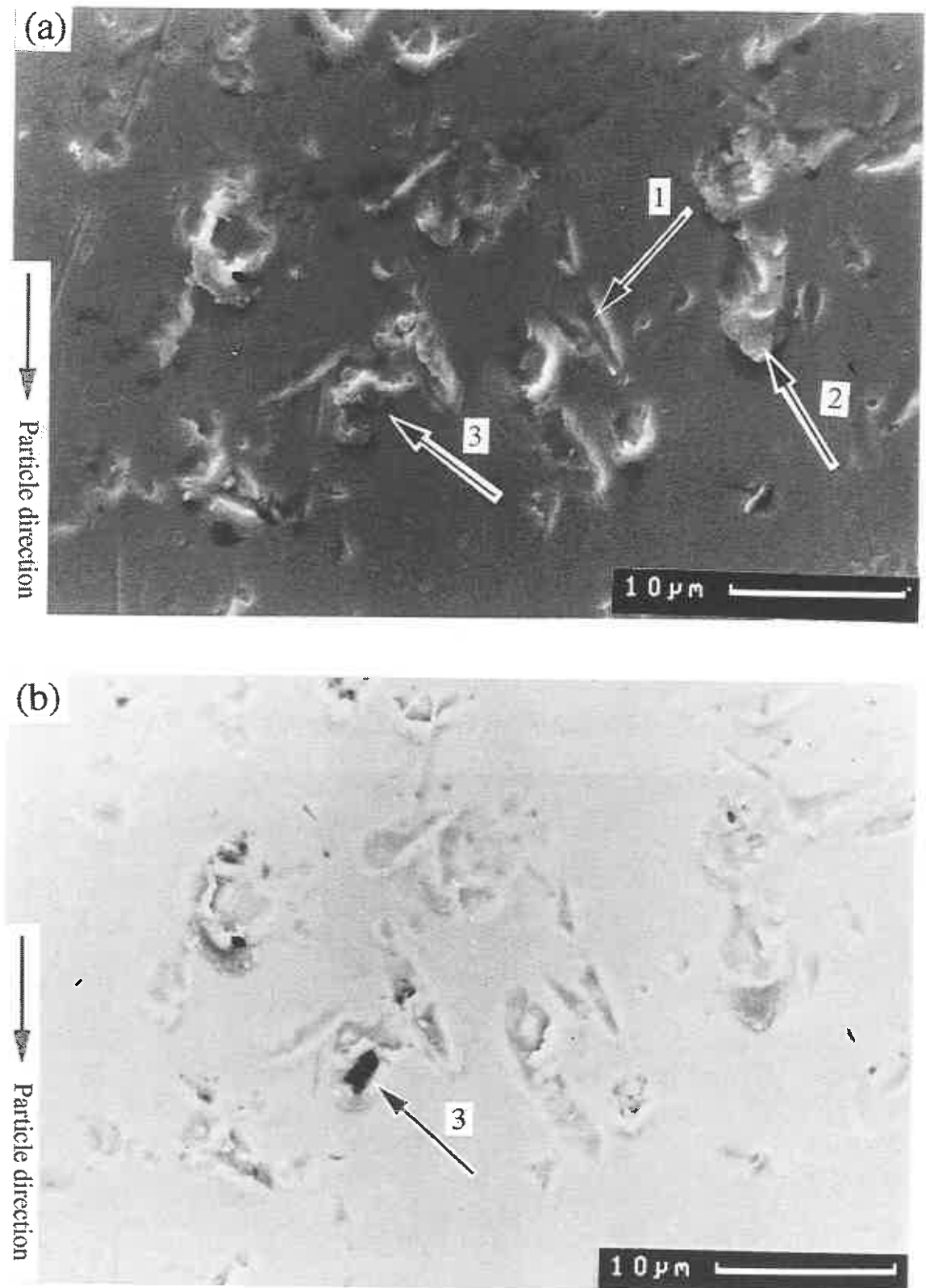


Fig. 9.7. (a) SEM secondary electron and (b) backscattered electron micrographs of mild steel impacted with 100 g of 80 mesh alumina at 45° and around 2.5 m s⁻¹. (1) indented crater, (2) lip of deformed metal at edge of impact crater and (3) particle fragment.

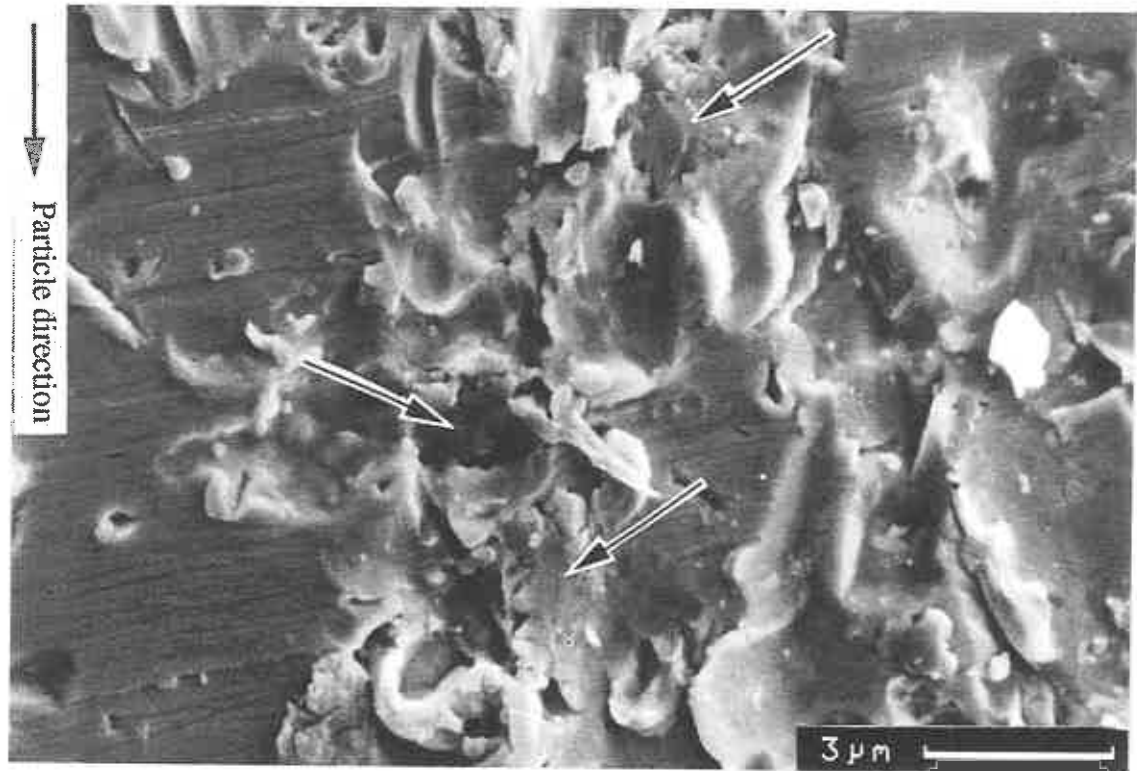


Fig. 9.8. SEM secondary electron micrograph of mild steel impacted with 400 g of 80 mesh alumina at 45° and around 2.5 m s^{-1} . Particle fragments are indicated by arrows.

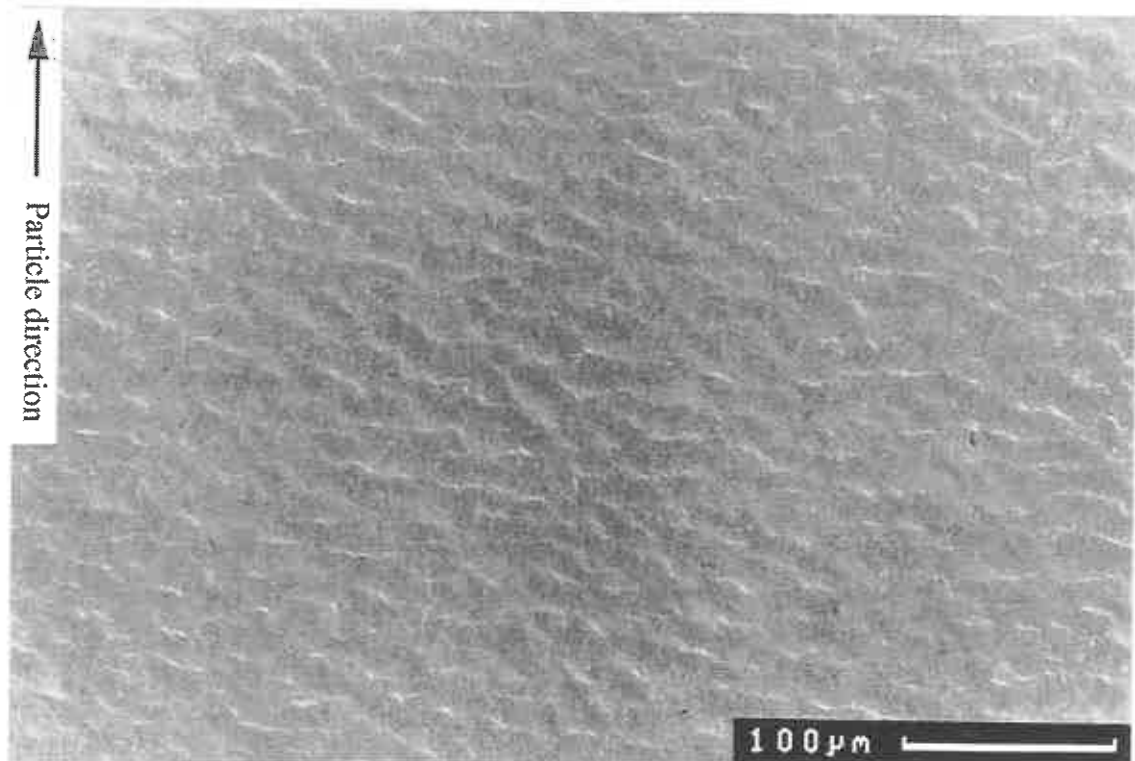


Fig. 9.9. SEM secondary electron micrograph of mild steel exposed in the fluidized bed test rig for 15 minutes at 2.5 m s^{-1} .

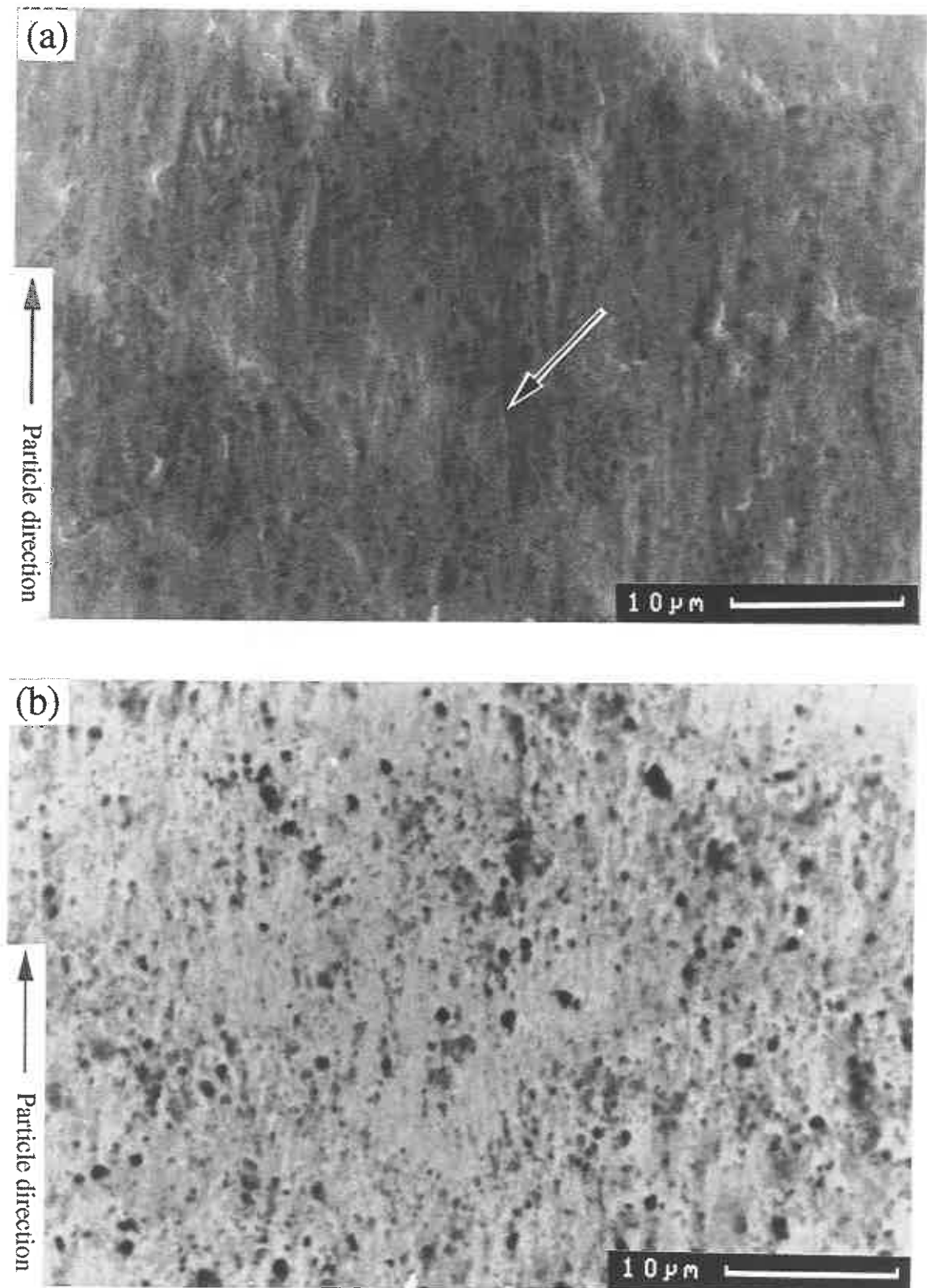


Fig. 9.10. High magnification SEM (a) secondary electron and (b) backscattered electron micrograph of mild steel exposed in the fluidized bed test rig for 15 minutes at 2.5 m s^{-1} . Arrow indicates a long abrasion scratch.

(ii) Fluidized bed specimen

A flat specimen exposed in the fluidized bed showed features somewhat different to the erosion drop tube specimens. The surface was covered with erosion ripples (Fig. 9.9) and, at higher magnification (Fig. 9.10a), the surface had a much smoother appearance than all the drop tube specimens. The surface was marked with both small impact craters and longer scratches indicating some three body abrasion as well as erosion. After 15 minutes the extent of embedment appeared to be similar to the eroded specimens, but with fewer numbers of larger particle fragments (Fig. 9.10b).

9.2.3. Summary

There were problems comparing the erosion rates at different angles quantitatively, partly due to the very low wear rates, but also due to the specimens being smaller than the drop tube diameter and changes in particle impact density over the erosion scar. Fluctuations in flux during a test affected the wear rate as the wear rate decreased with an increase in flux due to increased particle-particle interactions.

SEM micrographs of the eroded surfaces showed significant plastic deformation and lip formation at early stages with the development of a composite metal and alumina fragment composite at later times. The amount of embedment and, correspondingly, the incubation period for steady state erosion increased at the higher impact angles. The impact features on specimens exposed in the fluidized bed indicated less energetic erosion impacts and some three body abrasion.

9.3. Short term exposure experiments

9.3.1. Introduction

To obtain more relevant data for erosion-corrosion modelling, the impact conditions on the specimen within the fluidized bed needed to be measured quantitatively. Gold coated aluminium and steel specimens were exposed in the rig for a short time to investigate the flow pattern of particles impacting the cylindrical specimen. Also, to obtain quantitative data, glass beads were loaded into the rig so that the impact craters could be related to the impact velocity and angle. The erosion drop tube was used to compare impacts of known impact velocity and angle with impact craters on the specimens exposed in the fluidized bed test rig.

9.3.2. Experimental methods

Cylindrical bars were machined to the same dimensions as the tube specimens used in the cooled specimen tests and were attached to the uncooled side on the rotor with a special adapter using a 3/8" BSF thread. The surface was buffed to a high polish and then coated with gold in a sputter coater used to coat samples for SEM preparation. The specimen was then exposed in the fluidized bed test rig for a number of revolutions. It was initially thought that the process of inserting and removing the specimen from the fluidized bed would remove some of the gold coating but a test showed that the surface was virtually unaffected by this action.

Tests in the fluidized bed were conducted with gold coated aluminium and mild steel specimens at about 50° C for various length of times and rotational speeds and in beds of both glass beads and alumina.

The Vasquashene glass beads were obtained from Abrasive developments Ltd. in the 300 - 400 µm size range. Glass beads was used so that the particle impacts would be more uniform than the angular alumina so that this could, perhaps, be related to impact velocity and angle on the specimen. Fig. 9.11 shows that the sizes of the beads were not particular uniform as the cost of the glass spheres had to be cheap enough to fill the fluidized bed. The surfaces of some of the glass spheres were chipped.

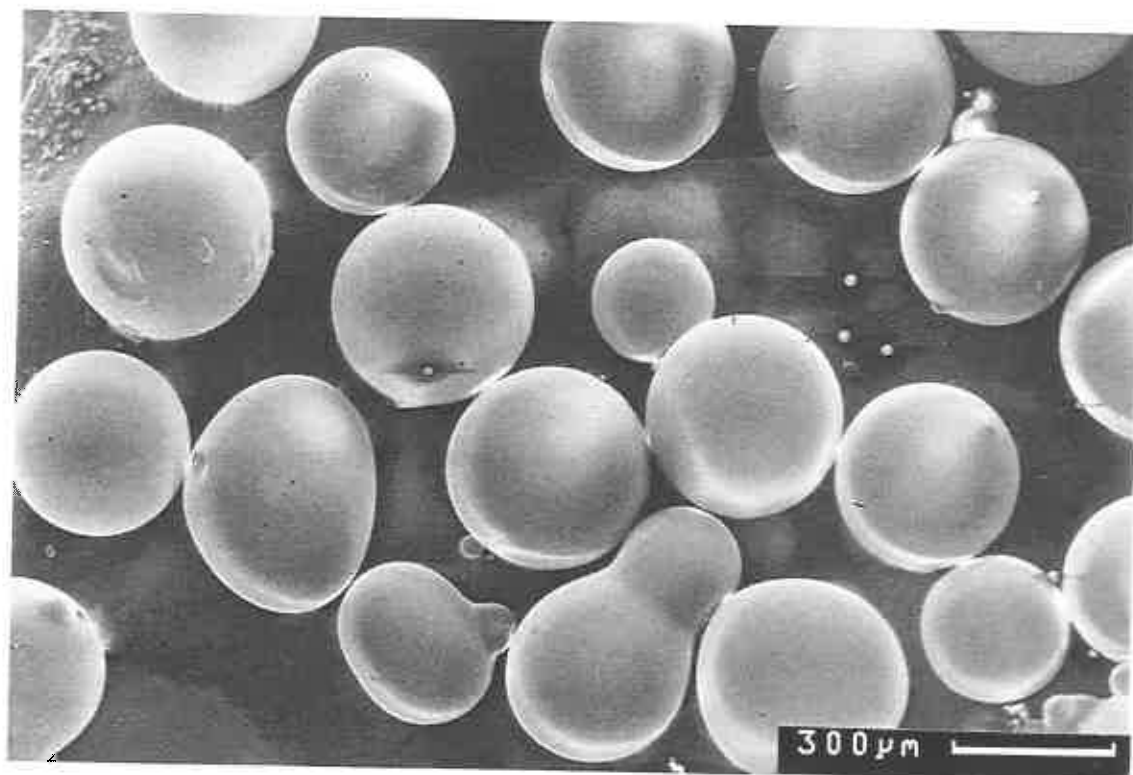


Fig. 9.11. SEM micrograph of the glass beads used in the fluidized bed.

Impact craters of the glass spheres at different impact angles were calibrated by using the erosion drop tube apparatus described in section 9.2. The erosion specimens were studied in the SEM and under an optical microscope using differential interference contrast (DIC) to give topographic contrast.

9.3.2. Results and discussion

9.3.2.1. Alumina particles

A gold coated aluminium specimen exposed in the rig for approximately 2 s and 5 revolutions at 200 revs min⁻¹ showed much of the gold coating removed over the region associated with the wear scar. Two types of contacts were observed; non damaging contacts (Fig. 9.12a) which removed the gold coat (Fig. 9.12b) but did not appear to damage the metal substrate, and damaging impacts which caused plastic deformation of the metal substrate (Fig. 9.12c and d). The damaging impacts tended to be smaller than the non-damaging contacts, only several microns across, and were more visible under the optical microscope (Figs. 9.12 - 9.15). The long marks across the length of the micrographs in Figs. 9.12 - 9.15 were not caused by particle impacts but were the machining marks not completely removed by surface polishing (Fig. 9.12e).

On the wear scar close to the leading edge some small impact craters were observed, probably from erosion type impacts (Fig. 9.12c), and also several larger impacts of the order of 50 µm long, where microploughing seems to have occurred probably by three body abrasion (Fig. 9.12d). The slightly lighter regions show the tracks of the non-damaging contacts (Fig. 9.12a) where the gold coating had been removed, and the dark areas at the end of these tracks were where the gold was left on the surface at the end of the contact (Fig. 9.12b). Moving towards the centre of the wear scar the longer ploughing impacts increased in number but shortened in length and the smaller erosion type impacts also appeared to increase in number (Figs. 9.13 and 9.14). The highest density of impacts appeared to occur in the centre of the wear scar, where the maximum wear rate occurred. Towards the back of the wear scar most of the impacts were small erosion type impact craters with virtually no deeper, ploughed impacts (Fig. 9.15). The impact craters were fairly elongated suggesting a glancing angle impact which was perhaps expected. Comparing the smaller erosion like impacts with those observed from the erosion drop tube (Fig. 9.16) at a similar impact velocity (2 m s⁻¹) showed that the impact craters were much smaller on the fluidized bed specimen.

Fig. 9.17 shows a backscattered electron micrograph from the front to the back edge of the bottom wear scar (showing the non damaging impacts as darker regions). There was a wide distribution of non damaging contact size over the width of the wear scar, from marks less than 1 μm across to some tens of microns long and up to 10 μm wide. The surface coating of gold removed by the contacts tended to be left on the surface at the end of the contact and therefore showed the direction of particle motion. The direction of most of these contacts was aligned from the front to the back of the specimen and clearly indicated a flow of particles over the specimen. The direction of some contacts were almost perpendicular to the general flow, with the particle motion towards the high velocity end of the specimen. These were probably formed initially as the specimen started rotating.

A similar experiment by MacAdam and Stringer (1991b) showed similar types of impact, both damaging and non-damaging, although the sizes of particle contacts and impact craters were much larger as the particle size used in their fluidized bed was 800 μm in diameter. The ratio of particle size to contact size was broadly similar in both studies.

After 1 min at 250 rev min^{-1} (Fig. 9.18) the coating on an aluminium specimen was almost completely removed over most the wear scar, and the impact craters covered most of the wear scar resembling the steady state wear scar seen on the erosion oxidation specimens. Despite this, the leading edge was still largely covered in gold (Fig 9.19) with a few small non-directional contacts and with tracks of particle contacts at the edge of the wear scar directed away from the leading edge. At the high velocity end the contacts are seen to move along the length of the specimen towards the endcap. The lack of particle contacts over the leading edge supported the idea of a dead cap of particles protecting the leading edge from direct particle impact. The surface behind the wear scar at around 90° also showed very few particle contacts.

9.3.2.2. *Glass beads*

(i) *Drop tube specimens*

Glass bead drop tube targets show discrete circular impact craters easily seen under an optical microscope using DIC. The shape of the impact crater barely changed with impact angle although some were slightly more elliptical at shallower impact angles. A typical size of an impact crater was between 10 and 20 μm in diameter (Fig. 9.20). As

well as the indent made by the glass beads there were also smaller areas of plastic deformation and lip formation over the impact crater (Fig. 9.21). The length of these marks increased at shallow impact angles which gave some indication of the angle of impact and it was thought this might indicate the angle of impact in the fluidized bed test rig.

(ii) *Fluidized bed specimens*

The appearance of the gold coated bar exposed in the fluidized bed of glass beads for approximately 9 revolutions at 250 revs min⁻¹ is shown in Fig. 9.22. The small regions of plastic deformation seen on the drop tube specimens were visible but it was very difficult to distinguish individual impacts due to the large number of impacts, and the indentation caused by the impact craters were not readily visible. The general appearance of the wear scar was very similar to that observed on the specimen impacted with alumina. The depth of deformation appeared to be less than the erosion drop tube targets and the appearance of the smaller, plastically deformed regions showed little elongation. Although a shorter exposure may have been useful the experiment did not yield any more useful information than using alumina particles, partly because only the rough areas on the glass spheres marked the surface, and the impact was not energetic enough to leave a visible crater.

9.3.3. Summary

It is difficult to be quantitative about impact conditions and also particle flux in these experiments. Due to the very high fluxes involved the time of exposure needed to observe individual impacts on the wear scar was less than a couple of seconds, over which time the rotor barely has enough time to reach its rotational speed and stop, so that the rotational speed of the specimen varied over the time of exposure.

The tests have shown that few particle contacts occurred in regions of low wear, at the leading edge and on the back of the specimen, and that maximum wear occurs where there was the highest density of damaging impacts. The type of wear varied across the wear scar changing from predominantly three body abrasion to erosion from the front to the back of the wear scar.

The erosion impacts of a drop tube eroded specimen were generally larger than the impacts on a specimen exposed in the fluidized bed at the same impact velocity probably due to fewer particle-particle interactions.

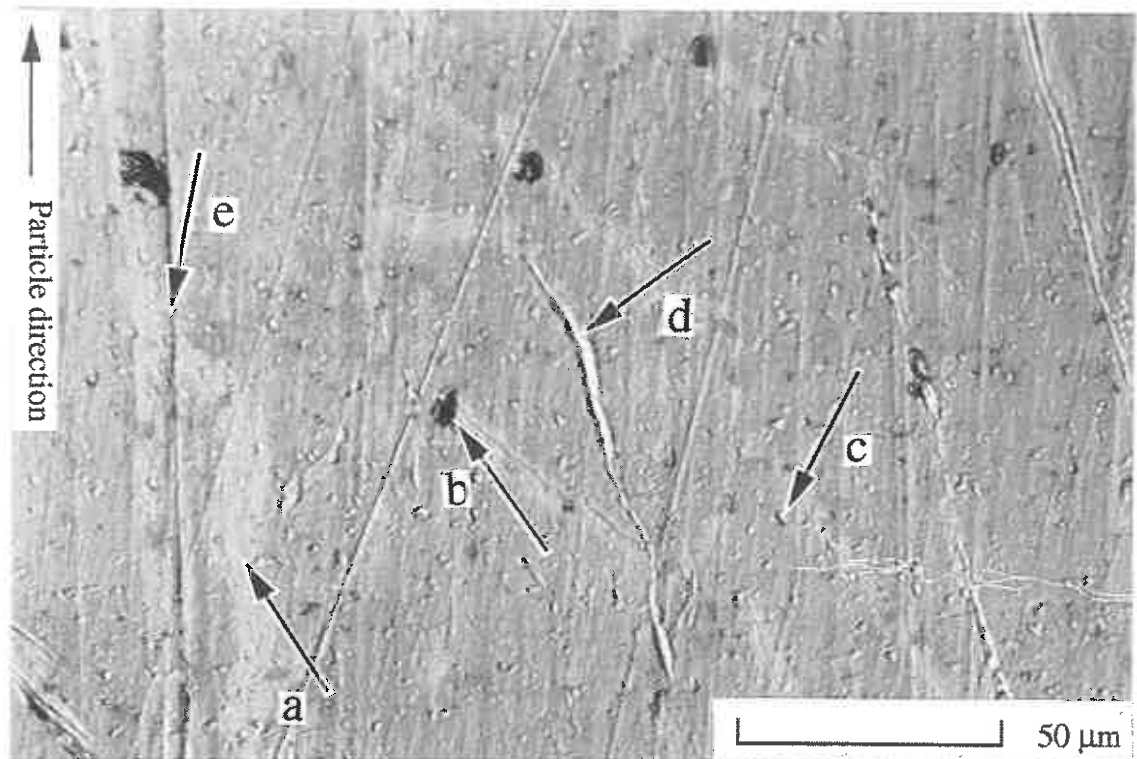


Fig. 9.12. Optical micrograph of the bottom wear scar at $\approx 20^\circ$ (close to the leading edge) of a aluminium specimen exposed in the fluidized bed of alumina at $200 \text{ revs min}^{-1}$ for approximately 2 s. (a) non-damaging contact, (b) gold coat debris (c) damaging erosion impact, (d) damaging ploughing impact and (e) machining marks.

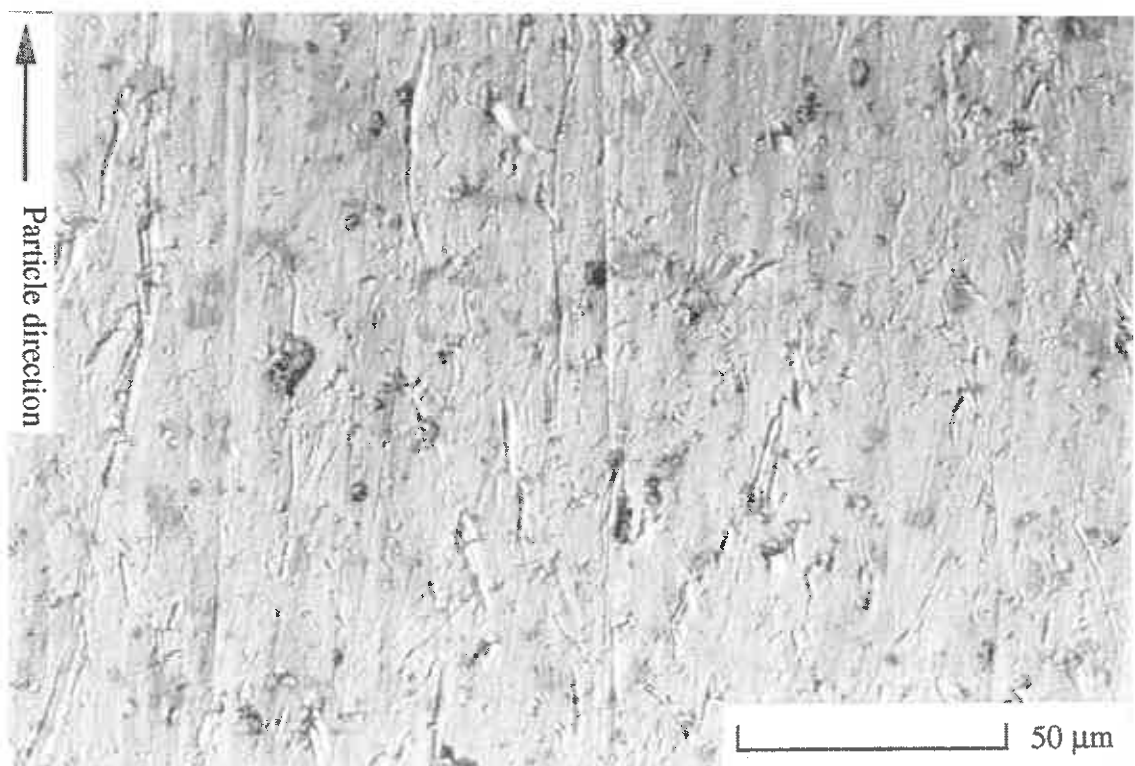


Fig. 9.13. Optical micrograph of the bottom wear scar at $\approx 37^\circ$ of a aluminium specimen exposed in the fluidized bed of alumina at $200 \text{ revs min}^{-1}$ for approximately 2 s.

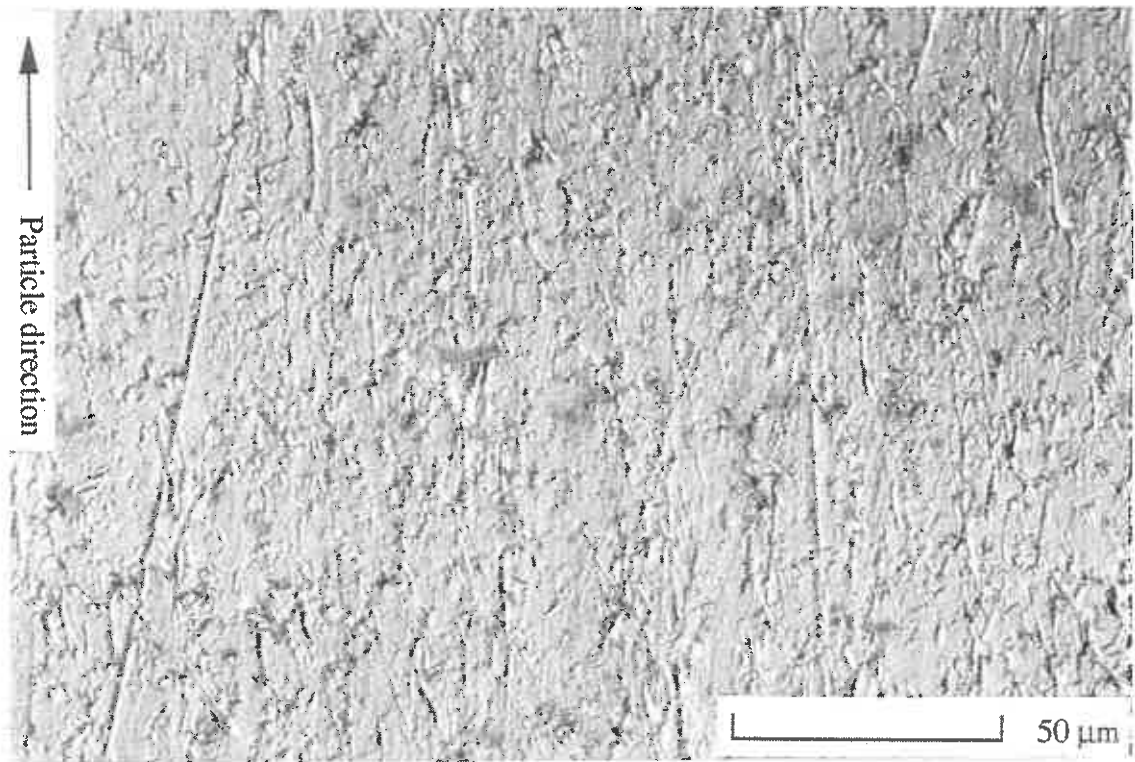


Fig. 9.14. Optical micrograph of the bottom wear scar at $\approx 46^\circ$ of a aluminium specimen exposed in the fluidized bed of alumina at $200 \text{ revs min}^{-1}$ for approximately 2 s.

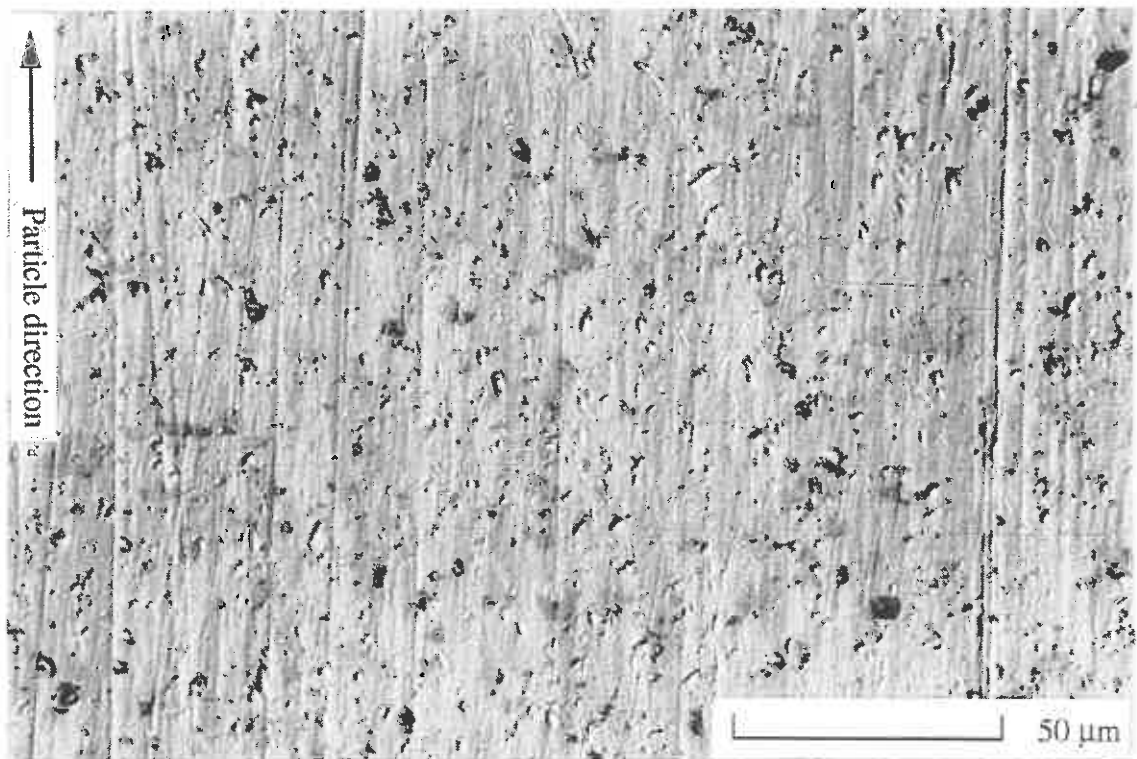


Fig. 9.15. Optical micrograph of the bottom wear scar at $\approx 65^\circ$ (near to the back edge) of a aluminium specimen exposed in the fluidized bed of alumina at $200 \text{ revs min}^{-1}$ for approximately 2 s.

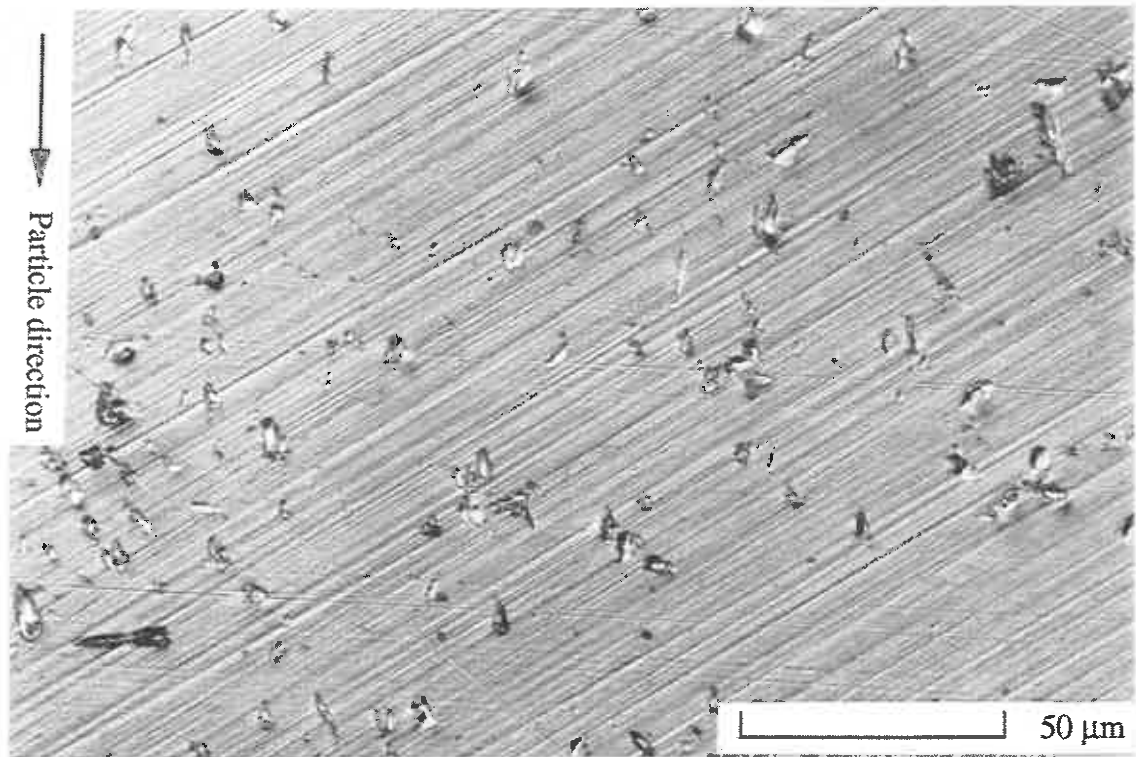


Fig. 9.16. Optical micrograph of an erosion target impacted with alumina at 15° and $\approx 2 \text{ m s}^{-1}$ using the erosion drop tube.

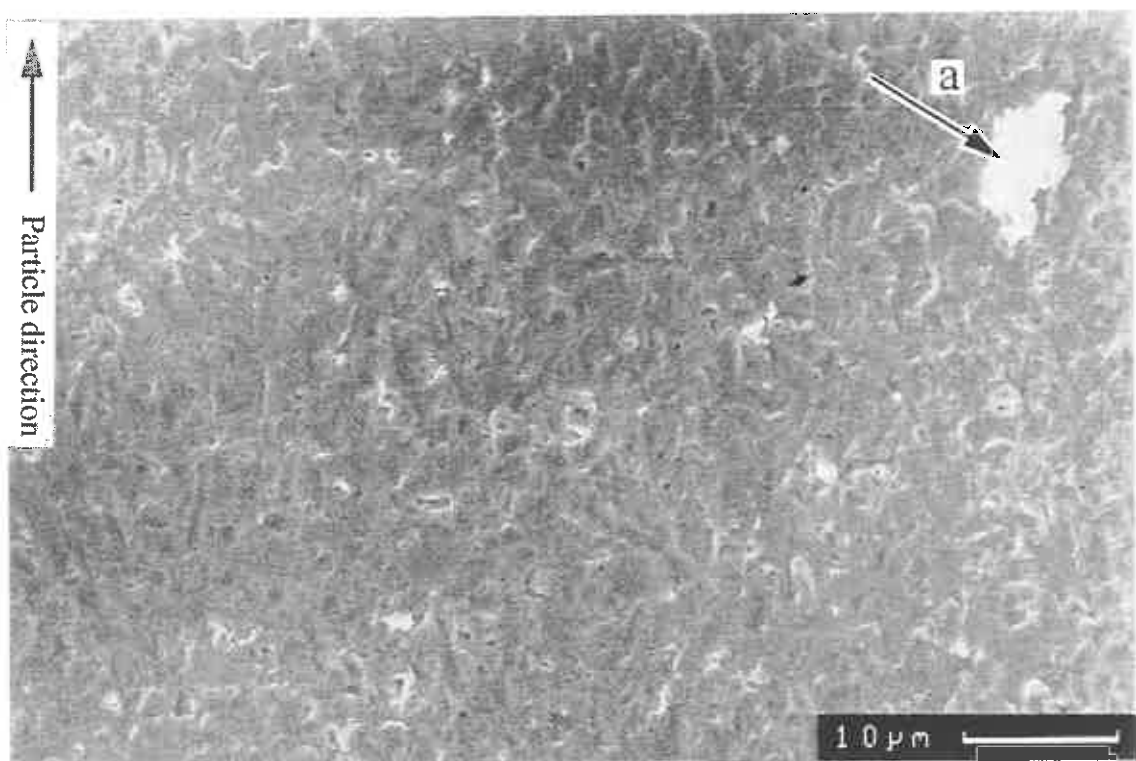


Fig. 9.18. SEM secondary electron image of the top wear scar of an aluminium specimen exposed in the fluidized bed of alumina for 1 min at $250 \text{ revs min}^{-1}$.
(a) remaining gold coating.

The back edge of
the bottom wear
scar (75°)

Particle
direction

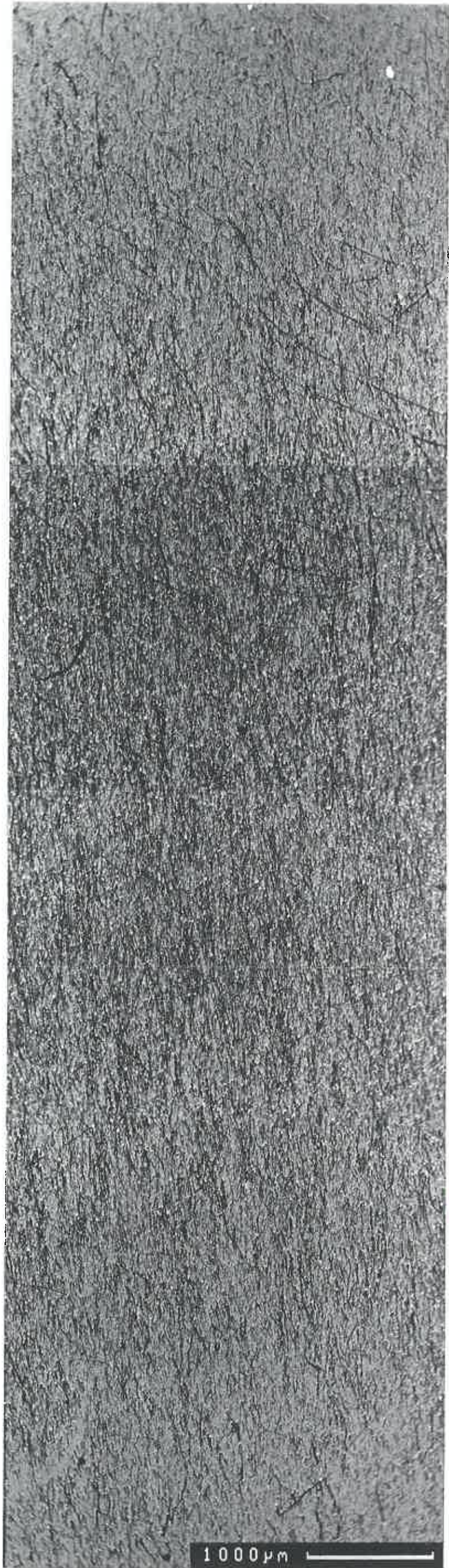


1

1

The front edge
of the bottom
wear scar (25°)

1000 μm



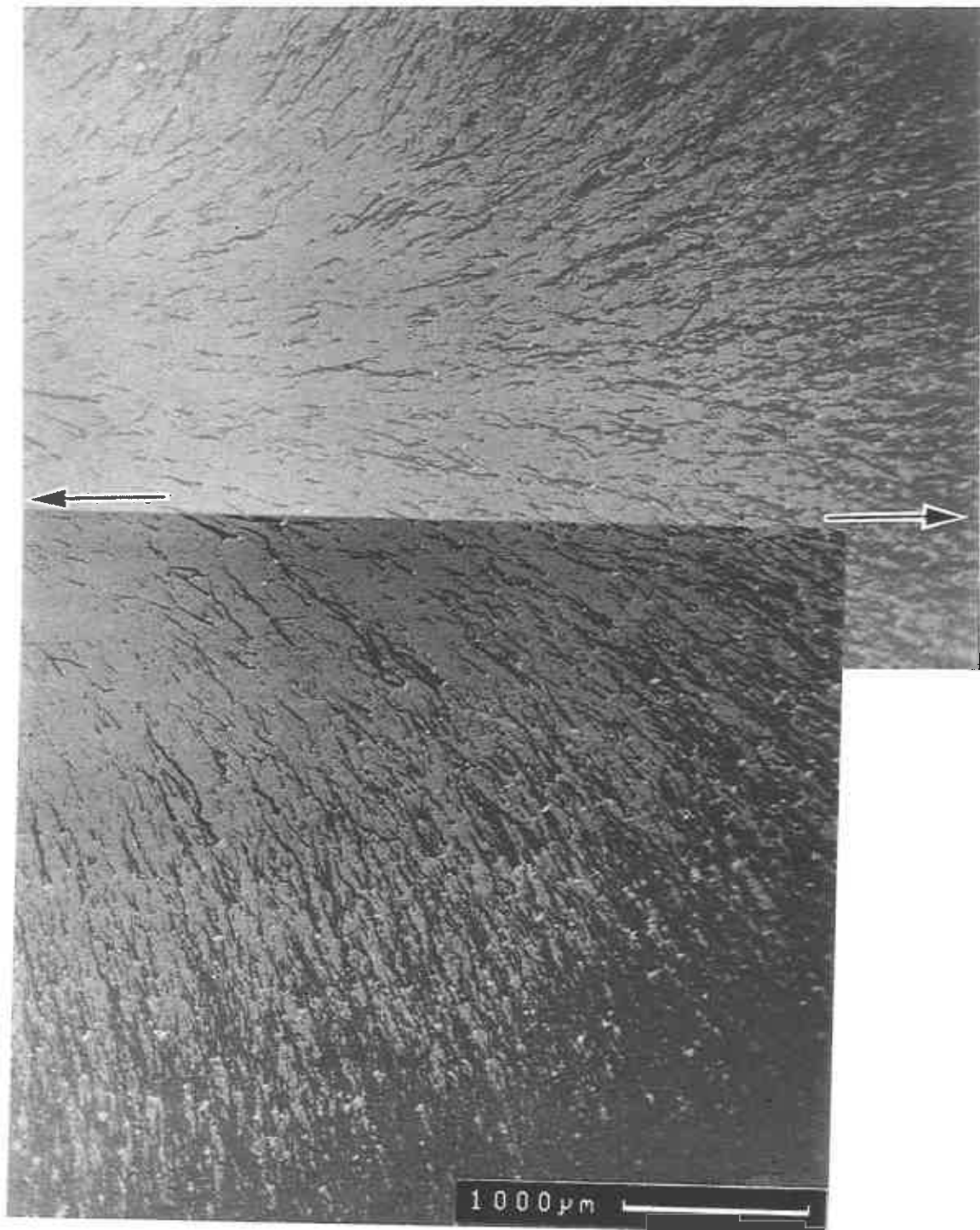


Fig. 9.19. SEM secondary electron image of the leading edge of an aluminium specimen exposed in the fluidized bed of alumina for 1 min at $250 \text{ revs min}^{-1}$. The image is located at the high velocity end of the specimen with the end of the specimen on the right.

Arrows mark the leading edge.

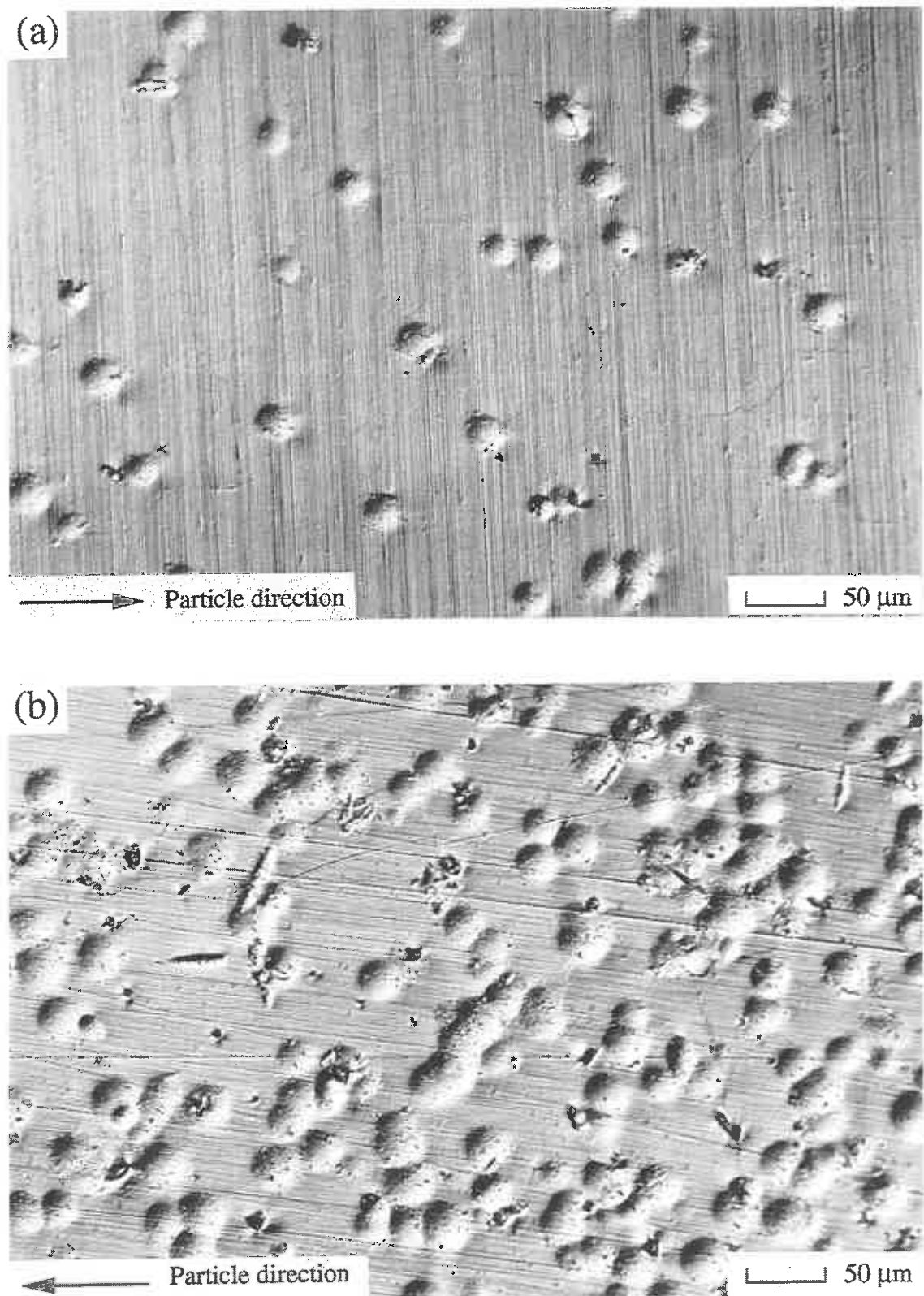


Fig. 9.20. Optical micrographs of impact craters formed by the impact of glass spheres with aluminium at approximately 2.5 m s^{-1} and at (a) 30° and (b) 75° .

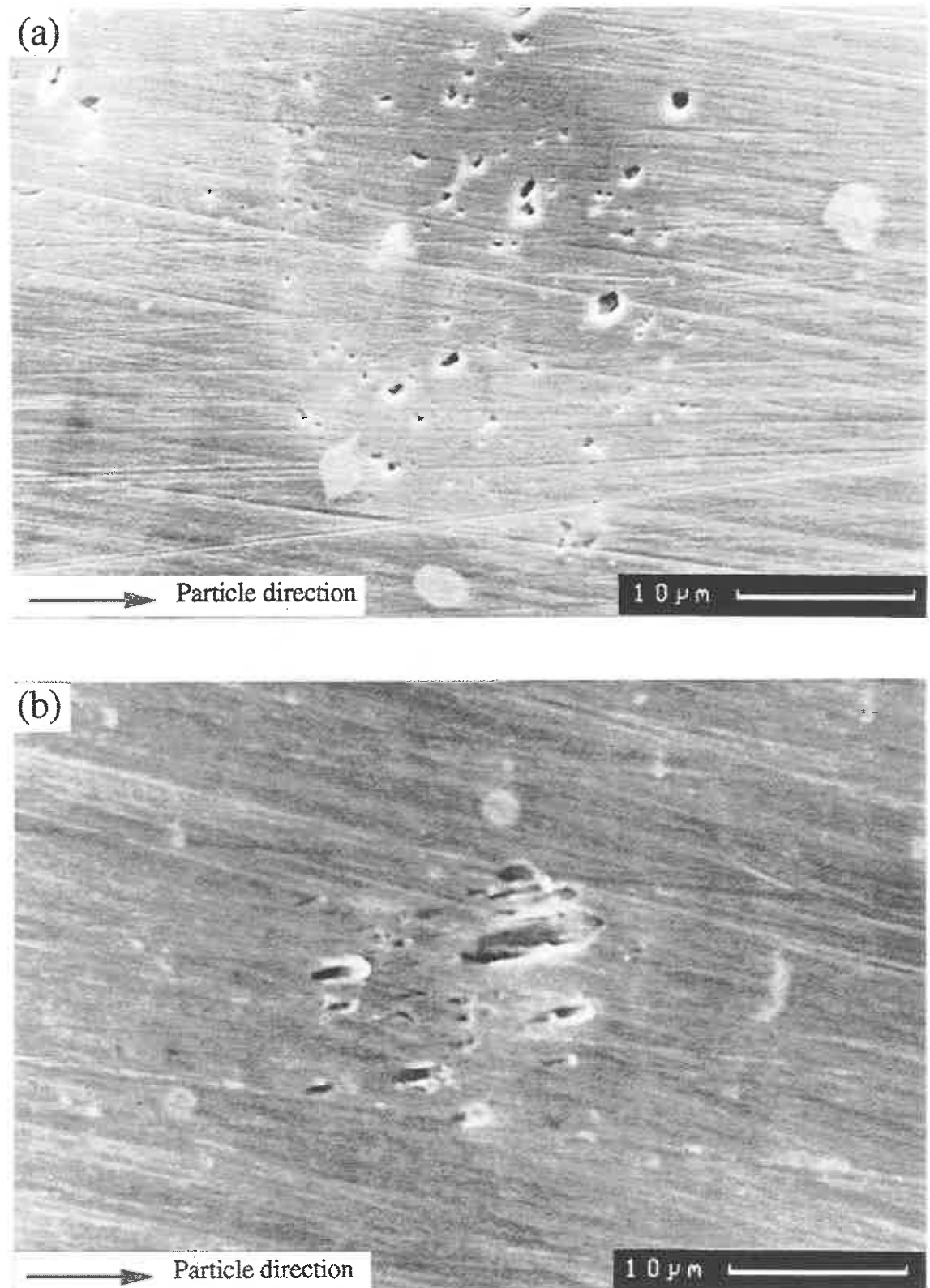


Fig. 9.21. SEM secondary electron micrographs of impact craters formed by the impact of glass beads with aluminium at approximately 2.5 m s^{-1} and at (a) 75° , and (b) 15° .

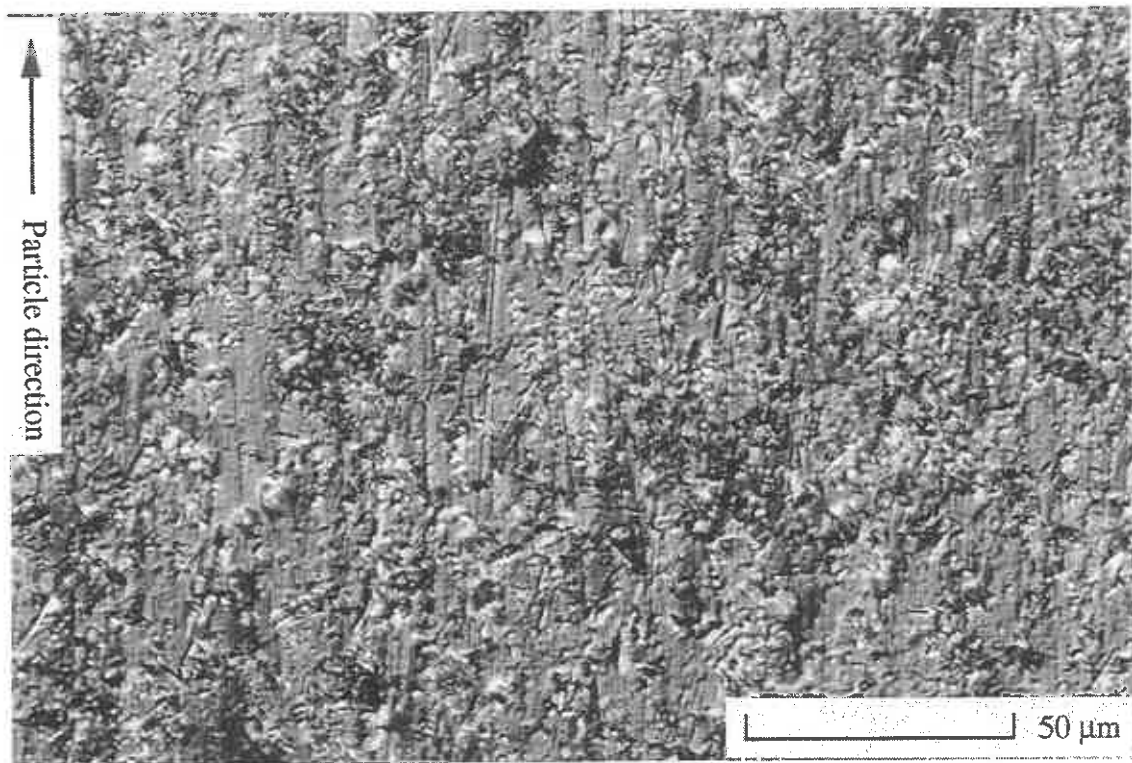


Fig. 9.22. Optical micrograph of the bottom wear scar of an aluminium bar exposed in a fluidized bed of glass beads for 9 revs at 20 revs min^{-1} . Centre of the wear scar at $\approx 2 \text{ m s}^{-1}$.

9.4. Silica tube experiments

9.4.1. Introduction

In an attempt to measure the erosivity of the fluidized bed as a function of temperature but without the influence of oxidation on the wastage rate, inert silica specimens were exposed in the fluidized bed. The aim of this experiment was to assess the extent of any changes in wastage rate that were not dependant on the changes in oxidation behaviour. Preliminary experiments were conducted.

9.4.2. Experimental methods

Silica glass tube specimens of the same dimensions as the tubular steel specimens used in the fluidized bed test rig were made by Wesley Coe Ltd. Their external surfaces were ground about their ends to reduce the specimen eccentricity when measured on the specimen measuring rig, although a typical specimen eccentricity was high at over 100 μm from peak to peak. The experimental methods used for the silica specimens were similar to those described in Chapter Five, except that a special holder was used to attach the silica tube to the test rig drive shaft (Fig 9.23).

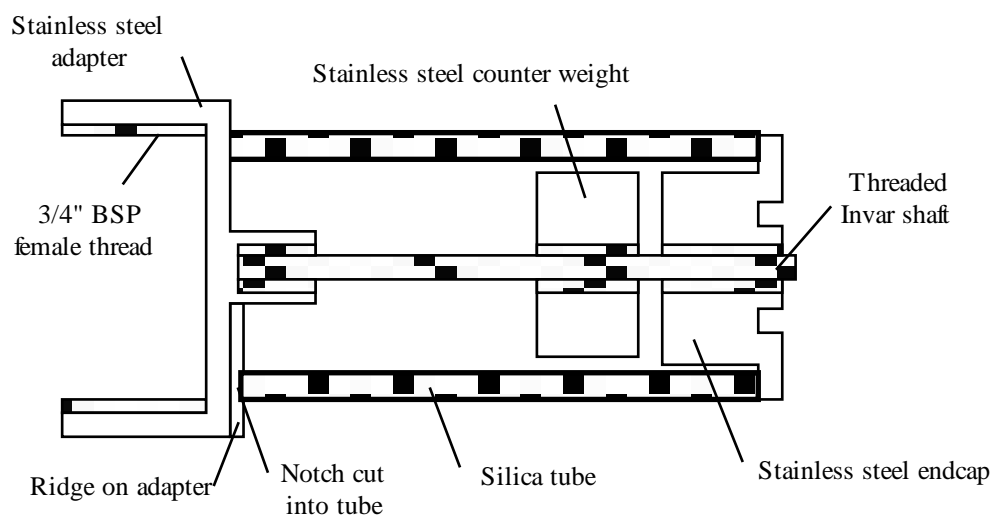


Fig. 9.23. Diagram of holder used to attach a silica tube specimen to the drive shaft of the fluidized bed test rig.

A small notch was cut into the end of the specimen with a diamond saw which allowed it to be fitted over a ridge on the specimen holder. This fixed the position of the specimen and prevented the specimen rotating during a test. The specimen was held in

place with an endcap tightened onto the end of the specimen. Due to the low thermal expansion of silica compared to most metals the silica tube loosened as the temperature increased, this meant that the endcap had to be retightened at a higher temperature. This caused a problem at the end of a test as the specimen cooled down when the holder contracted onto the specimen, making it difficult to undo and caused the specimen to fracture. Using Invar, a low expansion coefficient alloy for the central shaft of the holder, reduced the differential expansion but it still caused problems.

The methods of measuring specimen wastage were identical to those for the mild steel tube specimens except that care was required when tightening the drive wheel to the specimen, and a diamond tipped scribe was used to score the back of the tube. Interrupted tests were conducted at bed temperatures of 200° and 300° C and specimens at higher temperatures failed due to thermal expansion problems. A counter weight on the silica specimen holder was used to balance the two sides of the rotor.

9.4.3. Results

At 200° C a specimen was tested over 435 h with five interruptions, Fig. 9.24 shows the circumferential wear of the specimen at 2.35 m s⁻¹. A visible wear scar was narrow and at glancing impact angles, almost at ± 90° to the leading edge and is shown as a spike in wear. A broader region of wear was also measured at a lower impact angles but there were very few visible erosion features to indicate wear on the specimen.

Fig. 9.25 shows a graph of the average of the two maximum peak wear rates against velocity. The wear rate was very low with a maximum of about 0.25 μm h⁻¹ and no wear was detected below an impact velocity of 1.8 m s⁻¹ after 435 h.

The specimen exposed at 300° C had an initial wear rate of 12 μm h⁻¹ at 2.5 m s⁻¹ (Figs. 9.26 and 9.27) which was higher than the highest wear rate of mild steel at 8 μm h⁻¹. During this period the fluidized bed may have been slightly under fluidized, but not dramatically so. A subsequent exposure of another 15 hours with a well fluidized bed resulted in a lower wear rate that was comparable to that measured at 200° C at high impact angles but still a very high wear rate at lower impact angles (Fig. 9.27). No further measurements were made as the specimen cracked at the beginning of the next exposure. A mild steel specimen exposed in the bed on the other side of the rotor only showed a slight increase in its wastage rate during this exposure.

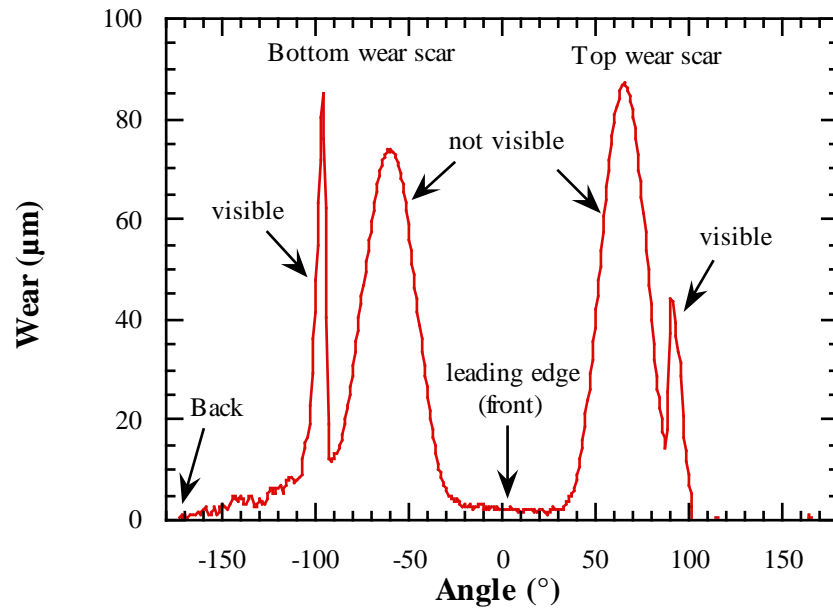


Fig. 9.24. Circumferential wear for silica exposed at 200°C and an impact velocity of 2.35 m s^{-1} for 435 h.

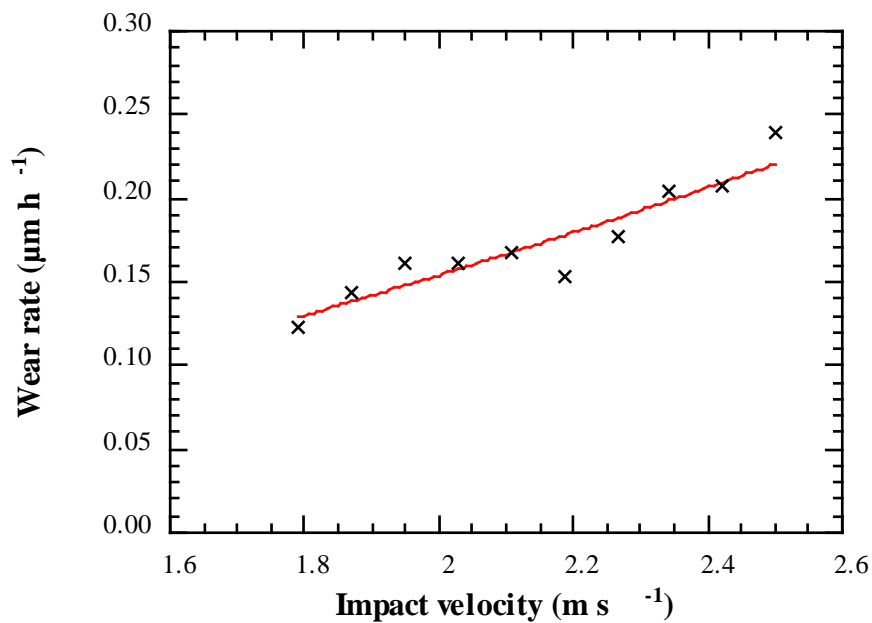


Fig. 9.25. Graph of wear rate against impact velocity for silica at 200°C .

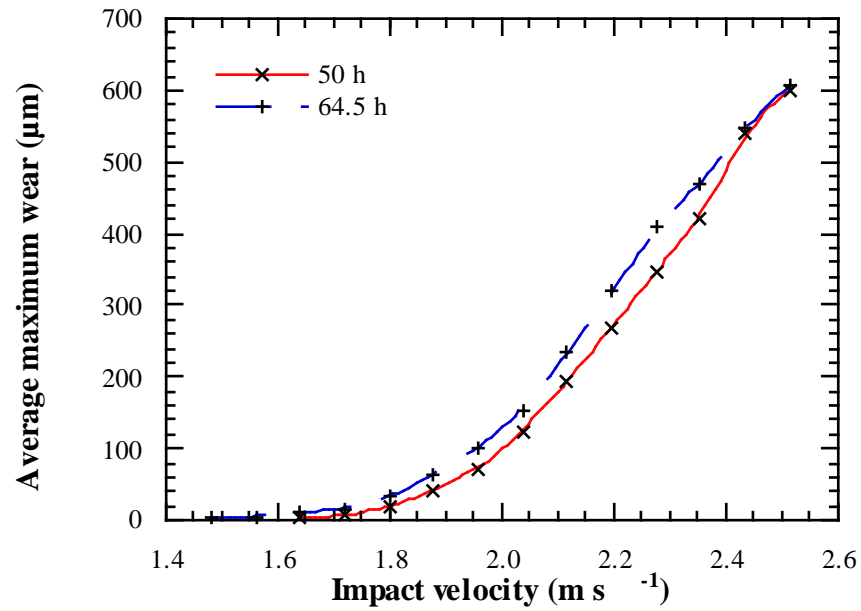


Fig. 9.26. Graph of wear against velocity for silica at 300° C.

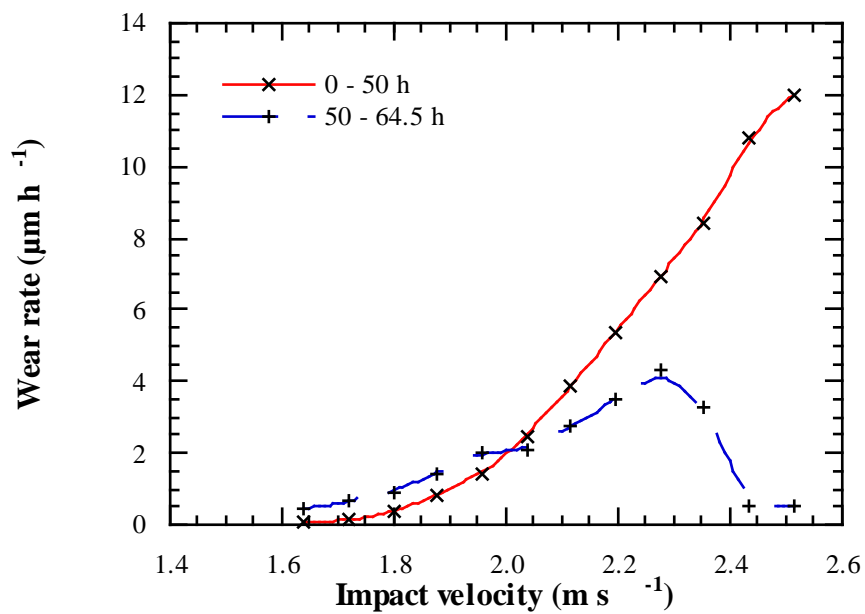


Fig. 9.27. Graph of wear rate against velocity for silica at 300° C over each of the two runs.

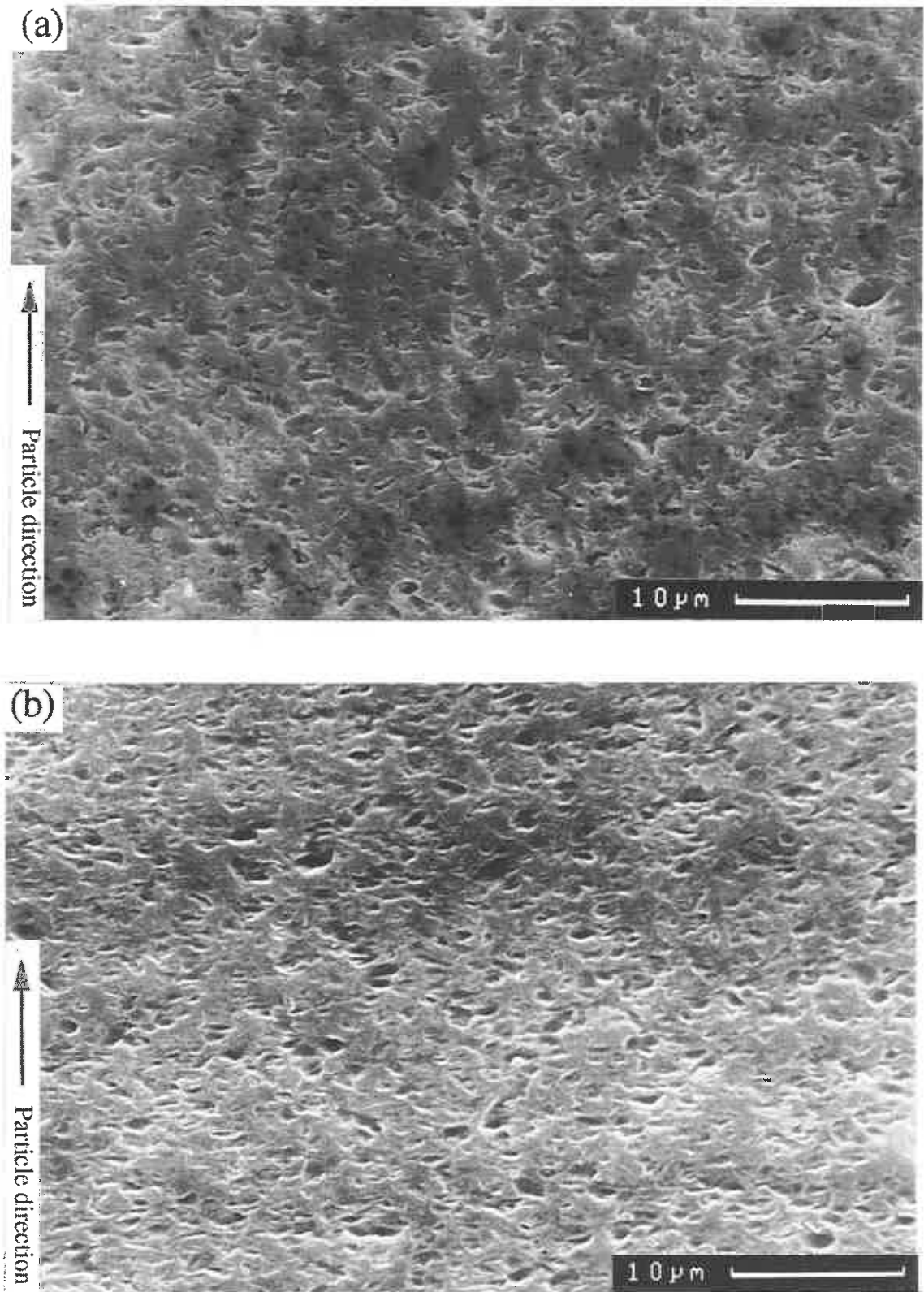


Fig. 9.28. SEM micrograph of the upper wear scar of a silica specimen exposed at (a) 300° C for 64.5 h and (b) 200° C for 435 h.

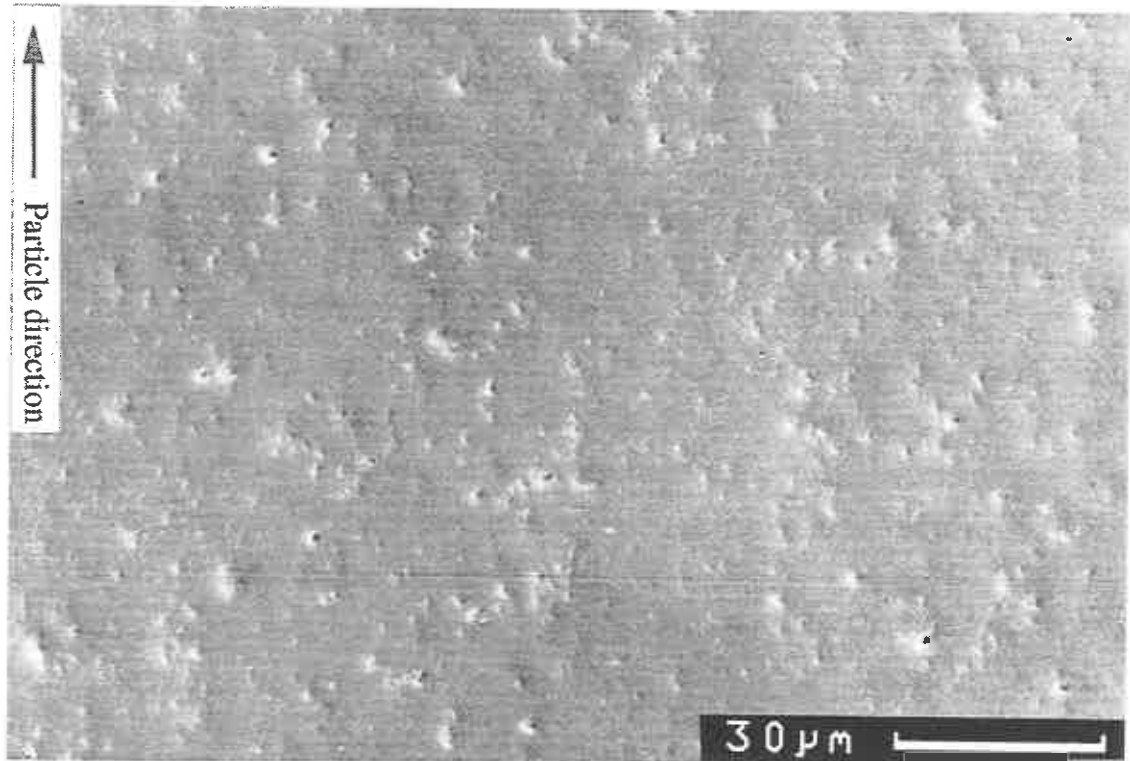


Fig. 9.29. SEM secondary electron micrograph of the worn region in front of the 'visible' wear scar of the silica specimen exposed at 300° C.

The wear scars of the specimen exposed at 300° C were very similar to those observed at 200° C. A visible wear scar was observed at glancing impact angle but, unlike at 200° C, the region of wear scar towards the specimen's leading edge was now just visible.

The microscopic appearance of the wear scars at both temperatures was very similar. The 'visible' area of the wear scar at glancing impact were covered in small impact craters over which brittle fracture had occurred (Fig 9.28 a and b). The region of the wear scar towards the leading edge had far fewer impact craters and a polished appearance, making it difficult to see with the naked eye (Fig. 9.29). There was no indication of why the wear rate was dramatically higher at 300° C.

9.4.4. Discussion

The experiment was difficult to conduct due to the low expansion and brittle nature of silica, especially at higher temperatures. The limited results obtained showed that the wear rate of silica was, perhaps, very sensitive to the fluidization of the bed, with a drop in fluidization possibly causing a dramatic increase in wear. The microscopic appearance of the wear scar, which suggested a brittle mechanism of removal at glancing impact angles, did not seem to change with the increase in wear rate. The mechanism of wear closer to the leading edge was unclear as few impact craters were observed, and yet the wear was comparable to the more visible region.

Observation of the effect of temperature on the wear of silica would be very difficult because of the sensitivity of the wear to other bed conditions.

9.4.5. Conclusions

Preliminary tests of exposing silica in the fluidized bed test rig were carried out. The results were inconclusive as the wear at 300° C was inconsistent and significantly higher than at 200° C, although the microscopic appearance of both specimens suggested no change in the wear mechanisms.

Chapter 10

Erosion-corrosion modelling

10.1. Introduction

To obtain a greater understanding of the erosion-corrosion mechanisms in the fluidized bed test rig, the results from simple computer models utilising experimental data described in Chapters Six - Nine were compared with experimental results. The models were of two types; erosion-corrosion maps which calculate the dominant erosion-corrosion regime over a range of variables, and models which calculate the wastage rate. The results of the erosion-corrosion maps are used to discuss the effect of several variables which are incorporated in the erosion-corrosion modelling.

10.2. Erosion-corrosion maps

An erosion-corrosion regime map displays a dominant erosion-corrosion regime or mechanism for a given set of experimental variables. This is usually mapped over two variables, typically velocity and temperature. Both Sundararajan (1991) and Stack and Bray (1995b) have constructed erosion-corrosion maps and Stack and Bray (1995b) have used the maps to predict safe and unsafe operating conditions for various materials. Their methods have been reproduced and adapted to calculate similar maps for the fluidized bed test rig environment.

10.2.1. Definition of systems

As previously described in Chapter Four, Sundararajan (1991) described five erosion-corrosion regimes (Fig. 10.1) and developed criteria to determine the most dominant erosion-corrosion regime for a particular environment. Parabolic growth kinetics and linear erosion rates were used to calculate a steady state thickness, Z_{ss} . A critical oxide thickness, Z_c , was defined above which the scale became brittle and was removed by cracking or chipping. The thickness of oxide growth between successive impacts if the oxide spalled was Z_b .

The depths of the plastic zones in the oxide and metal were L_o and L_m respectively. The dominant mechanism was defined from the following criteria;

- (i) **Pure oxide erosion** was dominant when $Z_{ss} < Z_c$ and $Z_{ss} > L_o$, i.e. when the scale was intact and the zone of deformation was confined to the scale.
- (ii) **Metal erosion** was dominant when $Z_{ss} < Z_c$ and $Z_{ss} < 0.1L_m$. The second condition ensures that the oxide was sufficiently thin when compared with the depth of plastic deformation and therefore behaved as part of the base metal.
- (iii) **Oxide affected erosion.** If $Z_{ss} < Z_c$ and neither $Z_{ss} > L_o$ nor $Z_{ss} < 0.1L_m$ were satisfied then the plastic deformation under erosion conditions was influenced by both the oxide and the metal.
- (iv) **Spalling modes.** If $Z_{ss} > Z_c$ then the oxide spalled before the steady state thickness was attained. If $Z_b > Z_c$ then the oxide was removed at each impact, so that the mechanism was oxidation controlled erosion (continuous), and if $Z_b < Z_c$ then several impacts occurred before spalling. Thus the mechanism was oxidation controlled erosion (spalling). The additional condition of a higher erosion rate than erosion alone was required although this was shown to be always true at temperatures greater than 35% of the melting point.

Stack and Bray (1995b) based their erosion-corrosion maps on the same erosion theory as Sundararajan but the definitions of the erosion-corrosion boundaries between mechanisms differed slightly. Four regimes were defined;

- (i) Erosion-dominated (E)
- (ii) Erosion-corrosion-dominated (EC)
- (iii) Corrosion-dominated 1 (C1)
- (iv) Corrosion-dominated 2 (C2)

with the boundaries defined as

- (a) The E and EC boundary was defined as:

$$Z_{ox} = 0.1L_m \quad (10.1)$$

where Z_{ox} was the oxide thickness

(b) The EC and C1 boundary corresponded to the formation of a critical oxide thickness:

$$Z_{\text{crit}} = L_o \quad (10.2)$$

(c) The boundary between C1 and C2 was defined as the at point at which the weight loss by erosion equals the weight gain by oxidation such that:

$$\Delta W = \rho_{\text{ox}} Z_{\text{ox}} - f \rho_{\text{ox}} Z_{\text{ox}} - \rho_{\text{ox}} Z_{\text{crit}} = 0 \quad (10.3)$$

where f was the stoichiometric factor which accounts for the percentage metal consumed in the formation of oxide.

10.2.2. Map construction

The criteria defined by Sundararajan (1991) can be summarised by a flow diagram shown in Fig. 10.2.

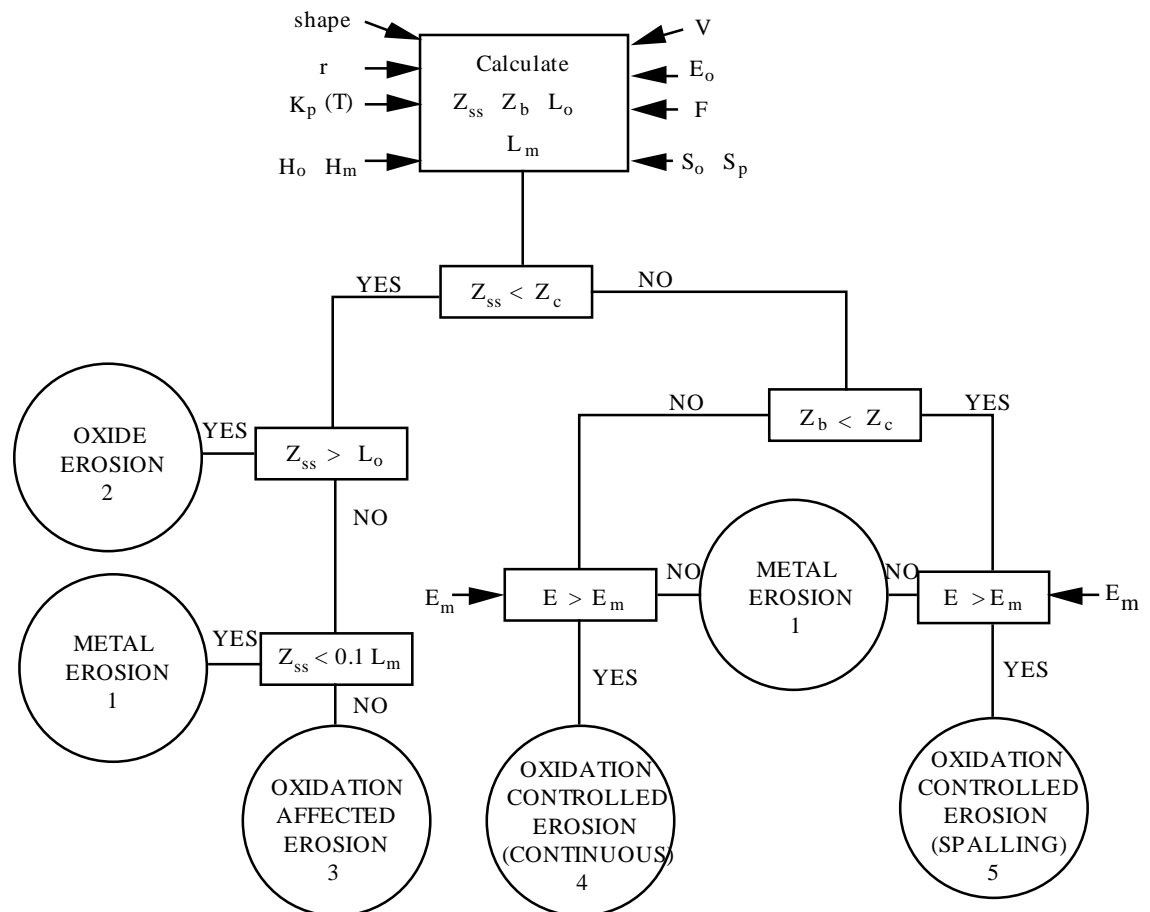


Fig. 10.2. A flow chart illustrating the validity conditions for various erosion-corrosion mechanisms, after Sundararajan (1991).

The relevant equations derived by Sundararajan for the calculation of Z_{ss} , Z_b , L_o and L_m were:

$$Z_{ss} = \frac{K_p \rho_o}{E_o F} \quad (10.4)$$

where K_p is the scaling constant (units $m^2 s^{-1}$) and can be expressed by:

$$K_p = 0.5C^2 A_o \exp\left(\frac{-Q}{RT}\right) \quad (10.5)$$

where C is a conversion constant, A_o is the Arrhenius constant, Q is the activation energy, R is the gas constant and T is the absolute temperature. E_o is the oxide erosion rate and can be described by:

$$E_o = E_{oo} \left(\frac{V}{V_o}\right)^n \quad (10.6)$$

where E_{oo} is the erosion rate constant, V is the impact velocity, V_o is a reference velocity and n is the velocity exponent.

$$Z_b(\text{sph.}) = 1.26 \left(\frac{K_p r}{\alpha V F}\right)^{1/2} (\rho_p H)^{1/4} \quad (10.7)$$

and

$$Z_b(\text{con.}) = 1.63 \left(\frac{K_p r}{\alpha F}\right)^{1/2} \left(\frac{\rho_p^{1/6} H^{1/3}}{V^{2/3}}\right)^{1/4} \quad (10.8)$$

where sph. and con. refer to spherical and conical particles, r is the particle radius, α is a constant of order unity, F is the particle flux ($kg\ kg^{-1}$), ρ_p is the particle density and H is the hardness of the material in which deformation occurs.

$$L(\text{sph.}) = \frac{2.56\beta r \rho_p^{1/4} V^{1/2}}{H^{1/4}} \quad (10.9)$$

$$L(\text{con.}) = \frac{2\beta r \rho_p^{1/3} V^{2/3}}{H^{1/3}} \quad (10.10)$$

where β is a constant of order unity and H is the hardness of the metal or oxide depending on whether the metal or oxide plastic deformation depth is calculated.

These equations were also used by Stack and Bray (1995b) for the construction of their maps. The oxide thickness, Z_{ox} , was calculated using t_b , the time between successive particle impacts, so that Z_{ox} was equivalent to Z_b in Sundararajan's definitions. This implies that Stack and Bray (1995b) assumed an oxide removal mechanism where the oxide was removed down to the oxide-metal interface over each particle impact crater. As it was not specifically mentioned it was assumed that for the calculation of the boundary between regimes E and EC the hardness of the metal, H_m , was used and for boundaries between regimes EC and C1, and C1 and C2 the hardness of the oxide, H_o , was used.

A computer program was written in FORTRAN to perform the Sundararajan calculations and construct the erosion-corrosion maps and is shown in Appendix A. The dominant mechanism over a range of variables, i.e. temperature and velocity at fixed impact conditions was calculated. The boundaries between each mechanism were calculated using a text input calculator (MathCad and MathPad) and these are shown in the figures in this Chapter. The Stack maps were calculated in a similar way using a text input calculator.

10.2.3. Results

10.2.3.1. Sundararajan's maps

Sundararajan's erosion-corrosion maps (Sundararajan, 1991) with variables velocity and temperature were reproduced with the computer program using his published data (the data is listed in Appendix B). The result using a variable critical thickness, a flux of $1.0 \text{ kg m}^{-2} \text{ s}^{-1}$ and a spherical particle geometry is shown in Fig. 10.3a and is compared with the published map Fig. 10.3b. Clearly the maps are not the same and the error appeared to be a typing error for the value of the conversion factor, C. Sundararajan quoted a value of $1.3 \cdot 10^{-4} \text{ m}^3 \text{ kg}^{-1}$ but using his equation defining C:

$$C = \frac{4M_{Fe}}{3M_o\rho_{Fe}} \quad (10.11)$$

where M is the molecular mass and ρ_{Fe} is the density of iron, C becomes $5.9 \cdot 10^{-4} \text{ m}^3 \text{ kg}^{-1}$. Using this value of C yielded the map shown in Fig 10.3c which was very similar to Fig. 10.3b but was shifted by 50° C to lower temperatures.

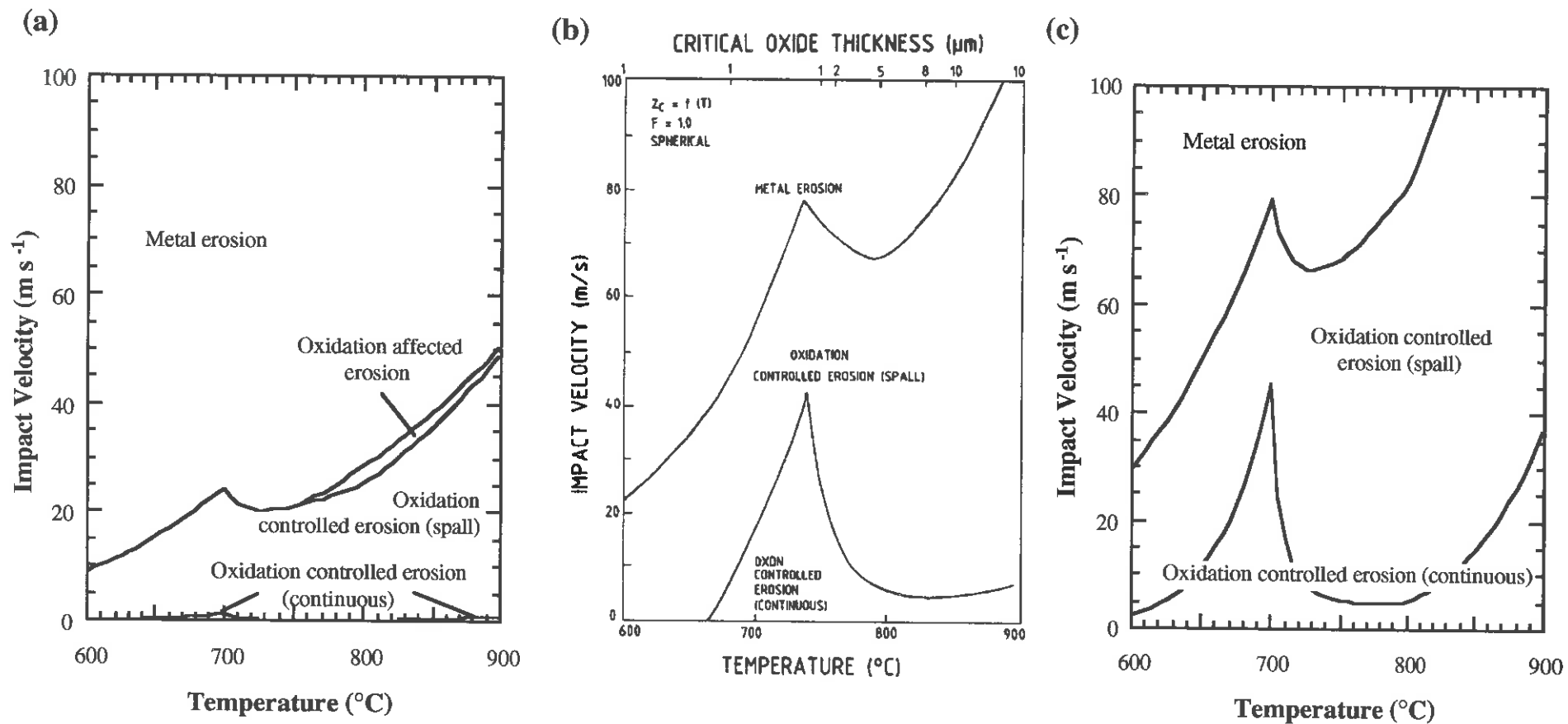
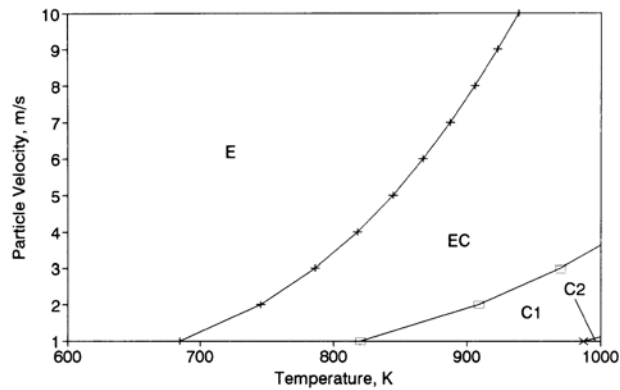


Fig. 10.3. Erosion-corrosion maps for spherical particles, flux = 1.0 kg/kg, and with a variable critical oxide thickness, (a) $C = 1e-4$, (b) after Sundararajan, (c) $C = 5.9e-4$.

The difference may have been caused by a plotting error, as the top axis showing the variable critical oxide thickness was plotted 50° C higher than described in the discussion. The problem was not the change in the definition of the critical thickness as this changed the shape of the map and the 50° C shift also occurred on maps which used a fixed critical thickness, so it seemed that Sundararajan simply plotted the results 50° C too high.

10.2.3.2. Stack and Bray's maps

(a)



(b)

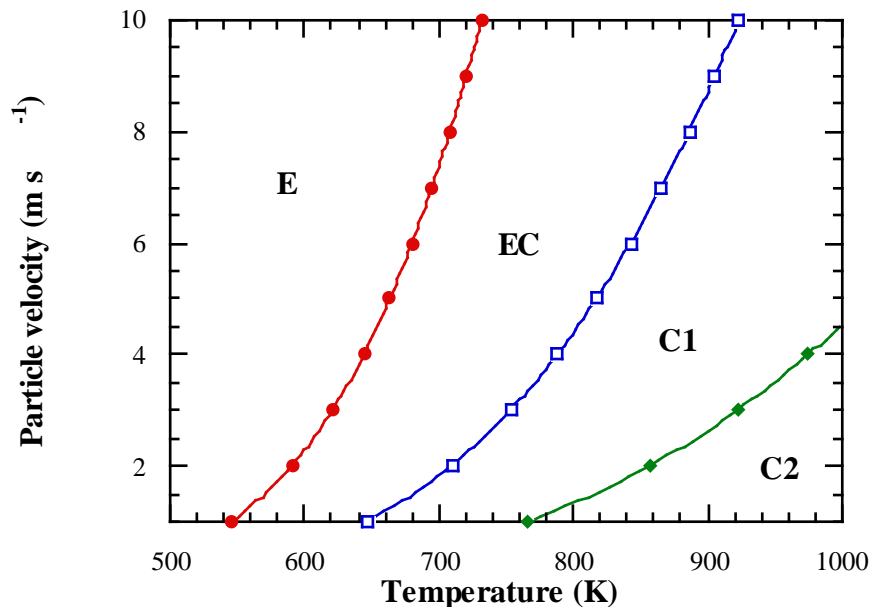


Fig. 10.4. (a) Published figure after Stack and Bray (1995b) and (b) reproduction of (a) using the data given by Stack and Bray for mild steel and at a particle flux of $0.1 \text{ g}^2 \text{ cm}^{-4} \text{ s}^{-1}$.

Reproducing Stack and Bray's (1995b) results using Stack and Bray's model and published data (Appendix B) also gave results which differed from those published. Fig. 10.4a shows the published erosion corrosion regime map of velocity against temperature, and Fig. 10.4b shows the calculated figure using the same published data. The boundary lines in Fig 10.4b are approximately 150 K lower than those in Fig. 10.4a. It is difficult to know if the difference is a mistake in the data published or that data other than that specified was used to construct a specific graph. However, the oxidation kinetic data given in the paper were incorrect as the data given for stainless steel yielded a higher parabolic rate constant than that given for mild steel at the same temperature.

10.2.3.3. Fluidized bed rig values

The two sections above describe the reproduction of work by Sundararajan and Stack and Bray using the published models and data and using the program in Appendix A. To calculate an erosion-corrosion map which represents the environment in the fluidized bed test rig the models were modified and suitable data used. This section describes those changes and the variables and constants used for all three systems are shown in Appendix B.

The values of activation energy, Q , and Arrhenius constant, A_o , were those measured experimentally and described in Chapter Eight. The value of the conversion constant, C , was derived and differed from equation 10.11:

$$C = \frac{M_{\text{Oxide}}}{\text{Val}_o M_o \rho_{\text{Oxide}}} \quad (10.12)$$

where M_{Oxide} and M_o are the molecular weight of the oxide and oxygen respectively, Val_o is the valency of the oxygen in the oxide and ρ_{Oxide} is the density of the oxide. This yields a value of $7 \cdot 10^{-4} \text{ m}^3 \text{ kg}^{-1}$ for magnetite. The flux, F , varies with velocity and can be described by the equation:

$$F = \rho_{\text{fb}} V \sin(\theta) \quad (10.13)$$

where V is the impact velocity, ρ_{fb} is the density of the fluidized bed in kg m^{-3} and θ is the angle of incidence. The density of the fluidized bed was estimated at 1800 kg m^{-3} by measuring the density of the slumped bed and adjusting this to take the change in volume of the bed due to fluidization into account. The bed volume increased as the temperature increased but this was not considered as the change was relatively small.

This gave an estimate of the particle flux if there was no particle deflection or particle-particle interaction before impact with the specimen.

The oxide erosion rate was taken from experimental data (Fig. 10.5) (Rogers, 1992b) of wastage rates of mild steel at 600° C where oxide erosion was the predominant mechanism. Assuming that the thickness loss rate can be expressed as a power law equation (as equation 10.6), the normalised erosion rate, E_o , and the thickness loss rate constant, E , are related by:

$$E_o = \frac{E\rho_p}{F} \left(\frac{V}{V_o} \right)^n \quad (10.14)$$

where V_o is 1, n is 5.6 and E is $2.5 \cdot 10^{-7} \mu\text{m s}^{-1}$. A velocity range of 1-3 m s^{-1} and temperature range of 100 - 800° C was used. This made Z_{ss} independent of flux but not of impact velocity.

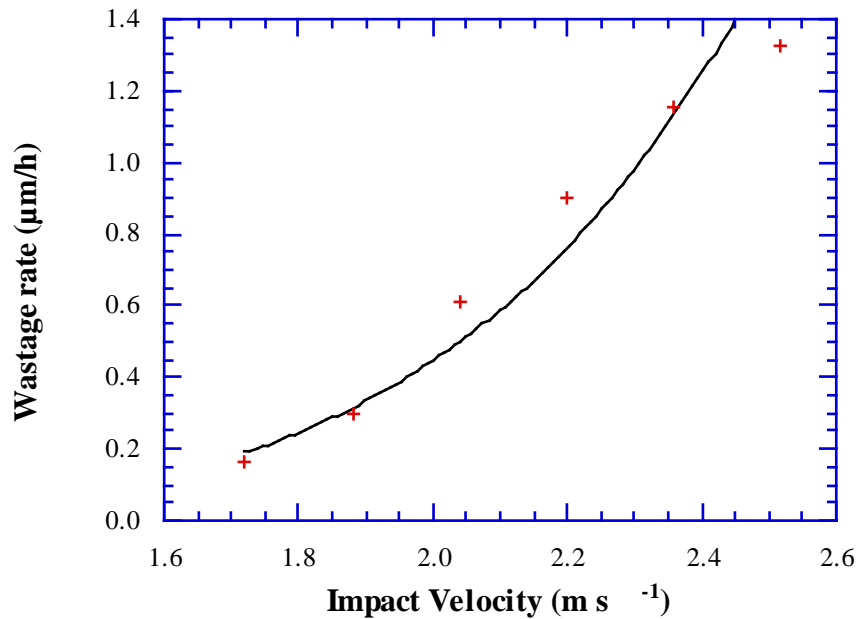


Fig. 10.5. Plot of wastage against velocity for mild steel at 600° C in the fluidized bed test rig.

(i) Sundararajan's maps

Using the model adapted to the fluidized bed environment (previous section) with a variable critical oxide thickness, spherical particle geometry and the long term oxidation kinetics described in Chapter Eight (the average parabolic rate constant measured over 15 h) resulted in Fig. 10.6. A transition from metal erosion to oxidation controlled erosion (spalling) was predicted as the velocity decreased and the temperature increased. A small region of oxidation affected erosion occurred where the steady state thickness was below the critical thickness.

The critical oxide thickness below 700° C was a constant 1 μm (Appendix B), and the boundary between metal erosion and the oxidation controlled erosion (spalling) occurred when the steady state thickness was equal to the critical oxide thickness. The map implied that the erosion-corrosion mechanism changed directly from metal erosion to oxidation controlled erosion (spalling) with an increase in temperature. Experimental results from the fluidized bed test rig showed a region of erosion-oxidation with a very thin interference oxide, thinner than 1 μm , between any metal erosion and spalling regimes.

The values of critical thickness used by Sundararajan's model were obtained from high velocity erosion experiments (Stephenson, 1983) and were perhaps less applicable to the low impact velocities experienced in the fluidized bed. However, spalled areas of oxide were observed at high temperatures (500° C and above on mild steel) where a thick oxide had developed over the wear scar. These spalled areas were around 10 - 30 μm in diameter, larger than the impact craters observed on the interference coloured wear scar (Fig. 6.22). With respect to temperature the position of this boundary on the erosion-corrosion regime map was approximately correct. However, the experimental results suggested a region of erosion-oxidation at lower temperatures than the region of spalling mechanisms.

Ignoring the spalling mechanisms (Fig. 10.7), a transition from metal erosion to oxidation affected erosion to oxide erosion regimes was observed as the velocity was reduced and the temperature increased. This was expected as the steady state thickness increases as the temperature increases and the velocity falls. Fig. 10.8 shows an approximate erosion-map constructed from the experimental results of mild steel in the fluidized bed test rig. In Figs. 10.6 and 10.7 the transition from metal erosion occurred

at a significantly higher temperature and the sensitivity of the boundaries to temperature was greater than in Fig. 10.8.

Experiments on the short term oxidation of mild steel, described in Chapter Eight, showed that the initial apparent parabolic rate constant was an order of magnitude higher than that at longer times. For thin, continually eroded oxides these oxidation kinetics are more relevant than oxidation kinetics measured over many hours. The effect of increasing the apparent parabolic rate constant by an order of magnitude (Fig. 10.9) shifted the oxide erosion and oxidation affected erosion regimes to lower temperatures as the oxide steady state thickness increased for a given temperature, but the shift was not sufficient to agree with the experimental results; the initial oxidation rate was only valid for thin oxides. For thicker oxides at higher temperatures long term kinetics are more appropriate although, in the fluidized bed test rig, the oxidation rate may be generally higher than the measured values due to factors such as tribological enhanced oxidation.

Figs. 10.6 - 10.9 were calculated assuming that the bed particles were spherical although the alumina particles used in the experiments were angular. Sundararajan used a model with conical-ended particles to simulate angular particles in the erosion map calculations. Fig. 10.10 showed that the impact crater diameters, calculated from the model of the conical particles, were closer to the crater size observed on the experimental specimens exposed in the fluidized bed test rig. Fig. 10.11 shows the effect of using conical particles to generate a regime map. When compared with Fig. 10.9 the erosion-oxidation and oxide erosion regimes became dominant at lower temperatures due to the reduction in the particle contact area. This was perhaps closer to the experimental results but metal erosion was still predicted at 300° C and 2 m s⁻¹.

One reason for the maps predicting metal erosion to such a high temperature may be the definitions of the erosion-corrosion mechanisms themselves. The dotted line in Figs. 10.7, 10.9 and 10.11 marked the position where the steady state thickness was equal to the critical thickness (1 µm below 700° C). The oxide thicknesses on the experimental specimen wear scars in the oxidation affected erosion regime were significantly thinner than 1 µm and yet the model predicted a steady state thickness of 1 µm close to the metal erosion and oxidation affected erosion regime boundary.

The velocity exponent, n , determined the gradient of the boundaries as the exponent

determines the rate of change of erosion rate with velocity. The exponent was determined using a power law curve fit from the set of data obtained at 600° C (Fig. 10.5). The experimentally determined exponents also varied with temperature (Fig. 6.9). At 500° C, n was 3.4 and the resultant regime map is shown in Fig. 10.12.

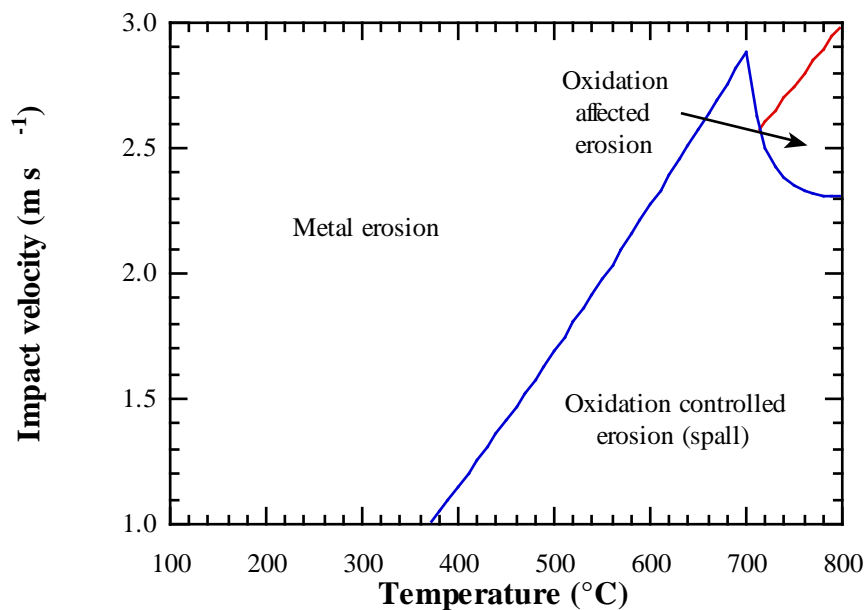


Fig. 10.6. An erosion-corrosion map representing conditions in the fluidized bed test rig, with a variable critical oxide thickness spherical particle and long term oxidation kinetics.

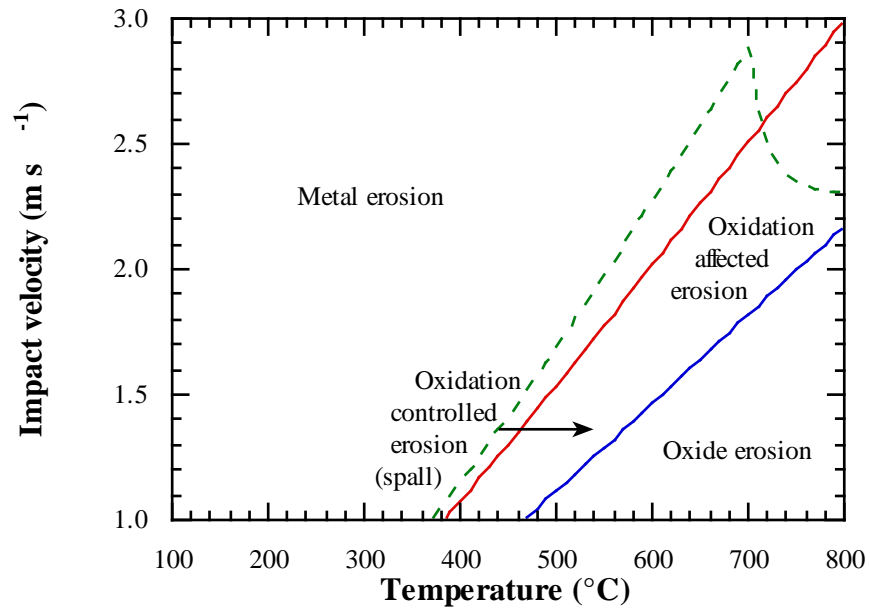


Fig. 10.7. As Fig. 10.6 but without the critical oxide thickness.

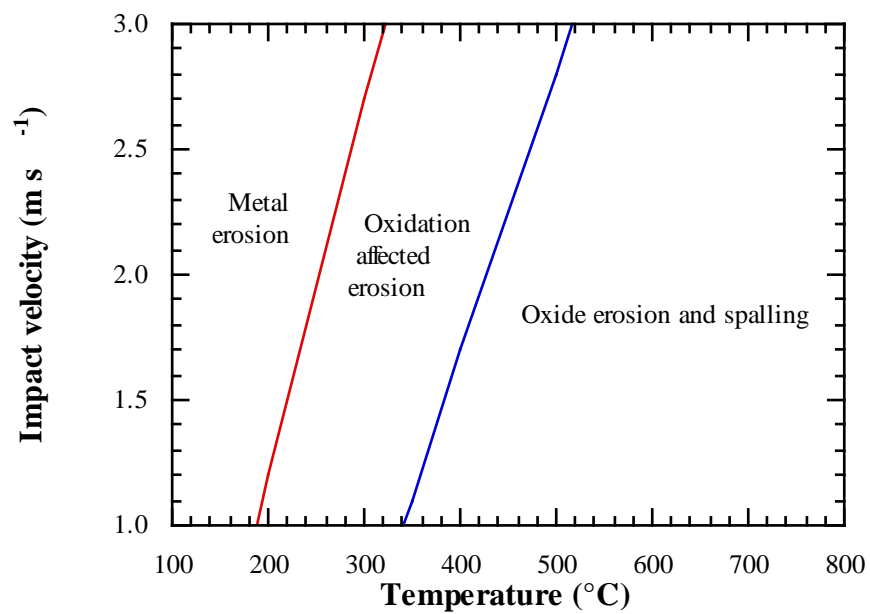


Fig. 10.8. Approximate erosion-corrosion map constructed from the experimental results of mild steel in the fluidized bed test rig.

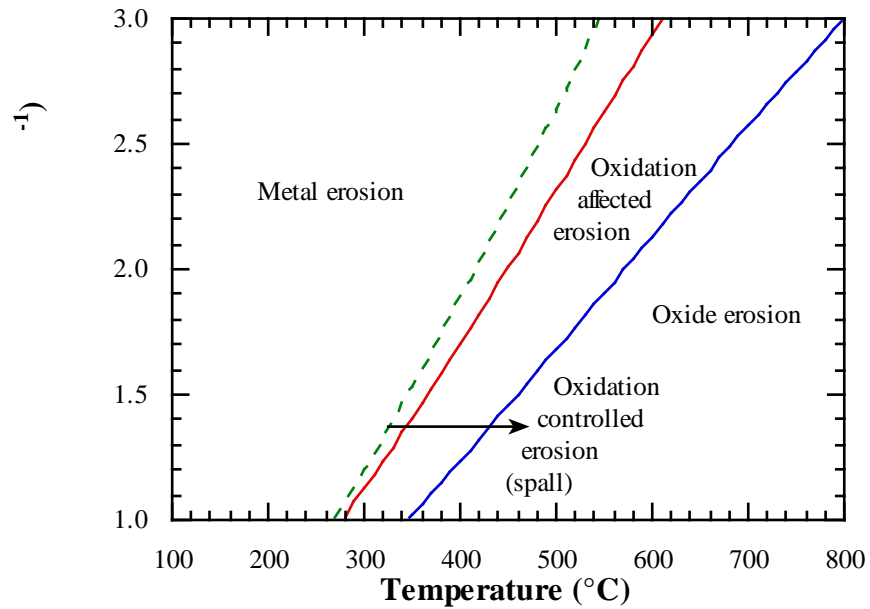


Fig. 10.9. As Fig. 10.7 but with an increase in oxidation rate by a factor of ten.

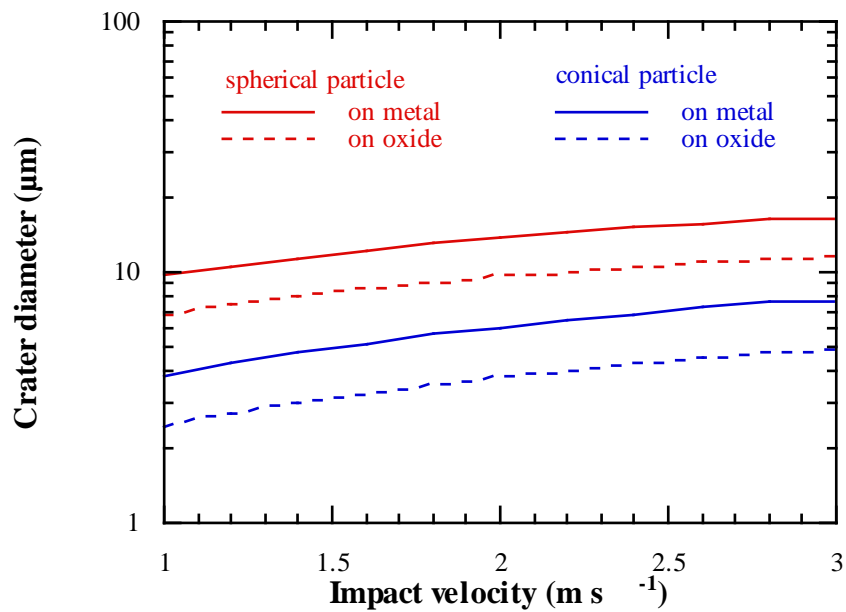


Fig. 10.10. Theoretical crater diameter for spherical and conical alumina particles of 240 μm diameter.

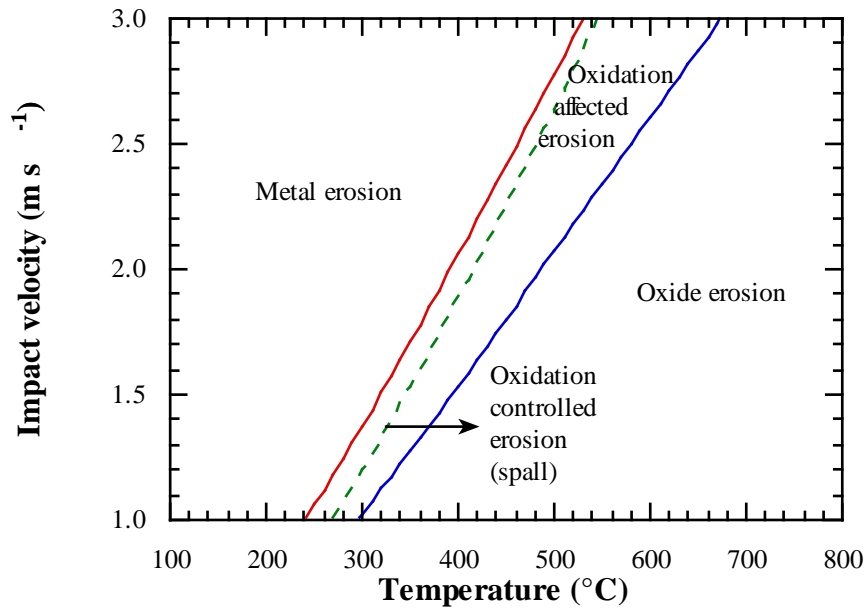


Fig. 10.11. As 10.9 but used model of a conical shaped particle rather than a spherical particle.

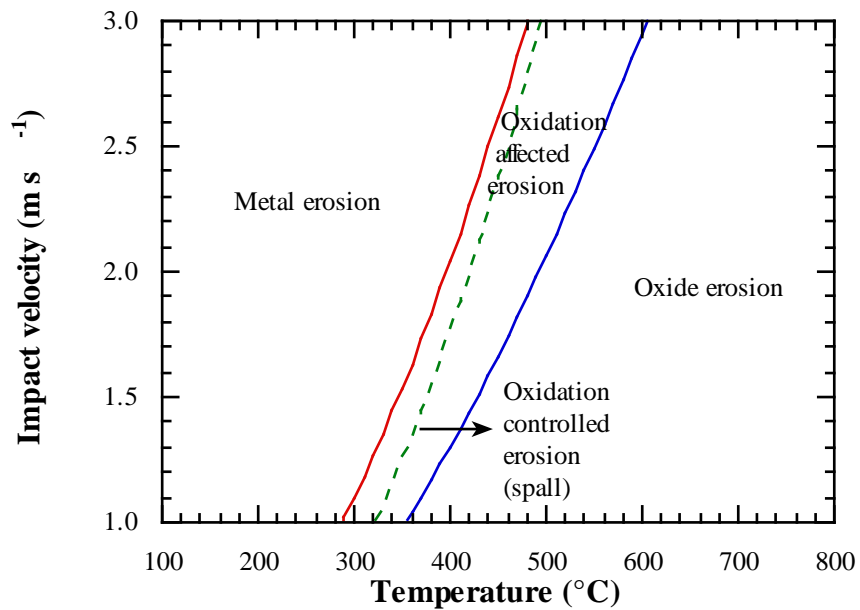


Fig. 10.12. As Fig. 10.11 but using a model of a conical shaped particle rather than a spherical particle and erosion data for 500° C.

(ii) Stack and Bray's maps

These maps were constructed by comparing the oxide grown between successive impacts and the particle deformation depth. Therefore, unlike Sundararajan's maps, the particle flux influenced the time between impacts and hence the oxide thickness grown between successive impacts, Z_b .

To assess the accuracy of the estimate of flux described above (which assumed no particle-particle interactions) the time between successive impacts at the same point on a surface was calculated and compared with experimental specimen wear scars exposed in the fluidized bed for a short time period. A surface that was entirely covered with impact craters would be exposed for a longer period than the time between successive impacts. SEM micrographs of the region of maximum wear of an aluminium specimen at an impact velocity of 2.0 m s^{-1} showed the surface to be entirely covered with impact craters after 1 min (Fig. 9.17) and only partially covered after 2 s (Fig. 9.13). Thus a time between successive impacts was approximated at about 10 seconds. Fig. 10.13 shows the time between successive impacts for spherical and conical particles at various impact angles. The effect of angle on the impact crater size was not considered simply the effect of angle on the flux in the fluidized bed as described in equation 10.14. Comparing this estimate with the theoretical time between impacts shown in Fig. 10.13 shows that the conical particles gave similar values to the experimental observations, while the spherical particle gave shorter times between successive impacts.

The resulting erosion-corrosion regime map relevant to the fluidized bed test rig environment with conical particle geometry, short term oxidation kinetics and various impact angles is shown in Fig. 10.14. The effect of impact angle was to reduce the flux and move the boundaries between the erosion-corrosion regimes to lower temperatures. However, even at an impact angle of 30° , metal erosion was predicted to almost 700° C at 2.0 m s^{-1} . This model did not give very accurate predictions and was less accurate than the model proposed by Sundararajan probably because the mechanism of material removal was assumed to be the same at all oxide thicknesses.

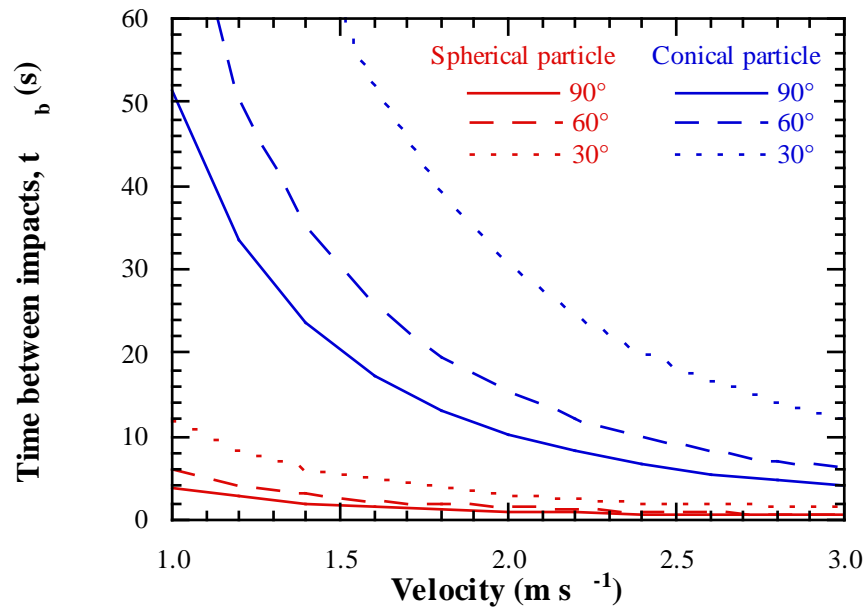


Fig. 10.13. Theoretical time between successive impacts for spherical and conical particle at various impact angles.

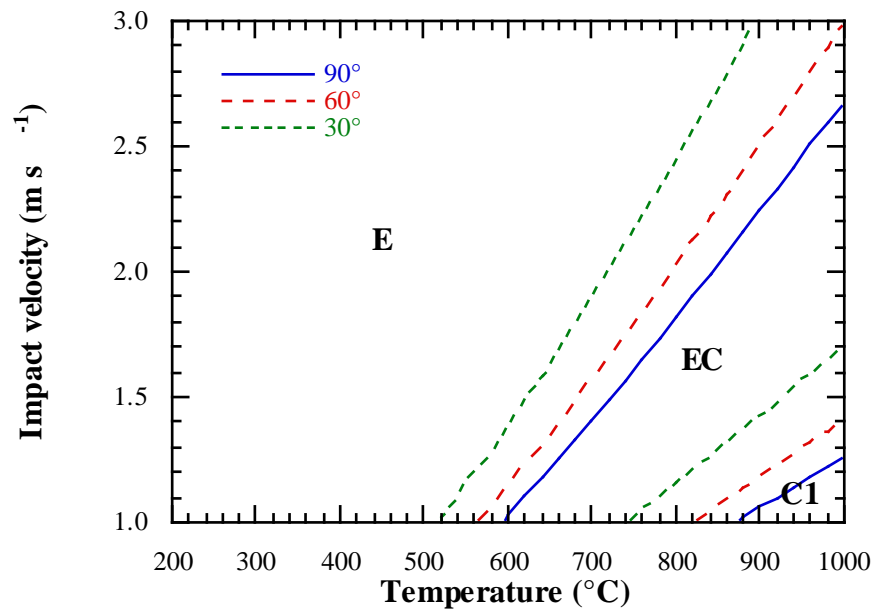


Fig. 10.14. Erosion-corrosion regime map calculated using the Stack and Bray model for a conical particle, and initial oxidation kinetics at several impact angles.

10.2.4. Conclusions

Erosion-corrosion regime maps constructed by Sundararajan (1991) and Stack and Bray (1995b) were reproduced and applied to model the environment experienced in the fluidized bed test rig. Reproduction of both authors results found errors in the published work; a plotting error by Sundararajan and an unknown error by Stack and Bray.

The model predictions for the fluidized bed test rig do not agree with experimental results from erosion-corrosion studies as both models tended to predict metal erosion at a higher temperature than observed in practice. This may be due to model definitions of the regime transitions which were not suitable for low impact velocities, as both the calculated impact area and time between impacts approximately agreed with experimental observations.

10.3. Erosion-corrosion wear modelling

The aim of the erosion-corrosion maps was to calculate a dominant erosion-corrosion mechanism for a given set of environmental conditions. This however did not provide information of the probable wastage rate associated with the mechanism.

Several erosion-corrosion models and corresponding methods for the measurement of wear rates are described below and the results of these models are compared with the experimental results described in Chapter Six and differences are discussed.

10.3.1. Introduction

Markworth *et al.* (1991) derived a parilinear equation for erosion enhanced corrosion in terms of oxide thickness, which is the most convenient unit to use when relating to the fluidized-bed rig, as wastage is measured as a thickness loss rather than a weight change. This type of mechanism was considered by Sundararajan for calculation of the steady state oxide thickness, Z_{ss} .

The equation derived was (also equation 4.5):

$$\dot{S} = \frac{ac}{S^k} - bS \quad (10.15)$$

where S is the oxide thickness, k denotes the order of the oxidation kinetics ($k=0$ linear

kinetics, $k=1$ parabolic kinetics), a is the oxidation rate constant, c is the Pilling-Bedworth ratio and b is a constant. The erosive part of the equation, $-bS$, was used so that an algebraic solution to the equation could be obtained. However, a computer program was written which solved the equation analytically so that this erosion term could be changed. The program was written in FORTRAN using a simple Runge-Kutta subroutine to solve the differential equation (Appendix C). The program solved values of the oxide thickness, $X(1)$, and the position of the oxide/metal interface, $X(2)$, over a given time period. This allowed the oxide/air and oxide/metal interface to be plotted using a graphics program to show the change in oxide profile with time. The program was adjusted to calculate the wastage rate over a range of temperatures so that the temperature dependence could be investigated. The oxide kinetics used were the longer term oxidation kinetics measured experimentally (Chapter Eight) unless otherwise stated.

Other erosion-oxidation mechanisms which were easily modelled were the oxidation controlled erosion (spalling) mechanism described by Sundararajan (1991), and the oxide removal model assumed by Stack and Bray (1995b). The oxide removal model was similar to the oxidation controlled erosion (continuous) mechanism described by Sundararajan (1991) but was valid at any oxide thickness rather than above a critical oxide thickness. For the oxide removal mechanism an oxide thickness, Z_b , allowed to grow between subsequent impacts, was removed over each contact area, and the resulting wear rate, W_o , was:

$$W_o = \frac{Z_b}{t_b} \quad (10.16)$$

where t_b is the time between impacts.

For the oxidation controlled erosion (spalling) mechanism the wastage rate, W_s was:

$$W_s = \frac{Z_c}{t_c} \quad (10.17)$$

where t_c is the time it takes to grow an oxide thickness of Z_c .

Thus for parabolic oxidation:

$$t_c = \frac{Z_c^2}{2K_p} \quad (10.18) \text{ also } (4.9)$$

10.3.2. Results and Discussion

10.3.2.1. Paralineer erosion-oxidation

Fig. 10.15 shows the change in oxide profile over time at 500° C using equation 10.15 with $b = 0.1$. The oxide/air interface is the bottom line with increased wastage moving up the graph. The erosion rate increased as the oxide thickness increased which is shown in Fig. 10.15 as a small increase in the gradient of the oxide/air interface. The oxidation rate decreased with oxide thickness and was evident as a shallowing of the oxide metal interface. After a short time the oxide attained a steady state value and the erosion rate remained constant.

After replacing the term $-bS$ in equation 10.15 with a constant erosion rate (Fig. 10.16) the gradient of the oxide/air interface remained constant. The erosion rate was the same as that used for the erosion-corrosion maps for a velocity of 2 m s^{-1} . A large initial oxide thickness, as in the case of a preoxidised specimen, reached the same steady state thickness (Fig. 10.17).

The wastage rate remained the same with an increase in temperature (500° to 600° C in Fig. 10.18) as it was fixed by the constant wear rate, b , but the steady state oxide thickness increased. The wastage rate was dependent upon changes in the erosion rate and, if a change with temperature was to be observed, the erosion rate needed to have a temperature dependence.

In order to introduce a temperature dependence in the wastage rate it was assumed that only the oxide was removed when the erosion rate was greater than the oxidation rate and therefore the wastage rate became dependent on the oxidation rate. Fig. 10.19 showed the result of this behaviour, as the temperature is decreased a decrease in wastage occurred beyond a critical temperature. The position of the critical temperature occurs when the oxidation and erosion rates are equal and therefore depends on the relative values of the oxidation and erosion rate. Above the critical temperature the wastage rate is dependent on the erosion rate and therefore constant with temperature. The maximum wastage rate was fixed by the erosion rate which, in this case, was measured experimentally at high temperatures and was lower than the maximum wastage observed experimentally at intermediate temperatures. This behaviour was not observed experimentally at higher temperatures as the wastage rate decreased due to the

formation of a thick protective oxide. This implied that for this model to mirror the experimental results the oxide erosion rate would need to equal the maximum wastage rate observed experimentally and also decrease at higher temperatures, although no physical reason can be given for this change.

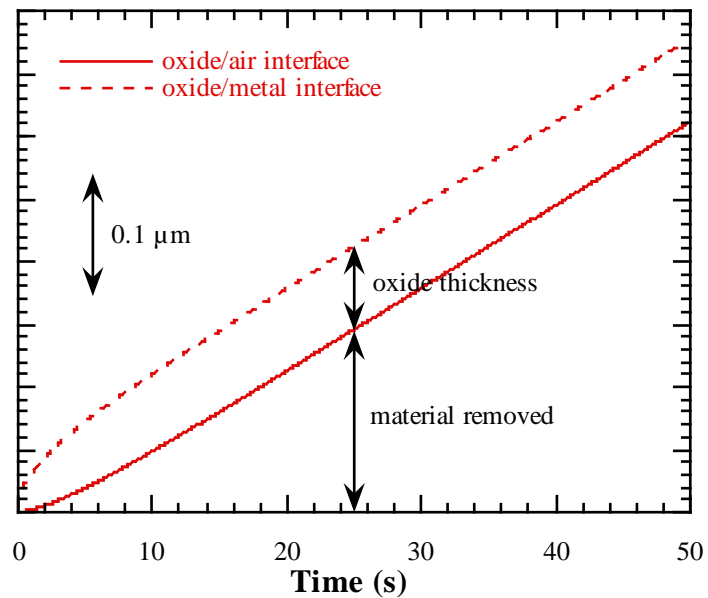


Fig. 10.15. Oxide profile over time with the erosion rate at 0.1 of the oxide thickness and at 500° C.

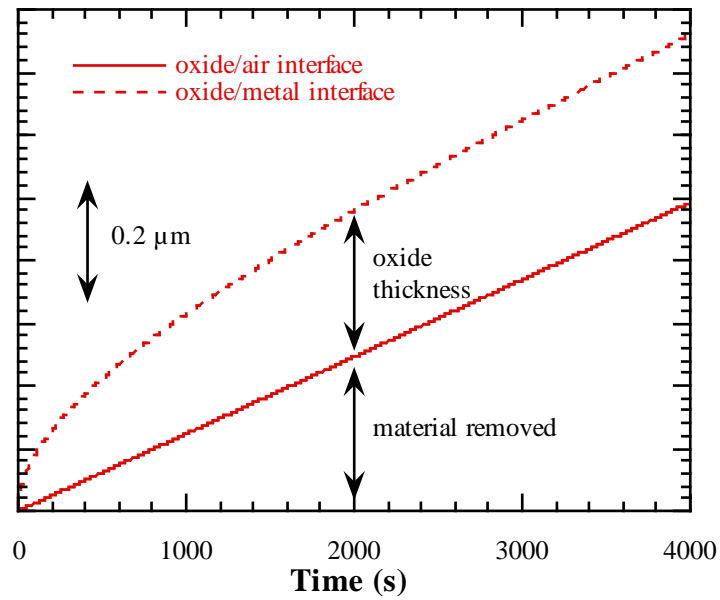


Fig. 10.16. Oxide profile over time with a constant erosion rate as used for the erosion-corrosion maps and at 500°C and velocity 2 m s^{-1} .

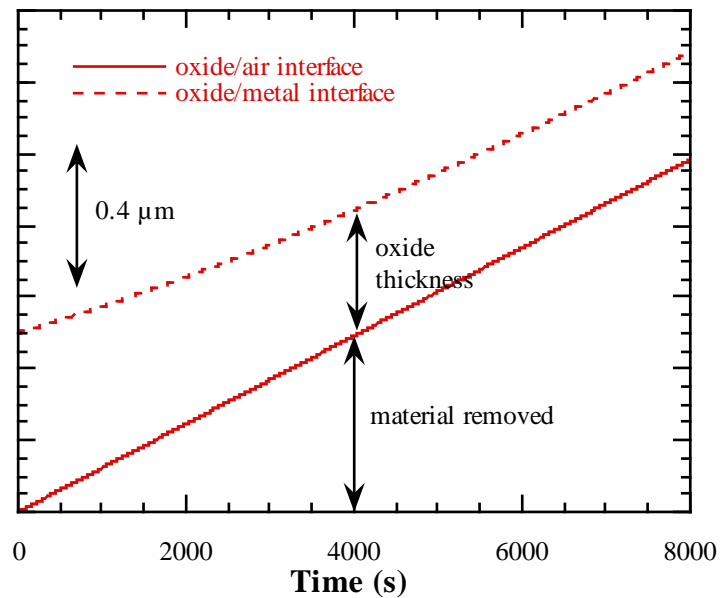


Fig. 10.17. Oxide profile over time with a constant erosion rate as used for the erosion-corrosion maps and at 500°C , velocity 2 m s^{-1} and with an initial oxide thickness of $0.5 \mu\text{m}$.

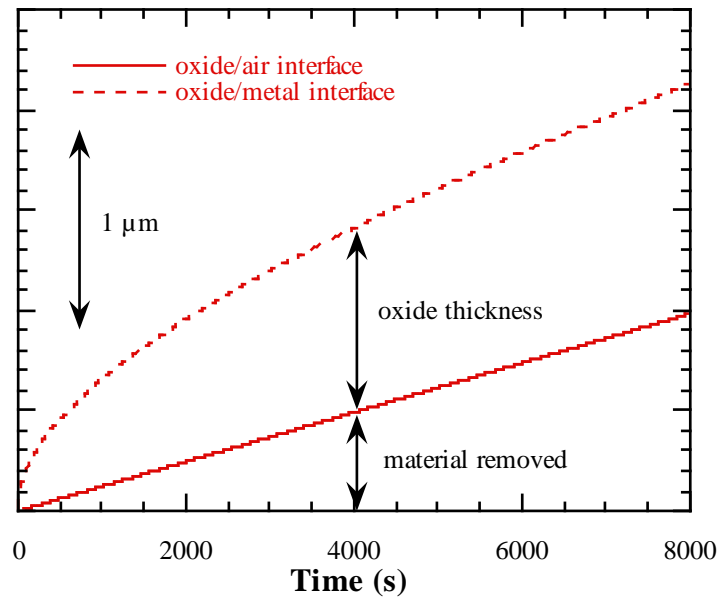


Fig. 10.18. Oxide profile over time with a constant erosion rate as used for the erosion-corrosion maps at 600° C, and velocity 2 m s⁻¹.

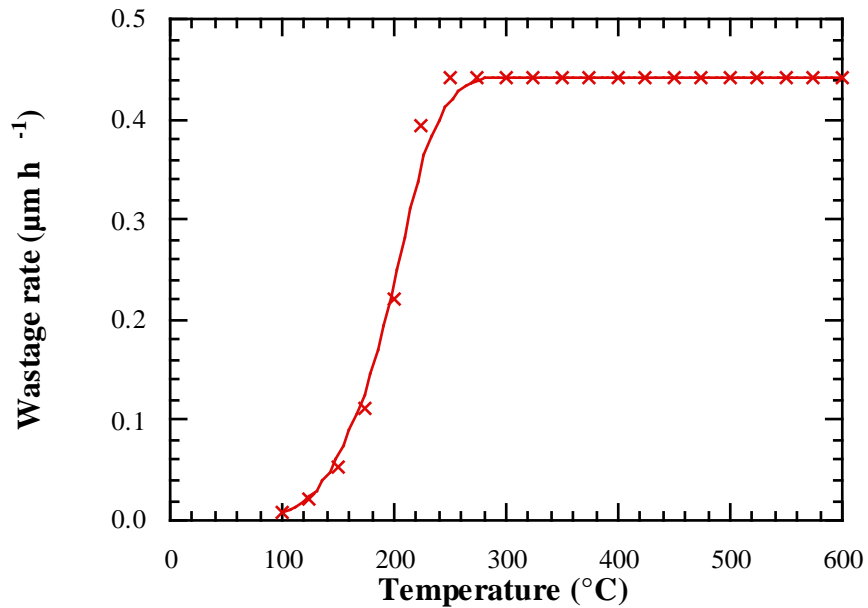


Fig. 10.19. Wastage rate of the oxide air interface against temperature, with no erosion of the metal.

10.3.2.2. Oxide removal and spalling erosion-oxidation models

Fig. 10.20 shows the predicted erosion for the oxide removal mechanism for conical particles at an impact angle of 30° using both the initial maximum oxidation rate constant and the longer term average. A rapid increase in the wastage rate with temperature occurred, which was similar to the increase in wastage shown in Fig. 10.19, as the oxide removed was controlled by the oxidation rate. The higher oxidation kinetics increased the wastage rate at any given temperature.

Fig. 10.21 shows the wear predicted for the oxidation controlled erosion (spalling) for similar conditions, again at the two sets of oxidation kinetics and for a critical thickness, Z_c , of 1 and 10 μm . The wastage again increased rapidly with temperature but at a higher temperature than the oxide removal mechanism. The wear rate was independent of any erosion variables as spalling occurred at a fixed oxide thickness.

The erosion-corrosion maps calculated in section 10.2 predicted a change in mechanism as the temperature increased. The oxide removal mechanism is likely to be dominant at low temperatures when the oxidation rate is low and the oxide is easily removed by each impact. At higher temperatures, as the oxidation rate increases, the oxide is able to form a protective oxide and is removed periodically once a critical oxide thickness is reached and spalling occurs. The wastage from low to high temperature was modelled by considering a change in mechanism from the oxide removal to the spalling mechanism at intermediate temperatures. The initial oxidation kinetics measured in Chapter Eight were suitable where the oxide is thin during the oxidation removal mechanism and the longer term oxidation kinetics are suitable for the spalling mechanism when the time between oxide growth was several hours (Fig. 10.22). For example, at 450°C the time to reach a critical oxide thickness of 1 μm was about 6 hours.

Fig 10.23 shows the variation of the wear rates of the two mechanisms with temperature at an impact velocity of 2 m s^{-1} and angle of 30° with a transition between the two mechanisms to give a graph of wastage rate against temperature similar to the experimental results. The transition was assumed to be gradual from 300°C , over approximately 110°C , so that over this period the oxide was perhaps only partially removed by each impact until the oxide becomes protective enough to be periodically removed by spalling.

At the initial point of transition from the oxide removal mechanism, which was chosen to fit the experimental results, the ratio, R , of oxide thickness grown between successive impacts, Z_b , and the impact deformation depth was calculated at 0.0042. This was significantly smaller than the 0.1 used to define the boundary between metal erosion and the erosion-corrosion mechanisms in the construction of the erosion-oxidation maps by Stack and Bray (1995b) who used the same model. The oxide thicknesses, Z_b , associated with the oxide removal mechanism were very thin; at 2 m s^{-1} and 300°C the oxide thickness was 26 nm which would have the appearance of a violet interference wear scar oxide (from Table 6.1). Experimentally thin interference coloured oxide films were observed up to 350°C so a transition from the oxide removal mechanism seemed appropriate at around 300°C . Fig. 10.24 shows the effect of using $R = 0.0042$ rather than 0.1 in equation 10.1 for the construction of the erosion-corrosion map based on Stack and Bray's model. The boundary between metal erosion and erosion-corrosion shifts to lower temperatures in closer agreement to the experimental results (Fig. 10.8).

Reducing the velocity caused the wastage rate, using the oxide removal mechanism to decrease for a given temperature. The depth of deformation also decreased so that the temperature at the same ratio, R , decreased with velocity. Fig. 10.25 showed the effect of changing velocity while maintaining the same ratio, R , at the initial and end point of the transitional temperature range.

The results were similar to the experimental results (Fig 6.10) at higher and lower velocities than 2 m s^{-1} , with similar maximum wastage rates, a lower temperature at maximum wastage as the velocity was reduced and a widening of the bell shaped curve at higher temperatures. The major differences were that the wastage behaviour at lower temperatures, specifically 200°C , predicted by the oxide removal mechanism gave lower values than those observed experimentally and the wastage behaviour of the spalling mechanism at high temperatures increased with temperature. The model relied on oxidation kinetics which were measured above 350°C , and extrapolated to lower temperatures. The actual rate constants may vary significantly from the extrapolated values if the dominant oxidation mechanism differed from those at higher temperatures, especially at low temperatures and short time periods where oxide nucleation may become significant.

Experimentally the wastage at 600°C was similar to that measured at 500°C (Fig. 6.11) although, at higher temperatures, the rapid oxidation rate of mild steel may cause an

increase in wastage. The critical oxide thickness may also be expected to increase at higher temperatures which would reduce the increase in wastage rate predicted by the spalling mechanism at a fixed critical thickness of 1 μm (Fig 10.21 shows the wastage for a critical oxide thickness of 10 μm).

Despite the very simple nature of the two erosion-corrosion mechanisms, their combination of wastage rates and oxide thickness values were similar to observed experimentally values when predicted over a wide temperature range.

10.3.3. Conclusions

A computer program was written which used a para-linear equation to model erosion-corrosion. The program successfully modelled the important behaviour of erosion-corrosion.

Various points emerged;

- (i) A steady state oxide thickness was reached whether the metal has been pre-oxidised or not.
- (ii) The erosion determined the wastage rate. If the temperature was increased the wastage rate remained the same but the oxide thickness increased.
- (iii) If the metal was assumed to be erosion resistant, the wastage rate decreases at low temperatures when the erosion rate is greater than the oxidation rate. The wastage rate was then controlled by the oxidation rate. A bell shaped curve occurred if the erosion rate also decreases with temperature.

Modelling wastage by considering a change from an oxide removal mechanism to an oxide spalling mechanism using some semi empirical results gave sensible predictions which agreed well with the experimental results.

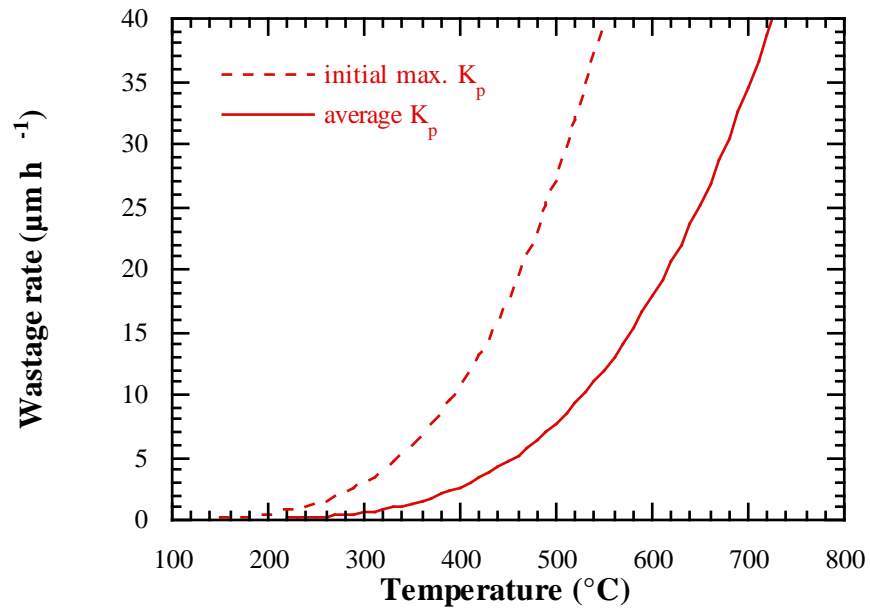


Fig. 10.20. Graph of wastage rate against temperature for the oxide removal mechanism with conical particles impacting at 2 m s^{-1} and 30° .

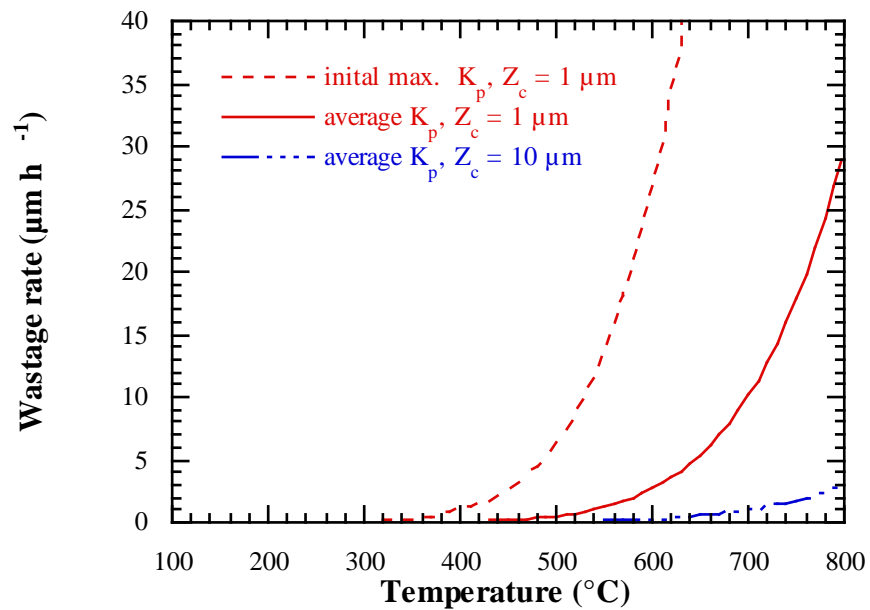


Fig. 10.21. Graph of wastage rate against temperature for the oxidation controlled erosion (spalling) mechanism. Independent of erosion variables.

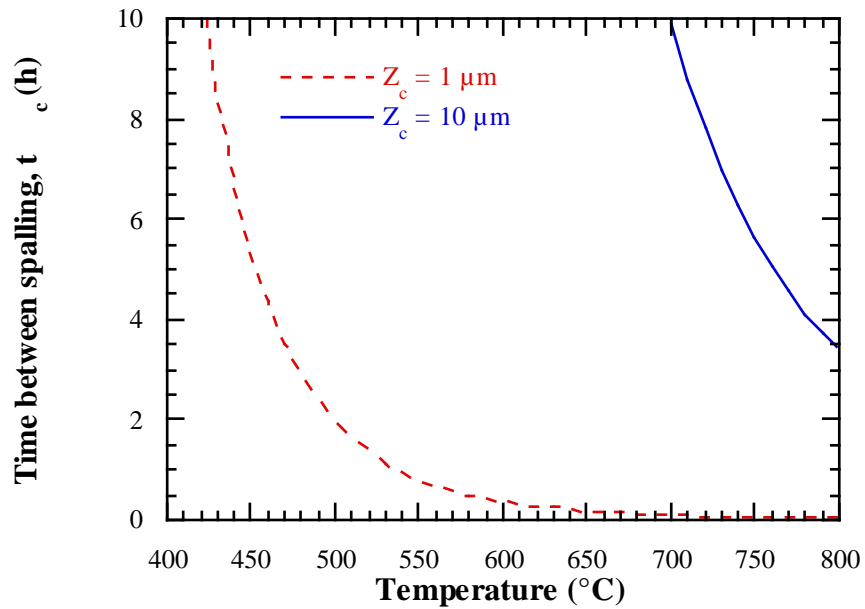


Fig. 10.22. Time between spalls for the longer term oxidation kinetics and a critical oxide thickness of 1 and 10 μm .

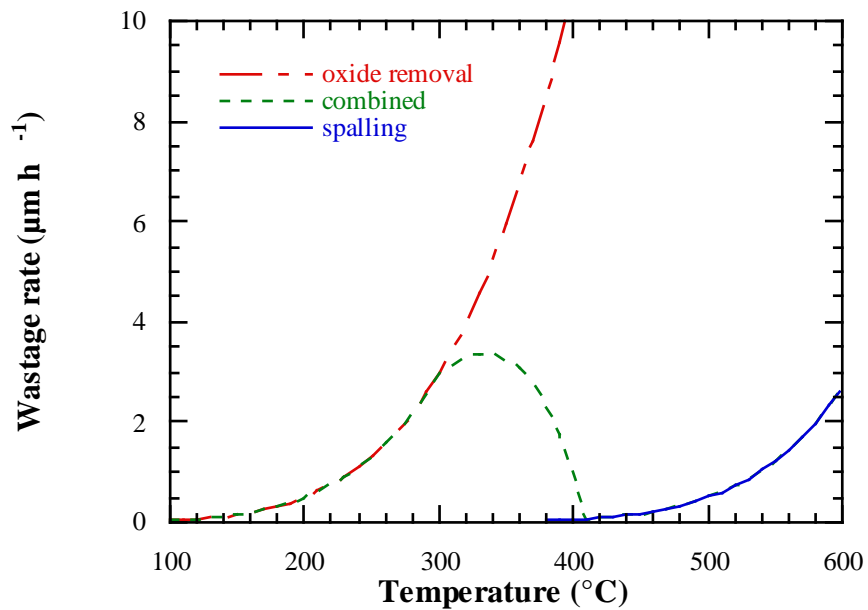


Fig. 10.23. The wastage rate at 2 m s^{-1} for a conical particle impacting at 30° combining the oxide removal and oxide spalling mechanisms.

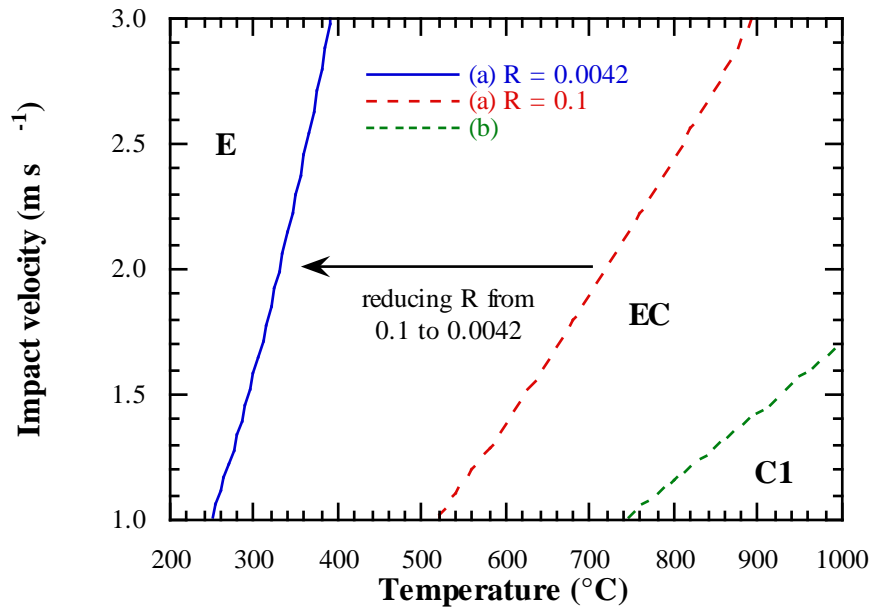


Fig. 10.24. As Fig. 10.14 at an impact angle of 30° showing the effect of using $R = 0.0042$ rather the $R = 0.1$ on the definition of the boundary between metal erosion and erosion-corrosion regimes.

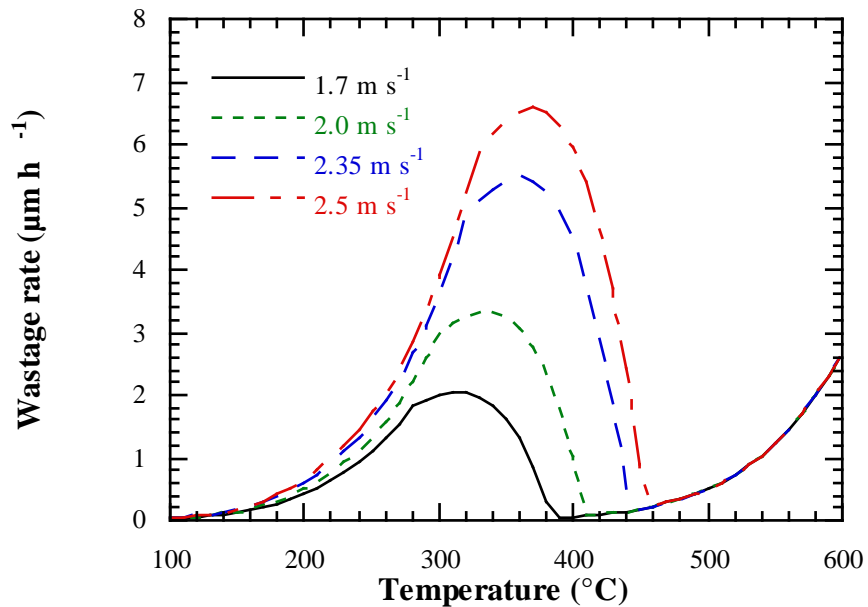


Fig. 10.25. The effect of velocity on the wastage rate for a conical particle impacting at 30° combining the oxide removal and oxide spalling mechanisms.

Appendix A

FORTRAN program for constructing erosion-corrosion maps

Program listed uses Sundararajan constants (see Appendix B) and a variable critical thickness.

Declaration of variable types.

```
INTEGER I
REAL*8 ZSS,ZC,ZB,Eo,Eoo,F,LO,LM,Kp,Po,Pp,Ho,Hm,r,n,V,Vo,Ao,
1Q,Rc,T,ONE,TWO,THREE
CHARACTER*1 LINE(31)
```

Defining constants and variables.

```
n = 3.0
Ho = 3.0E09
Hm = 0.5E09
Eoo = 1.0E-06
Vo = 10
C = 5.9E-04
Ao = 1E5
Q = 210E03
Rc = 8.314
Po = 5400
Pp = 3200
r = 1E-04
F = 1.0
```

Loop to calculate dominant mechanism over range of temperatures (600-800° C) at each velocity from 101-1m s⁻¹.

```
DO 13 V = 101, 1, -5
I = 0
DO 11 T = 873, 1173, 10
I = I + 1
```

Defining variable critical thickness, can be replaced by a constant.

```
IF (T .LT. 973) THEN
ZC = 1E-06
ENDIF
IF (T .GT. 1073) THEN
ZC = 1E-05
ENDIF
IF (T .GT. 973 .AND. T .LT. 1073) THEN
ZC = (1+0.09*(T-973))*1E-06
ENDIF
```

Calculating values for determining dominant mechanism. The constants and are left out as their value is unity.

```
Kp = 0.5*(C**2)*Ao*EXP(-Q/(Rc*T))
Eo = Eoo*(V/Vo)**n
ZSS = ONE(Kp, Po, Eo, F)
ZB = TWO(Kp, r, V, F, Pp, Ho)
LO = THREE(r, Pp, V, Ho)
```

LM = THREE(r, Pp, V, Hm)

Determining dominant mechanism with each mechanism numbered between 1 to 5. The erosion rate is assumed to be higher than the metal erosion rate.

```

IF (ZSS .LT. ZC) THEN
  IF (ZSS .GT. LO) THEN
    LINE(I) = "2"
  ELSE
    IF (ZSS .LT. (0.1*LM)) THEN
      LINE(I) = "1"
    ELSE
      LINE(I) = "3"
    ENDIF
  ENDIF
ELSE
  IF (ZB .LT. ZC ) THEN
    LINE(I) = "5"
  ELSE
    LINE(I) = "4"
  ENDIF
ENDIF
11 CONTINUE

```

Writing an array of numbers representing mechanisms over a range of temperatures for a velocity.

```

WRITE(*,101) LINE
101 FORMAT(1X,31A)
13 CONTINUE
END

```

Functions to calculate equations

```

FUNCTION ONE(W, X, Y, Z)
REAL*8 ONE,W, X, Y, Z
ONE = ((W*X)/(Y*Z))
END

```

```

FUNCTION TWO(I, J, K, L, M, N)
REAL*8 TWO,I, J, K, L, M, N
TWO = 1.26*(((I*J)/(K*L))**0.5)*((M*N)**0.25)
END

```

```

FUNCTION THREE(I, J, K, L)
REAL*8 THREE,I, J, K, L
THREE = (2.56*I*(J**0.25)*(K**0.5))/(L**(0.25))
END

```

Appendix B

Variables and constants used for erosion-corrosion map construction

Constants/variables	Symbol	Values			Units
		Sundararajan's	Stack's	Fluidized Bed	
Hardness of oxide	H_o	3.0	3	4.0	GPa
Hardness of metal	H_m	0.5 (2.0)	0.5	1.0	GPa
Parabolic rate constant	K_p^o				$kg^2 m^{-4} s^{-1}$
Arrhenius constant	A_o	$10^5 (10^4 10^6)$	6.5	$3 \cdot 10^{-4}$ (long) $5.5 \cdot 10^{-4}$ (short)	$kg^2 m^{-4} s^{-1}$
activation energy	Q	210	82.5	93 (long) 82.5 (short)	$kJ mol^{-1}$
stoichiometric factor	f		0.7		
Erosion rate of oxide	E_o				$kg kg^{-1}$
erosion rate constant	E_{oo}	$10^{-6} (10^{-5} 10^{-7})$		$9.9 \cdot 10^{-9}$	$kg kg^{-1}$
reference velocity	V_o	10		1	$m s^{-1}$
velocity exponent	n	3		5.6	
Density of oxide	ρ_o	5400	5400	5200	$kg m^{-3}$
Density of particle	ρ_p	3200	3200	4000	$kg m^{-3}$
Erodent radius	r	100	200	120	μm
Conversion factor for transforming K_p^o to K_p	C	$5.9 \cdot 10^{-4}$		$7 \cdot 10^{-4}$	$m^3 kg^{-1}$
Particle flux rate	F	1.0 (0.1,10.0)	1.0	$1800 \cdot V$	$kg m^{-2} s^{-1}$
Particle shape		Spherical (Conical)	Spherical	Spherical and Conical	
Critical oxide thicknesses	Z_c				
constant		(1,10)			μm
variable		$1 < 700^\circ C$ $1 + 0.09(T - 700) 700 - 800^\circ C$ $10 > 800^\circ C$			μm
Impact velocity	V	5-100	1-10	1-3	$m s^{-1}$
Test temperature	T	600-900	327-727	200-800	$^\circ C$

K_p = scaling constant = $0.5C^2A_o \exp(-Q/RT)$, E_o = erosion rate of oxide = $E_{oo}(V/V_o)^n$

$C = 4M_{Fe}/3M_{O_2}\rho_{Fe}$ or correctly $C = M_{oxide}/M_{O_2}Val_o\rho_{oxide}$; M is the molecular weight; ρ_{Fe} is the density of iron ($7860 kg m^{-3}$); ρ_{oxide} is the density of the oxide and Val_o is the valency of the oxygen in the oxide.

Appendix C

FORTRAN program to calculate oxide profile over time

This program calculates the oxide thickness and wastage over time using a Runge-Kutta method. It can easily be extended to calculate wastage rates as a function of temperature.

Declaration of variables

```
INTEGER I,N
```

```
REAL*8 T,DT,X(2),DX(2),W1(2),W2(2),W3(2),W4(2)
```

Defining constants and starting values, N = No. of differential equations, T = Time, DT = Time interval, X(1) = Oxide thickness, and X(2) = Position of oxide metal interface.

```
N = 2
```

```
T = 0.0E0
```

```
DT = 1.0E0
```

```
X(1) = 0.001E0
```

```
X(2) = 0.001E0
```

Writes out data headings

```
WRITE (*,10) 'Time (sec)', 'Ox-air', 'Ox-met'
```

```
10 FORMAT (A22, A20, A19)
```

```
WRITE (*,*)
```

```
WRITE (*,11) T, X(2)-X(1), X(2)
```

```
11 FORMAT (3F21.7)
```

```
DO 12 I = 1,50
```

```
CALL RKUTTA (X,DX,W1,W2,W3,W4,N,T,DT)
```

```
WRITE (*,11) T, X(2)-X(1), X(2)
```

```
12 CONTINUE
```

```
END
```

Defines differential equation. Units for AO are in $\mu\text{m}^2 \text{s}^{-1}$

```
SUBROUTINE DXBDT (X,DX,N,T)
```

```
INTEGER N
```

```
REAL*8 T,X(N),DX(N),Q,R,A,B,AO,TEMP
```

```
TEMP = 773.0D0
```

```
Q = 1.0E5
```

```
R = 8.314E0
```

```
AO = 7.35E0
```

```
B = 0.1E0
```

```
A = AO*EXP(-Q/(R*TEMP))
```

```
DX(1) = (A/X(1))-(B*X(1))
```

```
DX(2) = A/X(1)
```

```
END
```

Solves differential equation at given time T

```

SUBROUTINE RKUTTA(X,DX,A,B,C,D,N0,T0,DT)
INTEGER I,N,N0
REAL*8 T0,DT,T,H,Z,X(N0),DX(N0),A(N0),B(N0),C(N0),D(N0)
N = N0
Z = T0
H = DT/3
DO 1 I = 1, N
    D(I) = X(I)
1  CONTINUE
T = Z

CALL DXBDT (X,DX,N,T)
DO 2 I = 1,N
    A(I) = H*DX(I)
    X(I) = D(I) + A(I)
2  CONTINUE
T = Z + H

CALL DXBDT (X,DX,N,T)
DO 3 I = 1,N
    B(I) = H*DX(I)
    X(I) = D(I) + (A(I) + B(I))*0.5D0
3  CONTINUE

CALL DXBDT (X,DX,N,T)
DO 4 I = 1,N
    B(I) = H*DX(I)
    X(I) = D(I) + (A(I) + B(I)*3)*0.375D0
4  CONTINUE
T = Z + DT*0.5D0

CALL DXBDT (X,DX,N,T)
DO 5 I = 1,N
    C(I) = H*DX(I)
    X(I) = D(I) + (A(I) - B(I)*3 + C(I)*4)*1.5D0
5  CONTINUE
T = Z + DT

CALL DXBDT (X,DX,N,T)
DO 6 I = 1,N
    Z = D(I)
    D(I) = H*DX(I)
    X(I) = Z + (A(I) + C(I)*4 + D(I))*0.5D0
    DX(I) = (A(I)*2 - B(I)*9 + C(I)*8 - D(I))/10
6  CONTINUE
T0 = T0 + DT
END

```

Chapter 11

Conclusions and Future work

11.1. Conclusions

Studies of erosion-corrosion in the fluidized bed test rig showed that there was no significant difference in the wastage behaviour of specimens exposed isothermally and those in a temperature gradient at the same metal temperature. The position of the thermocouple was critical when measuring the specimen metal temperature as the temperature measured at the back of the specimen was shown to be up to 200° C cooler than the temperature measured by a similar thermocouple attached to the wear scar during a test. The cooled specimen's visual and microscopic appearance after the test generally agreed with isothermally tested specimens at similar metal temperatures but there were some inconsistencies and therefore some doubt over the accuracy of the temperature measurements of the wear scar.

Factors other than the presence of a temperature gradient may explain the differences reported between the laboratory fluidized bed erosion-corrosion studies and FBCs. Experiments have shown that the temperature on the region of wear was significantly higher than unworn regions in close proximity where temperature measurements may have been taken.

Accurate oxidation tests of mild and some low alloy steels using a thermogravimetric balance showed that the apparent initial parabolic rate constant was approximately an order of magnitude higher than at longer times. The initial oxidation kinetics were perhaps more relevant to erosion-oxidation modelling as the equilibrium oxide thickness observed in the erosion-corrosion tests was typically very thin.

Drop tube erosion tests showed a large degree of metal deformation at low impact velocities. The erosion craters were larger than those observed at similar velocity in the fluidized bed probably due to the larger particle-particle interactions. Due to the high particle flux in the fluidized bed short term exposure experiments did not yield accurate quantitative values for flux, although some useful estimates were obtained.

The silica tube specimens exposed in the fluidized bed test rig presented many experimental difficulties and showed very inconsistent wear at 300° C which was dramatically higher than at 200° C. There was no evidence of a change in mechanism at the different temperatures.

Simple erosion-corrosion models were used to construct erosion-corrosion regime maps relevant to the environment in the fluidized bed test rig. The models tended to predict metal erosion to higher temperatures than observed experimentally. The calculated steady state oxide thickness was comparable to that observed experimentally so the definition of the transition from metal erosion was probably unsuitable for low velocity impacts. Using the experimental results to define a transition point between an oxide removal and spalling erosion-corrosion model, the changes in wastage behaviour with impact velocity were reproduced with some success.

11.2. Future work

Further tests examining the effect of a temperature gradient on erosion-corrosion are required so that the temperature gradient between the bed and specimen is increased to values closer to those observed in fluidized bed combustors. This would require a temperature difference between the bed and the specimen of up to 600° C rather than the 250° C obtained in the test rig. The current rig, in its present form, is achieving close to its maximum potential temperature difference. A new design of rotor is required that uses an enclosed cooling system (i.e. which is not vented above the bed) and which cools a smaller part of a specimen so that the heat removed from the bed is reduced, as any increase in cooling in a specimen of the current size would remove more heat than the electric furnace surrounding the bed can replace.

The need to assess the accuracy of the wear scar temperatures is important and to establish whether the hotter wear scar was primarily due to the flow of hotter bed particles over the wear scar. This is of interest to laboratory studies and FBCs as the worn areas may be hotter during wear which may change the perceived wastage-temperature behaviour.

The reduction of particle deposition, seen at lower temperatures under a temperature gradient, is worth investigating as it is not fully understood why deposition occurs at some temperatures and not at others. Although the results suggested that the wastage decreased at lower temperatures in the absence of deposition, the formation of a particle

deposit layer was shown to be very wear resistant and may prove useful in reducing wastage by erosion-corrosion.

More short time exposure tests may establish a more accurate time between subsequent impacts at various points on the specimen by observing the time it takes to saturate the wear scar with impacts. This information may allow a better estimate of the particle flux in the fluidized bed test rig to be calculated.

Any further tests on examining the erosion of silica in the fluidized bed test rig need to be of long duration with few interruptions to reduce the chance of the specimen cracking at the end of each exposure. An accurate method of measuring the extent of fluidization of the fluidized bed is required in order to reduce any effect of variations of fluidization which may have caused the inconsistent wear of silica.

Oxidation experiments were only accurate enough to obtain short term oxidation kinetics above 350° C, so that the oxidation rate constants at lower temperature used in the erosion-oxidation models were obtained from extrapolating the experimental data. A more accurate method of obtaining the short term oxidation kinetics at lower temperatures is required to improve the models. Oxide dissolution techniques could be used for measuring the thickness of thin films to obtain some quantitative short term oxidation kinetics at low temperatures.

The computer modelling described in this thesis was based on very simple erosion-oxidation models and as a result is difficult to develop further. A more flexible model would consider a combination of many individual impacts so that a suitable erosion-corrosion mechanism and associated material removal can be considered for each impact. For example, this would allow modelling of variations in surface morphology on a single sample and the effect of changing environmental conditions.

Chapter 12

References

Anand, K., Hovis, S. K., Conrad H., and Scattergood R.O. (1987), "Flux effects in solid particle erosion," Wear, **118**, 243-257.

Bellman, R. and Levy, A.V. (1981), "Erosion mechanism in ductile metals," Wear, **70**, 1-27.

Birks, N. and Meier, G. H. (1983), "Introduction to High Temperature Oxidation of Metals," (London: Edward Arnold).

Bitter, J. G. A. (1963), "A study of erosion phenomena (part II)," Wear, **6**, 169-190.

Boggs, W. E., Kachik, R. H., and Pellisser, G. E. (1965), "The effect of oxygen pressure on the oxidation of polycrystalline zone-refined iron," Journal of the Electrochemical Society, **112**, 539-546.

Botterhill, J. S. M. (1983), "Fluidized bed behaviour" in "Fluidized beds, combustion and applications" J. R. Howard, ed. Applied science publishers Ltd. (London).

Brain, S. and Minchener, A. (1990), "Minimisation of wastage in bubbling atmospheric fluidised bed boilers," proc. 4th Int. Conf. on Corrosion-Erosion-Wear of Materials at Elevated Temperatures, A.V. Levy (ed.), NACE, Houston, TX.(Berkeley, CA) paper 40.

Bruce, D. and Hancock, P. (1970), "Influence of specimen geometry on the growth and mechanical stability of surface oxides formed on iron and steel in the temperature range 570° - 800° C," Journal of the Iron and Steel Institute, **208**, 1021-1024.

Burnard, G. K. (1995), "Clean coal technologies: background and current status," proc. Clean Coal Technologies The Institution of Mechanical Engineers, (IMEchE HQ, London England. 13 June 1995).

Caplan, D. and Cohen, M. (1966), "The effect of cold work on the oxidation of iron from 400° - 600° C," Corrosion Science, **6**, 321-335.

Chang, Y. and Wei, F. (1989), "Review, High temperature oxidation of low alloy steels," Journal of Materials Science, **24**, 14-22.

Chang, S. L., Pettit, F. S., and Birks N. (1990), "Interaction between erosion and high-temperature corrosion of metals: The erosion-affected oxidation regime," The Oxidation of Metals, **34**(1), 23-45.

Christman, T. and Shewmon, P. G. (1979), "Erosion of strong aluminum alloy," Wear, **52**, 57-70.

Cooper, J. F. (1995), "The development of VESTA, GEC ALSTHOM's standard range of clean burn coal fired power plant," proc. Clean Coal Technologies, The Institution of Mechanical Engineers, (IMEchE HQ, London England. 13 June 1995).

Cousens, A. K. and Hutchings, I. M. (1983), "Influence of erodent particle shape on the erosion of mild steel," proc. 6th International Conference on Erosion by Liquid and Solid Impact, J. E. Field and N.S. Corney (ed.), University of Cambridge (Cambridge), paper 41.

Cox, G. C., McEnaney, B., and Scott, V. D. (1972), "A chemical diffusion model for partitioning of transition elements in oxide scales on alloys," Philosophical Magazine, **26**, 839-851.

Entwisle, M. J., Hutchings, I. M. and Little, J. A. (1987), "Evaluation of a novel fluidized bed erosion rig," proc. 7th Int. Conf. Erosion by Liquid and Solid Impact, J. P. Dear and J. E. Field (ed.), Cavendish Lab, University of Cambridge. (Cavendish Lab., Cambridge England. 7-10 Sept. 1987), paper 71.

Entwisle, M. J. (1990), "Erosion-corrosion of iron-chromium alloys in a fluidized bed environment," PhD dissertation, (University of Cambridge).

EPRI (1995), "PFBC: Maturing Technology," EPRI.

Evans, A. G. and Wilshaw, T. R. (1976), "Quasi-static particle damage in brittle solids - I Observations, analysis and implications," Acta Metallurgy, **24**, 939-956.

Evans, A. G., Gulden, M. E., and Rosenblatt, M.E. (1978), "Impact damage in brittle materials in the elastic-plastic response regime," Proc. R. Soc. London Ser. A, **361**, 343-365.

Eubanks, A. G., Moore, D. G. and Pennington, W. A. (1962), "Effect of surface roughness on the oxidation rate of iron," Journal of the Electrochemical Society, **109**, 382-389

Evans, U. R.(1968), "The Corrosion and Oxidation of Metals: First Supplementary Volume," (London: Edward Arnold).

Finnie, I. (1960), "Erosion of surfaces by solid particles," Wear, **3** , 87-103.

Finnie, I., Wolak, J. and Kabil, Y. (1967), "Erosion of metals by solid particles," Journal of Materials, **2**, 682-700.

Fraunhofer, J. A. and Pickup, G. A. (1970), " Some observations on the reproducibility of high temperature scaling behaviour of Fe and low alloy steels," Corrosion Science, **10**, 253-260.

Geldart, D. (1973), Powder Technology, **7**, 285.

Glover, D. M. (1980), "Heat effects on oxidation rates and kinetics," Corrosion Science, **20** , 1185-1193.

Griess, J. C., Devan, J. H. and Maxwell, W. A. (1978)," Effect of a high heat flux on the corrosion of 2.25 Cr - 1 Mo steel in superheated steam," Materials Performance, **17**, No. 1, 9-15.

Hall, D. J. and Saunders, S. R. J. (1990), "Corrosion-erosion of alloys exposed in fluidized bed combustors," E. Bachelet *et al.* (ed.), Kluwer Academic Publishers, Dordrecht (Liège), 157-166.

Hertz (1882), "On the elastic contact of solids," J. Reine und Angewandte Mathematik, **92**, 156-171.

Hockey B. J. (1971), "Plastic deformation of aluminium oxide by indentation and abrasion," Journal of the American Ceramics Society, **54**, 223-231.

Hogmark, S., Hammarsten, A. and Soderberg, S. (1983), "On the combined effect of corrosion and erosion," proc. 6th International Conference on Erosion by Liquid and Solid Impact J. E. Field and N. S. Corney (eds.), Cambridge University Press (Cambridge), paper 37.

- Holtzer, G. J. and Rademakers, P. L. (1991), "Studies of 90 MWth AKZO and 4 MWth TNO FBC show excellent erosion-corrosion results," proc. 11th Int. Conf. on Fluidized Bed Combustion, E. J. Anthony (ed.), ASME, New York, 743-753.
- Hussey, R. J., Sproule, G. I., Caplan, D. and Graham, M. J. (1977), "The growth and structure of oxide films formed on Fe in O₂ and CO₂ at 550° C," Oxidation of Metals, **11**(2), 65-79.
- Hutchings, I. M. (1979), "Mechanisms of the erosion of metals by solid particles," in Erosion: Prevention and Useful Applications (ed. W.F. Adler) (Philadelphia: ASTM), 59-76.
- Hutchings, I. M. (1981), "A model for the erosion of metals by spherical particles at normal incidence," Wear, **70**, 269-281.
- Hutchings, I. M. and Levy, A. V. (1986), "Thermal effects in the erosion of ductile metals," proc. Corrosion-Erosion-Wear of Materials at Elevated Temperatures. A.V. Levy (ed.), NACE, Houston TX (Berkeley, CA) 121-133.
- Hutchings, I. M., Little, J. A. and Ninham, A. J. (1991), "Low velocity erosion-corrosion of steels in a fluidized bed," proc. 4th Int. Conf. on Corrosion-Erosion-Wear of materials at Elevated Temperatures. A. V. Levy (ed.), NACE, Houston, TX. (Berkeley, CA.), paper 14.
- Jacobson, S., Wallen, P. and Hogmark, S. (1987), "Fundamental aspects of abrasive wear studied by a new numerical simulation model," proc. Wear of Materials K. C. Ludema (ed.), ASME (Houston, TX).
- Kahveci, A. I. and Welsch, G. (1983), "High temperature oxidation of Fe-3wt% Cr alloy," Scripta Metallurgica, **17**, 121-126.
- Kang, C. T., Petit, F. S. and Birks, N. (1987), "Mechanisms in the simultaneous erosion-oxidation attack of nickel and cobalt at high temperature," Metall. Trans. A, **18**, 1785-1803.
- Kara, F., Rogers, P.M., Hutchings, I. M. and Little, J. A. (1996), " Microstructural characterisation of surface layers formed on a low alloy steel during erosion-oxidation in a fluidized bed," to be published in Journal of Materials Science.

- Kato, K. (1990), "Wear Mode Transitions," Scripta Metallurgica, **24**, 815-820.
- Khanna, A. S. and Gnanamoorthy, J. B. (1985), "Effect of cold work on the oxidation resistance of 2.25Cr-1Mo steel," Oxidation of Metals, **23**, 17-33.
- Kofstad, P. (1988), "High Temperature Corrosion," (London: Elsevier)
- Kosel, T. H. (1992), "Solid particle erosion," in ASM Handbook, Friction Lubrication and Wear Technology (ASM International), 199-213.
- Labun, P. A., *et al.* (1982), "Microstructural investigation of the oxidation of an Fe-3% Cr alloy," Metallurgical Transactions A, **13A**, 2103-2112.
- Lawn, B. R. and Swain, M. V. (1975), "Microfracture beneath point indentations in brittle solids," Journal of Material Science, **10** 113-122.
- Lawn, B. R. and Wilshaw, T. R. (1975), "Review: Indentation fracture, principles and application," Journal of Materials Science, **10**, 1049-1081.
- Lawn, B. R. and Fuller, E. R. (1975), "Equilibrium penny-like cracks in indentation fracture," Journal of Materials Science, **10**, 2016-2024.
- Levy, A. V., Slamovich, E. and Jee, N. (1986), "Elevated temperature combined erosion-corrosion of steels," Wear, **110**, 117-149.
- Levy, E. K. and Bayat, F. (1990), "Effects of bubbling on tube wastage in fluidized bed combustors," proc. 4th Int. Conf. on Corrosion-Erosion-Wear of Materials at Elevated Temperatures, A.V. Levy (ed.), NACE, Houston, TX.(Berkeley, CA) paper 24.
- Lewis, E. C., Canonico, D. A. and Vincent, R. Q. (1990), "Metal wastage experiences in BFBC environments," proc. 4th Int. Conf. on Corrosion-Erosion-Wear of Materials at Elevated Temperatures, A.V. Levy (ed.), NACE, Houston, TX.(Berkeley, CA) paper 20.
- Little, J. A., Hutchings, I. M. and Entwisle, M. J. (1987), "Erosion-corrosion testing of fluidized bed combustor materials: a new experimental method," proc. 3rd Int. Conf. on Corrosion-Erosion-Wear of Materials at Elevated Temperatures. A.V. Levy (ed.), NACE, Houston, TX. (Berkeley, CA), 324-328.

- Liu, Y. Y. and Natesan, Y. (1988), "Oxidation-Erosion of metals and alloys: models, verification and prediction," Surface and Coatings Technology, **36**, 407-417.
- MacAdam, S. S. and Stringer, J. (1987), "Development of a unique laboratory scale fluidized bed wear testing unit," proc. Int. Conf. Wear of Materials K.C. Ludema (ed.), ASME (Denver, Colorado).
- MacAdam, S. S., Stringer, J. and Levy, A. V. (1989), "A novel laboratory test procedure for studying in-bed erosion - Design and some early results," proc. 10th Int. Conf. on Fluidized Bed Combustion (San Francisco, CA), 1219-1224.
- MacAdam, S. S. and Stringer, J. (1991a), "The nature of bubble-induced wear of in-bed tubes in FBC environments," proc. 4th Int. Conf. on Corrosion-Erosion-Wear of materials at Elevated Temperatures. A.V. Levy (ed.), NACE, Houston, TX. (Berkeley, CA.), paper 17.
- MacAdam, S. S. and Stringer, J. (1991b), "Particle impact and impact distribution within a fluidized bed combustor environment," Wear, **141**, 373-394.
- MacAdam, S. S. and Stringer, J. (1993a), "Some effects of bed particle properties on wear in fluidized bed combustors," Wear, **169**, 141-152.
- MacAdam, S. S. and Stringer, J. (1993b), "Temperature dependence of steel wastage in a bubbling fluidized bed simulator," Corrosion, **49**, 156-169.
- MacAdam, S. S. and Stringer, J. (1995), "The circumferential distribution of wastage on in-bed tubes in fluidized bed combustors," Wear, **186-187**, 156-169.
- Malik, S. (1990), "Oxidation of metals in a temperature gradient," PhD dissertation, University of Kent at Canterbury.
- Mamoun, M. M. (1975), "Analytical models for the erosive-corrosive wear process." (Argonne National Laboratory).
- Markworth, A. J., Nagarajan, V. and Wright, I. G. (1991), "An approach to modelling simultaneous high-temperature oxidation and erosion," Oxidation of Metals, **35**(1), 89-106.

Minchener, A. J. and Kelsall, G. J. (1990), "The control of NO_x emissions from PFBC systems," Journal of the Institute of Energy, **June**, 85-91.

Misra, A. and Finnie, I. (1980), "A classification of three-body abrasive wear and design of a new tester," Wear, **60**, 111-121.

Misra, A. and Finnie, I. (1981a), "On the size effect in abrasive and erosive wear," Wear, **65**, 359-373.

Misra, A. and Finnie, I. (1981b) , "Correlations between two-body and three-body abrasion and erosion of metals," Wear, **68**, 33-39.

Montrone, E. D. (1990), "Metal wastage experience in pressurized fluidized bed combustor environments," proc. 4th Int. Conf. on Corrosion-Erosion-Wear of Materials at Elevated Temperatures, A.V. Levy (ed.), NACE, Houston, TX.(Berkeley, CA) paper 21.

Moore, J. J.(1990), "Chemical Metallurgy," 2nd edn. (London: Butterworth and Co.).

NCB (1985), "Fluidized combustion of coal," National Coal Board, London.

Neilson, J. H. and Gilchrist, A. (1968), "Erosion by a stream of solid particles," Wear, **11**, 111-122.

Nicholls, J. R. and Stephenson, D. J. (1995), "Monte Carlo modelling of erosion processes," Wear, **186-187**, 64-77.

Ninham, A. J., Entwisle, M. J., Hutchings, I. M. and Little, J. A. (1989a), "A laboratory-scale fluidized bed rig for high-temperature tube wastage studies," proc. 10th Int. Conf. on Fluidized Bed Combustion. A.M. Manaker (ed.), ASME, New York. (San Francisco, CA), 1219-1224.

Ninham, A. J., Entwisle, M. J., Hutchings, I. M. and Little, J. A. (1989b), "Erosion-corrosion of austenitic and ferritic alloys in a fluidized bed environment," proc. Corrosion '89, April 1989 (ed.), NACE, Houston, TX. (New Orleans, LA.). Also published in Corrosion, **46**, 296-301 (1990).

Ninham, A. J., *et al.* (1991), "Temperature Gradient effects in erosion-corrosion," proc. 4th Int. Conf. on Corrosion-Erosion-Wear of materials at Elevated Temperatures. A.V.

Levy (ed.), NACE, Houston, TX. (Berkeley, CA.), Paper 23.

Païdassi, J. (1956), "Sur l'Oxydation du fer dans l'Air dans l'Intervalle 400° - 700° C," Acta Metallurgica, **4**, 227-229.

Parkinson, M. (1987), "Current work on cold modelling of FB systems," EPRI Workshop: Wastage of in-bed surfaces in fluidized bed combustors, Argonne, Illinois, paper 5.1.

Perrow, J. M., Smeltzer, W. W. and Embury, J. D. (1968), "The role of structural defects in the growth of nickel oxide films," Acta Metallurgica, **16**, 1209-1218.

Pilling, N. B. and Bedworth, R. E., (1923) Journal of the Institute of Metallurgy, **23**, 529

Pinder, L. W. (1977), "Oxidation kinetics and scale morphology of mild steel and low chromium alloy steels in N₂/20%O₂ between 500° and 850° C," (CEGB Scientific Services department Midlands Region).

Pfeil, L. B. (1929), "The oxidation of iron and steel at high temperatures," The Journal of the Iron and Steel Institute, **119**(1), 501-560.

Price, W. R. (1967), "On the effect of cold work on the oxidation of iron from 400° to 650° C," Corrosion Science, **7**, 473-474.

Rabinowicz, E., Dunn, L. A. and Russell, P.G. (1961), "A study of abrasive wear under three-body conditions," Wear, **4**, 245-255.

Rademakers, P. L. F. and Kettunen, P. O. (1986), "Materials requirements and selection for fluidized bed combustors," Proc. Int. Conf. High temperature alloys for gas turbine and other applications, W. Betz *et al.* (ed.), Reidel, Dordrecht Holland, (Liège, 6-9 Oct.), Vol. 1, 269-295.

Raman, R. K. S., Dayal, R. K., Khanna, A. S. and Gnanamoorthy, J.S. (1989), "Grain size effect on the oxidation behaviour of 2.25Cr-1Mo steel," Journal of Materials Science Letters, **8**, 277-278.

Rapp, R. A. (1984), "The high temperature oxidation of metals forming cation-diffusing scales," Metallurgical Transactions A, **15**, 765.

Rickerby, D. G. and Macmillan, N. H. (1980), "The erosion of aluminum by solid particle impingement at normal impact," Wear, **60**, 369-382.

Rishel, D. M., Pettit, F. S. and Birks, N. (1991), "Some principal mechanisms in the simultaneous erosion and corrosion attack of metals at high temperature," proc. 4th Int. Conf. on Corrosion-Erosion-Wear of materials at Elevated Temperatures. A.V. Levy (ed.), NACE, Houston, TX. (Berkeley, CA), Paper 16.

Rogers, P. M., Hutchings, I. M. and Little, J. A. (1990), "The Erosion-corrosion of nitrocarburized low alloy steels in a simulated FBC environment," proc. Int. Conf. on Surface Engineering: Current trends and future prospects. S.A. Meguid (ed.), Elsevier, London (Toronto), 29-38.

Rogers, P. M., Hutchings, I. M. and Little, J. A. (1992a), "TiN coatings for protection against combined wear and oxidation," Surface Engineering, **8**(1), 48-54.

Rogers, P. M. (1992b), "Erosion-corrosion of materials in a fluidized bed environment," PhD dissertation, (University of Cambridge).

Rogers, P. M., Hutchings, I. M. and Little, J. A. (1992c), "Surface features on a low alloy steel exposed in a simulated fluidized bed combustor environment," Wear, **154**, 269-285.

Rogers, P. M., Howes, T. E., Hutchings, I. M. and Little, J. A. (1995), "Wastage of low alloy steels in a fluidized bed environment," Wear, **186-187**, 306-315.

Saunders, S. R. J. (1984), "Effects of trace elements and environmental impurities on oxidation and hot-salt corrosion characteristics of superalloys," Metals Technology, **11**, 465-473.

Sethi, V. K. and Corey, R. G. (1987), "High Temperature erosion of alloys in oxidising environments," proc. 7th Int. Conf. Erosion by Liquid and Solid Impact. J.E Field and J.P. Dear (ed.), Cavendish Lab, University of Cambridge. (Cavendish Lab., Cambridge England. 7-10 Sept. 1987), paper 73.

- Sethi, V. K. and Wright, I. G. (1990), "A description of erosion-oxidation based on scale removal and scale erosion," proc. 4th Int. Conf. on Corrosion-Erosion-Wear of Materials at Elevated Temperatures A.V. Levy (ed.), NACE, Houston, TX.(Berkeley, CA) paper 18.
- Sewell, P. B. and Cohen, M. (1964), "The Oxidation of Iron Single Crystals around 200° C," Journal of the Electrochemical Society, **111**, 501-508.
- Sheldon, G. L. and Finnie, I. (1966), Trans. ASME Journal of Engineering for Industry, **88**, 387-392.
- Simms, N. J. and Little, J. A. (1987), "High-temperature oxidation of Fe-2 1/4-1Mo in oxygen," Oxidation of Metals, **27**(5/6), 283-299.
- Smeltzer, C. E., Gulden, M. E. and Compton, W. A. (1970), Journal of Basic Engineering Trans. ASME, **92**, 639-654.
- Stack, M. M., Stott, F. H. and Wood, G. C. (1991), "Erosion-corrosion of preoxidised Incoloy 800h in fluidised bed environments: effects of temperature, velocity, and exposure time," Materials Science and Technology, **7**, 1128-1137.
- Stack, M. M., Stott, F. H. and Wood, G. C. (1992), "The effect of pre-oxidation of chromia and alumina forming alloys on erosion in laboratory simulated fluidized-bed conditions," Corrosion Science, **33**(6), 965-983.
- Stack, M. M., Stott, F. H. and Wood, G. C. (1993), "Review of mechanisms of erosion-corrosion of alloys at elevated temperatures," Wear , **162-164**, 706-712.
- Stack, M. M., Lekatos, S. and Stott, F. H. (1995a), "Erosion-corrosion regimes: number, nomenclature and justification?," Tribology International, **28**, 445-451.
- Stack, M. M. and Bray, L. (1995b), "Interpretation of wastage mechanisms of materials exposed to elevated temperature erosion-corrosion using erosion-corrosion maps and computer graphics," Wear, **186-187**, 273-283.
- Stallings, J. W. and Stringer, J. (1990), "Mechanisms of in-bed tube wastage in fluidized-bed combustors," proc. 4th Int. Conf. on Corrosion-Erosion-Wear of Materials at Elevated Temperatures, A.V. Levy (ed.), NACE, Houston, TX.(Berkeley, CA) paper 19.

Stencel, J. M. *et al.* (1990), "Effect of chlorine on wastage of in-bed heat exchanger surfaces under FBC conditions," proc. 4th Int. Conf. on Corrosion-Erosion-Wear of Materials at Elevated Temperatures, A.V. Levy (ed.), NACE, Houston, TX.(Berkeley, CA) paper 32.

Stephenson, D. J., Nicholls, J. R. and Hancock, P. (1983), "The influence of scale/substrate properties on high temperature erosion in gas turbines," proc. 6th International Conference on Erosion by Liquid and Solid Impact J.E. Field and N.S. Corney (eds.), (Cambridge, England), paper 48.

Stott, F. H., Glascott, J. and Wood, G. C. (1987), "The sliding wear of in-situ formed oxides on iron and nickel-base alloys," proc. 3rd Int. Conf. on Corrosion-Erosion-Wear of Materials at Elevated Temperature. A.V. Levy (ed.), NACE, Houston TX. (Berkeley, CA.), 263-277.

Stott, F. H., Green, S. W. and Wood, G. C. (1989), "The influence of temperature on the erosion oxidation of steels in a fluidized-bed environment," Materials Science and Engineering, **A121**, 611-617.

Stott, F. H., Tiong, K. K. and Stack, M. M. (1991), "The influence of chromium on the erosion-corrosion of iron-base alloys under fluidized-bed conditions," proc. Eurocorr 91 I.Karl and M. bcd (ed.), (Budapest), 282-287.

Stringer, J. (1970), "Stress generation and relief in growing oxide films," Corrosion Science, **10**, 513-543.

Stringer, J. and Wright, I. G. (1986), J. Mater. Energy Syst., **8**, 319-331.

Stringer, J. and Wright, I. G. (1987), "Erosion/corrosion in FBC boilers," proc. Workshop on wastage of in-bed surfaces in fluidized bed combustors, EPRI, Palo Alto, CA, 1-1 - 1-38.

Stringer, J. and Stallings, J. (1991), "Materials issues in circulating fluidized-bed combustors," proc. 11th Int. Fluidized Bed Combustion Conf.: Clean energy for the world, E.J. Anthony (ed.), ASME, New York, 589-608

Stringer, J. (1995), "Practical experience with wastage at elevated temperatures in coal combustion systems," Wear, **186-187**, 11-27

Sundararajan, G. (1983), "An analysis of the localization of deformation and weight loss during single-particle normal impact," Wear, **84**, 217-235.

Sundararajan, G. and Shewmon, P.G. (1983), "A new model for the erosion of metals at normal incidence," Wear, **84**, 237-258.

Sundararajan, G. (1987), "A new model for two-body abrasive wear based on localization of plastic deformation," Wear, **117**, -35.

Sundararajan, G. (1990), "The solid particle erosion of metallic materials at elevated temperatures," proc. 4th Int. Conf. on Corrosion-Erosion-Wear of Materials at Elevated Temperatures. A.V. Levy (ed.), NACE Houston TX (Berkeley, CA), paper 11.

Sundararajan, G. (1991), "An analysis of the erosion-oxidation interaction mechanisms," Wear, **145**, 251-282.

Tilly, G. P. (1973), "A two stage mechanism of ductile erosion," Wear, **23**, 87-96.

Wada, S. and Watanabe, N. (1992), in Erosion of Ceramic Materials (ed. J.E. Ritter, Trans tech publishing).

Wager, C. (1933), Z. phys. Chem., **21**, 25.

Wang, B., Geng, G., and Levy, A. V. (1990), "Erosion-corrosion of tubing steels at simulated fluidized bed combustor convection pass conditions," proc. 4th Int. Conf. on Corrosion-Erosion-Wear of materials at Elevated Temperatures. A.V. Levy (ed.), NACE, Houston, TX. (Berkeley, CA), Paper 15.

Wang, B. Q., Geng, G. Q. and Levy, A. V. (1991a), "Erosion-corrosion of 1018 steel eroded at low velocities by CFBC bed material," proc. 8th Int. Conf. on Wear of Materials K. C. Ludema, R. G. Bayer (eds.), ASME, New York, (Orlando, FL), 703 - 707

Wang, B. Q., Geng, G. Q. and Levy, A. V. (1991b), "Effect of microstructure on the erosion-corrosion of steels," Wear, **151**, 351-364.

Wang, B. Q., Geng, G. Q. and Levy, A. V. (1993a), "Erosion and corrosion of cooled 1018 steel," Wear, **161**, 41-52.

Wang, B., Geng, G. and Levy, A.V. (1993b), "Effect of microstructure on material wastage in a room-temperature fluidized-bed wear-test rig," Wear, **165**, 25-33.

Weast, R.C. (1976-1977), "Handbook of Chemistry and Physics", F-279.

Wheeldon, J. M., Stallings, J. W., Sethi, V. K. and Wright, I. G. (1990), "Preliminary results from a programme to identify bed material properties which may have promoted loss from evaporator tubing in TVA's 20-MWe bubbling AFBC pilot plant," proc. 4th Int. Conf. on Corrosion-Erosion-Wear of Materials at Elevated Temperatures, A.V. Levy (ed.), NACE, Houston, TX.(Berkeley, CA) paper 22.

Wiederhorn, S. M. and Lawn, B. R. (1979), "Strength degradation of glass impacted with sharp particles: I, Annealed Surfaces," Journal of the American Ceramic Society, **62**, 66-70.

Wiederhorn, S. M. and Hockey, B. J. (1983), "Effect of material parameters on the erosion resistance of brittle materials," Journal of materials science, **18**, 766-780.

Winter, R. E. and Hutchings, I. M. (1974), "Particle erosion of ductile metals: a mechanism of material removal.," Wear, **27** , 121-128.

Zhang, H., Hou, P.Y. and Stringer, J. (1996), "The effect of temperature gradient on steel tube wastage in a bubbling fluidized bed simulator," to be published in Wear.

Zum Gahr, K. H. (1987), "Microstructure and wear of materials," Tribology series Vol. 10 (Amsterdam: Elsevier)

Zum Gahr, K. H. (1988), "Modelling of two-body abrasive wear," Wear, **124**, 87-103.